# Measurement of the $t\bar{t}$ Production Cross Section using the Semileptonic Final States in $pp$ Collisions at $\sqrt{s} = 7\ TeV$ with 35.3 $pb^{-1}$ of ATLAS Data


by

Xiaowen Lei


---

A Dissertation Submitted to the Faculty of the


Department of Physics


In Partial Fulfillment of the Requirements
For the Degree of

Doctor of Philosophy

In the Graduate College


The University of Arizona


2011

# THE UNIVERSITY OF ARIZONA
# GRADUATE COLLEGE

As members of the Dissertation Committee, we certify that we have read the dissertation prepared by Xiaowen Lei
entitled Measurement of the $t\bar{t}$ Production Cross Section using the Semileptonic Final States in $pp$ Collisions at $\sqrt{s} = 7\ TeV$ with 35.3 $pb^{-1}$ of ATLAS Data
and recommend that it be accepted as fulfilling the dissertation requirement for the Degree of Doctor of Philosophy.

Date: 20 May 2011

Kenneth Johns

Date: 20 May 2011

Elliott Cheu

Date: 20 May 2011

Li-Zhi Fang

Date: 20 May 2011

Shufang Su

Date: 20 May 2011

William Wing

Final approval and acceptance of this dissertation is contingent upon the candidate's submission of the final copies of the dissertation to the Graduate College.
I hereby certify that I have read this dissertation prepared under my direction and recommend that it be accepted as fulfilling the dissertation requirement.

Date: 20 May 2011

Dissertation Director: Kenneth Johns

# Statement by Author

This dissertation has been submitted in partial fulfillment of requirements for an advanced degree at the University of Arizona and is deposited in the University Library to be made available to borrowers under rules of the Library.



Signed: Xiaowen Lei

# ACKNOWLEDGEMENTS

First and foremost, I must thank my advisor, Professor Kenneth Johns, for his guidance, support, and friendship over the past several years. Ken's insight, enthusiasm, and intelligence has set an example for me to follow. I would also like to thank Professor Elliott Cheu, Professor Shufang Su, Professor Li-Zhi Fang, and Professor William Wing, for agreeing to be my committee members, and for the valuable suggestions and discussions on my dissertation.

I would like to thank all the faculty, staff, and other members in the Arizona EEPP group. I feel lucky to have worked in this wonderful group, which provides a variety of physics and detector related research opportunities. Thanks everyone for keeping your doors open and always being so cheerful. I want to thank my fellow grad students in the group, especially Caleb Lampen, who I spent a lot of time with at CERN. I still remember the first time when Caleb and I went to CERN. There is nothing better than a friend's familiar face in an unfamiliar place.

Thanks to all the people I worked with on the ATLAS experiment. Special thanks to Diego Casadei, Kyle Cranmer, and Allen Mincer in the trigger missing $E_T$ slice group. I learned a lot from them at the weekly missing $E_T$ slice meetings. Thanks to Anna Hendrich for the discussions on the top likelihood method for the $t\bar{t}$ cross section measurement. And thanks to Lisa Shabalina for providing very useful documentation. To my friends at CERN, Yue Zhou, Jinghui Zhang, and Zhiling Chen, all I can say is thank you for all the help while I was there, and wish you happiness every single day.

Thanks to all my friends in Arizona. Especially Si, it is always good to be a classmate with you and to discuss problems with you. You really know a lot. Lu, I still remember the very first day I came to Tucson. I stayed at your place, and your hospitality will be passed one by one to the incoming Chinese graduate students. Sheng, you showed me what a person with strong determination can and should do. Baijie, its hard to find a female friend here, but you are the best. And Regina, I always hope I can be as happy as you every day.

I can't thank my parents in China enough. Even though you are not here with me today, I would have never come this far without your unconditional love and support. Also thanks to Bingyan, my younger sister, who is also one of my best friends.

Finally, I thank you, Liang, your love has enriched every day of my life.

# Table of Contents

TABLE OF CONTENTS – *Continued*

TABLE OF CONTENTS – *Continued*

TABLE OF CONTENTS – *Continued*

# List of Figures

List of Figures – *Continued*

LIST OF FIGURES – *Continued*

LIST OF FIGURES – *Continued*

LIST OF FIGURES – *Continued*

# List of Tables

LIST OF TABLES – *Continued*

List of Tables – *Continued*

List of Tables – *Continued*

# Abstract

A measurement of the production cross section for top quark pairs ($t\bar{t}$) in $pp$ collisions at $\sqrt{s} = 7\ TeV$ is presented using data recorded with the ATLAS experiment at the Large Hadron Collider in 2010. Events are selected in the $t\bar{t}$ semileptonic decay channel by requiring a single lepton (electron $e$ or muon $\mu$), large missing transverse energy and at least four jets. In a data sample of 35.3 $pb^{-1}$, 396 $e + jets$ events and 653 $\mu + jets$ events are observed. A multivariate top likelihood is built from four variables including a $b$-tagging variable. A fit to the top likelihood distribution is employed to extract the $t\bar{t}$ cross section separately in the $e + jets$ and $\mu + jets$ channel. A combined fit to the top likelihood distribution in both channels is employed to extract a combined cross section. The $t\bar{t}$ cross section, assuming a top mass of 172.5 $GeV$, is found to be:

$$e + jets \text{ channel: } \sigma_{t\bar{t}} = 164.4^{+16.2}_{-15.4}(\text{stat})^{+31.2}_{-36.2}(\text{syst})^{+5.8}_{-5.4}(\text{lumi})\ pb$$

$$\mu + jets \text{ channel: } \sigma_{t\bar{t}} = 167.8^{+13.9}_{-13.4}(\text{stat})^{+30.9}_{-34.8}(\text{syst})^{+5.9}_{-5.5}(\text{lumi})\ pb$$

$$e + jets \text{ and } \mu + jets \text{ combined: } \sigma_{t\bar{t}} = 166.4^{+10.5}_{-10.2}(\text{stat})^{+31.7}_{-33.6}(\text{syst})^{+5.9}_{-5.5}(\text{lumi})\ pb$$

The measurement agrees with approximate NNLO perturbative QCD calculations.

# Chapter 1

# Introduction

The goal of particle physics is to describe the fundamental building blocks of matter and their interactions. Currently it is believed that the elementary building blocks of nature consist of 12 fermions (spin-$\frac{1}{2}$), their associated antiparticles, and the gauge bosons (spin-integer) that mediate the interactions between them. The elementary particles interact by four fundamental interaction forces: the electromagnetic (EM) interaction, the weak interaction, the strong interaction, and the gravitational interaction. Studying the fundamental particles and interactions improves our understanding of nature. Historically, discoveries in particle physics have also led to practical uses (electricity, nuclear power, medical diagnosis and treatment, etc.).

Our current understanding of the fundamental particles and interactions is embodied in the Standard Model (SM). This model has been tremendously successful in describing a wide variety of phenomenons in the particle physics domain. However, it is esthetically unsatisfactory in that it contains many parameters that are not predicted by the theory. Other theoretical difficulties include the hierarchy problem and the strong CP (Charge-Parity) problem (See Section 2.1.4). The Standard Model also does not describe the gravitational interaction. It is generally felt that a more fundamental theory is waiting to be discovered. Thus physicists are constantly searching for an observation that violates the Standard Model.

Within the Standard Model, the 12 fermions are grouped into three generations of leptons and quarks. The quarks are different from the leptons in that they are always bound by the strong interaction and form particles called hadrons. There are two types of hadrons: baryons and mesons. Protons and neutrons are examples of baryons. While everyday matter consists only of electrons, protons, and neutrons, at high energies comparable to those shortly after the Big Bang, other elementary particles also play a major role. The conditions needed to produce these particles can be obtained in the laboratory through the use of particle accelerators.

Currently the world's most powerful accelerator is the Large Hadron Collider (LHC), located at CERN (the European Organization for Nuclear Reserach), in Geneva, Switzerland. The LHC currently collides proton-proton pairs ($pp$) at a center-of-mass energy ($\sqrt{s}$) of 7 $TeV$.

This dissertation investigates one of the six quarks, the top quark ($t$). The topic of the dissertation is to measure the top quark pair ($t\bar{t}$) production cross section in $pp$ collisions at $\sqrt{s} = 7\ TeV$. The measurement is performed in the semileptonic final states of the $t\bar{t}$ decay ($t\bar{t} \rightarrow e + jets$ and $t\bar{t} \rightarrow \mu + jets$). It utilized approximately 35.3 $pb^{-1}$ of data produced by the Large Hadron Collider. The data was collected by the ATLAS experiment in 2010. This measurement is one of the first measurements of the $t\bar{t}$ cross section at this energy. This measurement, though statistically limited, provides an early test of the SM at this energy. It also boosts our confidence that we understand SM $t\bar{t}$ production at this energy so that we can begin to search for anomalous behavior such as $t\bar{t}$ resonances that would signal Beyond the Standard Model (BSM) physics. Understanding the knowns is a necessary step before searching for new unknowns.

## 1.1 Importance of Top Quark Physics

The top quark was discovered by the DØ and CDF experiments at the Fermilab Tevatron in Batavia, Illinois, in 1995. Its discovery completes the three generation structure of quarks of the Standard Model. Having been discovered just more than a decade ago, top quark physics remains a field of extensive research. A recent review on top quark physics can be found in [1]. Viewed as just another SM quark, the top quark may seem rather uninteresting. However, There are several reasons why top quark physics is important.

First, the top quark is distinguished by its large mass. With a mass of around 172 $GeV$, it is the heaviest elementary particle observed so far. What's more, the top mass is intriguingly close to the electroweak symmetry breaking (EWSB) scale ($v \sim 246\ GeV$ [2]). This suggests that the top quark may be very important for understanding aspects of the EWSB. Further, the top quark couples strongly with the Higgs sector due to its large mass. This could indicate that all new physics in connection with the EWSB should couple preferentially to the top quark. As a result, some Beyond Standard Model (BSM) theories consider that the top quark plays a fundamental role in the EWSB mechanism. This makes understanding top quark physics important for the search of new physics.

Due to its large mass, the top quark has a unique short life time ($\tau_{top} = 1/\Gamma_{top} \approx 5 \cdot 10^{-25}\ s$), which is almost an order smaller than the characteristic time of the QCD hadronization ($\sim 1/\Lambda_{QCD} \approx 3 \cdot 10^{-24}\ s$). This means the top quark decays before it couples to other quarks to form hadrons and gives physicists a unique opportunity to study a "bare" quark.

## 1.2 Importance of $t\bar{t}$ Cross Section

The topic of the dissertation is the measurement of the $t\bar{t}$ production cross section in the semileptonic decay final states in $pp$ collisions at $\sqrt{s} = 7\ TeV$. The general goal is to make a benchmark test of perturbative QCD (Quantum Chromodynamics, see Section 2.1.3) by comparing experimental measurement with the theoretical prediction. Although the Standard Model is highly successful, we still need to probe every corner of it through measurement. Deviations from the theory may give hints to the direction of new physics. This is especially true for QCD, which is still not as well tested as the EW (electroweak) theory (see Section 2.1.1).

The $t\bar{t}$ cross section measurement could be a test of new physics, since non-SM processes could significantly increase or decrease the cross section. Precise determination of the $t\bar{t}$ cross section is also very important for searches of new physics channels at the LHC, because $t\bar{t}$ production is a major background for some channels of Higgs search, as well as for various BSM signals. The results of the $t\bar{t}$ cross section measurement in the semileptonic channels can also be used in consistency checks with measurement in other channels.

In addition to serving as a probe to the SM, a rigorous cross section measurement contributes to measurements of top properties such as mass, charge and decay properties. The selection criteria and the signal/background discrimination procedures used in this dissertation can also be used in measurement of the top properties. Further, a well established $t\bar{t}$ sample can be effectively used to understand and commission physics objects reconstructed in the ATLAS detector, including leptons, jets, and missing transverse energy (missing $E_T$, or $\not{E}_T$).

### 1.3 Cross Section Measurement

In particle physics, the cross section, $\sigma$, is the effective area representing interaction probability for a given process. For collider experiments such as the LHC, the cross section generally can be written as:

$$\sigma = \frac{N}{\int \mathcal{L}\, dt} \tag{1.1}$$

where $N$ and $\int \mathcal{L}\, dt$ are respectively the number of events and the integrated luminosity for a period of time.

Because the top quark decays almost instantaneously, it is detected through detecting its decay products. The measurement of the $t\bar{t}$ production cross section is typically performed in one of the $t\bar{t}$ decay final states, or decay channels. In this dissertation the measurement is performed in the semileptonic final states of the $t\bar{t}$ decay. Events in the final state are selected using a series of selection criteria. The $t\bar{t}$ cross section is written as:

$$\sigma_{t\bar{t}} = \frac{N_{t\bar{t}}}{\epsilon_{t\bar{t}} \times \mathrm{BR} \times \int \mathcal{L}\, dt} \tag{1.2}$$

where $N_{t\bar{t}}$ is the number of $t\bar{t}$ events in the semileptonic final state, $\epsilon_{t\bar{t}}$ is the efficiency of the selection criteria, $BR$ is the branching ratio of the final state, and $\int \mathcal{L}\, dt$ is the integrated luminosity.

After the event selection, a top likelihood approach was used to further discriminate the $t\bar{t}$ signal and the remaining backgrounds in data. This approach preserves the statistics and lessens the dependence on Monte Carlo for background determination. The number of $t\bar{t}$ events in the selected data is extracted by a maximum likelihood (ML) fit to the likelihood discriminant distribution in data using signal and background likelihood templates.

The rest of this dissertation is organized as follows. In Chapter 2, we give an overview of the Standard Model, followed by the theory for $t\bar{t}$ production and decays. The most accurate theoretical predictions are given. In Chapter 3, we describe the experimental apparatus: the LHC used to produce data and the ATLAS experiment used to collect data. In Chapter 4, we give an description of the procedure through which data recorded by the ATLAS detector is reconstructed and physics objects are identified. In Chapter 5, we describe the data and Monte Carlo samples used in this analysis. In Chapter 6, the event selection criteria used to select candidate events from the $e + jets$ and $\mu + jets$ final states are described. The signal selection efficiency is measured and the expected data composition is presented. In Chapter 7, we describe the top likelihood approach for further discrimination of the signal and background. In Chapter 8, we describe the procedures for extracting the number of signal events in data. In Chapter 9, the results of the $t\bar{t}$ cross section measurement are given. In Chapter 10, the results are compared with theoretical calculations as well as results from other measurements. A discussion on possible future improvements and directions is included.

# Chapter 2

# Theory

This chapter begins with an overview of the Standard Model (SM) in Section 2.1. Section 2.2 provides an outline of the theoretical formalism for calculating the $t\bar{t}$ production cross section, as well as results of recent theoretical calculations for $pp \to t\bar{t}$ at 7 $TeV$ based on the SM. The last section, Section 2.3, describes the three decay channels of the top quark pair ($t\bar{t}$), with a focus on the semileptonic channel, in which our measurement is performed. The branching ratios (BRs) are given for the different decay channels.

## 2.1 Standard Model

The Standard Model (SM) of elementary particles combines the Electroweak (EW) theory and Quantum Chromodynamics (QCD) to describe three of the four known fundamental interaction forces: the electromagnetic (EM) interaction, the weak interaction, and the strong interaction. Ever since it was formulated, the Standard Model has been spectacularly successful in its agreement with experimental measurements. The SM particles are summarized in Table 2.1, along with their discovery dates. The only particle predicted by the Standard Model but still not discovered is the Higgs boson.

Many experiments have confirmed the predictions and calculations of the SM to a high precision [2]. The theoretical predictions of the EM interaction have been the most stringently tested, with the fine structure constant $\alpha$ verified by experiment to a precision of $10^{-8}$. The EW theory has been tested to an order of roughly $10^{-3}$, by doing a global fit of its free parameters and then comparing individually measured values of the parameters with the values from the fit. The QCD theory is not tested as well as the EW theory. For example, the QCD inclusive jet cross section has been verified to an order of $10^{-1}$.

Currently, no experiment has seen significant discrepancy from the Standard Model. However, there are still aspects of the theory that are not satisfying. Some of these as-

| | Generation | | |
|---|---|---|---|
| | I | II | III |
| leptons | $\nu_e$ (1953)<br>$e$ (1897) | $\nu_\mu$ (1962)<br>$\mu$ (1936) | $\nu_\tau$ (2000)<br>$\tau$ (1975) |
| quarks | u (1968)<br>d (1968) | c(1974)<br>s(1968) | t (1995)<br>b (1977) |
| gauge bosons | | $g_1,...g_8$ (1979)<br>$\gamma$ (1900)<br>$W^{\pm}$,$Z^0$ (1983) | |

Table 2.1: Summary of the elementary matter particles and the gauge bosons, with the dates of discovery given in parentheses [3].

pects will be discussed in Section 2.1.4. Theories that attempt to address some of the shortcomings of the SM are referred to as Beyond Standard Model (BSM) theories.

Within the Standard Model, the 12 fermions that comprise matter are grouped into three generations of leptons and three generations of quarks, summarized in Table 2.2. The particles in the second and third generations are identical to those in the first except that they are more massive. Each of these particles has an associated antiparticle, which is not shown in the table. An antiparticle can be thought of as a "symmetric" copy of the corresponding particle, with the same mass and spin, and opposite charge. Antiparticles are denoted with a superscipted line over the greek letter. For example, antitop is $\bar{t}$. The quarks also carry one of three types of color charges commonly referred to as red, blue and green. The colors are denoted by subscripts, for example, the top quarks with different colors are $t_r$, $t_g$ and $t_b$. Antiquarks carry anticolors.

The three interaction forces described by the Standard Model are mediated by corresponding gauge bosons: the photon ($\gamma$) for the electromagnetic interaction, the $W$ and $Z$ bosons ($W^{\pm}$, $Z^0$) for the weak interaction and the gluons ($g$) for the strong interaction. It is postulated that a spin-2 boson called the graviton mediates the fourth force, the gravity. However, if one attempts to build a theory with graviton in the same fashion as with the other gauge bosons, one quickly finds divergences in calculation rendering the theory nonrenormalizable. In Table 2.3, the relative strength of the four interaction forces

| Generation | Particle | Spin | Charge (Q/e) | Mass | $N_{baryon}(B)$ | $N_{lepton}(L)$ |
|---|---|---|---|---|---|---|
| Leptons | | | | | | |
| 1 | electron | $\frac{1}{2}$ | -1 | 0.511 $MeV$ | 0 | 1 |
| | $\nu_e$ | $\frac{1}{2}$ | 0 | < 2 $eV$ | 0 | 1 |
| 2 | muon | $\frac{1}{2}$ | -1 | 106 $MeV$ | 0 | 1 |
| | $\nu_\mu$ | $\frac{1}{2}$ | 0 | < 0.19 $MeV$ | 0 | 1 |
| 3 | tau | $\frac{1}{2}$ | -1 | 1777 $MeV$ | 0 | 1 |
| | $\nu_\tau$ | $\frac{1}{2}$ | 0 | < 18.2 $MeV$ | 0 | 1 |
| Quarks | | | | | | |
| 1 | up | $\frac{1}{2}$ | $+\frac{2}{3}$ | 1.7–3.3 $MeV$ | $\frac{1}{3}$ | 0 |
| | down | $\frac{1}{2}$ | $-\frac{1}{3}$ | 4.1–5.8 $MeV$ | $\frac{1}{3}$ | 0 |
| 2 | charm | $\frac{1}{2}$ | $+\frac{2}{3}$ | 1.18–1.34 $GeV$ | $\frac{1}{3}$ | 0 |
| | strange | $\frac{1}{2}$ | $-\frac{1}{3}$ | 70–120 $MeV$ | $\frac{1}{3}$ | 0 |
| 3 | top | $\frac{1}{2}$ | $+\frac{2}{3}$ | 172.0 ± 0.9 ± 1.3 $GeV$ | $\frac{1}{3}$ | 0 |
| | bottom | $\frac{1}{2}$ | $-\frac{1}{3}$ | $4.19^{+0.18}_{-0.06}$ $GeV$ | $\frac{1}{3}$ | 0 |

Table 2.2: Summary of elementary particles and some of their properties [2]. The three generations of leptons are commonly denoted as $e$, $\nu_e$; $\mu$, $\nu_{mu}$ and $\tau$, $\nu_\tau$. The three generations of quarks are commonly denoted as u, d; c, s; and t, b. The generations are ordered increasingly by mass. Note that natural units are used here as well as other parts of this dissertation, which means that $c = 1$ and mass has the same unit as energy.

is summarized in terms of the order of magnitude of their coupling constants at a fixed distance. The mediator gauge bosons are also shown in the table along with their spin and mass. Note that there are eight different types of gluons, mediating the strong interaction between quarks with three different colors.

| Force | Coupling Constant | Strength | Meditator | Spin | Mass |
|---|---|---|---|---|---|
| Strong | $\alpha_s$ | 60 | Gluon | 1 | 0 |
| Electromagnetic | $\alpha$ | 1 | Photon | 1 | $< 1 \times 10^{-18}\ eV$ |
| Weak | $\alpha_W$ | $10^{-4}$ | $W^{\pm}$ | 1 | 80.4 GeV |
| | | | $Z^0$ | 1 | 91.2 GeV |
| Gravity | $\alpha_g$ | $10^{-36}$ | Graviton | 2 | ? |

Table 2.3: Summary of the interaction forces and their gauge bosons [2, 3]. In general, the coupling constant of the forces is dependent on the energy scale or equivalently the distance scale. The strength of the force between two particles depends in addition on the type of the particles considered. Here the strength is quoted relative to the electromagnetic force between two up quarks at a distance of $3 \times 10^{-17}\ m$. The mass of the gluon quoted here is the theoretical value. Note that a mass as large as a few $MeV$ may not be precluded.

Both the EW theory and the QCD theory that comprise the Standard Model are based on the symmetry principle of local gauge invariance. The Lagrangian of a gauge theory is required to have a continuous local symmetry, meaning it is unchanged under a continuous group of local (position-dependent) transformations. A Lagrangian including an ordinary kinematic energy term does not satisfy this requirement. By introducing gauge fields into the derivative operators in the Lagragian and forming gauge-covariant derivative operators, the Lagrangian of the theory is made to be invariant under a group of continuous local transformations, called local gauge transformations. The term "gauge" refers to the redundant degrees of freedom in choosing the configuration of the physical system.

The beauty of gauge theories lies in the fact that interaction forces as well as the conservation laws they obey arise naturally from the symmetry of the model. In the Lagrangian mechanism, conservation laws appear as symmetries of the Lagrangian. Generators of the symmetry transformations correspond to conserved physics quantities, such as electric charge in electrodynamics, weak isospin in EW theory and color in quantum chromodynamics. By constructing a Lagrangian with local gauge invariance as described above, gauge fields are introduced naturally and subsequently act as the mediators of interaction forces. In this way the interaction forces are specified. Corresponding to each generator of the gauge symmetry transformations, there is one gauge field introduced. The force associated with the gauge field conserves the physics quantity associated with the generator.

The best known force, the electromagnetic interaction, is described by Quantum Electrodynamics (QED), an abelian gauge theory of $U(1)_{EM}$ symmetry. The generator of the symmetry is the electric charge ($Q$). All charged fermions, including charged leptons and all quarks, can interact electromagnetically through the exchange of photons.

The weak force is described by the nonabelian symmentry $SU(2)_L$. All 12 fermions can interact via the weak force, but left-handed fermions and right-handed fermions interact differently. Left-handed fermions and right-handed antifermions are represented as doublets and they can interact through the exchange of both $W^{\pm}$ bosons (charged current) and $Z$ boson (neutral current), while right-handed fermions and left-handed antifermions can only interact via neutral current interaction.

The EM interaction and the weak interaction are unified in the EW symmetry and are described by the $SU(2)_L \otimes U(1)_Y$ symmetry group. The strong interaction is described in the QCD theory by the $SU(3)_C$ nonabelian group. Only quarks can interact via the strong interaction. Finally, combining the EW theory and the QCD theory, the Standard Model unifies all three interactions by the $SU(3)_C \otimes SU(2)_L \otimes U(1)_Y$ symmetry group. The Standard Model is the simplest renormalizable gauge theory that encompasses all the currently known elementary particles and the interaction forces among them.

There is vast literature on the Standard Model and the gauge interactions [3, 4]. Here only brief descriptions of a few major points are discussed in the following section.

### 2.1.1 Electroweak Theory

The Electroweak (EW) theory, also known as the Glashow-Weinberg-Salam theory, is constructed to be invariant under the $SU(2)_L \otimes U(1)_Y$ symmetry group. Under this symmetry, the forces are specified by the weak isospin $I$, the generator of the $SU(2)_L$ gauge transformation; and the weak hypercharge $Y$, the generator of the $U(1)_Y$ gauge transformation, related to the charge by $Q = I_3 + Y/2$. In the EW theory, left-handed fermions are represented as weak-isospin doublets and transform under both $SU(2)_L$ and $U(1)_Y$:

$$\begin{pmatrix} u \\ d \end{pmatrix}_L \begin{pmatrix} c \\ s \end{pmatrix}_L \begin{pmatrix} t \\ b \end{pmatrix}_L \begin{pmatrix} e \\ \nu_e \end{pmatrix}_L \begin{pmatrix} \mu \\ \nu_\mu \end{pmatrix}_L \begin{pmatrix} \tau \\ \nu_\tau \end{pmatrix}_L \tag{2.1}$$

while the right-handed fermions are represented as weak-isospin singlets and only transform under $U(1)_Y$. In addition, the masses of the neutrinos are often approximated to zero for convenience, in which case right-handed neutrinos do not exist.

The requirement of gauge invariance under the electroweak symmetry group necessitates four gauge bosons: three gauge bosons for the $SU(2)_L$ group, typically denoted $W^1$, $W^2$, $W^3$ and one for the $U(1)_Y$ group, typically denoted $B^0$. The EW gauge bosons listed in Table 2.3 can be written as linear combinations of these bosons:

$$W^{\pm} = \left(W^1 \mp W^2\right) / \sqrt{2} \tag{2.2}$$

$$Z^0 = W^3 cos\theta_W - B^0 sin\theta_W \tag{2.3}$$

$$\gamma = W^3 cos\theta_W + B^0 sin\theta_W \tag{2.4}$$

where $\theta_W$ is the weak mixing angle also known as the Weinberg angle.

The theory of the electroweak interaction described above is not yet a satisfactory one, for two reasons. Firstly, the four gauge interaction bosons in this theory are all massless, while experimentally, only the electromagnetic mediator, the photon, is massless. All the three weak gauge bosons ($W^{\pm}$, $Z^0$) have heavy masses (shown in Table 2.3). In addition, the global $SU(2)$ invariance of the isospin forbids mass terms for the fermions. This problem is solved by the Higgs mechanism, discussed in next session.

Another thing to note, specifically about the weak interaction between quarks, is that there is a mixing between the weak interaction eigenstates and the mass eigenstates. As a result, quarks are allowed to couple weakly to quarks from different generations. The mixing is described by the unitary Cabibbo-Kobayashi-Maskawa (CKM) matrix, with small off-diagonal elements.

### 2.1.2 Higgs Mechanism

The Higgs mechanism is an elegant solution to the above-mentioned mass problem in the EW theory, without breaking renormalizability of the theory. It makes use of the spontaneous symmentry breaking process, through which the symmetry of the Lagrangian of a theory gets broken by the physical vacuum of the system. For every generator of the symmetries that are spontaneously broken by the vacuum, a massless spin-zero particle, known as a Goldstone boson, will appear (for theories satisfying certain requirements[4]). In a locally gauge invariant field theory, by choosing an appropriate gauge, the additional degrees of freedom provided by the Goldstone bosons become the longitudinal degrees of freedom of the gauge bosons.

To apply the Higgs mechanism to the EW theory, first we introduce a complex doublet (the Higgs doublet) of scalar fields:

$$\phi = \begin{pmatrix} \phi^+ \\ \phi^0 \end{pmatrix} \tag{2.5}$$

into the theory, which transforms as a $SU(2)_L$ doublet. The potential energy term of the doublet is:

$$V(\phi) = \mu^2 \phi^\dagger \phi + \lambda \left(\phi^\dagger \phi\right)^2 \tag{2.6}$$

with $\mu^2 < 0$ and $\lambda > 0$.

And then, a vacuum expectation value of the scalar field is chosen:

$$\langle\phi\rangle_0 = \begin{pmatrix} 0 \\ v/\sqrt{2} \end{pmatrix} \tag{2.7}$$

where $v = \sqrt{-\mu^2/|\lambda|}$, which breaks both the local gauge symmetries $SU(2)_L$ and $U(1)_Y$, but conserves the $U(1)_{EM}$ symmetry. As a result of this, three massless Goldstone bosons are generated, corresponding to three generators of the broken symmentries. By "gauging away" the Goldstone bosons, three extra degrees of freedom from the Higgs doublet become masses of the gauge bosons of the broken symmetries ($W^\pm$ and $Z$), while the photon, corresponding to the unbroken $U(1)_{EM}$ symmetry, remains massless.

The remaining one degree of freedom from the Higgs doublet leads to a new massive scalar particle: the Higgs boson. The Yukawa couplings between the Higgs doublet and the leptons or the quarks are also added to the Lagrangian of the Standard Model, from which the masses of the leptons and quarks result. Because the Higgs Mechanism generates all the masses for the particles, the Higgs boson is commonly known as the ”God particle”. As of present, the Higgs boson remains the only undetected particles predicted by the Standard Model.

### 2.1.3 QCD

Quantum Chromodynamics (QCD) is the currently accepted gauge field theory for describing the strong interaction. A good reference on QCD and its applications in collider physics is [5]. Only a brief introduction is provided here. The $t\bar{t}$ cross section measurement presented in this dissertation provides a test of QCD. Aspects of QCD relevant for the $t\bar{t}$ cross section measurement will be discussed in detail in Section 2.2.

The QCD theory is based on the $SU(3)_C$ symmetry group, where “C” stands for the color charge, the generator of the symmetry. It is the color charge that allows quarks to coexist inside some hadrons in otherwise identical state, without violating the Pauli Exclusion Principle. Quarks carry three types of color charges, commonly referred to as red, green and blue, while antiquarks carry corresponding anticolor charges. Under the $SU(3)_C$ group, quarks transform as color triplets. Gauge invariance under this symmetry group requires eight massless gauge bosons, called gluons, each in a linearly independent color state that is a superposition of color and anticolor. Unlike the neutral photon, gluons can interact themselves via the strong force.

As mentioned at the beginning of this chapter, the strong interaction is different from the electroweak interactions in that free quarks do not exist. They are always confined by the strong force inside hadrons, which are color singlets, i.e., with total color charges of zero. There are two types of hadrons, called baryons and mesons. Baryons are formed by three quarks ($qqq$ or $\overline{qqq}$) with different colors, while mesons are formed by a quark and a antiquark ($q\bar{q}$) with matching color and anticolor. The phenomenon that only color singlet particles may exist in isolation is termed color confinement. Quarks and gluons, viewed as constituents of hadrons, are termed partons.

Although QCD has not been proved to be a color confining theory, it is found that the strong coupling "constant" $\alpha_s$ of QCD decreases at larger energy or smaller distance. This property, known as "asymptotic freedom", helps to explain why permanently confined quarks behave within hadrons as if they are free particles. At small distances inside hadrons, $\alpha_s$ is small and therefore quarks behave as quasi-free partons. At distances larger than the size of a hadron, $\alpha_s$ becomes very large, preventing quarks from escaping from hadrons. The QCD mass scale ($\Lambda_{QCD}$), defined as the energy scale at which $\alpha_s$ approaches infinity, is measured to be $\sim 200\ MeV$.

When pairs of partons are produced via hard scattering process, such as in high-energy $pp$ collisions at the LHC, they remain quasi-free for a very brief period of time. During this process $\alpha_s$ is small enough ($\ll 1$) for perturbative QCD to be applied. As the two quarks separate from each other, the gluon fields form narrow tubes of color charge, pulling the quarks together. At some point the potential energy between the pair of quarks becomes large enough to pull new $q\bar{q}$ pairs out from the vacuum. As the original $q\bar{q}$ pair separates further, additional $q\bar{q}$ pairs are produced, until the kinematic energy of the original $q\bar{q}$ is small enough and no further $q\bar{q}$ pairs can be produced. Since quarks can not exist freely, the final-state quarks undergo a process termed hadronization, in which they are joined by the strong force and form new hadrons. As a result, experiments do not detect free scattered partons. Rather, they detect narrow cones of hadrons, termed jets. The momentum of a jet reflects the momentum of its originating quark, or gluon (for a gluon jet).

### 2.1.4 Standard Model and Beyond

As stated at the beginning of this section, the Standard Model has been tremendously successful at describing a wide variety of phenomenons in the particle physics domain. However, there are still aspects of the theory that are unsatisfying, suggesting that the Standard Model is incomplete or an approximation of a more general theory. Theories that attempt to address some of the shortcomings of the SM are referred to as Beyond Standard Model (BSM) theories.

First, from a theoretical perspective, the Standard Model seems unnatural in several aspects. One example is the large number of free parameters in the theory. Not considering the neutrinos' masses, the Standard Model has a total of 19 free parameters [2]. There are the three gauge coupling parameters $g$, $g'$, $g_3$ respectively for the $SU(2)_L$, $U(1)_Y$ and $SU(3)_C$ groups, or equivalently, the fine structure constant $\alpha$, the weak mixing angle $\theta_W$ and the strong coupling constant $\alpha_s$:

$$\alpha = \frac{e^2}{4\pi} = \frac{g^2 g'^2}{4\pi(g^2 + g'^2)} \tag{2.8}$$

$$sin^2\theta_W = \frac{g'^2}{(g^2 + g'^2)} \tag{2.9}$$

$$\alpha_s = \frac{g_3^2}{4\pi} \tag{2.10}$$

The rest of the parameters include the nine fermion masses, the four CKM mixing parameters and the vacuum expectation value (VEV), $v$, of the Higgs boson. The last parameter is the QCD vacuum angle $\theta$ which appears in the CP (Charge-Parity) violating term in the QCD Lagrangian.

The Standard Model is esthetically unsatisfactory in that it contains so many parameters that are not predicted by the theory. Further, the Higgs mechanism, through which $W$ and $Z$ bosons and the fermions acquire their masses, is employed in an ad hoc way. Other theoretical difficulties include the hierarchy problem and the strong CP problem. A statement of the hierarchy problem is why the mass of the Higgs boson is much smaller than the Planck mass. A statement of the strong CP problem is why the QCD vaccum angle $\theta$ has to be tuned close to zero according to experimental results. Besides the theoretical problems, the Standard Model also leaves many questions unanswered. It does not provide a theory of gravitation. Particles predicted by Standard Model do not account for dark matter and dark energy, which together constituents 96% of the energy density in the universe. The Standard Model also can not explain the matter-antimatter imbalance observed.

A number of BSM theories have been proposed, in order to solve some or all of the problems of the Standard Model. There is supersymmetry (SUSY) theory, which proposes the symmetry between fermions and bosons. There are also theories with large extra dimensions, which provide a scenario to explain the weakness of gravity relative to the other forces. A number of these BSM models predict new production channels for the top quark. It is possible a measurement of the $t\bar{t}$ production cross section may show hints of the predictions.

## 2.2 Top Quark Pair Production

The $t\bar{t}$ production cross section is calculated using the theory of heavy quark production. In high-energy hadron-hadron collisions, heavy quarks ($q = t, b, c$) are produced via hard scattering between two partons, one from each hadron. The general form of heavy quark pair production cross section in collisions between hadron $A$ and $B$, expressed in terms of the parton distribution functions (PDFs), $f_i^A\left(x_A, \mu_f^2\right)$ and $f_j^B\left(x_B, \mu_f^2\right)$, and the short-distance partonic cross sections $\hat{\sigma}_{ij}$ for the process $ij \to q\bar{q}X$, is [6]:

$$\sigma\left(s, m^2\right) = \sum_{i,j} \int_0^1 dx_A \int_0^1 dx_B f_i^A\left(x_A, \mu_f^2\right) f_j^B\left(x_B, \mu_f^2\right) \hat{\sigma}_{ij}\left(\hat{s}, m^2; \alpha_s\left(\mu_r^2\right), \mu_r^2, \mu_f^2\right) \quad (2.11)$$

where

$s$ is the squared center-of-mass energy of the colliding hadrons $A + B$

$m$ is the mass of the heavy quark

$x_A(x_B)$ is the fractional momentum carried by the hard scattering parton in hadron $A(B)$

$\hat{s}$ is the squared center-of-mass energy of the colliding partons $i + j$:

$$\hat{s} = x_A x_B s \quad (2.12)$$

$\mu_r$ is the renormalization scale, at which the strong coupling constant $\alpha_s$ is evaluated

$\mu_f$ is the factorization scale, at which the PDFs $f_i^A$ and $f_i^B$ are evaluated

Note that $X$ in $ij \to q\bar{q}X$ denotes particles produced in addition to the heavy quark pair, e.g., gluons from soft radiation. These gluons appear as additional jets in the final state. It is not easy to tell which jets come from the heavy quark pair and which jets come from the gluons. As a result, an inclusive cross section is considered, with all the additional particles taken into account.

Equation 2.11 is a direct application of the QCD factorization theorem. The theorem states that the exact cross section, summed over all orders of $\alpha_s$, can be separated into the long-distance part, the PDFs, and short-distance partonic cross sections [7]. The PDF describes the probability of the hard scattering parton in a hadron to carry a fractional momentum $x$. It is independent of the particular hard scattering process, but is dependent on the factorization scheme chosen and the factorization scale $\mu_f$, an arbitrary energy scale set to define the separation between short-distance and long-distance effects. After the factorization, the short-distance cross section $\hat{\sigma}$ should be collinear safe, with all the collinear divergent terms factored into the PDF. The partonic cross section $\hat{\sigma}$ is also dependent on the factorization scheme and scale. However, the exact cross section, or measured cross section, $\sigma$, is by defintion independent of the factorization, with the scheme and scale dependence of the PDF and $\hat{\sigma}$ cancelling each other.

The partonic cross sections involved in calculating $\sigma(s, m^2)$ in Equation 2.11 can be expanded into a perturbative series in the strong coupling constant $\alpha_s$:

$$\hat{\sigma}\left(\hat{s}, m^2, \mu_r^2\right) = \frac{\alpha_s^2\left(\mu_r^2\right)}{m^2}\mathcal{F}_{ij}^{(0)}\left(\hat{s}, m^2\right) + \frac{\alpha_s^3\left(\mu_r^2\right)}{m^2}\mathcal{F}_{ij}^{(1)}\left(\hat{s}, m^2\right) + ... \tag{2.13}$$

and calculated using perturbative QCD. The coupling $\alpha_s$ is dependent on the renormalization scheme chosen and the renormalization scale $\mu_r$, an arbitrary energy scale at which the ultraviolet subtraction in renormalization is performed. However, the cross section summed over all orders is by definition independent of the renormalization. When the power series is truncated at order-$n$ of $\alpha_s$, the calculated cross section will have a $\mu_r$ dependence at $\sim O\left(\alpha_s^{n+1}\right)$.

The parton distribution function includes effects from processes occurring at small energy scales ($\alpha_s \sim 1$), and therefore is not calculable by perturbation theory. Instead, it is extracted in certain physics processes by comparing the measured hadronic cross section and calculated partonic cross section at certain order of $\alpha_s$. PDFs extracted this way can be used in other processes for cross section calculations at certain order of $\alpha_s$. The hadronic cross section calculated this way, using the "fixed-order" PDF, has a $\sim O\left(\alpha_s^{n+1}\right)$ dependence on the factorization scale $\mu_f$.

The modified minimum subtraction ($\overline{MS}$) scheme has been widely used as the standard scheme for renormalization and factorization, and therefore is used for the calculations here. To simply calculations, the renormalization and factorization scales are conventionally chosen to be equal to each other, $\mu_r = \mu_f = \mu$, but it is not required to do so.

In the following sections, Equation 2.11 is applied to calculate the $t\bar{t}$ production cross section. As the first step, one needs to decide on the renormalization scale $\mu_r$ at which $\alpha_s$ is evaluated.

### 2.2.1 The Strong Coupling Constant

In general, coupling constants in a gauge theory become running coupling constants after renormalization of ultraviolet divergences in the theory. The measurable values of the running coupling constants are determined by the actual energy exchanged in a physics process, typically denoted $q$. As an example, the fine coupling constant $\alpha$ becomes larger at larger energy. The running of $\alpha$ can be physically explained as a "bare" electron charge which is screened by virtual electron-positron pairs. This results in an "effective" charge that increases with increasing energy. The effective charge is the measurable electron charge. Oppositely, for non-abelian gauge theories such as the QCD theory, the running coupling constant can decrease at larger energy, or smaller distance. This is referred to as the "asymptotic freedom" property of non-abelian gauge theories. It results from the antiscreening effect by the virtual vector boson loops. When antiscreening dominates, the theory is asymptotically free.

At high energy ($q \gg \Lambda_{QCD}$), the running of the strong coupling constant $\alpha_s$, as a function of the energy scale $\mu$, is described to all orders by the renormalization group equation as:

$$\begin{aligned} \beta(\alpha_s) &= \frac{\partial \alpha_s\left(\mu^2\right)}{\partial ln\left(\mu^2\right)} = \mu^2 \frac{\partial \alpha_s\left(\mu^2\right)}{\partial \mu^2} \\ &= -b_0 \alpha_s^2(\mu) - b_1 \alpha_s^3(\mu) + O\left(\alpha_s^4(\mu)\right) \end{aligned} \tag{2.14}$$

where

$$b_0 = \frac{33 - 2N_f}{12\pi} \tag{2.15}$$

$$b_1 = \frac{153 - 19N_f}{24\pi^2}. \tag{2.16}$$

Here $N_f$ is the number of flavors of quarks participating in the virtual loops, i.e., quarks with a mass less than the energy $q$. Solving this equation at lowest order yields:

$$\alpha_s\left(\mu^2\right) = \frac{\alpha_s\left(\mu_0^2\right)}{1 + b_0\alpha_s\left(\mu_0^2\right) ln\left(\mu^2/\mu_0^2\right)} \tag{2.17}$$

where $\mu_0$ is an arbitrary starting point.

For convenience, $\alpha_s$ is usually written in terms of the QCD mass scale, $\Lambda_{QCD}$, the constant of integration in:

$$ln\frac{\mu^2}{\Lambda_{QCD}} = -\int_{\alpha_s(\mu)}^{\infty}\frac{dx}{\beta(x)} \tag{2.18}$$

Therefore, at lowest order,

$$\alpha_s\left(\mu^2\right) = \frac{1}{b_0 ln\left(\mu^2/\Lambda_{QCD}^2\right)} \tag{2.19}$$

Solving Equation 2.18 at next to leading order ($O\left(\alpha_s^3\right)$) gives:

$$\alpha_s\left(\mu^2\right) = \frac{1}{b_0 ln\left(\mu^2/\Lambda^2\right)}\left[1 - \frac{b_1}{b_0^2}\frac{ln\left(ln\left(\mu^2/\Lambda^2\right)\right)}{ln\left(\mu^2/\Lambda^2\right)}\right] \tag{2.20}$$

From the two equations above, one can clearly see that $\alpha_s$ logarithmically approaches infinity as $\mu$ decreases towards QCD mass scale. The mass scale $\Lambda_{QCD}$ can be extracted from experimental measurement. Its value depends on the renormalization scheme, the order of calculation, as well as the number of quark flavors, $N_f$. Using the $\overline{MS}$ scheme, $\Lambda_{QCD}$ is measured to be $\sim 200\ MeV$ for $N_f = 5$.

The fact that $\alpha_s$ becomes larger than one at small energies affects the application of perturbative QCD. For the perturbative approach to be valid, the energy scale of the physics process needs to be large enough so that $\alpha_s$ it is much less than one. The choice of the renormalization scale $\mu_r$ is arbitrary, but is usually chosen to be on the order of the energy scale of the physics process. In the case of the $t\bar{t}$ cross section, the scale $\mu_r$ is typically chosen to be on the order of the mass of the top quark. At this scale, the coupling constant has a value of around 0.1.

### 2.2.2 Partonic Cross Sections

The partonic cross sections for $t\bar{t}$ production are calculable by perturbative theory, because at the scale of the top mass ($m_t \gg \Lambda_{QCD}$), the strong coupling constant $\alpha_s$ is much less than one. The calculation begins by writing the $t\bar{t}$ partonic cross sections in terms of dimensionless functions $\mathcal{F}_{ij}$:

$$\hat{\sigma}_{ij}\left(\hat{s}, m_t^2; \alpha_s^2\left(\mu^2\right), \mu^2\right) = \frac{\alpha_s^2\left(\mu^2\right)}{m_t^2}\mathcal{F}_{ij}\left(\rho, \alpha_s\left(\mu^2\right), \frac{\mu^2}{m_t^2}\right) \tag{2.21}$$

and expanding $\mathcal{F}_{ij}$ into a perturbative series of the QCD coupling constant $\alpha_s$, as [5]:

$$\mathcal{F}_{ij}\left(\rho, \alpha_s\left(\mu^2\right), \frac{\mu^2}{m_t^2}\right) = \mathcal{F}_{ij}^{(0)}(\rho) + 4\pi\alpha_s\left(\mu^2\right)\left[\mathcal{F}_{ij}^{(1)}(\rho) + \overline{\mathcal{F}}_{ij}^{(1)}(\rho) ln\frac{\mu^2}{m_t^2}\right] + O\left(\alpha_s^2\right) \tag{2.22}$$

where $\rho = 4m_t^2/\hat{s}$. Note that $\mu_r$ and $\mu_f$ are taken to be equal to each other and denoted as $\mu$ in the equation.

#### 2.2.2.1 The Leading Order Calculation

The dimensionless functions $\mathcal{F}_{ij}$ are calculated order by order by evaluating the appropriate Feynman diagrams. At lowest order, or leading order (LO), $t\bar{t}$ pairs can be produced either from the partonic process of quark-antiquark annihilation, or gluon-gluon fusion:

$$q\left(p_1\right) + \overline{q}\left(p_2\right) \rightarrow t\left(p_3\right) + \bar{t}\left(p_4\right) \tag{2.23}$$

$$g\left(p_1\right) + g\left(p_2\right) \rightarrow t\left(p_3\right) + \bar{t}\left(p_4\right) \tag{2.24}$$

Figure 2.1 shows the leading order Feynman diagrams for the $q\bar{q}$ annihilation channel and gluon fusion channel of $t\bar{t}$ production.

The leading order partonic cross sections for the different channels, corresponding to $\mathcal{F}_{ij}^{(0)}$ in the expansion, are obtained by integrating respective differential cross sections, which are written in terms of squared matrix elements, over the entire momentum space of the $t\bar{t}$ pair. The results are proportional to $\alpha_s^2$:

$$\hat{\sigma}(q\overline{q} \rightarrow t\bar{t}) = \frac{1}{27}\frac{\pi\alpha_s^2\beta\rho(2+\rho)}{m_t^2} \tag{2.25}$$

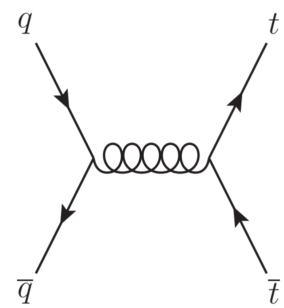


(a) Quark-antiquark annihilation

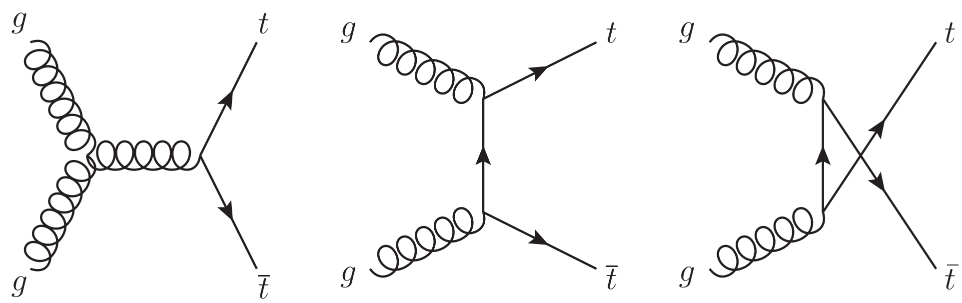


(b) Gluon-gluon fusion

Figure 2.1: Feynman diagrams for leading order $t\bar{t}$ production

$$\hat{\sigma}(gg \to t\bar{t}) = \frac{\pi\alpha_s^2\beta\rho}{192m_t^2}\left[\frac{1}{\beta}(\rho^2 + 16\rho + 16)ln\left(\frac{1+\beta}{1-\beta}\right) - 28 - 31\rho\right] \quad (2.26)$$

$$\hat{\sigma}(gq \to t\bar{t}) = \hat{\sigma}(g\overline{q} \to t\bar{t}) = 0 \quad (2.27)$$

where $\beta = \sqrt{1-\rho}$ is the velocity of the top quarks in the center-of-mass frame. Note that the leading order cross section does not have direct dependence on $\mu_r$ or $\mu_f$, because it has neither ultraviolet nor collinear divergence. Also, the leading order terms vanish both at the partonic threshold ($\beta \to 0$, equivalently $\rho \to 1$), and at high energy ($\rho \to 0$). At leading order, the cross section of $qg$ channel is zero, but this channel can contribute in higher orders.

#### 2.2.2.2 Higher-Order Corrections

Naively, the leading order calculation presented in last section should be fairly reliable for the $t\bar{t}$ production cross section, because $\alpha_s$ is expected to be small in the $t\bar{t}$ production process. However, the contribution at $O(\alpha_s^n)$ also depends on the coefficient of $\alpha_s^{(n)}$, and often these coefficients misbehave. This could result in significant contribution from the high order corrections. In addition, the LO cross section has a relatively large scale dependence, improvable by higher-order calculations. In view of the excellent data-taking capability of experiments like the DØ and CDF at Fermilab and the ATLAS and CMS at the LHC, it is very important to improve the theoretical accuracy of the total cross section of the $t\bar{t}$ production.

The following example helps to understand why higher-order corrections to the heavy quark pair production cross section can be large at hadron-hadron colliders. At hadron-hadron colliders, the cross section for the leading-order process $gg \to gg$ is about 100 times larger than the cross section for $gg \to q\bar{q}$ [6]. As a result, the higher-order process for $q\bar{q}$ production

$$\begin{aligned} g + g &\to g + g \\ &\quad\hookrightarrow q + \overline{q} \end{aligned} \tag{2.28}$$

is suppressed by a power of $\alpha_s$, but enhanced $\sim 100$ times by the coefficient in the expansion. Therefore, this process may have a sizable contribution compatible to the leading order $q\bar{q}$ production.

Theoretical developments have improved the LO results of heavy quark pair production cross section by taking into account the next-to-leading-order (NLO) corrections and further, the next-to-next-leading-order (NNLO) corrections [8, 9].

Unlike the leading order calculation, the higher-order corrections do not generally vanish near the partonic threshold ($\beta \to 0$). In fact, after factoring out the collinear divergent terms into the PDFs, the higher-order differential cross sections still contain collinear terms which are logarithmically divergent at the threshold, of the following form [8]:

$$\left[\frac{ln^l(\beta)}{\beta}\right]_+ \tag{2.29}$$

where $l \leq 2n - 1$ at the $n$th order in the $\alpha_s$ expansion. Physically, these terms come from soft gluon processes near the threshold. After convolution with the PDFs, these terms will give finite but large corrections near the threshold. Therefore, similar to the above example ($gg \to q\bar{q}g$), at higher orders, corrections from these logarithms might be compatible with cross sections at lower orders of $\alpha_s$. To preserve the predictability of the perturbative calculation, these logarithmically enhanced corrections at all orders of $\alpha_s$ are resummed into the perturbative expansion at finite order of $\alpha_s$, using a technique termed soft gluon resummation. The most important correction of this kind is referred to as the the leading logorithmic (LL) correction. And NLL, NNLL refer to next-to-leading-logorithmic and next-to-next-to-leading-logorithmic corrections. A more detailed summary of the resummation technique is available in [8] and [9].

### 2.2.3 Parton Distribution Functions

As mentioned before in this section, the parton distribution function (PDF) describes the probability of a hard scattering parton in a hadron to carry a fractional momentum $x$. Since the PDFs contain effects from long-distance physics, they are not calculable by perturbation theory. Instead, their values are extracted from experimental data. On the other hand, the evolution of the PDFs with the energy scale $\mu$ is theoretically predicted, much like the running of the strong coupling constant $\alpha_s$. The evolution of the PDFs is described to all orders by the Gribov-Lipatov-Altarelli-Parisi (GLAP) evolution equation, or simply known as the Altarelli-Parisi equation [5, 7]:

$$\mu^2 \frac{d}{d\mu^2} f_i(x,\mu^2) = \frac{\alpha_s \mu^2}{2\pi} \sum_{j=q,\bar{q},g} \int_x^1 \frac{d\xi}{\xi} P_{ij}\left(\frac{x}{\xi}, \alpha_s\left(\mu^2\right)\right) f_j\left(\xi,\mu^2\right) \tag{2.30}$$

where $i = q, \overline{q}, g$. $P_{ij}$ are called the Altarelli-Parisi evolution kernels and are calculable by perturbation theory, with the LO term at $\mathcal{O}(\alpha_s)$.

The GLAP equation of PDF evolution ensures that one can measure the PDFs at a certain energy scale and use the equation to get the PDFs at another energy scale. The PDFs are usually measured at a certain energy by making a global fit, with certain parametrization, to experimental data from one or more processes where perturbative QCD applies. The most accurate results usually come from deep inelastic scattering ($eq \to eq$) data. The Drell-Yan process ($q\bar{q} \to l^+l^-$), as well as other hard scattering processes, are also used in the measurement of the PDFs.

Commonly used PDFs include those from the CTEQ collaboration, the MRS collaboration, and the NNPDF collaboration [10, 11, 12]. In this analysis PDFs from all collaborations are used. The CTEQ66 PDFs are used for most of the Monte Carlo (MC) sample generation, as well as for the theoretical calculation of $t\bar{t}$ cross section. For estimation of systematic error associated with PDF uncertainties, all three of the CTEQ66, MSTW08, and NNPDF2.0 PDFs are used [13].

### 2.2.4 Results for Top Quark Pair Production at the LHC

The production of the $t\bar{t}$ pairs at the LHC occurs predominantly through gluon-gluon fusion. Theoretical calculations have shown that the fraction of $t\bar{t}$ pairs from gluon-gluon fusion is about 90% at the LHC [8]. In contrast, at the Fermilab Tevatron, the $t\bar{t}$ production is dominated by the quark-antiquark annihilation. In Run I, at a center-of-mass energy ($\sqrt{s}$) of 1.8 $TeV$, this channel contributes about 90% of the total cross section. In Run II, at $\sqrt{s} = 1.96\ TeV$, this channel contributes about 85% [2].

The primary reason for the different dominating channels at the LHC and at the Tevatron is that, at lower energies, the parton flux is dominated by quarks, while at higher energies, the parton flux is dominated by gluons. At the Tevatron, $t\bar{t}$ production occurs close to the threshold. The fractions of momentum of the protons carried by the partons, $x_i \approx x_j \approx x_{thr} = \frac{2m_t}{\sqrt{s}}$. At the Tevatron, $x_{thr} \approx 0.2$, where the quark distribution functions are much larger than that for the gluon. In comparison, at the LHC, $x_{thr} \sim 0.025$, in which case gluon PDF dominants and the $gg \to t\bar{t}$ channel becomes the most important channel. Combined with the large parton cross section for this channel, this results in around 90% contribution to the total cross section [8].

The most recent theoretical prediction for the $t\bar{t}$ cross section at 7 $TeV$ has been calculated within the ATLAS top physics working group using the HATHOR program [9, 14, 15]. The HATHOR program is a general tool for the calculation of heavy quark cross section in hadronic collisions. It takes into account recent theoretical developments such as approximate NNLO perturbative QCD corrections [15].

The theoretical prediction of the $t\bar{t}$ cross section used in this analysis is calculated with the HATHOR program using the CTEQ66 PDFs. The predicted $t\bar{t}$ cross section for a top mass of 172.5 $GeV$ is [16]:

$$\sigma_{t\bar{t}}^{approx\ NNLO} = 164.57^{+4.30}_{-9.27}(\text{scale})^{+7.15}_{-6.51}(\text{PDF})\ pb \tag{2.31}$$

where the error due to the scale uncertainty is estimated by varying the renormalization and factorization scales ($\mu_r$, $\mu_f$) between $m_t/2$ and $2m_t$, and the error due to the PDF uncertainty is estimated by varying the PDF by its error bands [14].

The HATHOR program is also used to derive the dependence of the predicted $t\bar{t}$ cross section on the center-of-mass energy ( $\sqrt{s}$). The plots is shown in Figure 2.2. From the plot, we observe that the $t\bar{t}$ cross section in $pp$ collisions at 7 $TeV$ is about 20 times larger than in $p\overline{p}$ collisions at 2 $TeV$. At 14 $TeV$ it will be 100 times larger than at 2 $TeV$. This means that, while tops are rare events at Tevatron, it is produced in large quantities at the LHC. The LHC is a top factory. Also notice the different predictions for pp and $p\overline{p}$ collisions. For both 7 TeV and 14 TeV at LHC, the results are almost identical for pp and $p\overline{p}$ collisions. This is because at such high energies, the gluon fusion dominates the production. This is also the reason why LHC could be built as a $pp$ collision machine without worring loss of cross section.

Figure 2.2 also includes results from $t\bar{t}$ cross section measurements performed at DØ and CDF, using Tevatron Run I and Run II data. These results are consistent with the Standard Model predictions. However, these results are statistically limited, making it important to repeat the analysis with more data collected at the LHC. The $t\bar{t}$ cross section at 7 $TeV$ has not been measured and is the subject of this dissertation.

## 2.3 Top Quark Pair Decay

Within the Standard Model, the top quark decays almost exclusively through the $t \to Wb$ channel via the weak interaction. The $W$ boson decays almost instantaneously, either leptonically into lepton-neutrino pair approximately 1/3 of the time, or hadronically into a light quark pair approximately 2/3 of the time. The anti-top quark decays in the same way. This decay mode is illustrated in Figure 2.3.

The next most likely decay modes are decays of the top quark into lighter flavor quarks: $t \to Ws$ and $t \to Wd$. The Standard Model also predicts a very small rate of

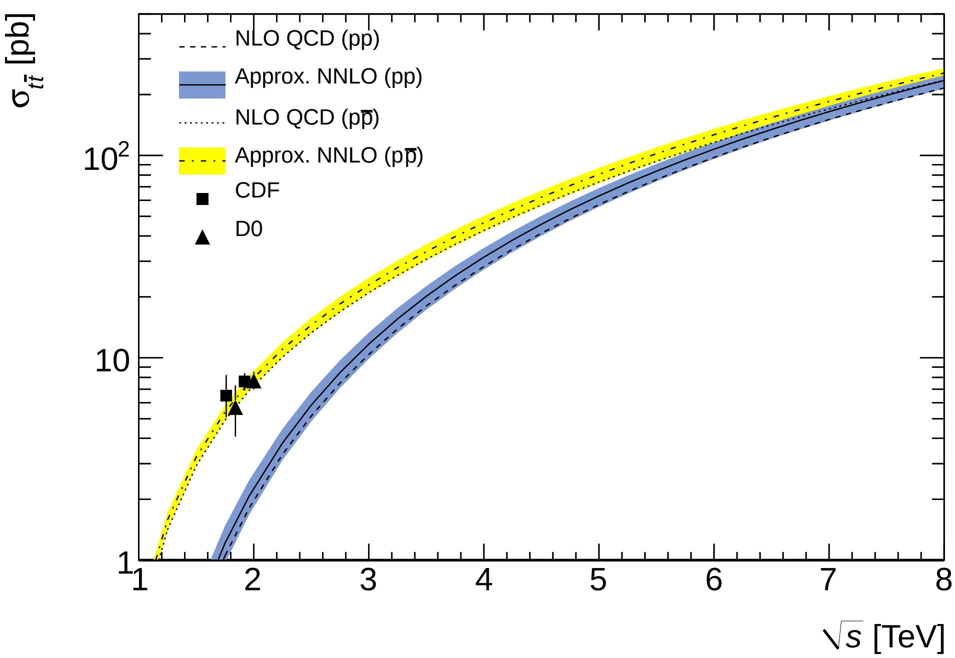


Figure 2.2: The theoretical $t\bar{t}$ cross section as a function of the center-of-mass energy. The figure also includes results from measurements performed at DØ and CDF using Tevatron Run I ( $\sqrt{s}$ = 1.8 $TeV$) and Run II ( $\sqrt{s}$ = 1.96 $TeV$) data [17, 18, 19, 20].

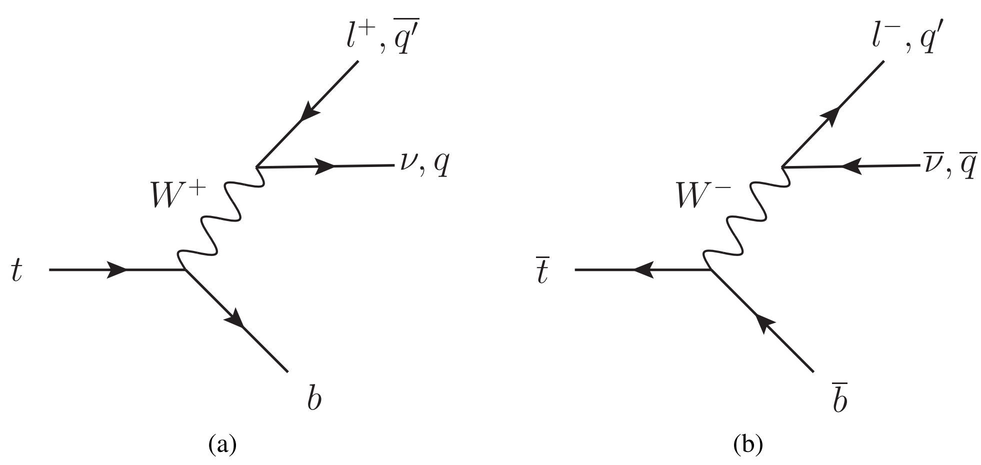


Figure 2.3: Decay of the top quark and the anti-top quark. Top quark (left). Anti-top quark (right).

flavor changing neutral current (FCNC) decays of the top quark, which is completely nonexistent at tree level.

### 2.3.1 Top Quark Decay

The Standard Model involves three generations of quarks, which transform under the weak interaction as doublets (Section 2.1.1). Because the weak interaction eigenstates of the quarks are mixing states of the mass eigenstates, the top quark can also decay directly into lower-generation quarks. The mixing is described by the unitary Cabibbo-Kobayashi-Maskawa (CKM) matrix [3]:

$$\begin{pmatrix} d^w \\ s^w \\ b^w \end{pmatrix} = \begin{pmatrix} V_{ud} & V_{us} & V_{ub} \\ V_{cd} & V_{cs} & V_{cb} \\ V_{td} & V_{ts} & V_{tb} \end{pmatrix} \cdot \begin{pmatrix} d^m \\ s^m \\ b^m \end{pmatrix} \tag{2.32}$$

The possible decay modes for the top quark at tree level are $t \to Wb$, $t \to Ws$ and $t \to Wd$. The branching ratio of each channel is proportional to the square of the respective CKM matrix element $|V_{tq}|^2$, where $q = b, s, d$. Assuming the unitarity of the matrix, recent measurements indicate that $V_{td} < 0.014$ and $V_{ts} < 0.043$ and $V_{tb} > 0.999$ [2]. It follows that the branching ratio for the channel $t \to Wb$ is close to unity:

$$\mathcal{B}(t \to Wb) > 0.998 \tag{2.33}$$

With a mass above the $Wb$ threshold, and $V_{tb}$ close to unity, the SM decay width of the top quark is dominated by the two-body channel $t \to Wb$. Neglecting terms of order $m_b^2$, $\alpha_s^2$ and $(\alpha_s/\pi)\, M_W^2/m_t^2$, the top quark decay width including the next-to-leading-order (NLO) QCD correction can be expressed in terms of the top mass, $m_t$, the mass of the W boson, $m_W$, the strong coupling constant, $\alpha_s$, and the Fermi constant $G_F$ [2]:

$$\Gamma_t = \frac{G_F m_t^3}{8\pi\sqrt{2}} \left(1 - \frac{m_W^2}{m_t^2}\right)^2 \left(1 + 2\frac{m_W^2}{m_t^2}\right)^2 \left[1 - \frac{2\alpha_s}{3\pi}\left(\frac{2\pi_2}{3} - \frac{5}{2}\right)\right] \tag{2.34}$$

The NLO QCD correction lower the LO decay rate by $\sim$ 10%, yielding at NLO $\Gamma_t = 1.29\ GeV$ at $m_t = 171\ GeV$ [2]. This transfers to a unique short lifetime $\tau_t = 1/\Gamma_t \approx 5 \cdot 10^{-25}\ s$.

### 2.3.2 Top Quark Pair Decay Final States

As the top quark decays almost exclusively into a $W$ boson and a $b$ quark, the $t\bar{t}$ decays almost one hundred percent of the time into two $W$ bosons and two $b$ quarks. The $b$ quarks hadronize before they decay, and form two $b$-jets with high transverse energy ($E_T$) and high transverse momentum ($p_T$). The two $W$ bosons can each decay either leptonically, leaving a high-$p_T$ lepton and high missing transverse energy (missing $E_T$, or $\not{E}_T$) in the detector, or hadronically, forming two light quark jets. From an experimental point of view, the $t\bar{t}$ final states can be categorized according to the number of $W$ bosons that decays leptonically, into three channels: the semileptonic channel, the dilepton channel and the all-hadronic channel. Figure 2.4(a) shows the three decay channels and the final states included in each channel.

The possibility of a $W$ boson decaying into any weak interaction doublets are roughly the same. The Born-level branching ratios of the three $t\bar{t}$ decay channels can be calculated by simply counting the number of final states they contain. There are three generations of leptons, and two generations of light quarks. Also considering that each light quark doublets have three different colors, there are 81 possible final states in total. The branching ratios are estimated to be 4/9, 1/9 and 4/9 for the semileptonic, dilepton, and full-hadronic channels. Figure 2.4(b) shows the measured branching ratios for the different final states. The measured BRs are close to the estimation by simple counting.

Because the $\tau$ lepton has a short life time and can decay both leptonically and hadronically, it cannot be identified as a lepton in the same way as electron and muon. Therefore, usually only electrons and muons, including those from $\tau$ leptonic decays, are considered for leptonic analyses. This decreases the rates of the semileptonic and dilepton channel. The three decay channels are discussed one by one in the following paragraphs. The final states included in each channel and their respective branching ratios are summarized in Table 2.4.

The semileptonic channel is also called the lepton plus jets ($l + jets$) channel. In this channel, only one of the two $W$ bosons decays leptonically. It is often regarded as the "golden" channel, because it has relatively small background thanks to the presence of a

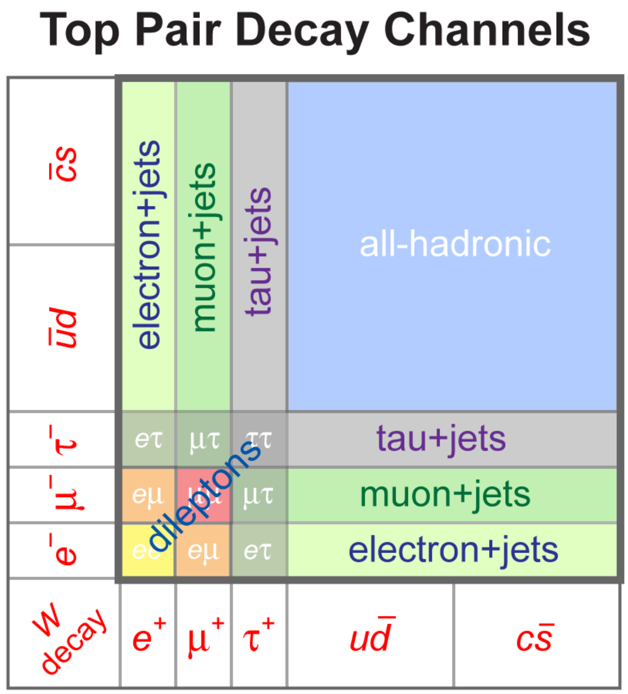


(a) $t\bar{t}$ decay channels

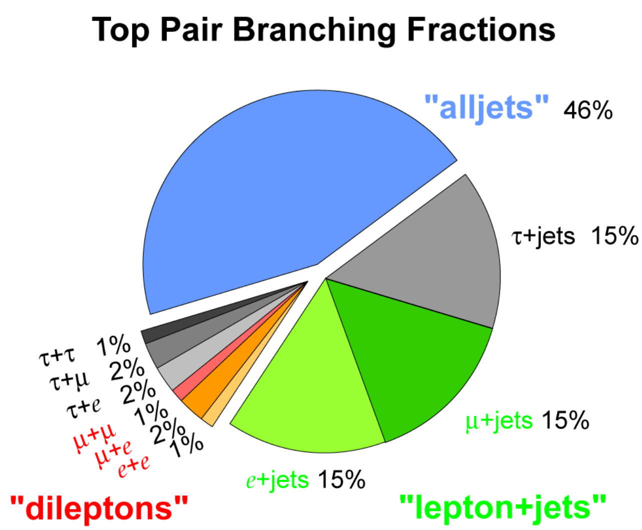


(b) $t\bar{t}$ decay branching ratios

Figure 2.4: $t\bar{t}$ decay channels and their branching ratios

| Channel | Decay mode | BR at Born level | BR [2] |
|---|---|---|---|
| $e + jets$ | $t\bar{t} \to e^{+}\nu_e(e^{-}\overline{\nu}_e)q\overline{q}'b\bar{b}$ | 12/81 | (17.21±0.22)% |
| | $t\bar{t} \to e^{\pm}_{\tau}q\overline{q}'b\bar{b} + \nu$'s | – | |
| $\mu + jets$ | $t\bar{t} \to \mu^{+}\nu_\mu(\mu^{-}\overline{\nu}_\mu)q\overline{q}'b\bar{b}$ | 12/81 | (17.14±0.22)% |
| | $t\bar{t} \to \mu^{\pm}_{\tau}q\overline{q}'b\bar{b} + \nu$'s | – | |
| $ee$ | $t\bar{t} \to e^{+}\nu_e e^{-}\overline{\nu}_e b\bar{b}$ | 1/81 | (1.583±0.028)% |
| | $t\bar{t} \to e^{+}_{\tau}e^{-}_{\tau}b\bar{b} + \nu$'s | – | |
| $\mu\mu$ | $t\bar{t} \to \mu^{+}\nu_\mu\mu^{-}\overline{\nu}_\mu b\bar{b}$ | 1/81 | (1.571±0.027)% |
| | $t\bar{t} \to \mu^{+}_{\tau}\mu^{-}_{\tau}b\bar{b} + \nu$'s | – | |
| $e\nu$ | $t\bar{t} \to e^{+}\nu_e\mu^{-}\overline{\nu}_\mu b\bar{b}$ | 2/81 | (3.154±0.055)% |
| | $t\bar{t} \to e^{\pm}_{\tau}\mu^{\mp}_{\tau}b\bar{b} + \nu$'s | – | |
| all-jets | $t\bar{t} \to q\overline{q}'q\overline{q}'b\bar{b}$ | 36/81 | (45.70±0.37)% |
| | $t\bar{t} \to \tau$ final states | 17/81 | (21.60±0.18)% |

Table 2.4: Top quark pair decay branching ratios. $e_\tau$, $\mu_\tau$ denotes $e$, $\mu$ from $\tau$ leptonic decays.

lepton in the final state, and also simultaneously has a high branching ratio. As shown in Table 2.4, this channel includes the $e + jets$ and $\mu + jets$ final states, both of which includes $\tau + jets$ events where $\tau$ decays leptonically.

The semileptonic channel is the decay channel used in the analysis presented in this dissertation. The final state of this channel is characterized by one high $p_T$ lepton, large missing $E_T$, two high $p_T$ $b$-jets, and two high $p_T$ light quark jets from the hadronic $W$ decay. The high $p_T$ lepton plays an important role in eliminating many background events to obtain a high signal-over-background ($S/B$) ratio. Also, high $p_T$ leptons provide simple efficient triggers. The major background for this channel is the W boson production in association with jets, where W decays leptonically (($W \to l\nu$)+jets). Details on the backgrounds for this channel are given in Chapter 6.

The diLepton channel is also known as the fullly leptonic channel. In this channel both $W$ bosons decay leptonically. This channel is the cleanest, because few other processes have two high-$p_T$ leptons and significant missing $E_T$, especially for the $e\mu$ decay mode. However, the branching ratio for this channel is only about 10.3% in total, and is even smaller when the $\tau$ leptons are not taken into account.

The kinematics of the $t\bar{t}$ pairs in dilepton events cannot be fully reconstructed. This raises another difficulty in this channel. The two neutrinos from the leptonic $W$ decays are measured by the total missing $E_T$ in the detector, for there is only one value for each event. Additional kinematic constraints are often added in order to solve this problem.

The fully hadronic channel is also called the all-jets channel. In the all-jets channel, both of the $W$ bosons decays hadronically. This channel has the largest branching ratio at roughly 46.2%. However, the lack of any high-$p_T$ lepton in the final state makes it difficult to suppress the background processes. This channel suffers large QCD multi-jet background, and thus has a good $S/B$ ratio. The systematic errors in this channel also tend to be large, both because jets are more difficult to measure accurately, compared to the leptons, and because the QCD multi-jet background is not very well modeled by Monte Carlo simulation.

# Chapter 3

# Experimental Apparatus

The Large Hadron Collider (LHC) is currently the world's largest hadron collider, with protons accelerated in a 27-kilometer-circumference synchrotron and colliding at never-before-reached energy. The LHC is designed to collide $pp$ pairs at a center-of-mass energy ($\sqrt{s}$) of 14 $TeV$ at a high peak luminosity of $10^{34}$ $cm^{-2}s^{-1}$, and is currently colliding at a center-of-mass energy of 7 $GeV$. The ATLAS (acronym for A Toroidal LHC Apparatus) detector is one of the two general-purpose detectors positioned on the synchrotron ring, aimed to detect new rare physics. This chapter presents an overview of the LHC and the ATLAS detector, with a focus on the ATLAS subdetectors used to measure the energy and momentum of leptons, jets and missing $E_T$ (missing transverse energy, the neutrino signature). A brief description of the ATLAS trigger and data acquistion (TDAQ) system is also presented.

## 3.1 Large Hadron Collider

The LHC occupies the old LEP (Large Electron-Positron Collider) tunnel at CERN, Geneva, at the Franco-Swiss border. The layout and the design of the LHC ring is documented in detail in [21, 22]. The tunnel is about 27 kilometers long and about 100 meters deep underground. The basic layout of the LHC ring mirrors that of LEP. As shown in Figure 3.1, it is composed of eight arcs and eight straight sections, with the straight sections measuring approximately 528 meters each. The straight sections can serve as experimental or utility insertions. Four of these insertions are used as experimental insertions, out of which two are high-luminosity interaction points. Starting from the high-luminosity insertion point used for the ATLAS detector (Point 1), these sections are called Point 1 though Point 8 respectively.

Currently there are a total of six official LHC experiments. The second high-

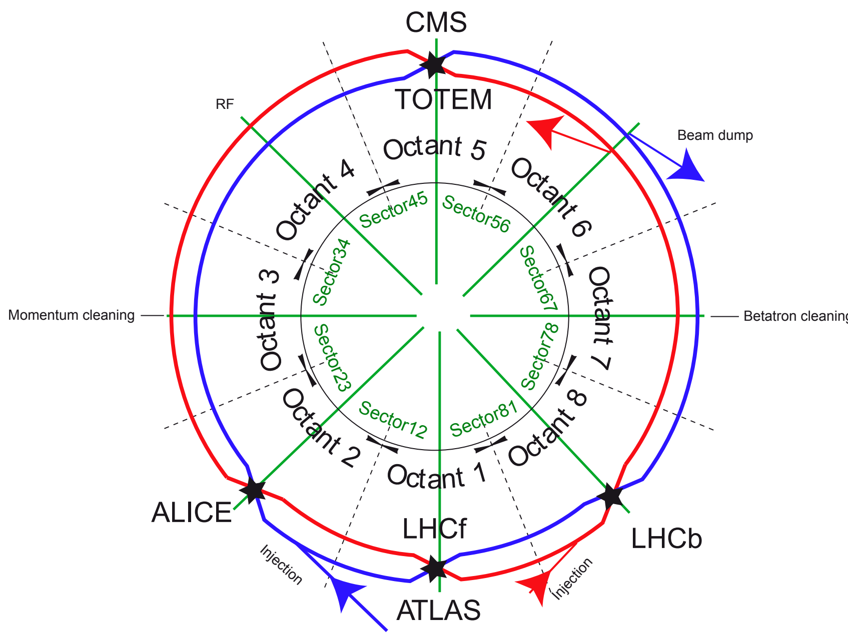


Figure 3.1: Layout of the LHC ring with the four interaction points [23]

luminosity insertion point on the LHC ring (Point 5), located diametrically opposite to Point 1, is used for the other general purpose detector, the Compact Muon Detector (CMS). There are two medium-size special-purpose experiments, ALICE at Point 2 and LHCB at Point 5. ALICE is designed to study heavy ion (Pb-Pb) collision physics, and LHCB focuses on the study of B quark physics. There are also two small-scale special-purpose experiments, LHCf and TOTEM. LHCf aims to investigate the origin of ultra-high-energy cosmic ray by means of studying neutral particles produced in the very forward region of pp or nucleus-nucleus collisions. Because of its compact size and the large distances between its two subdetectors, LHCf shares Point 1 with the ATLAS detector. For similar reasons, TOTEM (acronym for Total Elastic and Diffractive cross section Measurement) shares Point 5 with the CMS detector.

The LHC synchrotron uses a total of about 1600 bending and focusing magnets: 1232 identical dipole magnets, for keeping particles in their nearly circular orbits, and 392 identical quadruple magnets for focusing the beams. The dipoles are placed in the curved sections of the LHC ring and the quadrupoles in the straight sections. In addition, other types of magnets, such as sextuple, octupole and decapole magnets, are used at various locations for orbit correction and other purposes. All of these magnets make use of superconducting niobium-titanium (Nb-Ti) cables and operate at a low temperature of 1.9 $K$. The performance of the Nb-Ti superconductor is boosted by the very low temperature. As a result, very strong ($8-8.5\ T$) central field is attainable in the LHC dipoles, maximising the bending power and the beam energy achievable. To reach the low temperature, superfluid helium is used for cooling. Figure 3.2 shows a three dimensional cut-away view of the LHC dipoles.

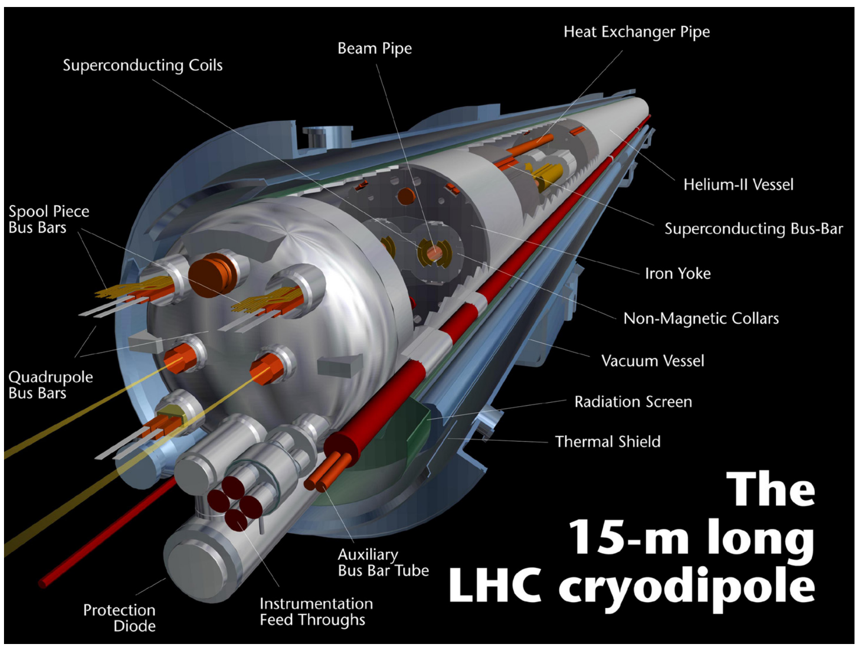


Figure 3.2: Cut-away view of one of the LHC dipoles [23]

Before entering the LHC main ring, protons need to go through a pre-acceleration chain, called the LHC injector chain, which increases their energy to 450 $GeV$. The design of the LHC injector chain is documented in [24]. The pre-acceleration chain involves a linear accelerator (LINAC) and three smaller synchrotron rings. Figure 3.3 shows the injection scheme of LHC. Protons are produced in a duoplasmatron source and preaccelerated in a radio-frenquency (RF) cavity to 750 $KeV$. After this, they are injected into the LINAC which increases their energy to 50 $MeV$. Afterwards, they are injected step by step into the Proton Synchrotron Booster (PSB), the Proton Synchrotron (PS), and the Su-per Proton Synchrotron (SPS). The protons stay in each of the three rings until they reach the targeted high energy. They leave the PSB at 1.4 $GeV$ and leave the PS at 25 $GeV$. In the SPS, they reach the energy 450 $GeV$, and are subsequently injected into the LHC synchrotron, where they are accelerated up to a maximum of energy. In Figure 3.3, the corresponding proton velocity at the end of each acceleration step is denoted.

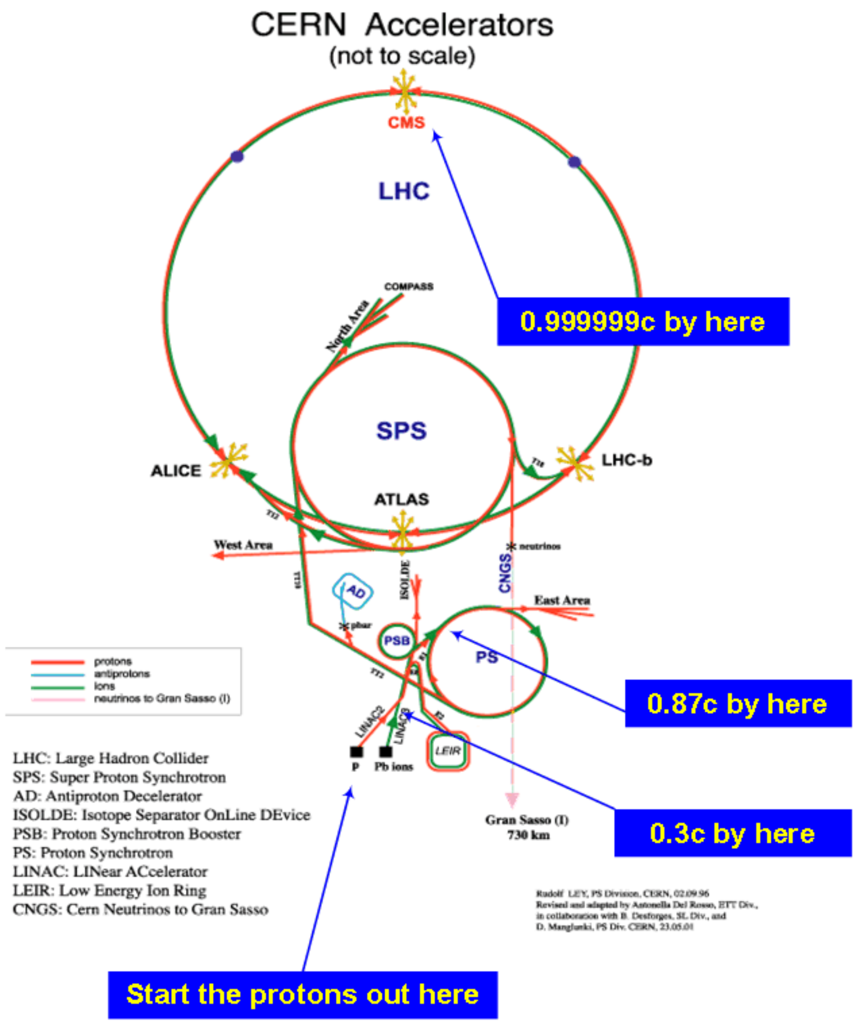


Figure 3.3: The LHC machine and its injection scheme [23]

Beams injected in the LHC synchrotron is captured, accelerated and stored using two 400 $MHz$ superconducting RF cavity systems, one for each beam. Both RF systems are concentrated around the center of Point 4, and each system contains eight RF cavities, operating at the temperature 4.5 $K$. A second RF system at lower frequency (200 $Hz$) may be installed after the initial running, in order to reduce injection loss and ease operation.

Proton collisions occur at Point 1 and Point 5 in bunches separated by 25 $ns$. At the design peak luminosity of $\mathcal{L} = 10^{34}\ cm^{-2}s^{-1}$, there are a total of 2808 proton bunches per direction, and each bunch contains $10^{11}$ protons.

On September 19th, 2008, the LHC suffered a quench incident during commissioning of the final LHC sector (sector 3-4) for operation at beam energy 5 TeV, resulting in a large helium leak into the tunnel and serious mechanical damages to 24 dipole magnets and 5 quadruple magnets [25, 26, 27, 28]. After a yearlong shutdown during which replacement magnets were installed, damages were repaired, and quench monitoring system was improved, the LHC resumed operation in late 2009. Successful running at center-of-mass energy of 900 $GeV$ and 2.38 $TeV$ was achieved.successfully under intial conditions, In Match 2010, the LHC began running at center-of-mass energy of 7 $TeV$. The plan is to run until the end of 2011 or until 1 $fb^{-1}$ of data is collected, whichever comes first. A yearlong shutdown in 2012 is scheduled to prepare the machine to operate at its design energy. Finally in 2013, the LHC should be ready to run at the design energy of $\sqrt{s} = 14\ TeV$.

### 3.2 ATLAS Detector

The ATLAS (A Toroidal LHC ApparatuS) detector is a general purpose particle physics experiment, constructed hermetically in a set of cylindrical layers around the beam pipe and two sets of end-cap disks [29, 30, 31, 32]. Moving outward from the interaction point, the ATLAS detector consists of three major detector systems: the inner detector (ID), the calorimeter and the muon spectrometer (MS). The inner detector, enclosed in the magnetic field of the solenoid, is used to detect the tracks of particles before their energy is abosorbed and measured in the calorimeter. Muons can pass through the calorimeter with little perturbance. The muon spectrometer improves the resolution of the muon tracks, by reconstructing their tracks in the magnetic field of the toroid. The solenoid and the toroid are the two components of the ATLAS superconducting magnet system, which produces perhaps the most complicated magnetic field in particle physics to date. Figure 3.4 shows the size and layout of the ATLAS detector. The three component detectors are shown in cut-away view and denoted with different colors.

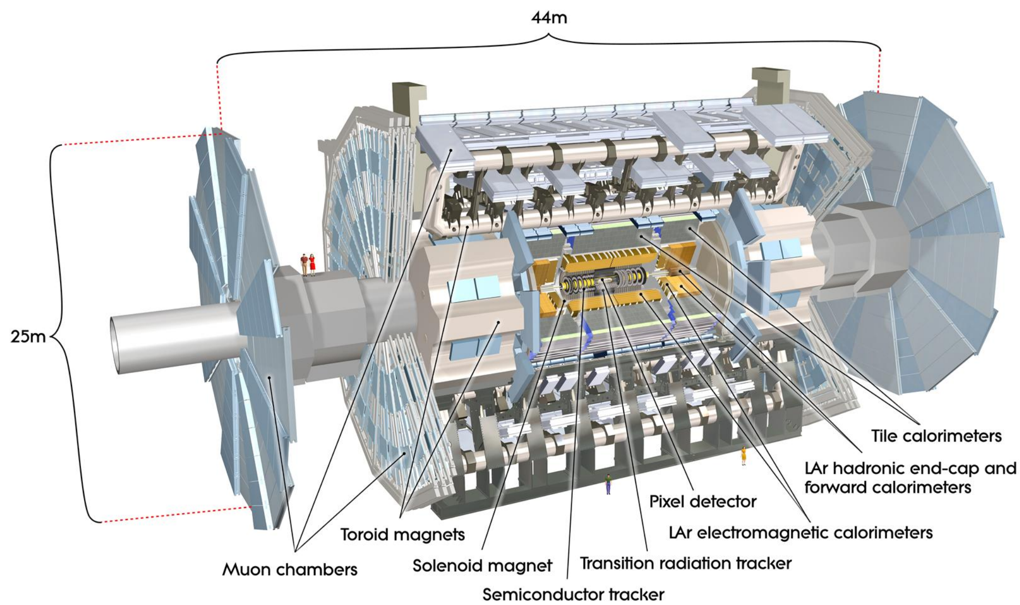


Figure 3.4: Cut-away view of the ATLAS detector [33]. The detector is 25 $m$ in height and 44 $m$ in length, and has a weight of approximately 7000 tons.

The barrel and the two end-caps of the ATLAS detector cover almost the full solid angle around the interaction point. Positions within the detector are described by a right-handed coordinate system, with the origin at the interaction point. The $z$-axis follows the beam direction, pointing to the LHC Point 8. The $x$-axis points to the center of the LHC ring and the $y$-axis points upwards. The side of the detector with positive $z$ is defined as side-A and the side with negative $z$ as side-C. Due to the detector's symmetry around the $z$ axis and the event topology of the collisions, in many cases, a cylindrical coordinate system of $z$, the pseudorapidity $\eta$ and the azimuthal angle $\phi$ is used instead. The pseudorapidity is related to the polar angle by

$$\eta \quad = \quad -ln[tan(\theta/2)] \tag{3.1}$$

The general performance goals of the ATLAS detector are summarized in Table 3.1. For the inner detector and the muon spectrometer, the requirement is on the momentum resolution $\sigma_{p_T}/p_T$, which can be expressed as:

$$\frac{\sigma_{p_T}}{p_T} \sim \frac{\sigma_s}{s} \sim \frac{p_T \sigma_s}{L^2 B} \tag{3.2}$$

where $s$ is the sagitta of the particle track, $B$ is the strength of the magnetic field, and $L$ is the length of the arc of the track, determined by the size of the tracking detector. For the calorimeter, the requirement is on the energy resolution $\sigma_E/E$. In the following sections, descriptions will be given for the magnet system and the three major subdetector systems, followed by an introduction to the ATLAS trigger system.

| **Detector component** | **Required resolution** | **$\eta$ coverage** | |
|---|---|---|---|
| | | Measurement | Trigger |
| Inner tracking | $\sigma_{p_T}/p_T = 0.05\% p_T \oplus 1\%$ | $\pm 2.5$ | |
| EM calorimetry | $\sigma_E/E = 10\%/\sqrt{E} \oplus 0.7\%$ | $\pm 3.2$ | $\pm 2.5$ |
| Hadronic calorimetry (jets) | | | |
| barrel and end-cap | $\sigma_E/E = 50\%/\sqrt{E} \oplus 3\%$ | $\pm 3.2$ | $\pm 3.2$ |
| forward | $\sigma_E/E = 100\%/\sqrt{E} \oplus 10\%$ | $3.1 < \lvert\eta\rvert < 4.9$ | $3.1 < \lvert\eta\rvert < 4.9$ |
| Muon spectrometer | $\sigma_{p_T}/p_T = 10\%$ at $p_T = 1\ TeV$ | $\pm 2.7$ | $\pm 2.4$ |

Table 3.1: General performance goals of the ATLAS detector [32]. The units for E and $p_T$ are in GeV.

### 3.2.1 Magnet System

The ATLAS magnet system features a hybrid system of one thin superconducting solenoid magnet and three large superconducting toroids (one barrel and two end-caps). Their position in the ATLAS detector and their geometry are shown in Figure 3.4. The solenoid, aligned to the beam axis and placed inside the calorimeter volume, provides an axial magnetic field of about 2 $T$ for the inner detector. In order to minimise the material in front of the barrel calorimeter, the solenoid shares the same vacuum vessel with the barrel Liquid Argon (LAr) calorimeter. The barrel and end-cap toroids provide magnetic field for the barrel and end-cap muon tracking chambers, respectively. The strength of the toroid magnetic field is approximately 0.5 $T$ in the central region and 1 $T$ in the end-cap regions. The end-cap toroids are rotated relative to the barrel toroid by 22.5°, in order to provide radial overlap with the barrel toroid. In this way the bending power in the overlap region is maximised. The ATLAS toroid magnets are perhaps the most complicated magnetic system to date, in particle physics. In Table 3.2, the relevant parameters for both the solenoid and the toroids are summarized. All of the superconducting magnets operate at 4.5 $K$.

| Properties | Features | Unit | Solenoid | Barrel toroid | End-cap toroids |
|---|---|---|---|---|---|
| **Size** | Inner diameter | $m$ | 2.46 | 9.4 | 1.65 |
| | Out diameter | $m$ | 2.56 | 20.1 | 10.7 |
| | Axial length | $m$ | 5.8 | 25.3 | 5.0 |
| | Number of coils | | 1 | 8 | $2 \times 8$ |
| **Coils** | Turns per coil | | 1154 | 120 | 116 |
| | Nominal current | $kA$ | 7.73 | 20.5 | 20.5 |
| | Magnet stored energy | $GJ$ | 0.04 | 1.08 | $2 \times 0.25$ |
| | Peak field | $T$ | 2.6 | 3.9 | 4.1 |
| | Field range | $T$ | 0.9–2.0 | 0.2–2.5 | 0.2–3.5 |

Table 3.2: Relevant parameters of the ATLAS magnet systems [32]

Precise determination of the magnetic field is crucial in order to meet the requirement on the momentum measurement precison of charged tracks in the inner detector and the muon spectrometer. For the solenoid, it is required that the fractional bending power $\sigma_B/B < 5 \times 10^{-4}$. The solenoid field is determined by in-situ mapping. For the toroids, it is required that the errors on the measured fractional bending power, the accuracy of the relative position of the toroid coils, and the 2nd-coordinate resolution of the muon chambers together degrade the momentum resolution by no more than 5%. Due to the rapidly varying field and very large volume, in-situ mapping by conventional techniques is impractical for the toroid. A less conventional technique is used: the field in space is reconstructed by comparing the readings of ~1840 B-field sensors with magnetric field simulations.

### 3.2.2 Inner Detector

The inner detector (ID) is the innermost part of the ATLAS detector [34, 35, 36]. It reconstructs the tracks of charged particles curved by the magnetic field of the solenoid. It also tries to identify them using the charge/mass ($Q/m$) ratio from the track, and the distance from the particle's originating point to the interaction point, and so on. Due to close vicinity to the interaction point, a high-granunarity detector with high momentum resolution is required. The detector should also be able to handle the high rates and the high radiation near the interaction point. There are three subdetectors, all with multi-layers in both the barrel and the end-caps: the semiconductor pixel tracker (Pixel tracker), the semiconductor tracker (SCT) using silicon microstrips, and the transition radiation tracker (TRT). Figure 3.5 shows a cut-away view of the inner detector, where the dimensions are also indicated. The inner detector covers the pseudorapidity ($\eta$) range up to $|\eta| < 2.5$.

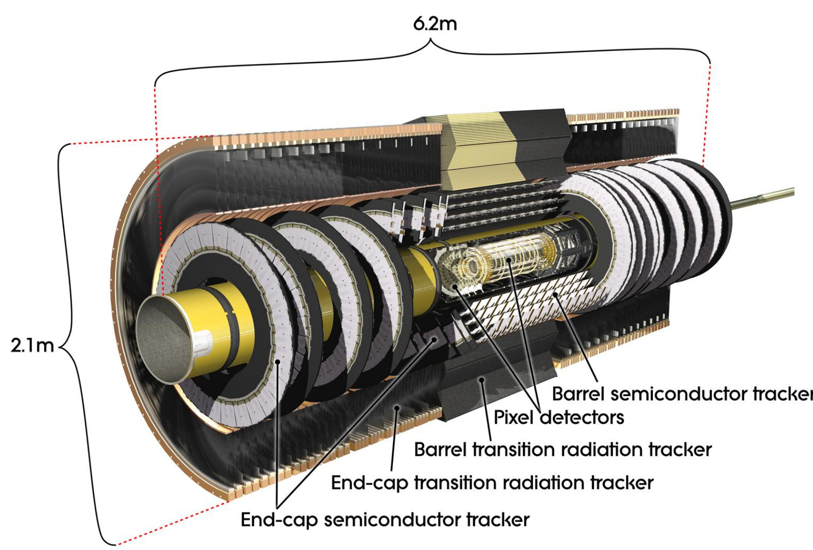


Figure 3.5: Three-dimensional cut-away view of the inner detector [37]

The Pixel tracker and the SCT are both silicon semiconductor detectors. They are similar in concept and function. The Pixel tracker uses small pixels as its basic detecting unit, while the SCT uses long, narrow silicon microstrips. Together, the two detectors provide at least seven precision measurement points along particle tracks. The Pixel tracker consists of 1456 barrel modules and 288 end-cap modules. These are all identical models, each with 47232 pixel elements, with nominal pixel size of 50 $\mu m \times 400$ $\mu m$. The very fine two-dimensional segmentation enables a very high point resolution, which is about 12 $\mu m$ in the bending plane. There are three barrel Pixel layers in the radial range $50.5 < R < 122.5$ $mm$ and six end-cap disks in the radial range $88.8 < R < 149.6$ $mm$. The innermost barrel layer, called the B-layer, is only 50.5 $mm$ away from the beam line and enhances the ability to identify secondary vertices for $b$-tagging. The radius of the B-layer has been optimized considering two opposing performance requirements: the impact parameter resolution and the pattern recognition capabilities. In addition, The B-layer is designed to be removable because its position near the beam line makes it susceptible to radiation damage.

The SCT consists of 2112 modules distributed in four barrel layers in the radial range $299 < R < 514$ $mm$, and 1976 modules distributed in nine disks in each end caps in the radial range $275 < R < 560$ $mm$. All the barrel models are identical, while the end-cap modules have three designs at different radial locations. Nevertheless, all the modules have similar construction. Every module has one group of strips on each side, glued back-to-back, with the back-side strips rotated 40 $mrad$ relative to the front-side strips. The pitch of the strips is 80 $\mu m$, leading to an intrinsic point resolution of 23 $\mu m$ per single side measurement in the coordinate perpendicular to the strip direction. The 40 $mrad$ stereo provides the transverse measurement capability, and also improves the precision measurement resolution to about 16 $\mu m$. The SCT plays a very important role in the inner detector for tracking in the bending plane, because it measures the track over a much longer distrance than the Pixel, with approximately the same spatial resolution. According to Equation 3.2, this means better transverse momentum resolution than the Pixel. It also provides more sampling points compared to the Pixel.

The outermost component of the inner detector, the TRT, uses a different technique. It is a straw tracker combined with transition-radiation detection for electron identification. This choice is based on the relatively low cost of the detector and its intrinsic radiation hardness. The TRT also helps to minimise the material in the tracking volume, because it introduces much less material per tracking point compared to the semiconductor trackers. The basic detecting unit of the TRT is drift tubes with 4 $mm$ diameter. There are 52544 axial straws of 144 *cm* length at radii between 554 *mm* and 1082 *mm* in the barrel part of the TRT, and 122880 radial straws of 37 *cm* length at radii between 617 *mm* and 1106 *mm* in each of the two end-cap parts. The straws are installed in three cylindrical layers of barrel TRT modules and $20 \times 2$ disks of end-cap modules. Each module contains multiple layers of straws. Polypropylene/polyethylene foils are installed in the space between the layers of straws as the radiator, and xenon-based gas mixture is employed to detect transition-radiation X-rays emitted by high energy electrons passing through the radiator.

With a small average distance between the straws, the TRT provides a large number of tracking points (typically 36) per track. Performance studies have shown that the TRT provides excellent pattern recognition and Level 2 triggering capabilities when combined with the semiconductor trackers. The relatively low resolution per tracking point (130 $\mu m$) is compensated by the large number of measurements and the bigger size of the detector (Equation 3.2).

Table 3.3 summarizes the major parameters of the ID subdetectors. Performance studies also show that the detectors behave reasonablely well at the high rates of the nominal LHC luminosity of $10^{34}$ $cm^{-2}s^{-1}$. The system is also capable of of withstanding the high radiation environment near the beamline, up to the 10-year design life time of the experiment under the LHC nominal luminosity, except the B-layer, which will have to be replaced after approximiately three years under the nominal luminosity. In order to maintain an adequate noise performace after radiation damange, the two semiconductor trackers are enclosed in a cold envelope. The TRT is desgined to operate at room temperature.

### 3.2.3 Calorimeters

The ATLAS calorimeter system includes electromagnetic (EM) calorimeters and hadronic calorimeters. The EM calorimeters are located in front of the hadronic calorimeters, because the EM radiation length is smaller than the hadronic radiation length; and they also have finer granularity than the hadronic calorimeters, because the EM showers are usually dense and well localized while the hadronic showers are more widely spread. Together, the two calorimeter systems play a central role in ATLAS, by providing precision mea-

| System | Position | Resolution $\sigma$ ($\mu m$) | Channels ($10^6$) | $\eta$ coverage |
|---|---|---|---|---|
| **Pixels** | 1 removable barrel layer | $R\phi = 10, z = 115$ | 13.2 | ±2.5 |
| | 2 barrel layers | $R\phi = 10, z = 115$ | 54 | ±1.7 |
| | 2 × 3 end-cap disks | $R\phi = 10, R = 115$ | 26.4 | 1.7–2.5 |
| **SCT** | 4 barrel layers | $R\phi = 16, z = 580$ | 3.2 | ±1.4 |
| | 2 × 9 end-cap disks | $R\phi = 16, R = 580$ | 3.0 | 1.4–2.5 |
| **TRT** | 73 axial barrel straw planes | 170(per straw) | 0.1 | ±0.7 |
| | 160 radial end-cap straw planes | 170(per straw) | 2.5 | 0.7–2.5 |

Table 3.3: Main parameters of the inner detector [32]

surements of and identification information for electrons, photons, jets and missing $E_T$ and triggering on these objects. The Liquid Argon (LAr) sampling technique is used for all EM calorimeters up to $|\eta| < 3.2$, and also for hadronic calorimeters from $|\eta| = 1.5$ to 4.9, the acceptance limit [38]. For $0 < |\eta| < 1.7$, a less expensive iron-scintillator hadronic calorimeter called the Tile calorimeter is used because of the large area required [39].

The layout of the calorimeter is shown in Figure 3.6. The calorimeter is composed of a barrel and two end-caps. Each end-cap is housed in an end-cap cryostat. The inside part of the barrel consists of two identical LAr EM barrels (EMBA), housed together with the solenoid in the central cryostat. Outside the EMBA, there are two Tile barrels and two extended Tile barrels (TileCal). The end-cap part contains, at lower pseudorapidity, the LAr EM end-cap (EMEC) inside, and the LAr hadronic end-cap (HEC) outside. The LAr forward calorimeter (FCAL), also located in the end-cap cryostat, extends the pseudorapidity coverage to $|\eta| = 4.9$. In the region of $|\eta| < 1.8$, there is an additional instrumental LAr layer, called the presampler detector, which is not shown in the figure. The presampler is used to correct for the energy lost upstream of the calorimeter.

The EMBA and the EMEC constitute the precision EM calorimeter. They are lead-LAr detectors with accordion-shaped absorbers and electrodes. In the $\eta$ region matched to the inner detector ($0 < |\eta| < 2.5$), the EM calorimeter has three sampling layers in depth and fine lateral granularity, ideally suited for precision measurements of electrons and photons. Over the range $2.5 < |\eta| < 3.2$ and in the overlap region between the EMBA and the EMEC, the EM calorimeter has two sampling layers and coarser gran-

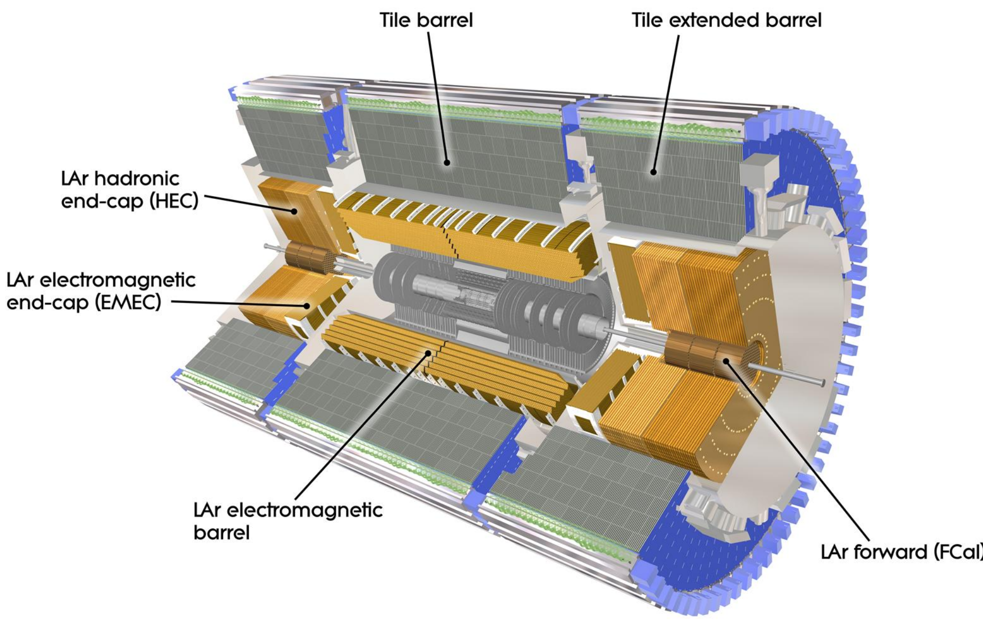


Figure 3.6: Three-dimensional cut-away view of the ATLAS calorimeter [40]

ularity. The hadronic calorimeters and the FCAL also have coarser granularity than for the precision EM calorimeter region. The coarser granularity in the respective regions has been tested to be sufficient to satisfy the physics requirements for jet reconstruction and missing $E_T$ measurements. The TileCal in the barrel and the HEC in the end-cap constitute the hadronic calorimeter. The TileCal uses tile scintillator and steel absorber. The HEC is a copper-LAr detector. The FCAL, a copper/LAr plus tungsten/LAr detector, provides both EM coverage and hadronic coverage in the forward region.

The longitudinal and lateral segmentation of the pseudorapidity coverage, and the transverse segmentation for the calorimeter are summarized in Table 3.4 and 3.5. The total thickness of the calorimeter is 11 interaction length ($\lambda$) at $\eta = 0$. This depth provides good containment for EM and hadronic showers, and limits punch-throughs into the muon system. Together with the large $\eta$ coverage, this depth also ensure a good missing $E_T$ measurement.

In total, there are approximately 180,000 calorimeter read-out cells. These cells are combined by the calorimeter reconstruction software to form discrete objects, either fixed-

| | Barrel | | End-cap | |
|---|---|---|---|---|
| | **LAr electromagnetic barrel (EMBA)** | | **LAr electromagnetic endcap (EMEC)** | |
| | number of layers | $\lvert\eta\rvert$ *coverage* | number of layers | $\lvert\eta\rvert$ coverage |
| Presampler | 1 | $\lvert\eta\rvert < 1.52$ | 1 | $1.5 < \lvert\eta\rvert < 1.8$ |
| Calorimeter | 3<br>2 | $\lvert\eta\rvert < 1.35$<br>$1.35 < \lvert\eta\rvert < 1.475$ | 2<br>3<br>2 | $1.375 < \lvert\eta\rvert < 1.5$<br>$1.5 < \lvert\eta\rvert < 2.5$<br>$2.5 < \lvert\eta\rvert < 3.2$ |
| | | Granularity $\Delta\eta \times \Delta\phi$ versus $\lvert\eta\rvert$ | | |
| Presampler | 0.025×0.1 | $\lvert\eta\rvert < 1.52$ | 0.025×0.1 | $1.5 < \lvert\eta\rvert < 1.8$ |
| Calorimeter 1st layer | 0.025/8×0.1<br>0.025×0.025 | $\lvert\eta\rvert < 1.40$<br>$1.40 < \lvert\eta\rvert < 1.475$ | 0.050×0.1<br>0.025×0.1<br>0.025/8×0.1<br>0.025/6×0.1<br>0.025/4×0.1<br>0.025×0.1<br>0.1×0.1 | $1.375 < \lvert\eta\rvert < 1.5$<br>$1.425 < \lvert\eta\rvert < 1.5$<br>$1.5 < \lvert\eta\rvert < 1.8$<br>$1.8 < \lvert\eta\rvert < 2.0$<br>$2.0 < \lvert\eta\rvert < 2.4$<br>$2.4 < \lvert\eta\rvert < 2.5$<br>$2.5 < \lvert\eta\rvert < 3.2$ |
| Calorimeter 2nd layer | 0.025×0.025<br>0.075×0.025 | $\lvert\eta\rvert < 1.40$<br>$1.40 < \lvert\eta\rvert < 1.475$ | 0.050×0.025<br>0.025×0.025<br>0.1×0.1 | $1.375 < \lvert\eta\rvert < 1.425$<br>$1.425 < \lvert\eta\rvert < 2.5$<br>$2.5 < \lvert\eta\rvert < 3.2$ |
| Calorimeter 3rd layer | 0.050×0.025 | $\lvert\eta\rvert < 1.35$ | 0.050×0.025 | $1.5 < \lvert\eta\rvert < 2.5$ |
| | | | **LAr hadronic endcap (HEC)** | |
| | | | number of layers | $\lvert\eta\rvert$ coverage |
| | | | 3 | $1.5 < \lvert\eta\rvert < 3.2$ |
| | | Granularity $\Delta\eta \times \Delta\phi$ versus $\lvert\eta\rvert$ | | |
| Outer wheel | | | 0.1×0.1 | $1.5 < \lvert\eta\rvert < 2.5$ |
| Inner wheel | | | 0.2×0.2 | $2.5 < \lvert\eta\rvert < 3.2$ |
| | | | **LAr forward calorimeter (FCAL)** | |
| | | | number of layers | $\lvert\eta\rvert$ coverage |
| | | | 3 | $3.1 < \lvert\eta\rvert < 4.9$ |
| | | Granularity $\Delta x \times \Delta y$ ($cm^2$) versus $\lvert\eta\rvert$ | | |
| FCAL1 | | | 3.0×2.6<br>~four times finer | $3.15 < \lvert\eta\rvert < 4.30$<br>$3.10 < \lvert\eta\rvert < 3.15$<br>$4.30 < \lvert\eta\rvert < 4.83$ |
| FCAL2 | | | 3.3×4.2<br>~four times finer | $3.24 < \lvert\eta\rvert < 4.50$<br>$3.20 < \lvert\eta\rvert < 3.24$<br>$4.50 < \lvert\eta\rvert < 4.81$ |
| FCAL3 | | | 5.4×4.7<br>~four times finer | $3.32 < \lvert\eta\rvert < 4.60$<br>$3.29 < \lvert\eta\rvert < 3.32$<br>$4.60 < \lvert\eta\rvert < 4.75$ |

Table 3.4: Main parameters of the LAr calorimeter

| | Barrel | | Extended Barrel | |
|---|---|---|---|---|
| Tile calorimeter (TileCal) | | | | |
| | number of layers | $\|\eta\|$ coverage | number of layers | $\|\eta\|$ coverage |
| | 2 | $\|\eta\| < 1.0$ | 2 | $0.8 < \|\eta\| < 1.7$ |
| Granularity $\Delta\eta \times \Delta\phi$ versus $\|\eta\|$ | | | | |
| Layers except last | 0.1×0.1 | $\|\eta\| < 1.0$ | 0.1×0.1 | $0.8 < \|\eta\| < 1.7$ |
| Last layer | 0.2×0.1 | $\|\eta\| < 1.0$ | 2.2×0.1 | $0.8 < \|\eta\| < 1.7$ |

Table 3.5: Main parameters of the Tile calorimeter

size projective towers in the $\eta \times \phi$ plane, or clusters formed by topological clustering or sliding window clustering. Topological clusters are formed by grouping cells according to their neighbour relations. These objects serve as the input to the reconstruction of the physics objects, which will be described in Chapter 4.

### 3.2.4 The Muon Spectrometer

In common with the other two generations of leptons, the muon has weak interaction and electromagnetic interaction, but no strong interaction. Therefore it rarely produces hadronic showers. (The tau lepton, however, has a large mass and can decay to hadrons through weak interaction. And the hadrons in its decay products can produce hadronic showers.) Because of its large mass compared to electron, the muon less frequently produces electromagnetic showers via bremsstrahlung. Thus, the main energy loss mechanism for muons is ionization. As a result, muons can pass though the calorimeters with little perturbation and reach the muon spectrometer (MS). The muon spectrometer is the outermost subsystem of the ATLAS detector. At the LHC, very high-energy ($\gtrsim 100\,GeV$) muons can be produced. At such a high energy, the sagitta of the muon track in the relatively small inner detector becomes too small to be accurately measured, degrading the momentum resolution (Equation 3.2). This makes the muon spectrometer extremely important in detecting high-energy muons.

The muon spectrometer includes high-precision tracking chambers for accurate momentum measurement and fast response chambers for effective triggering [41, 42, 43, 44, 45]. Because the expected rates vary with pseudorapidity ($\eta$), four different technologies are used to cover different $\eta$ regions. There are two types of precision measurement chambers. MDT (monitored drift tubes) covers the region up to $|\eta| = 2.7$, except for the innermost end-cap layers which go up to $|\eta| = 2.0$. In the innermost end-cap layers, CSC (cathode strip chambers) is used to cover the region from $|\eta| = 2.0$ to $|\eta| = 2.7$, due to its higher rate capabilities and timing resolution. The MDTs are drift chambers formed by aluminum tubes with 3 *cm* diameter and lengths ranging from 70 *cm* to 630 *cm*. The CSCs are multi-wire proportional chambers (MWPC) with cathode strip readout orthogonal and parallel to the wires. It has a symmetric cell in which the anode wire pitch and anode-cathode spacing are both 2.54 *mm*. The precision cathode readout strips are oriented orthogonal to the anode wires. The readout pitch is either 5.31 *mm* or 5.56 *mm*, depending on the size of the chamber.

There are also two types of trigger chambers: RPC (resistive plate chambers) is used in the barrel and covers the region up to $|\eta| = 1.05$. And TGC (thin gap chambers) is used in the end-caps and covers $1.05 < |\eta| < 2.4$. The RPCs are gaseous parallel electrode-plate detectors operated in avalanche mode. The basic detecting element of the RPCs is a narrow gas gap of 2 *mm* width formed by two parallel resistive bakelite plates. The signal is read out by two orthogonal sets of metal strips, each connected via capacitive coupling on either plate. The readout strip pitch varies from 23 *mm* to 35 *mm* in different trigger layers. The TGCs are multi-wire chambers operated in saturated mode, with a design similar to that of MWPC, but with anode-to-cathode pitch (1.4 *mm*) smaller than anode-to-anode pitch (1.8 *mm*). Signal is read out directly from groups of 4–20 wires, as well as from orthogonal cathode strips. The readout strips are fan-shaped, becoming wider as the radius increases. The width and length of the strips also vary for different types of chambers. The strip width varies between 1.46 *cm* and 4.91 *cm*, and the strip length varies between 104 *cm* and 216 *cm*.

Figure 3.7 shows the layout of the ATLAS muon spectrometer in three-dimensional cut-away view. The naming scheme of the locations and the types of the muon chambers is depicted in Figure 3.8. The barrel chambers are arranged in three cylindrical layers at radii of about 5 *m*, 7.5 *m*, and 10 *m*. And the end-cap chambers are arranged in four sets of disks at distances of about 7.4 *m*, 10.8 *m*, 14 *m* and 21.5 *m*. All the stations are subdivided in $\eta$ into several segmentations (rings), as shown in Figure 3.8. For MDTs, CSCs, and RPCs, the entire system is also divided symmetrically into eight azimuthal sectors. Every octant contains pairs of slightly overlapping large and small chambers, each covering approximately half of the $\phi$ region, with the larger chambers slightly farther away from the interaction point. The TGCs are arranged differently, in that the system is divided into 12 azimuthal sectors, and within the sectors the arrangement of the chambers is also different in different trigger layers.

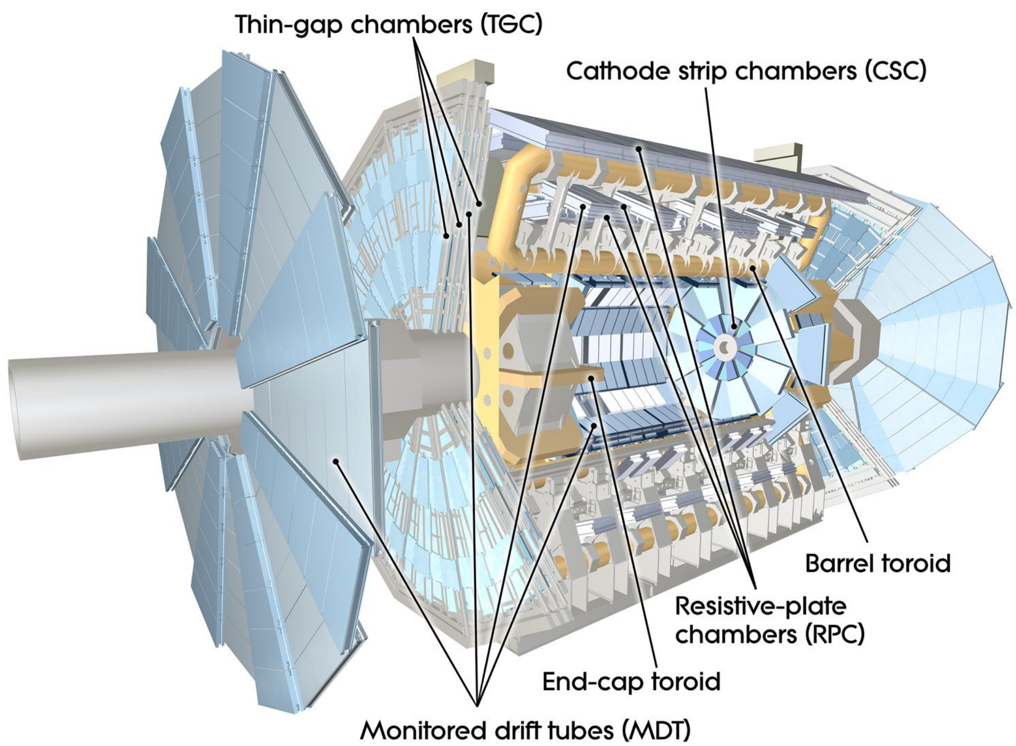


Figure 3.7: Three-dimensional cut-away view of the ATLAS muon detector [46]

Muon precision chambers are installed at all of the muon chamber stations, and are arranged so that particles from the interaction point traverse three stations of chambers. The positions of these stations are optimized for good hermeticity and optimum momentum resolution. At the inner stations, the MDTs are constructed of 2 multilayers of 4 monolayers of drift tubes; at other stations, they are constructed of $2 \times 3$ monolayers of drift tubes. The drift tubes of the MDTs are aligned perpendicular to the beam axis and

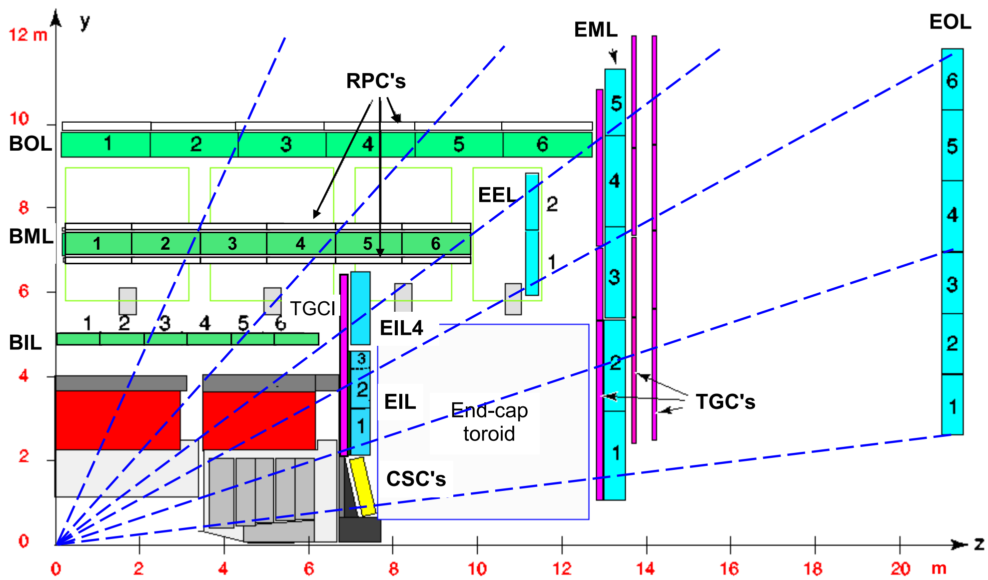


Figure 3.8: A side view of the layout of the ATLAS muon detector [32]. Locations and types of the chambers are denoted by three letters: $Y_1Y_2Y_3$. $Y_1$ describes the region and it takes the value of B (barrel), E (end-caps), or F (forward), where F is used only for CSCs; $Y_2$ describes the station and it usually takes the value of I (inner), E (extra), M (middle), and O (outer). $Y_3$ describes the size of a chamber and it is usually L (large) or S (small). For example, *BIL* denotes large chambers located at the inner layer of the barrel. Combinations of the $Y_1$, $Y_2$, $Y_3$ mentioned above are sufficient to describe the location and type of any MDT chamber. For CSC, RPC and TGC, $Y_2$ and $Y_3$ also take other values for more specific description. For example, $Y_2 = 1, 2, 3$ for RPC and TGC, denoting the first, second, and third trigger planes.

approximately parallel to the magnetic field lines, providing $z$ coodinate measurement in the barrel and $\eta$ ($R$) coordinate measurement in the end-caps. The typical single-tube resolution of the MDTs is 80 $\mu m$. The multilayer structure boosts the measurement of a $2 \times 4$-layer ($2 \times 3$-layer) MDT to an effective resolution of of 30 (35) $\mu m$. At the innermost station of each of the end-caps, CSCs with four planes make precision coordinate measurement in $\eta$ ($R$), with a typical single-plane resolution at 60 $\mu m$, and combined resolution of four planes in a chamber at 40 $\mu m$. The CSCs also provides measurement in $\phi$, the second coordinate which is orthogonal to the bending direction.

Muon trigger chambers are installed in trigger layers. Two layers of RPC chambers (refered to as RPC1 and RPC2 stations) are mounted on the BM station. A third layer (refered to as RPC3 station) is mounted on the BO station. Each RPC chamber is made of two rectangular detector layers containing one gas gap and two readout strip panels. One set of the strips, called the $\eta$ strips, is parallel to the MDT wires, and the other set of strips, called the $\phi$ strips, measures the coordinate orthogonal to the bending direction. The RPCs have excellent timing performance, with a single-layer time resolution of 1.5 $ns$ and signal FWHM of 5 $ns$. TGCs are installed at the EI and EM stations. They are constructed as double-gap units, called doublets, and triple-gap units, called triplets. One layer of TGC triplets (TGC1) is placed in front of the MDTs at the EM station, and two layers of doublets (TGC2 and TGC3) behind the MDTs. The EM TGCs provide the end-cap muon trigger, and their readout strips measure the second coordinate $\phi$. An additional layer of TGC triplets (TGCI) are installed at the EI station, but it is only used for measuring the second coordinate. The TGCs have a time resolution of 4 $ns$, not as good as that of the RPCs, but good enough to ensure 99% efficiency for a 25 $ns$ gate, the width of which is equal to the LHC bunching crossing time.

Table 3.6 summarizes the main parameters of the four subsystems of the muon detector. Note that the resolutions listed in the table are intrinsic values. The spatial resolution does not include the chamber-alignment uncertainties. To achieve an optimum performance, the positions of the muon chambers are monitored with optical alignment systems, and can be reconstructed using a combination of optical system alignment and track-based alignment. Displacements of up to $\sim$ 1 $cm$ are corrected for in the offline analysis.

| | | Chamber resolution (RMS) in | | | Measurements/track | | Number of | |
|---|---|---|---|---|---|---|---|---|
| **Type** | **Function** | $z/R$ | $\phi$ | time | barrel | end-cap | chambers | channels |
| MDT | tracking | 35 $\mu m$ ($z$) | – | – | 20 | 20 | 1150 | 335 $k$ |
| CSC | tracking | 40 $\mu m$ ($R$) | 5 $mm$ | 7 $ns$ | – | 4 | 32 | 30.7 $k$ |
| RPC | trigger | 10 $mm$ ($z$) | 10 $mm$ | 1.5 $ns$ | 6 | – | 544 | 373 $k$ |
| TGC | trigger | 2 – 6 $mm$ ($R$) | 3 – 7 $mm$ | 4 $ns$ | – | 9 | 3588 | 318 $k$ |

Table 3.6: Main parameters of the four subsystems of the muon detector [32]. The quoted spatial resolution (columns 3,4) does not include chamber-alignment uncertainties.

### 3.2.5 ATLAS Trigger and Data Acquisition System

The high luminosity at LHC proposes a major challenge for the ATLAS trigger system. At the LHC design collision energy $\sqrt{s} = 14\ TeV$, the total inelastic cross section is $\sim 70\ mb$ (the number is slightly smaller at 7 $TeV$) [30, 47, 48]. At the design luminosity $10^{34}\ cm^{-s} s^{-1}$, this gives an interaction rate of $\sim 10^9\ Hz$. However, protons are constrained to travel in ”squeezed” bunches, separated by 25 $ns$. At the design luminosity, there are 2808 proton bunches per each direction in the synchrotron. Therefore the event rate is 40 $MHz$ to be exact, with $\sim 23$ collisions per bunch.

On the other side, the typical event size of an ATLAS event is $\sim 1.6\ MB$ [49]. Considering the capability of the ATLAS permanent storage system, this limits the event rate that can be recorded to $\sim 200\ Hz$ [49]. A three tier trigger system is necessary in order to reduce the 40 $MHz$ to $\sim 200\ Hz$, and, in the mean time, to select the interesting hard-scattered events at a high efficiency.

The ATLAS Trigger and Data-Acquisition system (TDAQ) uses three levels of triggering to achieve efficient online event selection: L1 (Level 1), L2 (Level 2) and the EF (Event Filter) [50, 51, 52, 53, 54]. Together, L2 and EF are known as the HLT (High Level Trigger). This infrastructure is illustrated in Figure 3.9. On the left side of the figure, it is shown that each of the three trigger levels refines the selections made at the previous level and reduces the event rate further. The right side of the figure shows the data flow of the DAQ system.

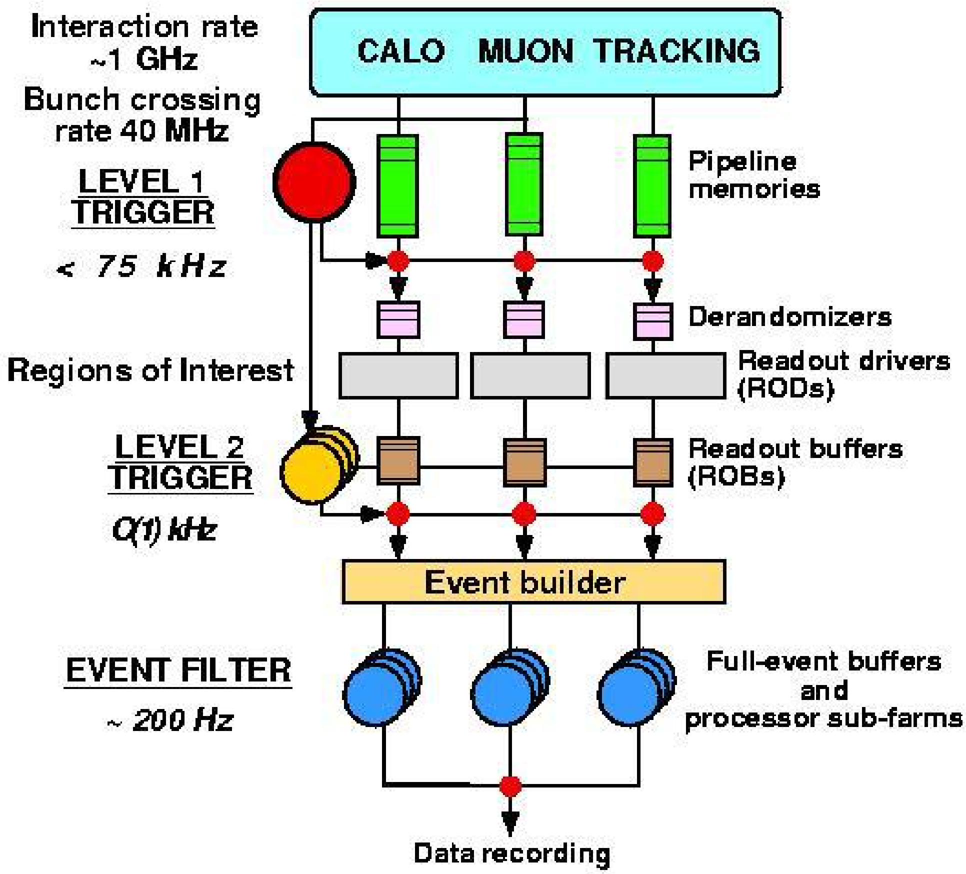


Figure 3.9: Block diagram of the Trigger/DAQ system [30]

The L1 trigger rejects the majority of low-energy events, reducing the rate to below 75 kHz. Due to the very limited processing time available at L1, the trigger is hardward-based. It is implemented in the electronics and firmware installed on the detector and uses only a limited amount of information from the detector. A selection for high $p_T$ electrons, jets and missing $E_T$ is made using reduced granularity information from all the calorimeters. Unlike the calorimeter trigger, high $p_T$ muons are triggered with dedicated muon trigger chambers, as already mentioned in Section 3.2.4. Figure 3.10 shows the L1 muon trigger principle in side view. In the barrel the trigger is based on a strip hit in the first RPC station and a range of strips hit in the second or/and third station. In the end-caps, the trigger is based on a coincidence between a strip hit in TGC3 station, and a range of strips hit in the TGC2 or/and TGC1 station.

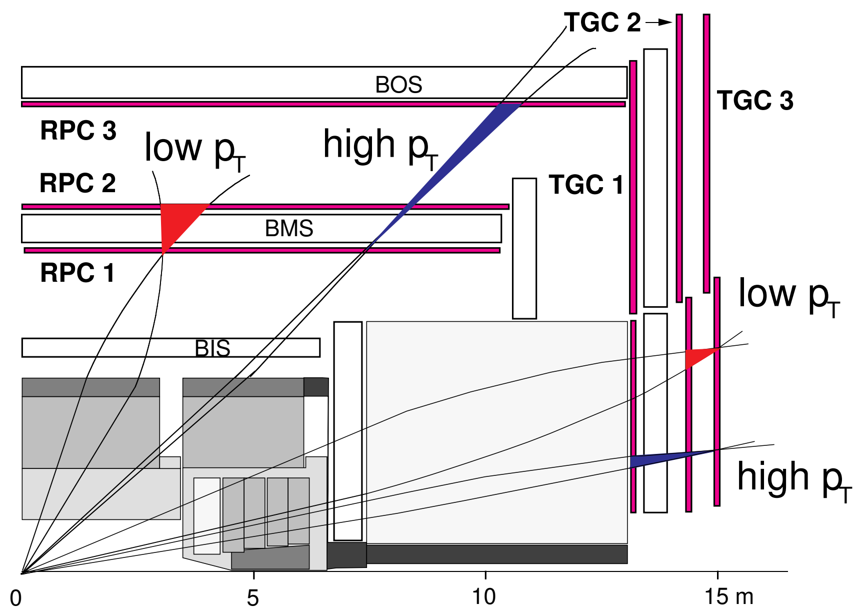


Figure 3.10: L1 Muon triggering principle [41]

The initial results from the L1 calorimeter and L1 muon triggers are processed by the Central Trigger Processor (CTP), which implements a trigger menu made up of combinations of trigger selections. The L1 trigger has a latency of $\sim 2.5\mu s$. During this time, the data from all detectors are stored in pipeline memories until a decision is made. For events passing L1 decision, the data is passed, through the Read Out Drivers (RODs) and then the Read Out Buffers (ROBs), to the High-Level Trigger (HLT) system. The L1 trigger also produces Region-Of-Interest (ROI) information for all potential trigger objects, which is used to seed the HLT trigger algorithms.

The L2 and EF trigger together reduces the rate by a factor of order $10^3$. Unlike the L1 trigger, which is based on very fast custom-made electronics, the HLT is software based and runs primarily on large commercial computer farms located near the detector. It is forseen to install for the final HLT farm $\sim$ 500 L2 and $\sim$ 1800 EF computing units, each with dual CPU sockets with quad-core processors [55, 56]. The HLT trigger is a combination of high rejection power with fast limited precison algorithms at L2, and modest rejection power with slower, high precision algorithms at EF.

The fast timing requirement at L2 doesn't allow for processing information from the whole detector. As a result, the ROIs passed from L1 are used to limit the amount of input data to the L2 algorithms. Using full granularity information from the ROIs ($\sim 2\%$ of the whole detector information), the L2 trigger reduces the event rate to $O(1)\ kHz$. The L2 trigger has a latency of $\sim 40\ ms$.

The data and the decision of the L2 trigger is sent to the Event Builder (EB), which combines the information from different parts of the detector to form whole events. Subsequently, the assembled events are sent to the Event Filter, which uses offline-like algorithms on complete information from the L2 ROIs to make a final selection. The EF trigger reduces the rate to the target number $\sim 200\ Hz$.

During the EF latency of $\sim 4\ s$, the data is cached in the full-event buffers. After the EF decision, the accepted events are recorded and moved to the ATLAS permanent event storage at the CERN computer center, and subsequently distributed to analysis centers around the world.

The triggers used in this analysis will be described in Chapter 6.

# Chapter 4

# Event Reconstruction and Object Identification

The data collected by the ATLAS detector consists of immediate detector responses from a huge number of readout channels. It is recorded as digitized "hits" and stored in bytestream format (Raw). The information contained in this data needs to be processed carefully and converted into "objects" representing products of the collision, such as tracks, vertices, leptons and jets, which can then be used by physicist for different types of physics studies. The whole process of converting the detector responses into physics objects with their properties is called event reconstruction. The process of using information left by particles in the detector to identify the type of the particles is called object identification (Id), or particle identification. In general, event reconstruction and object identification aims to achieve best signal efficiency, purity, and background rejection, and to provide the best possible measurements of the physics quantities. The identification criteria used are usually dependent on the type of the analysis.

The ATLAS reconstruction is mostly done in the common offline analysis software framework called the Athena analysis framework [49, 57, 58]. The analysis presented in this dissertation is based on data reconstructed in Release 16.0.2 of Athena. Different formats of data with different details are produced during reconstruction and analysis, currently including RDOs (Raw Data Objects), ESDs (Event Summary Data's), AODs (Analysis Object Data's), and DPDs (Derived Physics Datasets) [59, 60]. The different formats of data are suited for different purposes. Generally AODs and DPDs are used for physics analyses, and ESDs are used for physics studies and reprocessing. Although in principle data in any of these formats is accessible to a user wishing to perform data analysis, a user should only need to access the AODs, DPDs, and ESDs in small quantities. This largely lessens pressure on the ATLAS computing resources.

This first section in this chapter gives a brief description of the data reconstruction chain, and the data analysis procedure. The subsequent sections describe aspects of event reconstruction and object identification related to the $t\bar{t}$ analysis in this dissertation, including recent performance results. Reconstruction of the $t\bar{t}$ events involves every aspect of the ATLAS detector. Here all the physics objects in $t\bar{t}$ semileptonic final states are discussed, including electrons, muons, jets, and missing $E_T$. The ATLAS CSC (Computing System Challenge) notes are used as a reference of general information about reconstructing and identifying these objects [61]. And dedicated twiki pages are used as references for up-to-date technical details [62, 63, 64, 65, 66, 67, 68, 69].

## 4.1 Reconstruction and Analysis Procedures

Figure 4.1 shows the steps in the ATLAS data reconstruction chain, and the output of each step. The bytestream data is first converted to RDO (Raw Data Object) format, in which bytestream information is represented by C++ objects. Next, full reconstruction is run on the raw data objects to build physics objects. ESD (Event Summary Data) and AOD (Analysis Object Data) files are produced during this step. ESDs contain very detailed information of the reconstructed event, sufficient for re-reconstruction (track-refitting, jet re-calibration, etc.), which will typically be done several times. AODs contain a summary of the reconstructed event, and contain sufficient information for many physics analyses. AODs can be conveniently produced from the ESDs as well, without having to redo the reconstruction from raw data.

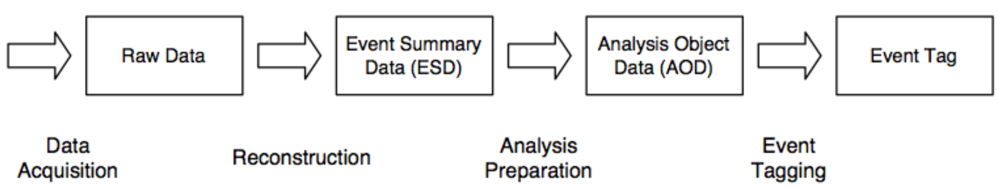


Figure 4.1: The ATLAS data reconstruction chain

In addition, tag data (TAG) is produced simultaneously with the ESDs or AODs. It is event-level meta data stored in a relational database, and supports efficient selection of events of interests for a given analysis, using first-level cuts via queries supported in the relational database [70]. The tag data information is not used in this analysis.

Currently, the common ATLAS data analysis procedure makes use of DPDs [60]. DPDs are produced by applying group-wide selections on ESDs or AODs. If produced from ESDs, the dataset is called DESD; and if from AODs, it is called DAOD. Three types of DPDs are defined: $D^1$PD, $D^2$PD and $D^3$PD. $D^1$PD and $D^2$PD are essentially small ESDs or AODs, after some data reduction or physics analysis selections. $D^3$PD is in plain rootuple format.

The primary DPD, $D^1$PD, is not specific to a certain analysis. It is produced centrally using the PrimaryDPDMaker, in which the data reduction strategies, classified as slimming, skimming and thinning, are implemented [71]. $D^2$PD and $D^3$PD are analysis specific, with selection criteria typically defined by a physics analysis group. $D^3$PD can be produced from any user analysis code, and it is decided by ATLAS that the contents of $D^3$PDs can be freely defined by user. It is conventional, however, for physics analysis groups to produce common $D^3$PDs suitable for all analyses performed within the group. In addition, individuals often make so-called $D^4$PDs or $D^5$PDs that are subsets of $D^3$PDs.

There have been a lot of efforts on the implementation of the DPD analysis scenario. Currently the top physics working group is converging towards using group-defined $D^3$PDs for most analyses. At the time when this analysis is done, however, the top group $D^3$PDs were not very well defined and did not have all the variables for our analysis. As such, the analysis in this dissertation is based on producing small rootuples from running on top group $D^2$PDs or user-defined $D^3$PDs and then doing analysis on the rootuples. The top group also employs common software built upon major Athena releases, called the TopPhys caches, for group-wide tasks. This analysis is based on TopPhys release 16.0.3.3.3 [72]. Known issues for this release are listed in [73].

## 4.2 Electron Reconstruction and Identification

Electron reconstruction uses information from the calorimeter and the inner detector. High-$p_T$ isolated electrons are reconstructed with the standard "egammaBuilder" algorithm, which starts with electromagnetic (EM) clusters with transverse energy above a threshold ($\sim$ 3 $GeV$), and searches for matching tracks in the inner detector (ID). The “egammaBuilder” is also responsible for isolated photon reconstruction.

The EM clusters are found in EM calorimeters, either with a default fixed-size “sliding window” algorithm or with an alternative algorithm which forms topological clusters based on connecting neighboring cells. Several cluster collections with different transverse sizes ($\Delta R = \sqrt{\Delta\eta^2 + \Delta\phi^2}$) are produced to satisfy the different requirements for different particle types. Electrons produce larger clusters than photons, as a result of both their slightly larger interaction probability in material compared to photon, and the fact that they bend in the magnetic field and radiate soft photons along a range in $\phi$.

The EM clusters can be separated into electron candidates and photon candidates by attempting to match with ID tracks. Electron candidates are obtained by matching EM clusters with energy $E$ to tracks in the ID with momentum $p$ such that $E/p < 10$ [61, 62]. Afterwards, the electron and photon candidates are calibrated separately.

In addition to this “egammaBuilder” algorithm, a “SofteBuilder” algorithm, seeded by tracks in the ID, is available for low-$p_T$ electron reconstruction. A third algorithm is dedicated to the reconstruction of forward electrons, where no track matching is required because of the limited coverage range of the ID. Reconstructed electrons from different algorithms are merged and the overlap between different algorithms is removed during the AOD production. The variable “*author*” is defined to indicate which algorithm created a certain electron. The standard electron is defined by:

$$author = 1 \parallel author = 3, \tag{4.1}$$

where “1” means the electron comes from the “egammaBuilder”, and “3” means both the “egammaBuilder” and the “softeBuilder” find the electron. In cases where both the algorithms find the same electron, the overlap is resolved and most parameters from the standard electrons are kept with a few exceptions.

In Athena release 15.3.0 and above, the four momentum of electrons and their error matrix are determined by combining the cluster four momentum measured in the EM calorimeter and the track four momentum measured in the ID. The energy $E$ is taken either from $E_{clus}$ or set by combining $E_{clus}$ and $p_{track}$, dependent on the value of a $\sigma$ parameter calculated, the $\eta$ is set dependent on the number of silicon hits, and the $\phi$ angle always comes from $\phi_{track}$. This method is shown in a diagram in Figure 4.2.

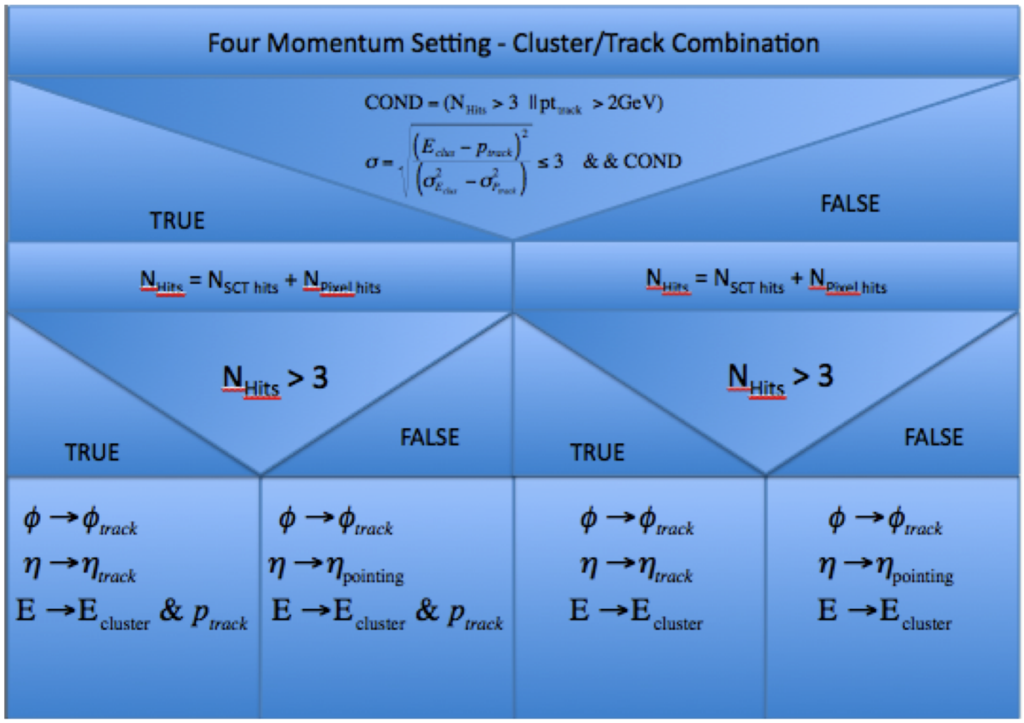


Figure 4.2: Electron combined four momentum setting: cluster/track combination [62]

At present, the covariance matrices for the combined four momentum of electrons are not yet validated on data. As a result, an alternative method is recommended by the Electron/Gamma physics group to always use $E_{clus}$ as the electron energy and take either $\eta_{clus}$ or $\eta_{track}$ as the electron $\eta$ depending on the number of silicon hits [74]. This analysis follows the recommendation to use the alternative method.

### 4.2.1 Electron Identification

Excellent identification capability for electrons is crucial for many important physics channels, including the $t\bar{t}$ production channel. Like many other processes, $t\bar{t}$ production is accompanied by a substantial QCD background. Therefore, powerful and efficient electron identification, with excellent jet rejection capability, is needed. At ATLAS, standard identification of high-$p_T$ electrons is based on cuts on many different variables (see Table 4.1), built from shower shape and track information from the calorimeter and the

| Type | Description | Variable name |
|---|---|---|
| | **Loose cuts** | |
| Acceptance of the detector | ⋆ $\|\eta\| < 2.47$ | |
| Hadronic leakage | ⋆ Ratio of $E_T$ in the first layer of the hadronic calorimeter to $E_T$ of the EM cluster (used over the range $\|\eta\| < 0.8$ and $\|\eta\| > 1.37$) | $R_{had1}$ |
| | ⋆ Ratio of $E_T$ in the hadronic calorimeter to $E_T$ of the EM cluster (used over the range $\|\eta\| > 0.8$ and $\|\eta\| < 1.37$) | $R_{had}$ |
| Second layer of EM calorimeter | ⋆ Ratio in $\eta$ of cell energies in $3 \times 7$ versus $7 \times 7$ cells | $R_\eta$ |
| | ⋆ Lateral width of the shower | $w_{\eta 2}$ |
| | **Medium cuts (includes Loose)** | |
| First layer of EM calorimeter | ⋆ Total shower width | $w_{\text{stot}}$ |
| | ⋆ Ratio of the energy difference associated with the largest and second largest energy deposit over the sum of these energies | $E_{ratio}$ |
| Track quality | ⋆ Number of hits in the pixel detector ($\geq 1$) | |
| | ⋆ Number of hits in the pixel and SCT ($\geq 7$) | |
| | ⋆ Transverse impact parameter (<5 mm) | $d_0$ |
| Track matching | ⋆ $\Delta\eta$ between the cluster and the track ($< 0.01$) | $\Delta\eta_1$ |
| | **Tight cuts (includes Medium)** | |
| $b$-layer | ⋆ Number of hits in the $b$-layer ($\geq 1$) | |
| Track matching | ⋆ $\Delta\phi$ between the cluster and the track ($< 0.02$) | $\Delta\phi_2$ |
| | ⋆ Ratio of the cluster energy to the track momentum | $E/p$ |
| | ⋆ Tighter $\Delta\eta$ cut ($< 0.005$) | $\Delta\eta_1$ |
| Track quality | ⋆ Tighter transverse impact parameter cut (<1 mm) | $d_0$ |
| TRT | ⋆ Total number of hits in the TRT $\leq 15$ | |
| | ⋆ Ratio of the number of high-threshold hits to the total number of hits in the TRT | |
| Conversions | ⋆ Electron candidates matching to reconstructed photon conversions are rejected | |

Table 4.1: Definition of variables used for loose, medium, and tight electron identification cuts for the central region of the detector ($|\eta| < 2.47$) [63, 75, 76]. The set of cuts and their values given in the table correspond to the quality type "ElectronTight_WithTrackMatch", used for winter 2010 top analysis. $\eta$ or $E_T$ dependent cut values are not included in the table and can be find in [75].

ID. These cuts have been optimised in a few bins in $\eta$ and $p_T$ [61, 75]. Three reference sets of cuts have been defined: loose, medium, and tight, with three corresponding quality levels defined. Currently the set of cuts and their values used for the quality levels are actively being optimised using first data. Table 4.1 shows the cuts corresponding to the quality type "ElectronTight_WithTrackMatch" used for the winter 2010 top analysis. In addition to the standard method, more advanced methods, such as the likelihood-based identification process are also implemented at ATLAS.

The efficiency for the cut based identification is evaluated on a $Z \to ee$ inclusive sample and shown in Figure 4.3, for the three reference identification selections "loose", "medium", and "tight" defined in Table 4.1.

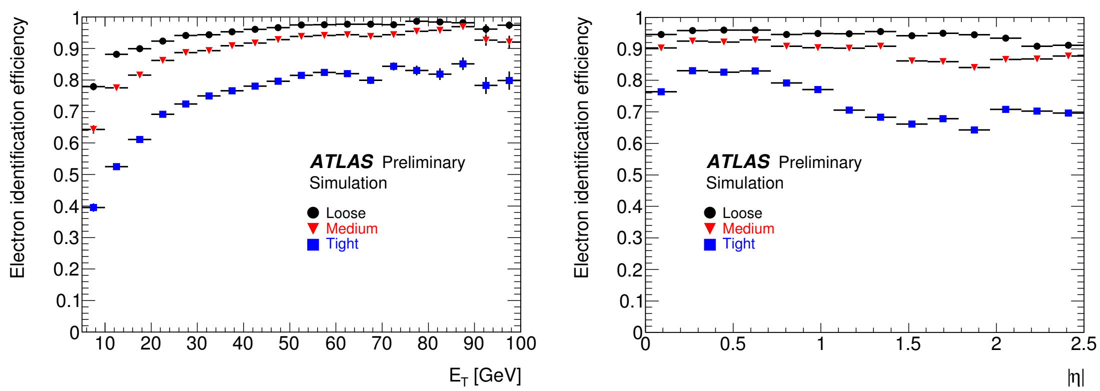


Figure 4.3: Electron efficiency vs $E_T$ (left) and vs $\eta$ (right) for the "loose", "medium", and "tight" selection for $Z \to ee$ [75]

The electron identification described so far does not include dedicated cuts on isolation, measured typically by transverse energy deposited in a cone of a certain radius minus the electron transverse energy. This is due to the fact that the electron isolation requirement is very analysis dependent. Table 4.2 summarises the different types of electrons according to their associated parent particle. Figure 4.4 shows the dependence of the calorimetric and track isolation variables using a cone size of $R_0 = \sqrt{\Delta\eta^2 + \Delta\phi^2} = 0.3$ on the electron transverse energy. In the recent software releases, e.g., Athena Release 16, four sets of cuts that exploit calorimetric and tracking isolation variables are defined. Each of them allow to retain 99%, 98%, 95% or 90% efficiency for isolated electrons from $Z$ decays. The set of cuts with 95% efficiency is used as the default isolation requirement.

The efficiencies and rejections of the isolation cuts in combination with the quality levels are listed in Table 4.3, for electrons with transverse energy $E_T > 20\ GeV$.

| Category | Type of particle | Type of parent particle |
|---|---|---|
| Isolated | Electron | $Z$, $W$, $t$, $\tau$ or $\mu$ |
| Non-isolated | Electron | $J/\psi$, $b$-hadron or $c$-hadron decays |
| Background electron | Electron | Photon (conversions), $\pi^0/\eta$ Dalitz decays, $u/d/s$-hadron decays |
| Non-electron | Charged hadrons, $\mu$ | |

Table 4.2: Classification of simulated electron candidates according to their associated parent particle [61]. Muons are included as source because of the potential emission of a Bremsstrahlung photon.

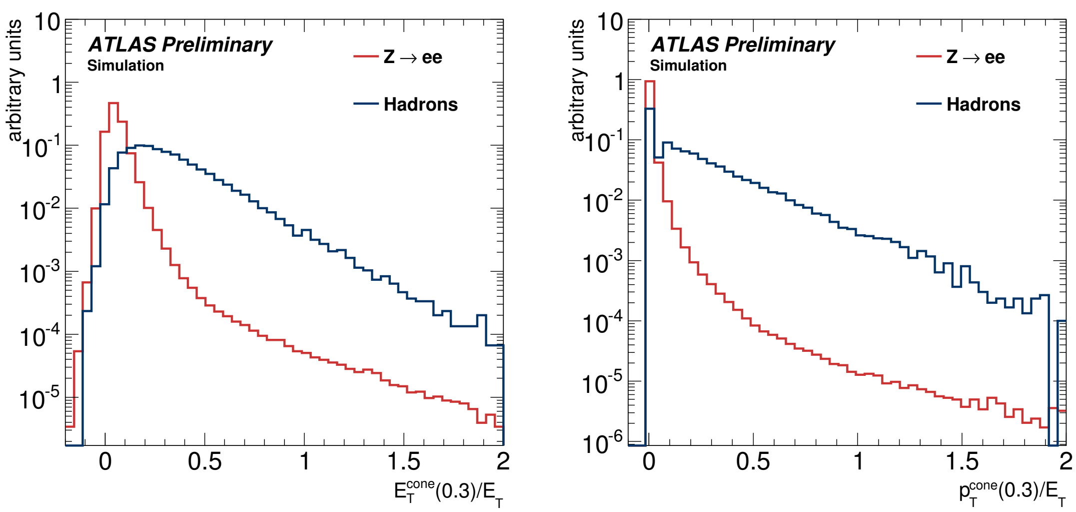


Figure 4.4: Calorimetric and tracking isolation energy normalised to the transverse energy, $E_T^{\text{cone}}/E_T$ and $p_T^{\text{cone}}/E_T$, for a cone of $R_0 = 0.3$ [75]. The electron candidates are required to have a transverse energy larger than 15 GeV and to pass the medium electron identification.

### 4.3 Muon Reconstruction and Identification

Muon reconstruction and identification is based on a combined usage of data from three ATLAS sub-detectors: the muon spectrometer (MS), the inner detector (ID), and the

| Cuts | $E_T > 20\ GeV$ | | | | | | |
|---|---|---|---|---|---|---|---|
| | Efficiency (%) | | Jet rej. (tot) | surviving candidates (%) | | | |
| | $Z \to ee$ | $b, c \to e$ | | iso | non-iso | bkg | had |
| | $\pm 0.03$ | $\pm 0.5$ | | | | | |
| Reco | 97.58 | - | $91.5 \pm 0.1$ | 0.1 | 0.8 | 23.3 | 75.8 |
| Loose | 94.32 | 36.7 | $1066 \pm 4$ | 0.3 | 1.9 | 56.7 | 40.4 |
| Medium | 90.00 | 31.5 | $6840 \pm 68$ | 6.0 | 9.9 | 50.5 | 33.4 |
| + isol. 99% | 88.87 | - | $10300 \pm 130$ | 9.2 | 7.6 | 56.2 | 27.0 |
| + isol. 98% | 87.99 | - | $13600 \pm 200$ | 11.7 | 5.8 | 58.7 | 23.8 |
| + isol. 95% | 85.06 | - | $20000 \pm 350$ | 16.0 | 3.5 | 60.5 | 20.0 |
| + isol. 90% | 80.67 | - | $27100 \pm 550$ | 16.9 | 2.6 | 60.7 | 16.8 |
| Tight | 71.59 | 25.2 | $(1.39 \pm 0.06) \cdot 10^5$ | 29.9 | 44.9 | 11.4 | 13.8 |
| + isol. 99% | 70.78 | - | $(1.98 \pm 0.11) \cdot 10^5$ | 42.3 | 32.7 | 12.5 | 12.5 |
| + isol. 98% | 70.16 | - | $(2.50 \pm 0.15) \cdot 10^5$ | 51.6 | 24.1 | 12.3 | 12.0 |
| + isol. 95% | 68.05 | - | $(3.79 \pm 0.28) \cdot 10^5$ | 65.5 | 13.3 | 11.7 | 9.5 |
| + isol. 90% | 64.83 | - | $(5.15 \pm 0.45) \cdot 10^5$ | 73.5 | 8.3 | 11.0 | 7.2 |

Table 4.3: Expected isolated electron efficiencies, non-isolated electron efficiencies, and jet rejections for the identification cuts and an $E_{\mathrm{T}}$-thresholds of 20 $GeV$ and $|\eta| < 2.5$ [75]. The efficiencies are computed on a $Z \to ee$ sample and rejections are computed on a filtered QCD dijet sample. The quoted errors are statistical. The total jet rejection includes hadron fakes and background electrons from photon conversions and Dalitz decays. The last four columns give the fraction of surviving electron candidates in the QCD dijet sample after each selection level.

calorimeter. The MS reconstructs standalone muon tracks and measures the momenta of charged particles at the entrance of the MS. The standalone muon tracks are extrapolated back to the beam line, and the energy loss in the calorimeter is added, in order to measure the muon momenta at the primary vertex. This reconstruction strategy is called the "standalone" muon reconstruction. The standalone muon measurements can be combined with measurements from corresponding ID tracks to improve the performance. This reconstruction strategy produces "combined" muons. In addition, "tagged" muons are produced, by propagating all ID tracks with sufficient momentum out to the MS and searching for matching segments in the inner and middle stations of the MS. The "tagged" muon reconstruction mainly aims to reconstruct low $p_T$ muon tracks. Lastly there is a reconstruction strategy which makes use of calorimeter tagging algorithms to reconstruct muons which failed to exit the calorimeter. The calorimeter tagging algorithms are not included in the discussion below.

### 4.3.1 Reconstruction Algorithms

For every strategy mentioned above, ATLAS provides at least two algorithms to choose from. These algorithms are grouped into two families: the Staco family and the Muid family. As a result, two separate muon collections exist in the AOD file: the "StacoMuonCollection", and the "MuidMuonCollection" which is used in this analysis. Reconstructions of the two collections use different algorithms at every step, which are summarized in Table 4.4.

| **Step during reconstruction** | **Algorithm** | |
|---|---|---|
| | Staco | Muid |
| standalone muon reconstruction | MuonBoy | Moore,MuidStandalone |
| combined muon reconstruction | STACO | MuidCombined |
| tagged muon reconstruction | MuTag | MuGirl,MuTagIMO |

Table 4.4: Algorithms used at every step during the muon reconstruction by the Staco and Muid families

For standalone muon reconstruction, the Staco family uses the "MuonBoy" algorithm, while the Muid family uses "Moore" for standalone tracking and "MuidStandalone" for inward extrapolation. At this step, however, despite the different implementations, the general procedures are essentially the same. Both families start by identifying Regions of Activity, which are seeded by the muon trigger chambers, and then employ a pattern recognition algorithm to form local segments in each of the three muon stations. Next, the local segments are connected via a three dimensional continuous track fit in the magnetic field. And finally the inward extrapolation is performed.

The major difference of the two families lies in the process of combining measurements from the MS and measurements from the ID. The Staco muon reconstruction attempts to statistically merge the two independent measurements from the ID track and the MS track. The Muid muon reconstruction performs a global fit of all the hits associated with the tracks in both detectors, taking into account also the calorimeter mass profile which is approximated by two scattering planes [65]. The latter algorithm is called “MuidCombined”. In “MuidCombined”, inner detector tracks corresponding to muon standalone tracks are found by cutting on $\chi^2_{match}$ formed by the difference in the five track parameters and their summed covariances between the standalone fit and the inner detector. A combined fit is then performed on matches with $\chi^2_{match} > 0.001$. If no match is found, a combined fit is attempted for the best match within a “road” around the standalone track.

In the Muid muon reconstruction, the tagged muons are found by the “MuonGirl” or the “MuTagIMO” algorithm. The “standalone” muons, the “combined” muons, and the “tagged” muons are merged to improve the muon finding efficiency, and possible overlaps between different algorithms are removed. Similar to the electron case, the variable “*author*” is defined to indicate the algorithm by which a certain muon is built.

### 4.3.2 Muon Identification

As in electron identification, three quality levels are defined for muon identification. For muons, the quality levels don’t correspond to a set of cuts as in the electron case. Instead, they regroups the four different types of muons, originally categorized according to the algorithms by which they are reconstructed and identified [77]. The definition of the quality levels for Muid muons are summarised in Table 4.5.

| Quality levels | Requirements |
|---|---|
| Tight | MuidCombined, or MuidStandalone at $\|\eta\| > 2.5$ |
| Medium | Tight, or MuidStandalone |
| Loose | Medium, or MuGirl, or MuTagIMO |

Table 4.5: Definition of quality levels for Muid muons [78]

On top of the quality level selection, a set of ID hit requirements listed in Table 4.6 are applied so as to suppress fake tracks and muons from hadron decays. In addition, the muon isolation, either track based or calorimeter based, is used as a powerful tool for rejecting muons from hadron decays. Figure 4.5 compares the distributions of the several isolation variables for data and Monte Carlo samples.

| | ID hit requirements |
|---|---|
| ID silicon hit requirement | Number of B layer hits > 0<br>Number of pixel hits > 2<br>Number of SCT hits ≥ 6<br>Number of pixel holes + number of SCT holes < 2 |
| TRT hit requirements: $\|\eta\| \leq 1.9$ | $N_{hits} + N_{outliers} > 5$<br>$N_{outliers} / (N_{hits} + N_{outliers}) < 0.9$ |
| TRT hit requirements: $\|\eta\| > 1.9$ | If $N_{hits} + N_{outliers} > 5$: $N_{outliers} / (N_{hits} + N_{outliers}) < 0.9$ |

Table 4.6: ID hit requirements for muon identification [79]. The cuts are restricted to the instrumented areas; dead or missing sensors crossed by a track are counted as hits.

### 4.4 Jet Reconstruction and Identification

The jet collection used in this analysis is the "CorrectedAntiKt4H1TopoEMJets", reconstructed with the anti-$k_T$ algorithm applied to calorimeter topological clusters [61, 81]. "4" denotes that the distance parameter $R$ of the algorithm (see Section 4.4.1) is 0.4, the default configuration in ATLAS for narrow jets. "H1" denotes that cell energy density calibration, so called H1-style, is used as the jet calibration scheme [82]. "EM" denotes that the jets are with EM+JES calibration, meaning that numerical-inversion-based Jet Energy

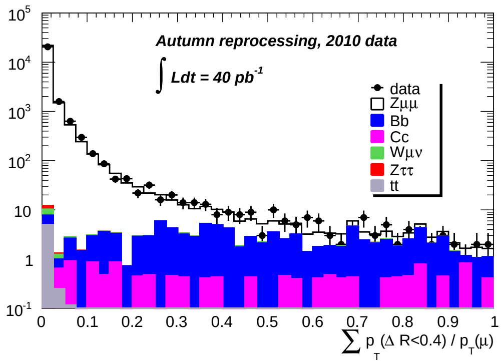


(a) Track isolation $\sum p_T(\Delta R < 0.4)/p_T(\mu)$

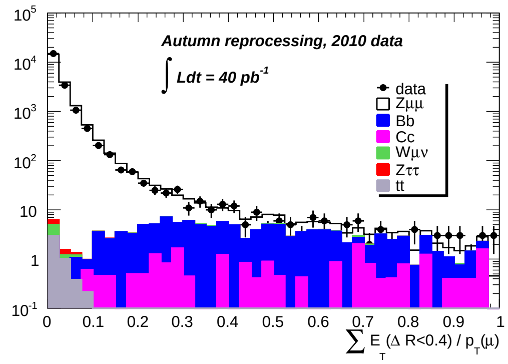


(b) Calorimeter isolation $E_T(\Delta R < 0.4)/p_T(\mu)$

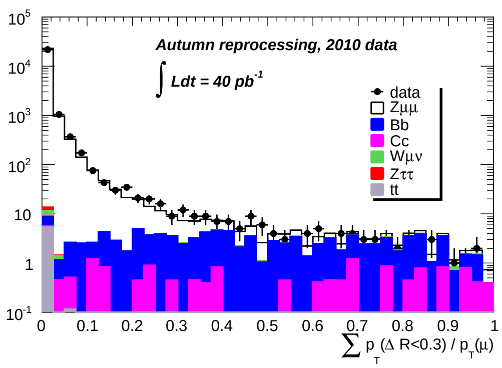


(c) Track isolation $\sum p_T(\Delta R < 0.3)/p_T(\mu)$

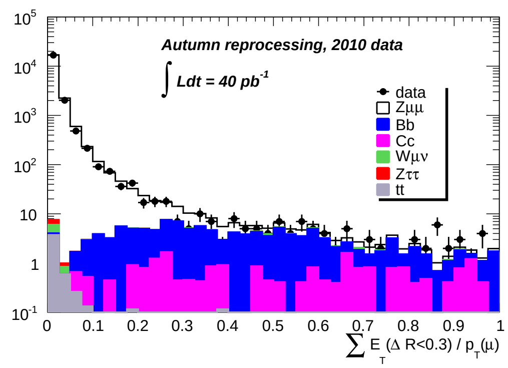


(d) Calorimeter isolation $E_T(\Delta R < 0.3)/p_T(\mu)$

Figure 4.5: Comparison of track and calorimeter isolation distributions measured in data and predicted by Monte Carlo for two different cone sizes [80]. The data distribution is measured with $Z \rightarrow \mu\mu$ decays using a "tag-and-probe" method.

Scale (JES) corrections are applied on calorimeter jets at EM scale [83, 84]. "Corrected" means the pile-up correction has been removed from the "AntiKt4H1TopoEMJets" in the AODs, which contains incorrect pile-up removal leading to some jets with negative energy and positive $p_T$ due to a software bug [85].

In ATLAS, an attempt is made to provide implementation of all relevant jet finding algorithms, including fixed-size cone algorithms, sequential recombination algorithms, and an algorithm based on event shape analysis. This is due to the fact that there is no universal jet finder for the hadronic final state in all topologies of interest. In $t\bar{t}$ production, which has a multijet final state, narrow jets are preferred in order to identify distinct jets. In the first section below, a description of the anti-$k_T$ algorithm, used in this analysis, is given. It has been decided by the Jet/ETmiss working group in spring 2009 to use the anti-$k_T$ algorithm as the main jet algorithm, and to provide support only for this algorithm in early data [66]. The main advantage of the anti-$k_T$ algorithm is that it is infrared safe.

### 4.4.1 Anti-$k_T$ Algorithm for Jet Reconstruction

The anti-$k_T$ algorithm belongs to the group of sequential recombination algorithms, which uses a recursive recombination scheme, based on pair-wise clustering of the initial constituents of the input calorimeter towers or clusters. The first of the sequential recombination algorithms, the $k_T$ cluster algorithm, is motivated by the coherent properties of QCD soft emission [86, 87]. It attempts to undo parton fragmentation, which, according to the parton splitting functions, is inversely proportional to a distance measure between any two particles $i$ and $j$, $d_{ij}$. The $k_T$ algorithm starts by clustering two particles with the smallest distance, and stops at a threshold defined by $d_i$. The distance measure $d_{ij}$ and the threshold $d_i$ are defined as following at hadron colliders [81]:

$$d_{ij} = min({k_T}_i^{2n}, {k_T}_j^{2n})\frac{(\Delta R)_{ij}^2}{R^2} \quad (4.2)$$

$$d_i = k_{T_i}^{2n} \quad (4.3)$$

where

$$
\begin{aligned}
n &= 1 && (4.4) \\
(\Delta R)^2_{ij} &= (y_i - y_j)^2 + (\phi_i - \phi_j)^2 && (4.5)
\end{aligned}
$$

where $y_{i,j}$ is the rapidity of events. Here $k_T$ denotes the transverse momentum of the particle. $R$ is the distance parameter, an adjustable parameter that sets the scale at which jets are resolved from each other. It allows for some control of the size of the jets.

Compared to the fixed-size cone algorithms, the cluster algorithms have the advantage of being both infrared safe and collinear safe. The original implementation of the $k_T$ algorithm was very slow for hadron colliders [88]. A faster implementation, available in the FastJet package, is used at ATLAS [81, 89]. Also included in the package are two variations of the $k_T$ algorithm, the Cambridge/Aachen algorithm and the anti-$k_T$ algorithm. In the Cambridge/Aachen algorithm, $n = 0$ in Equation 4.3, which means only the geometrical distance is considered [90]. In the anti-$k_T$ algorithm, used for this analysis, $n = -1$ in Equation 4.3, which means constituents with small $k_T$ are clustered first [91]. The disadvantage of this choice is that the meaning of the sequence has been lost. Despite that, the anti-$k_T$ algorithms have been verified to have sensible phenomenological behaviour. It also exhibits several distinct properties other algorithms don't have, notably an unusual resilience of its jet boundaries to soft radiation.

### 4.4.2 Jet Energy Scale

Jet energy scale (JES) corrections aim to transform the jet energy measured in the calorimeter into the energy corresponding to the underlying particle jet or parton jet. A number of mechanisms can cause the measured energy to deviate from the energy of the initial particle, including:

- Ratio of calorimeter response for electromagnetic showers and hadronic showers $e/h$, which is typically $> 1$ for non-compensating calorimeters.
- Energy lost in un-instrumented regions of the detector (dead material).

- Loss of energy deposits from part of the shower which is not contained in the calorimeter due to the finite size of the detector (leakage).
- Energy deposited in the detector due to processes other than the hard scattering of interest, including the underlying event, multiple proton-proton interactions, and pile-up. These processes are described in Chapter 5.
- Detector and electronic noises.
- The fraction of the jet energy excluded due to the finite size of the cluster (out-of-cone corrections).

Presently, ATLAS uses a simple calibration scheme that applies $p_T$ and $\eta$ dependent JES corrections to calorimeter jets at EM scale, which is referred to as the "EM+JES" scheme and restores on average the measured jet energy to its initial value [92]. The correction constants are derived using Monte Carlo simulation. Numerical inversion technique was used for converting corrections dependent on truth $p_T$ and $\eta$ to functions of reconstructed $p_T$ and $\eta$. More complicated calibration schemes, which make use of additional cluster-by-cluster or jet-by-jet information for reducing some sources of jet energy fluctuations, are currently under commissioning [93].

Jet energy scale calibrated with the "EM+JES" scheme have been validated up to 1 $TeV$ with several in-situ techniques [94, 95]. Its uncertainties have been evaluated using in-situ measurements of the single hadron response and an analysis of systematic variations in Monte Carlo simulations [96]. The total JES uncertainty is calculated for isolated jets as a sum of uncertainties from many sources such as the non-closure of the "JES" calibration, the calorimeter response, the detector simulation, the Monte Carlo event modelling, and the multiple proton-proton interactions. In addition, a systematics uncertainty due to close-by jets is estimated separately [97]. Latest JES uncertainty results for isolated anti-$k_T$ jets with $R = 0.4$ are summarized in Table 4.7. The numbers have been reduced compared to previous results thanks to increasing knowledge of the detector performance and more precise in-situ measurement of the single hadron response. Table 4.8 summarizes the additional systematic uncertainty for non-isolated jets.

| $\eta$ **region** | **Maximum fractional JES Uncertainty** | | |
|---|---|---|---|
| | $p_T = 20\ GeV$ | $p_T = 200\ GeV$ | $p_T = 1.5\ TeV$ |
| $0 \leq \lvert\eta\rvert < 0.3$ | 4.1% | 2.3% | 3.1% |
| $0.3 \leq \lvert\eta\rvert < 0.8$ | 4.3% | 2.4% | 3.3% |
| $0.8 \leq \lvert\eta\rvert < 1.2$ | 4.3% | 2.5% | 3.5% |
| $1.2 \leq \lvert\eta\rvert < 2.1$ | 5.2% | 2.6% | 3.6% |
| $2.1 \leq \lvert\eta\rvert < 2.8$ | 8.2% | 2.9% | |
| $2.8 \leq \lvert\eta\rvert < 3.2$ | 10.1% | 3.5% | |
| $3.2 \leq \lvert\eta\rvert < 3.6$ | 10.3% | 3.7% | |
| $3.6 \leq \lvert\eta\rvert < 4.5$ | 13.8% | 5.3% | |

Table 4.7: Summary of the maximum EM+JES jet energy scale systematic uncertainties for different $p_T^{jet}$ and $\eta^{jet}$ regions from Monte Carlo based study for anti-$k_T$ jets with $R = 0.4$ [96]. Isolated jets are defined by $R_{min} > 2.5 \times R$, where $R_{min}$ is the distance in $\eta$ and $\phi$ plane from the jet to the closest jet with $p_T > 7\ GeV$ at EM scale.

| $R_{min}$ range | R = 0.4 | |
|---|---|---|
| | $20 - 30\ GeV$ | $> 30\ GeV$ |
| $0.4 < R_{min} < 0.5$ | 2.7% | 2.8% |
| $0.5 < R_{min} < 0.6$ | 1.7% | 2.3% |
| $0.6 < R_{min} < 0.7$ | 2.5% | 2.7% |

Table 4.8: Summary of jet energy scale systematic uncertainty assigned for non-isolated jets accompanied by a close-by jet within the denoted $R_{min}$ ranges [97]. The second row in the table indicates the $p_T$ range of the non-isolated jets. Results are shown for the range $R < R_{min} < R + 0.3$. When the two jets are separated by a distance of $R + 0.3$ or more, the jet response becomes similar to that for the isolated jets and therefore no additional systematic uncertainty is needed.

The JES corrections described so far did not take into account the flavor dependence of the jet response. Jets originated from heavy flavor quarks differ from light flavor jets in several aspects. In particular, the fragmentation of the $b$-jets are harder than the lighter flavor jets and the $b$ hadron retains about 70% of the original $b$ quark momentum [61]. In addition, $b$-hadrons have a large branching ratio for semileptonic decays in which neutrinos are produced and their energies are lost. These effects lead to a lower average calorimeter response for the $b$-jets than for the light jets. Since the uncertainty results above were derived from samples with a certain flavor composition, an additional analysis dependent systematics needs to be added for the $b$-jet energy scale. For similar reasons, another additional systematics is also needed, to cover the effect of quark/gluon content fractions.

A common tool aimed for returning all the different terms of the JES uncertainty has been provided by the Jet/ETmiss working group. The tool is called the MultijetJESUncertaintyProvider. The version used in this analysis can be found in [98].

### 4.4.3 Jet Energy Resolution

Compared to electromagnetic objects, jets usually have a much larger energy resolution, due dominantly to large shower-by-shower fluctuations in the composition of the hadronic showers, referred to as the intrinsic fluctuations. Energy deposited by hadrons in the calorimeters can be decomposed as:

$$E_{dep} = E_{dep}^{EM} + E_{dep}^{had} \tag{4.6}$$

where $E_{dep}^{EM}$ is the EM component of the shower, due to neutral pions ($\pi^0$'s) produced in intra-nuclear cascades; $E_{dep}^{had}$ is the pure hadronic component of the shower. The fraction of $E_{dep}^{EM}$ can vary significantly shower by shower. Furthermore, not all of $E_{dep}^{had}$ is visible by the calorimeters. The invisible part of the energy deposit, $E_{dep}^{inv}$, including the lost nuclear binding energy, the neutrino energy, and the slow neutrons, also varies shower by shower. The effects of the intrinsic fluctuations on the jet energy resolution (JER) can be reduced by compensating the $e/h$ ratio during offline calibration, applying to calorimeter cells weights based on cell energy density or the longitudinal profile of the shower. As just mentioned in Section 4.4.2, calibration schemes with this kind of corrections are currently under commissioning at ATLAS.

The JER is commonly written in the following form:

$$\frac{\sigma(E)}{E} = \sqrt{\left(\frac{A}{\sqrt{E}}\right)^2 + \left(\frac{B}{E}\right)^2 + C^2} \quad (4.7)$$

where the first term under the square root is due to statistical fluctuations, including both sampling fluctuations and statistical fluctuations; the second term is the noise term, induced by detector and electronic noises; the third term is the constant term, originated from possible calibration errors and other systematic effects. A first in-situ measurement of the JER have been performed in Athena Release 15 with early 2010 data using the di-jet balance method and the bi-sector techniques [99]. Data/MC comparison shows that the JER in data is slightly higher than in MC almost in all $\eta$ regions by up to 10%. The numbers are currently being updated with more data and newer software release (Release 16).

Preliminary plots have been made comparing the JER for different calibration methods [100]. As expected, all of the more advanced methods yield smaller JER compared to the "EM+JES" calibration.

### 4.4.4 Jet Reconstruction Efficiency

The jet reconstruction efficiency and its associated uncertainties have been measured relative to track jets, using the tag-and-probe method with a sample of back-to-back di-jet events [85, 99]. The highest $p_T$ track jet is used as the tag, and a second track jet balancing the leading jet in $\phi$ is considered the probe. The efficiency is defined as:

$$\epsilon_{jetReco} = \frac{N^{matched}_{track\ jet\ probes}}{N_{track\ jet\ probes}} \quad (4.8)$$

where $N_{track\ jet\ probes}$ is the total number of track jet probes, and $N^{matched}_{track\ jet\ probes}$ is the number of track jet probes matching a calorimeter jet within $\Delta R = 0.4$.

The jet reconstruction efficiency has been measured for MC simulated minimum bias events and for the full 2010 data using the MinBias stream [85, 101]. Figure 4.6 shows the measured efficiency in data and MC as well as its data/MC correction scale factor. The MC agrees well with data. The Monte Carlo efficiency $\epsilon_{MC}$ agrees with data within $\pm 5\%$ for track jets with $p_T \geq 5\ GeV$ and within $\pm 2\%$ for track jets with $p_T \geq 15\ GeV$.

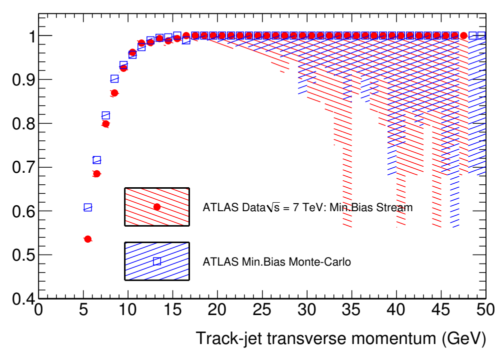


(a)

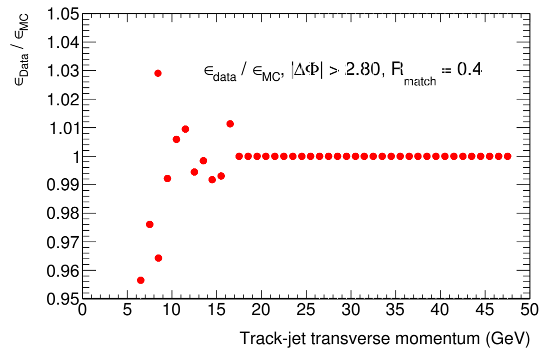


(b)

Figure 4.6: Calorimeter jet reconstruction efficiency with respect to track jets (left) and its data/MC correction scale factor (right) as a function of the probe track jet $p_T$ [85]. The efficiency and scale factors dependent on the track jet $p_T$ can be transformed with numerical inversion technique to functions of the calorimeter jet $p_T$.

Because of the rather different final state products in the $t\bar{t}$ events compared to di-jet events, the reconstruction efficiency for jets in $t\bar{t}$ events has been measured using a slightly different approach. In this case, one defines the efficiency as:

$$\epsilon_{jetReco} = \frac{N^{matched}_{track\ jets}}{N_{track\ jets}} \tag{4.9}$$

where $N_{track\ jets}$ is the total number of all reconstructed track jets, and $N^{matched}_{track\ jets}$ is the number of track jets matching a calorimeter jet within $\Delta R = 0.4$ out of all reconstructed track jets [102]. This method is used on $t\bar{t}$ Monte Carlo samples to extract the jet reconstruction efficiency.

A comparison of the second method with the tag-and-probe method applied on the minimum bias sample shows the two methods return similar efficiencies for jets with $p_T \geq 20\ GeV$. In spite of this, it is still decided that this method needs further studies. As the results from both of the two methods need further investigation, also considering that both methods show good data/MC agreement, it is decided not to correct MC to match data.

A conservative uncertainty of 2% on the jet reconstruction efficiency is recommended for estimation of systematic error associated with it [101].

## 4.5 *b*-Tagging

Reconstructed and identified jets can be further classified, according to the flavor of their originating quark or gluon, into light flavor jets ($u$, $d$, $s$, $g$), $c$-jets, or $b$-jets. This procedure is called heavy flavor tagging. $b$-tagging can be very important for physics studies involving $t\bar{t}$, as there are two real $b$-jets in the final state of $t\bar{t}$ decay. Several of the known properties of the $b$-jets can be used to distinguish them from lighter flavor jets. Among these the most important is the relatively long life time of hadrons containing a $b$ quark, which is of the order of 1.5 $ps$. The $b$-jets also tend to have a large transverse momentum as the result of the hard fragmentation and the relatively high mass of the $b$-hadrons. Finally, $b$-jets with semileptonically decaying $b$-hadrons are characterized by a soft electron or muon found within the jet cone. The leptons also have a relatively large transverse momentum and a large momentum relative to the jet axis, thanks again to the hard fragmentation and the high mass of $b$-hadrons. Compared to the light flavor jets, $c$-jets are harder to distinguish from $b$-jets, because the $c$-hadrons also decay semileptonically, and because of the relatively large mass of the $c$ quark.

Currently, there are two major types of $b$-tagging algorithms at ATLAS. The lifetime tagging algorithms tag $b$-jets by identifying charged tracks which are significantly displaced from the primary vertex, i.e., with a large impact parameter. The soft lepton taggers (SLTs) identify semileptonic $b$-jets with the presence of a soft electron or muon within the jet cone. While intrinsically limited by the small semileptonic branching ratio, the SLTs offer a good alternative or complement to the lifetime taggers. The SLTs also have the advantage that the correlations with other tagging algorithms are minimal.

The following lifetime tagging algorithms are implemented at ATLAS [61, 103]:

- **Impact paramter (IP) taggers** by usage of the statistical significance of the IP. It includes three likelihood ratio based algorithms: IP1D relies on the longitudinal IP significance $z_0/\sigma_{z_0}$, IP2D on the transverse IP significance $d_0/\sigma_{d_0}$, and IP3D uses both. In addition, it also includes two simpler algorithms, TrackCounting and JetProb. Both of them use only the transverse IP significance. TrackCounting requires the second highest $d_0/\sigma_{d_0}$ to be over a threshold [104]. JetProb bases its decision on a probability representing how much the jet in question is compatible with a prompt jet. The probability is derived from comparing the IP significance of each track in the jet with the IP resolution parameter $\mathcal{R}$ measured using prompt tracks [104].

- **Secondary vertex (SV) taggers**, the so called SV algorithms. This type of algorithms involves explicit reconstruction of an inclusive secondary vertex. Three properties of the secondary vertex are used: the invariant mass of all tracks associated with the vertex, the ratio of the $\sum E_{tracks\_of\_vertex}/\sum E_{tracks\_in\_jet}$, and the number of all two-track vertices from which the secondary vertex was built. Two likelihood ratio based SV taggers are defined: SV1, using the first two variables, and SV2, using all three variables. A third simpler algorithm, SV0, will be described in a bit more detail in Section 4.5.1, because it is the tagger used in this analysis.

- **JetFitter**, a relatively new heavy flavor tagging algorithm. It exploits the topological structure of the weak $b$-hadron or $c$-hadron decay inside the heavy flavor jet. The fragmentation of a $b$-quark results in a decay chain which has two vertices inside the jet: PrimaryVertex $\rightarrow B \rightarrow D$, where $B$ stands for a $b$-hadron and $D$ a $c$-hadron. The JetFitter algorthm employs a Kalman fitter to fit the decay chain in a single pass, in order to find the common line on which the primary vertex and the $b$-hadron and the $c$-hadron vertices lie, and also the positions of the vertices on this line approximating the $b$-hadron flight path. The discrimination between $b-$, $c-$ and light jets is based on a likelihood built with similar variables to the SV algorithms described above [61].

- **Combined lifetime taggers**, currently including the IP3D+SV1 tagger and the IP3D+JetFitter tagger. The latter is also called the JetFitterComb tagger. The total log likelihood of the combined tagger is calculated as a simple sum of the log likelihood values of the individual taggers. There is also ongoing efforts to use other multivariate approaches, such as the neural network (NN) and the boosted decision trees (BDT), in place of the simple likelihood and as a way to combine tagging algorithms [61]. These methods are not only used for combining lifetime taggers, but also used for combining all the tagging algorithms.

Of all the *b*-tagging algorithms described above, the lifetime algorithms based on likelihood ratio are the most powerful. The is because more information is used compared to simpler algorithms. On the other hand, they are harder to calibrate because they require knowledge of the probability density functions (pdfs) of all the discriminating variables for both the *b*- and the light jet hypotheses. For calibration, the Monte Carlo simulated distributions of these variables have to be validated and corrected with data. During the early data analysis, only the JetProb and the SV0 tagger are recommended [103]. In Section 4.5.1 we give a more detailed description of the SV0 tagger. The SV0 weight is used in the top likelihood method used in this analysis. The performance and calibration results for the SV0 tagger are presented. A performance comparison with other taggers is also made.

### 4.5.1 The SV0 Tagger

The SV0 tagger is a lifetime tagging algorithm based on explicit reconstruction of an inclusive secondary vertex from tracks associated with a jet [61, 105]. The vertex is inclusive in the sense that all decay products of the *b*-hadron, including the decay products of the subsequent *c*-hadron decay, are used to form the single vertex. The details on the whole process of vertex reconstruction and the reconstruction algorithms used can be found in the "Vertex Reconstruction for *b*-tagging" chapter of [61]. Most recent selection cuts used during different steps of the SV0 tagger, as well as those for selecting input tracks to the tagger, can be found in [105].

Using as input all selected tracks associated with a jet, the SV0 tagger starts by building all two-track pairs that form a good vertex ($\chi^2 < 4.5$), considering only tracks significantly displaced from the primary vertex [105]. The two-track vertices are required to be incompatible with the primary vertex by requiring the $\chi^2$ distance between the vertex and the primary vertex to be > 6.25. In addition, vertices consistent with $K_S^0$ and $\Lambda^0$ decays, photon conversion, or material interactions are removed. All tracks from the remaining two-track vertices are combined and fitted to a single vertex. An iterative procedure is used to remove the track with the largest $\chi^2$ contribution, until the fit probability is greater than 0.001, the vertex mass is less than 6 $GeV$, and the $\chi^2$ contribution from any track is $\leq 7$. Afterwards, the algorithm also tries to re-incorporate the tracks rejected during the formation of the two-track vertices into the vertex fit.

The SV0 tagger selects a $b$-jet by placing a cut on the SV0 weight. The SV0 weight is defined by the signed decay length significance, $L/\sigma(L)$, of the secondary vertex position with respect to the primary vertex. The sign of the decay length $L$ is given by the sign of its projection on the jet axis. Figure 4.7 shows the distribution of SV0 weight, the efficiencies and rejections for the SV0 tagger, measured in simulated $t\bar{t}$ events. The rejection is used in place of the mis-tagging rate for historical reasons [61]. It is simply the inverse of the mis-tagging rate. In Figure 4.8, a comparison of performance is given between SV0 and a few other taggers, where the rejection for light jets, $c$-jets and $\tau$-jets as a function of the $b$-tagging efficiency is presented. IP3D+SV1 and JetFitter clearly shows the best performance, as expected.

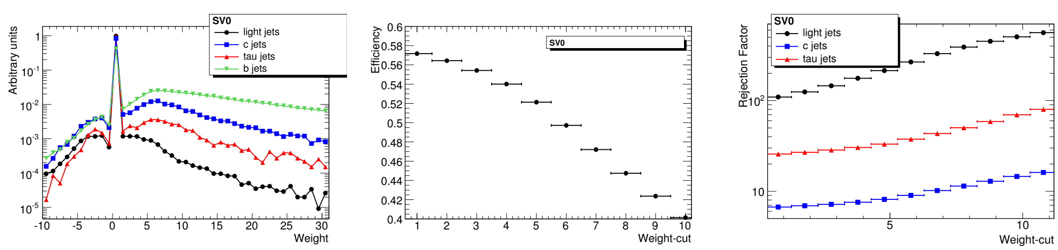


(a) (b) (c)

Figure 4.7: Weight (left), efficiency (middle) and rejection (right) of the SV0 tagger, measured on simulated $t\bar{t}$ sample, using AntiKt4TopoJets, non-purified jets, no event selection and considering all jets with $p_T > 15$ $GeV$ and $|\eta| < 2.5$ [103].

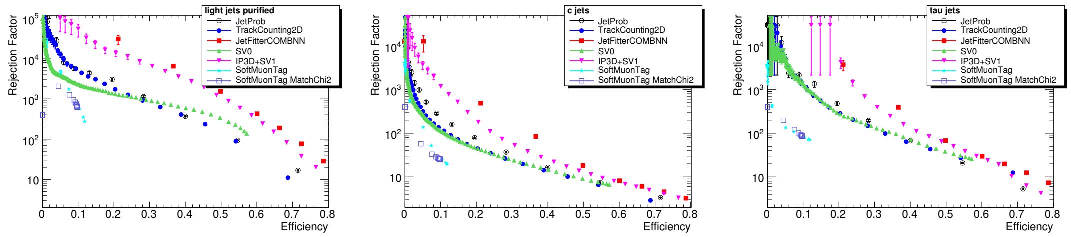


(a) (b) (c)

Figure 4.8: Comparison of rejection versus $b$-tagging efficiency for the TrackCounting, JetProb, SV0, IP3D+SV1, JetFitterComb and Soft Muon taggers for light jets (left), $c$-jets (middle) and $\tau$-jets (right), measured on simulated $t\bar{t}$ sample, using AntiKt4TopoJets, non-purified jets, no event selection and considering all jets with $p_T > 15\ GeV$ and $|\eta| < 2.5$ [103].

### 4.5.2 $b$-Tagging Calibration

The $b$-tagging calibration measures in data the $b$,$c$-tagging efficiencies and the light flavor mis-tagging rate, as well as the distributions of the variables used in $b$-tagging algorithms, and use the results to correct the Monte Carlo predictions. Ultimately, it would be desirable to calibrate directly the output weight distributions of the tagging algorithms. However, as of now the methodology for doing so has not yet been developed. In addition, a substantial amount of data is likely required for this kind of calibration. Instead, for early data the efficiencies and mis-tagging rate are calibrated with respect to one or more working points, defined by values of cuts applied on the weight distributions. Calibration results, parametrised as functions of jet $p_T$ and $\eta$, are provided for the SV0 tagger at the working point $w_{SV0} = 5.85$, and for the JetProb tagger at the working points $-log_{10}(w_{JetProb}) = 3.25$ and $-log_{10}(w_{JetProb}) = 2.05$. The SV0 working point correspond to a 50% $b$-tagging efficiency and 271 in light jet rejection on $t\bar{t}$ Monte Carlo sample.

The $b$-tagging efficiency for the SV0 and JetProb algorithms at the chosen operating points have been measured in data using the $p_T^{rel}$ method [103, 106, 107]. The method measures the tagging efficiency for jets containing $b$-hadrons decaying into muons. The selection of the candidate jets is based on the transverse momentum of the muon relative to the jet axis ($p_T^{rel}$). Other methods being studied include the System8 method, calibration with the $D^{\star}\mu$ final state of $b$ quark decays, and calibration in $t\bar{t}$ final states [103, 108, 109, 110]. The measurement of the mistag rate is performed on an inclusive jet sample. It involves combining results from two independent methods, the SV0 mass method and the negative tag rate method [103, 106, 111, 112]. The SV0 mass method uses the invariant mass spectrum of tracks associated with reconstructed secondary vertices to separate light and heavy flavor jets in the tagged sample. The negative tag rate method is based on measuring an inclusive negative tag rate. The negative tags are selected by reversing the sign of IP significance for IP taggers and reversing the sign of decay-length significance for SV taggers.

Results of the calibration are provided in terms of data/MC dependent scale factors (SF) that corrects the $b$-tagging performance in simulation to that observed in data. The SFs are $p_T$ and $\eta$ dependent. The SFs for the SV0 tagger are shown in Table 4.9 and Table 4.10. Currently, the tagging efficiency for $c$-jets is not measured separately in data. As a result, the scale factors for $c$-jets are taken to be the same as those for $b$-jets. This method assumes that the $b$- and $c$-tagging efficiencies should show similar behavior because they are both dominated by decays of long-lived heavy flavor hadrons. The uncertainties of the $c$-tagging scale factors are doubled so as to cover possible deviations from this assumption.

| **Jet $p_T$ region** | **SV0 SF** |
|---|---|
| $20 \leq p_T < 25$ $GeV$ | $0.872 \pm 0.208$ |
| $25 \leq p_T < 40$ $GeV$ | $0.925 \pm 0.105$ |
| $40 \leq p_T < 60$ $GeV$ | $0.942 \pm 0.074$ |
| $60 \leq p_T < 75$ $GeV$ | $0.947 \pm 0.102$ |
| $75 \leq p_T < 90$ $GeV$ | $0.947 \pm 0.150$ |
| $90 \leq p_T < 200$ $GeV$ | $0.947 \pm 0.200$ |

Table 4.9: The $b$-tagging scale factors and their uncertainties [103, 113]. The scale factors for $c$-jets are taken to be the same as that for $b$-jets but with the uncertainties doubled. The results are from the $p_T^{rel}$ method, which doesn't work very well for higher $p_T$ regions, above approximately 85 $GeV$ [106].

| Jet $pT$ region | SV0 SF | |
|---|---|---|
| | $0 \leq |\eta| < 1.2$ | $1.2 \leq |\eta| < 2.5$ |
| $20 \leq p_T < 25\ GeV$ | 1.19 ± 0.427 | 1.36 ± 0.484 |
| $25 \leq p_T < 40\ GeV$ | 1.36 ± 0.352 | 1.39 ± 0.324 |
| $40 \leq p_T < 60\ GeV$ | 1.03 ± 0.193 | 1.2 ± 0.19 |
| $60 \leq p_T < 90\ GeV$ | 1.07 ± 0.124 | 1.01 ± 0.216 |
| $90 \leq p_T < 140\ GeV$ | 0.949 ± 0.146 | 1.01 ± 0.186 |
| $140 \leq p_T < 200\ GeV$ | 1.05 ± 0.136 | 0.994 ± 0.285 |
| $200 \leq p_T < 300\ GeV$ | 1.29 ± 0.303 | 0.923 ± 0.598 |
| $300 \leq p_T < 500\ GeV$ | 0.85 ± 0.507 | 1.7 ± 1.35 |

Table 4.10: The mis-tagging scale factors and their uncertainties for central jets ($0 \leq |\eta| < 1.2$) and forward jets ($1.2 \leq |\eta| < 2.5$), after full combination of results from the two methods and application of run-dependent systematic uncertainties [103, 113].

## 4.6 Missing $E_T$ Reconstruction

The transverse missing energy in ATLAS is reconstructed from energy deposits in the calorimeter and reconstructed muon tracks. Usually, the missing $E_T$ reconstruction is dependent on the reconstruction of other physics objects. The missing $E_T$ object used in this analysis is the "MET_RefFinal_em_tightewtm" object, where "RefFinal" describes the algorithm by which it was reconstructed, "em" denotes that "EM+JES" jets are used in the reconstruction, and "tightewtm" means the missing $E_T$ was recalculated from the default "MET_RefFinal_em" by the Jet/ETmiss working group with electrons of quality type "ElectronTight_WithTrackMatch". More details of the quality cuts on the different objects used in the missing $E_T$ reconstruction can be found in [85].

The reconstruction of true missing $E_T$ is a big challenge for various reasons. First, the physics missing $E_T$ comes from neutrinos produced in the hard scattering processes of interest. Additionally, since muons are only minimum ionizing particles, their transverse momentum must be correctly accounted for. In addition to the physics sources, there are instrumental and fake sources of missing $E_T$. Instrumental sources include gaps and cracks in calorimeter, energy leak in the calorimeter, and dead sectors and channels. The details of these effects can only be understood with time. Sources of fake missing $E_T$ include neutrinos from semileptonic decays of heavy flavor hadrons, inefficiency in high-$p_T$ muon reconstruction, reconstructed fake high-$p_T$ muons. Finally, many soft processes, such as the underlying event, multiple proton-proton interactions, and pile-up, and coherent electronic noises, lead to energy deposits and/or muon tracks, and complicate the measurement of true missing $E_T$.

Two algorithms are used for missing $E_T$ reconstruction, the cell-based algorithm and the object-based algorithm, both aim to minimize the impact of different sources of fake missing $E_T$ [61]. To achieve this goal, it is very important to implement an effective noise suppression procedure. And it is essentially important to classify the energy deposits into various types and calibrate them accordingly. Common to both algorithms is the calorimeter noise suppression procedure. The two algorithms differ in classification of energy and its calibration.

The object-based algorithm starts from the reconstructed, calibrated, and identified objects in the event. The energy deposit outside these objects is further classified as low $p_T$ deposits from charged and neutral pions and calibrated accordingly. This algorithm has the capability to reliably reconstruct missing $E_T$ for physics channels that are sensitive to low $p_T$ deposits coming from neutral and charged pions, soft jets, the underlying event, and pile-up.

The cell-based algorithm is currently the default for reconstructing missing $E_T$. The algorithm starts from the energy deposits in calorimeter cells that survive a noise suppression procedure, adds muon correction from the standalone muons, and corrects for energy loss in the cryostat. The cells can be calibrated with calibration weights depending on their energy density. The final missing $E_T$ can be written as:

$$\not{E}_{x,y}^{Final} = \not{E}_{x,y}^{Calo} + \not{E}_{x,y}^{Cryo} + \not{E}_{x,y}^{Muon} \tag{4.10}$$

where

$$\not{E}_{x,y}^{Calo} = \sum_{TopoCells} E_T \tag{4.11}$$

Cells from topological clusters are used to calculate the calorimeter term. This naturally provides the noise suppression using topological clusters, which is optimized to suppress electronics noise as well as pile-up from minimum bias events, which keeping the single pion efficiency as high as possible.

The missing $E_T$ reconstructed from the steps above is the "MET_Final" term in the AOD file. It was used in early data-taking because it did not rely on the reconstruction of physics objects such as electrons and muons. With the calibration of the cells, the "MET_Final" can already give very good performance. Better performance is achieved by adding the final step: the refinement of the calibration of cells associated with each high-$p_T$ object. Cells are associated with reconstructed and identified high $p_T$ objects in a chosen order, and refined calibration of the object is used to replace the intitial calibrated cells. The reconstructed missing $E_T$ after the final step is called "MET_RefFinal", and it can be written as [61, 85]:

$$\begin{aligned} \not{E}_{x,y}^{RefFinal} = & \not{E}_{x,y}^{RefEle} + \not{E}_{x,y}^{RefPhoton} + \not{E}_{x,y}^{RelTau} \\ & + \not{E}_{x,y}^{RefbJet} + \not{E}_{x,y}^{RefJet} + \not{E}_{x,y}^{RefSoftJet} \\ & + \not{E}_{x,y}^{RefMuo} + \not{E}_{x,y}^{CellOut} \end{aligned} \tag{4.12}$$

where the ordering of the objects on the right side indicate the order of association of cells to these objects.

Performance of the missing $E_T$ have been evaluated specifically for the $t\bar{t}$ analyses [85]. Figure 4.9 shows the missing $E_T$ resolution and bias in the $t\bar{t} \to l + jets$ final states.

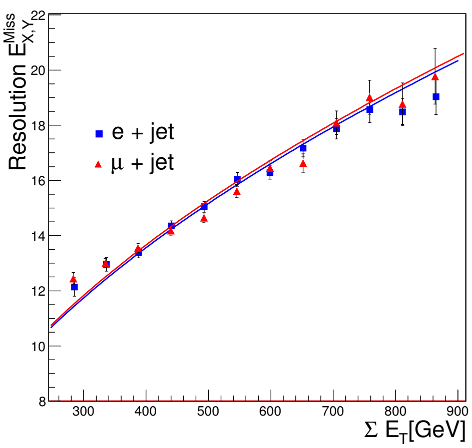


(a) Resolution, $\sigma\left(E_T^{miss}{}_{x,y}\right)$, of the two components (x,y) of $E_T^{miss}$ as a function of $\sum E_T$ for the $t\bar{t} \rightarrow e + jets$ channel (blue squares) and the $t\bar{t} \rightarrow \mu + jets$ channel (red triangles)

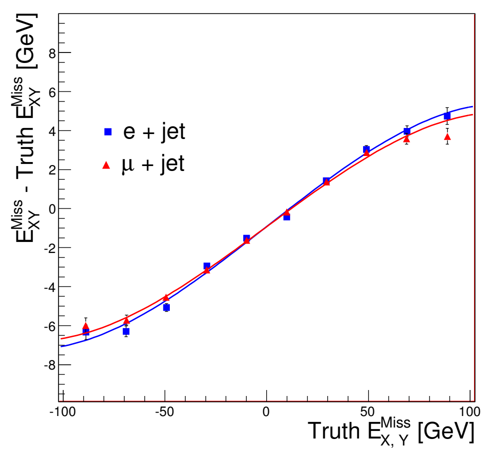


(b) Biases of the two components (x,y) of $E_T^{miss}$ as a function of the x truth value, for the $t\bar{t} \rightarrow e + jets$ channel (blue squares) and the $t\bar{t} \rightarrow \mu + jets$ channel (red triangles)

Figure 4.9: Resolution and Biases for missing $E_T$ in the $t\bar{t} \rightarrow l + jets$ channels [85]

# Chapter 5

# Data and Monte Carlo Samples

This dissertation uses $pp$ (proton-proton) collision data produced by the Large Hadron Collider (LHC) at a center-of-mass energy ($\sqrt{s}$) of 7 $TeV$, recorded by the ATLAS experiment during the year of 2010. Monte Carlo (MC) samples of both $t\bar{t}$ signal and background events also play an important role in this analysis. Both data and Monte Carlo samples are discussed in this chapter. In Section 5.1, we describe the data collection and luminosity determination, as well as the data quality criteria. In Section 5.2, we start with a brief description of the MC production procedure at ATLAS. In Section 5.2.1, we give a general description of the simulation of hard hadronic collison events. The MC generators used in this analysis are given a bit more detail. Then a brief description of the detector simulation is given in Section 5.2.2. In Section 5.2.3 we give the full list of all the MC samples used in this analysis. Detailed descriptions are given for the samples of $t\bar{t}$ signal and the $W + jets$ background.

## 5.1 Data Collection and Samples

In this analysis, $pp$ collision data produced by the Large Hadron Collider (LHC) and recorded by the ATLAS experiment during the year of 2010 is analyzed. The data was produced at a center-of-mass energy ($\sqrt{s}$) of 7 $TeV$. The data was streamed by the ATLAS trigger and data acquisition (TDAQ) system, which is responsible for writing out physics data streams used for different types of physics analyses [61, 114]. We used the physics electron and muon streams, which includes events passing at least one of the electron or muon triggers defined in the trigger menu. Skims of this data were produced within the top physics working group, by applying loose cuts on the leptons and jets in the events [115, 116].

The top physics group also produced common good runs lists (GRLs) for selecting good runs where all the subsystems of the ATLAS detector were fully operational and no serious data quality (DQ) problems were present [117]. The GRL used in this analysis is the common GRL used for the Moriond 2011 conferences [117]. After applying the GRL, the integrated luminosity of the data used is approximately 35.3 $pb^{-1}$.

This analysis uses reconstructed data from the autumn 2010 reprocessing of the whole dataset collected in 2010. Details about the reprocessing, including the software releases and condition database tags, are documented in [118].

### 5.1.1 Data Collection

The 7 $TeV$ data used in this dissertation corresponds to ATLAS runs 152166 to 167844, taken from March to October 2010. The peak luminosity during this period was $2.07 \times 10^{32}$ $cm^{-2}s^{-1}$. The peak luminosity corresponded to the LHC bunch structure of 348 collision bunches in 46 bunch trains, with bunch separation of 150 $ns$. The average number of protons per bunch was $4.12 \times 10^{11}$. The peak luminosity was achieved in Run 167607.

| Period | Subperiods | Run range |
|---|---|---|
| A | A1 | 152166–153200 |
| B | B1–B2 | 153565–155160 |
| C | C1–C2 | 155228–156682 |
| D | D1–D6 | 158045–159224 |
| E | E1–E7 | 160387–161948 |
| F | F1–F2 | 162347–162882 |
| G | G1–G6 | 165591–166383 |
| H | H1–H2 | 166466–166964 |
| I | I1–I2 | 167575–167844 |

Table 5.1: ATLAS data taking periods and subperiods in 2010 for $pp$ running. Taken from the COMA Data Period Documentation Interface [119].

Every run intended for physics analysis is assigned to a standard data period and a subperiod. The periods are labelled by single letters, A to Z, and are cycled every year. The subperiods are labelled by positive integers. The 2010 data periods are summarized in Table 5.1, along with the ranges of the run numbers they correspond to.

### 5.1.2 Luminosity Determination

The integrated luminosity ($\int \mathcal{L}\, dt$) is used in the calculation of the cross section, Equation 1.2. The uncertainty in the integrated luminosity is a systematic error on the cross section measurement. For this analysis the integrated luminosity is 35.3 $pb^{-1}$, with a relative uncertainty of 3.4% [120]. The value of the integrated luminosity for this analysis is calculated for the GRL and the triggers used in this analysis, using the LumiCalc tool [121]. The luminosity calculation is trigger specific, since different triggers can have different dead times.

The luminosity on the ATLAS experiment is determined by several different detectors and algorithms [120, 122]. At present, ATLAS relies on event-counting methods for the determination of the absolute luminosity [122]. The results are calibrated using van der Meer (vdM) scans [122].

Table 5.2 lists the five major counting algorithms used in the 2010 luminosity measurement, including three online algorithms and two offline algorithms. Two of the online algorithms are based on the LUCID (LUminosity measurement using Cerenkov Integrating Detector) detector. The other online algorithm is based on the BCM (Beam Conditions Monitor) detector. One of the two offline algorithms, the MBTS_timing algorithm, uses information from the MBTS (Minimum Bias Trigger Scintillators) detector. The other offline algorithm, the PrimVert algorithm, is based on tracks reconstructed in the ATLAS detector.

The luminosity measured with the above algorithms have been calibrated using all the five vdM scans taken in 2010. The uncertainty on the measurement is determined to be 3.4%, which arises mainly from the uncertainty on the bunch charge product [120]. The absolute luminosity is stored in a database for later use, on a LB (luminosity block) per LB base.

### 5.1.3 Data Quality

Operationally, despite the best efforts of the experimenters, defects in detector subsystems can occur and not all data recorded by ATLAS will be suitable for inclusion into physics

| Algorithm name | Counting technique |
|---|---|
| LUCID_EventAND | Reports the number of events with at least one hit on each LUCID detector side |
| LUCID_EventOR | Reports the number of events for which the sum of hits on both LUCID detector sides is at least 1 |
| BCM_EventOR | Reports the number of events for which the sum of hits on both BCM detector sides is at least 1 |
| MBTS_Timing | Reports the number of events with at least one hit on each MBTS detector side, plus a requirement that the timing of these hits occur within 10 $ns$ |
| PrimVtx | Reports the number of events with a primary vertex containing at least 4 tracks with $p_T > 150$ $GeV$ |

Table 5.2: Algorithms used for the determination of the luminosity on the ATLAS experiment [120]. The LUCID_EventAnd, LUCID_EventOR, and BSM_EventOR algorithm are online algorithms. The MBTS_Timing and PrimVtx algorithm are offline algorithms.

analyses. The primary tool for rejecting unsuitable data are data quality (DQ) flags, which are produced by both the detector subsystems and the offline combined performance working groups [123]. Figure 5.1 shows the DQ flags produced by different groups at different stages of the detector operation. The DQ flags present a simple red/yellow/green traffic light indication of data quality. The detector and performance groups oversee the assignment of these flags.

The mechanism for selecting or rejecting data is based on the concept of Luminosity Blocks (LBs). ATLAS runs are subdivided into these smaller time intervals of approximately two minutes. The selection of a valid sample of data in practice means selecting a specific set of LBs from a range of runs based on the DQ flags. All information needed to make the selection is stored in the conditions database called COOL. Analyzers makes use of a Good Run List Generator tool that provides an XML (text) file of good LB's to be used in a given analysis [124]. The file is called a GRL (Good Run List) file. The Atlas Run Query Tool can also be used to produce GRL's [123]. Software is also provide in the Athena GoodRunsLists package that reads the GRL files and rejects bad LB's in the data.

The GRL is also important for luminosity calculation. A software package called the

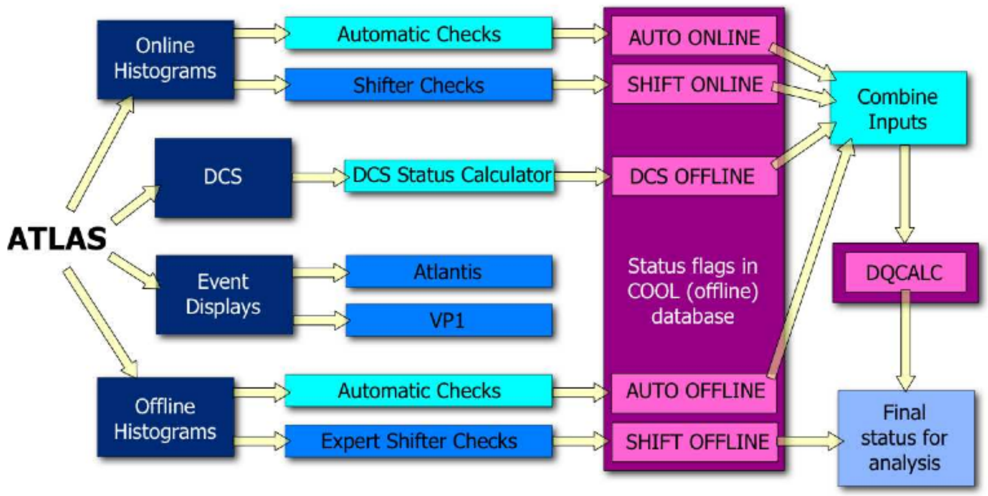


Figure 5.1: A schematic view of the ATLAS Data Quality Monitoring Framework

LumiBlockComps uses the GRL list to calculate the integrated luminosity associated with the list [121]. This can be done either from the command line using an executable called iLumiCalc or from within Athena using the iLumiCalcSvc class.

In this analysis we used iLumiCalc in order to determine the integrated luminosity.

## 5.2 Monte Carlo Production

Monte Carlo (MC) samples that simulate real data play an important role in particle physics analyses. Events in MC samples are generated according to theoretical probability distributions of observables in physics processes, which subsequently undergo full detector simulation and digitization. At this point, the MC samples are identical in format to RAW data, and both then undergo reconstruction as discussed previously. Monte Carlo samples are useful such as in developing new analysis methods in the absence of real data, in modeling backgrounds to new physics channels of interest, and modeling control regions for data-driven measurements. In this dissertation, MC samples are used for several purposes, including measurement of the $t\bar{t}$ selection efficiency, modelling of the shapes of the kinematic variables, as well as evaluation of the statistical and systematics errors. Descriptions of these uses can be found in relevant chapters.

Figure 5.2 illustrates the major processing stages in the Monte Carlo production data flow at ATLAS, and the data formats after different stages. Events simulated by MC generators are passed to the detector simulation after a particle filtering stage. Outputs of the detector simulation are then processed at the digitization stage and converted to digits similar as the outputs of the ADCs. Optionally a ROD (Read Out Driver) emulation algorithm can be run on the digits. Afterwards, the digits are transformed into the format of RDOs (Raw Data Objects).

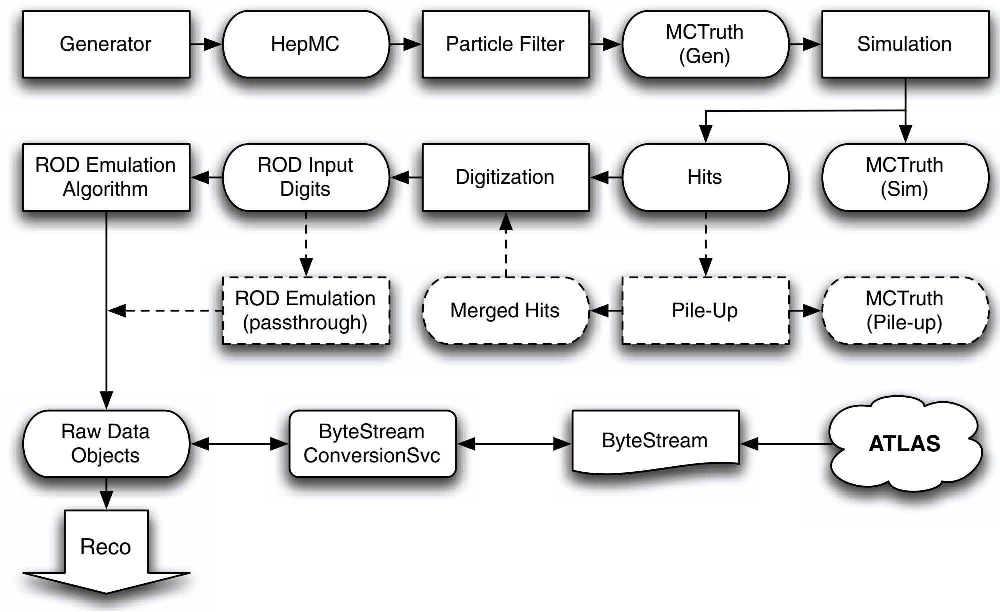


Figure 5.2: The simulation data flow [49]. Rectangles represent processing stages and rounded rectangles represent objects within the event data model. Pile-up and ROD emulation are optional processing stages.

At this stage, reconstruction software can be run on MC samples in the same way as on data, and produce files in the various formats used by analyzers (ESD, AOD, $D^3PD$, etc.). In this way, the RDO couples the simulation chain with the reconstruction chain, as illustrated in Figure 4.1. However, as described in Chapter 4, the starting point of data reconstruction is bytestream format. To reproduce this, an optional final stage can be added to convert the RDOs to bytestream files. Trigger simulation can also be run during reconstruction, without conversion to bytestream files. Another difference between reconstructed MC samples and reconstructed data is that the MC samples contain MC truth information from the generator, which can be used to associate reconstructed objects with the particles originally created by the generator.

### 5.2.1 Simulation of Hard Hadronic Collisions

Monte Carlo simulation aims to produce hypothetical physics events according to the probability distributions of known or possible theories. Like theoretical calculations, the MC simulation of hard hadronic collisions uses the QCD factorization and perturbative QCD. Because perturbative QCD provides predictions at a finite order of $\alpha_s$, the MC simulation of hard hadronic collisions is performed at a finite order of $\alpha_s$ as well. Figure 5.3 illustates the general structure of a hard hadronic scattering event simulated by MC generators. The major components include parton distribution functions that choose the initial partons, a hard scattering that produces hard partons, the evolution of the parton shower (PS), and the hadronization of the final state partons. At present, the subprocesses in the hard scattering event are usually simulated with several separate MC generators, with one program to produce hard processes, another to evolve the event through a parton shower algorithm, and sometimes a third to hadronize the colored products in the shower [125]. In cases where particles decay into other particles, such as in $t\bar{t}$ production, the decay can be simulated by internal or external decay software packages. [125] is used heavily as a reference for the descriptions of the MC generators in this section.

In order to correctly model hard hardronic collisions, all of the following processes must also be taken into account.

**The underlying event (UE)** includes all the non-hard-scattering interactions in a hard scattering event, including Initial and Final State Radiation (ISR/FSR), beam-beam remnants, and multiple parton-parton interactions. ISR/FSR is the QCD counterpart for EM radiation from an accelerated charge (QCD bremsstrahlung). Beam-beam remnants refer to parts of the hadrons that do not participate in the hard scattering processes. Multiple parton-parton interactions occur when more than one pairs of partons participate in (semi-)hard partonic interactions. Simulation of the underlying event is usually incorporated in the showering and hadronization steps of the simulation.

**Pile-up** occurs when one or more $pp$ (or $p\overline{p}$) interactions occur at the same time as

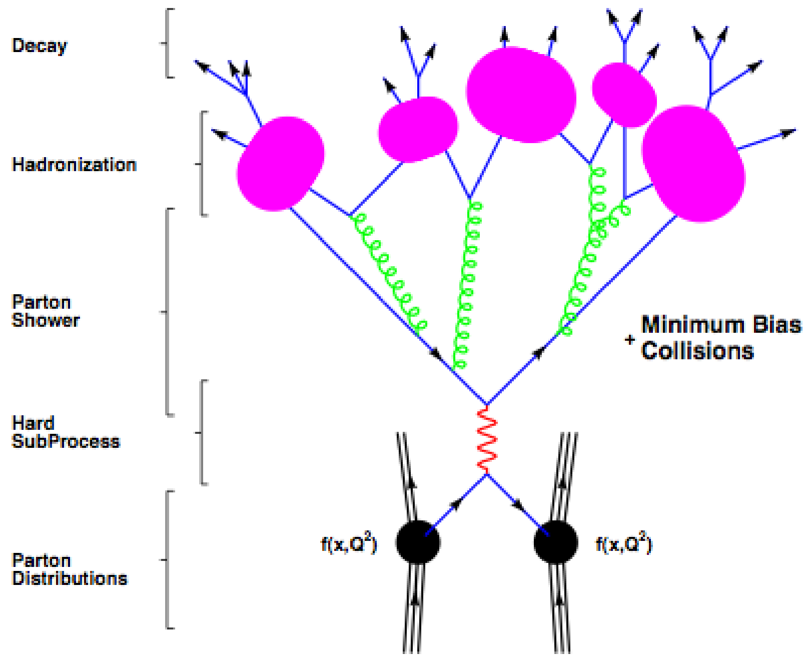


Figure 5.3: The general event structure of a hard hadronic scattering event [125]

the $pp$ collision with the hard scattering. It is simulated by superimposing minimum bias events over the hard scattering event. Minimum bias events are defined as collision events which show a minimum activity in the detector, not triggered by any high $p_T$ objects. The number of superimposed events is taken from a Poisson distribution with a mean dependent on the luminosity and minimum bias cross sections. At ATLAS, the superimposing of minimum bias events is part of the "pile-up" step in Figure 5.2, which overlays various type of events known collectively as "pile-up". In addition to minimum bias events, "pile-up" also includes cavern background, beam gas and beam halo events, detector responses to long-lived particles, as well as overlapping detector responses from interactions of neighboring bunch crossings [126]. All these "pile-up" effects can be modelled by simulation, or by data events from the so-called "zero bias" trigger.

The hard scattering of partons are described by Matrix Element (ME) generators. The ME generators must correctly implement, at a certain order of $\alpha_s$, all the components in the differential cross section equations of the hard scattering processes, such as the differentiation of Equation 2.11. The first step in the implementation is to sample the phase space of the differential cross section equation and generate candidate events from a uniformly distributed random number generator. The randomly generated events can then undergo an "unweighting" procedure to produce the frequency and distribution of events expected to happen in nature. With this approach the MC generator is used as an event generator. Usually, the "hit-and-miss" technique, also known as the acceptance-rejection routine, is used to "unweight" the events.

Alternatively, a cross-section integrator, which applies event weights to the randomly generated events, can be used instead of the unweighting procedure to create distributions from physical predictions. A cross section integrator has the advantage of being able to represent physical quantities more exactly. However, individual events in a cross section integrator do not represent actual events taking place in nature. Only the weighted distributions of a large number of events have physical meaning. Most of the MC samples used in this dissertation are generated with the unweighting procedure.

As seen in the $t\bar{t}$ cross section calculation in Chapter 2, higher-order corrections involving virtual particle loops are difficult to evaluate, as the partonic cross sections often involve divergences, which need to be cancelled. Due to this difficulty, most commonly used ME generators are based only on LO matrix elements. Here LO means no virtual emission diagrams are included. LO ME generators are also called tree-level ME generators. They allow computation of tree-level matrix elements with a fixed number of legs. Most ME generators used in this dissertation are at tree level.

ME generators including corrections from virtual particle loops are available at NLO. Two ME generators at NLO are used for $t\bar{t}$ signal: MC@NLO and POWHEG. One thing to notice about NLO ME generators is that, until quite recently, they are mostly used in the context of cross setion integrators, meaning only weighted events can be generated with them [125]. Furthermore, the event weights can be negative. As an example, the $t\bar{t}$ events generated by MC@NLO have event weights of values either 1 or -1. POWHEG is a relatively new generator in which unweighting procedure is used at NLO.

ME generators can be arbitrarily divided into two cartegories: those for specific processes and those for arbitrary processes. The first type features a predefined library of specific processes. The second type are general purpose programs which can write code to calculate matrix elements and generate events for arbitrary processes within some theory, e.g, the Standard Model. Most of the ME generators used in this dissertation, e.g., MC@NLO, Alpgen and AcerMC, are for specific processes. It is advantageous to use this type of generators considering that they are optimised using the kinematic distributions of particles in the specific processes.

Although physical information can be extracted from the ME generators, the processes simulated are not yet physical. For one thing, the ME generators outputs gluons and quarks as the final state particles, while in reality they should be confined within hardons. Therefore, the ME generators must be interfaced with Showering and Hadronization Generators (SHG) to give a complete description of the physics processes. The SHGs are general purpose tools able to simulate the evolution of parton showering and the hadronization. They are also called Parton Shower generators (PS). Pythia and Herwig are the two most commonly used MC generators for showering and hadronization.

Starting from fixed-order hard processes from the ME generators, the SHGs employ the parton shower approach (based on the GLAP equation, see Section 2.2.3) to evolve the event, allowing partons to split into pairs of other partons. The resultant partons are then grouped together into color-neutral hadrons following phenomenological hadronisation models tuned to experimental data. During these steps, estimations of higher-order corrections from real emission diagrams, including large logarithms at all orders, are added to the fixed-order predictions. As such, combining NLO ME generators with SHGs requires special care to avoid double counting because part of the higher order corrections are already taken care of by the NLO calculation.

SHG software programs often include within the package the modelling of the underlying event. As described above, the ISR/FSR is included in the parton shower part. The beam remnants and multiple interactions are usually included in the hadronization step, because they might be color-connected to products of the hard processes. There are also dedicated underlying event simulation program, such as Jimmy used in this dissertation. The underlying event is one of the least understood aspect of hadronic collisions, and must be tuned to data. In this analysis we used the AUET1 (ATLAS Underlying Event

Tune 1) and the AMBT1 (ATLAS Minimum Bias Tune 1) for the UE [127, 128, 129].

When combining ME generators with SHGs, one needs to pay attention to avoid double counting of the same final state. Take for example the processes of electronweak vector boson production in association with jets ($W/Z + jets$). The final state with $n$ partons can be obtained from a state with $n - m$ partons generated by the ME generator, with the extra $m$ partons addeded by the SHG, where $0 \leq m \leq n$. Although the partons from the SHG are in general softer than the partons from the ME generator, overlapped phase space regions will lead to double counting of the same $n$-parton final state. This problem can be solved by the Matrix Element Correction (MEC) in some cases, or by the CKKW and the MLM matching procedures [125, 130].

Brief descriptions are provided below for the ME generators and SHGs used in this dissertation. More information can be found in the manuals and other literatures for each generator, such as [131, 132, 133, 134, 135, 136, 137], as well as recent reviews on MC generators, such as [126]. An overview of different generators in the context of top quark physics can be found in [138].

#### 5.2.1.1 MC@NLO

MC@NLO is a next-to-leading order (NLO) ME generator with a predefined list of specific processes. It includes full NLO corrections to the LO perturbative QCD calculations. Incorporating the NLO matrix elements provides a better prediction of the event rates and improves the description of the first hard parton emission. Considering the large quantities of $t\bar{t}$ pairs produced at the LHC, it is very important to improve the accuracy of the generator predictions. As a result, MC@NLO is used as the default generator for the $t\bar{t}$ samples. MC@NLO is also used as the default generator generator for single top quark production. Currently MC@NLO is only interfaced to Herwig for parton showering and hadronization.

#### 5.2.1.2 ALPGEN

The ALPGEN generator is a tree level ME generator for specific processes that contains exact LO matrix elements for $2 \to n$ processes. Compared with $2 \to 1$ and $2 \to 2$ generators which generate extra jets through LL corrections from parton shower, with ALPGEN multijet final states such as in $W/Z + jets$ processes can be generated more accurately. Therefore ALPGEN is used by us as the default generator for $W/Z + jets$ samples. ALPGEN can be interfaced with HERWIG or PYTHIA for parton showering and hadronisation. The MLM matching precedure is incorporated in ALPGEN version 2.XX to solve the problem of double-counting multijet final states.

#### 5.2.1.3 HERWIG/JIMMY

HERWIG is a general purpose MC event generator for the simulation of lepton-lepton, lepton-hadron and hardon-hadron collisions. HERWIG standalone is frequently used as a useful reference generator. In this analysis it is interfaced with other ME generators for simulation of various samples. The program includes a wide range of hard scattering processes together with ISR/FSR, angular-ordered parton shower, hadronization based on the cluster model, hadron decays, as well as underlying event. In addtion, the external UE dedicated package JIMMY, which uses a multiple scattering model for the underlying event, can be used with HERWIG to simulate the underlying event.

#### 5.2.1.4 PYTHIA

PYTHIA is another general purpose MC event generator used in lepton-lepton, lepton-hadron and hardon-hadron colliders. Like HERWIG, it is often used standalone as a reference generator. In this analysis it is used in combination with other ME generators for simulation of various samples. In PYTHIA, the parton shower is $p_T$-ordered, with the color coherence implemented with explicit veto, and the hadronization is based on the string fragmentation model. PYTHIA also includes within it the simulation of the underlying event.

#### 5.2.1.5 Other MC generators

POWHEG is a relatively new NLO ME generators with a predefined list of specific processes. It can be interfaced with PYTHIA, HERWIG or HERWIG ++ for parton showering and hadronization. Currently it is used by us as an alternative generator for MC@NLO for cross checking the predictions of MC@NLO and studying MC generator systematics.

ACERMC is a tree-level MC generator for specific processes which can be interfaced to either PYTHIA or HERWIG. In this analysis it is used for producing $t\bar{t}$ samples used in the study of ISR/FSR systematics.

SHERPA (Simulation for High Energy Reactions of PArticles) is yet another multi purpose MC event generator for the simulation of physics processes at lepton colliders and hadron colloders. It is largely developped independently of the other two general purpose MC event generators, PYTHIA and HERWIG. In our analysis, SHERPA is used for producing $W + jets$ variation samples for studying $W + jets$ shape systematics.

### 5.2.2 Detector Simulation

Events generated by MC generators are passed on to a full simulation of the ATLAS detector based on the GEANT4 simulation toolkit [126, 139, 140]. The full simulation provides a precise description of the detector geometry including up-to-date information of active/inactive detector parts, and simulates all kinds of physics processes and detector responses caused by the passage of the particles through the detector, taking into account the present understanding of the detector and test beam results. As such, the full simulation provides a highly realistic simulation of the ATLAS detector. On the other hand, it is very time consuming, usually the most time consuming step in the simulation chain. Therefore, sometimes a fast simulation of the detector is performed instead, which smears the MC truth information directly with resolutions measured in full simulation. The package used for performing the fast simulation of the ATLAS detector is the Atlfast package [141].

All MC samples used in this dissertation are fully simulated.

### 5.2.3 List of MC Samples

The Monte Carlo samples relevant for the $t\bar{t}$ cross section measurement are listed in Table 5.3, including $t\bar{t}$ samples and samples for various backgrounds. The background samples represent different physics processes which have similar decay products as the $t\bar{t}$ signal and therefore can also pass the $t\bar{t}$ selection criteria. More descriptions of the backgrounds can be found in Chapter 6 and Chapter 7. Also included in the table are samples used for evaluation of the systematic errors. These samples are simulated with certain parameters varied from the values used for the nominal samples. Descriptions of the systematic errors can be found in Chapter 9. All samples are generated with bunch train pile-up configuration, represented by the tag $r$1831, and with AOD merging flag r1700 [142].

Detailed descriptions are given below on the simulation of the $t\bar{t}$ signal and the $W+jets$ background, which is predicted by theory to be the dominating background. Another important background, the QCD background, is not covered here, because it is evaluated using data driven methods. Brief descriptions are provided on simulation of small addtional backgrounds. Wherever variation samples are involved, information is provided on the generators and the parameters for simulation of both the nominal sample and the variation samples.

#### 5.2.3.1 Simulation of the $t\bar{t}$ Signal

For the nominal analysis, the production and decay of the $t\bar{t}$ signal is simulated using MC@NLO 3.41, followed by HERWIG 6.510 and JIMMY 4.31 for parton showering, hardronization and the underlying event. Variation samples are generated with POWHEG 2.13 + HERWIG/JIMMY and POWHEG 2.13 + PYTHIA 6.423 generators, for the study of MC generator systematics including from ME generators and from SHG generators. All of these samples implement full $t\bar{t}$ spin correlations according to the same prescription. Additional samples generated with ACERMC 3.7 + PYTHIA 6.243 are used in the study of the ISR/FSR systematics.

All the signal MC samples are generated inclusively for $t\bar{t}$ semileptonic and dilepton decay final states. Leptons include $e$, $\mu$ and $\tau$, with the decay of the $\tau$ simulated by

| **Sample ID** | **Generator** ME + PS | **Process** | **XSec** ($pb$) | **$k$-factor** |
|---|---|---|---|---|
| $t\bar{t}$ | | | | |
| 5200 | MC@NLO + HERWIG/JIMMY | No fully hadronic decay | 80.107 | 1.116 |
| 5205 | ACERMC + PYTHIA | No fully hadronic decay | 58.228 | 1.53 |
| 5860 | POWHEG + HERWIG/JIMMY | No fully hadronic decay | 79.117 | 1.13 |
| 5861 | POWHEG + PYTHIA | No fully hadronic decay | 79.117 | 1.13 |
| 117255 | ACERMC + PYTHIA | No fully hadronic decay ISR$\downarrow$ | 58.23 | 1.53 |
| 117256 | ACERMC + PYTHIA | No fully hadronic decay ISR$\uparrow$ | 58.23 | 1.53 |
| 117257 | ACERMC + PYTHIA | No fully hadronic decay FSR$\downarrow$ | 58.23 | 1.53 |
| 117258 | ACERMC + PYTHIA | No fully hadronic decay FSR$\uparrow$ | 58.23 | 1.53 |
| 117259 | ACERMC + PYTHIA | No fully hadronic decay I+FSR$\downarrow$ | 58.23 | 1.53 |
| 117260 | ACERMC + PYTHIA | No fully hadronic decay I+FSR$\downarrow$ | 58.23 | 1.53 |
| Single Top | | | | |
| 8340-8343 | MC@NLO + HERWIG/JIMMY | $t$-channel, leptonic decay | – | 1.00 |
| 8344-8345 | MC@NLO + HERWIG/JIMMY | $s$-channel, leptonic decay | 0.47 | 1.00 |
| 8346 | MC@NLO + HERWIG/JIMMY | $Wt$-channel, all W decays | 14.59 | 1.00 |
| $W/Z + jets$ | | | | |
| 7680-7705 | ALPGEN + HERWIG/JIMMY | $W \rightarrow e\nu/\mu\nu/\tau\nu$, no filter | – | 1.20 |
| 7650-7675 | ALPGEN + HERWIG/JIMMY | $Z \rightarrow ee/\mu\mu/\tau\tau$, no filter | – | 1.20 |
| $Wb\bar{b} + jets$ | | | | |
| 7280-7283 | ALPGEN + HERWIG/JIMMY | All leptonic decays | – | 1.20 |
| $Wc\bar{c} + jets$ | | | | |
| 7284-7287 | ALPGEN + HERWIG/JIMMY | All leptonic decays | – | 1.20 |
| $Wc + jets$ | | | | |
| 7288-7292 | ALPGEN + HERWIG/JIMMY | All leptonic decays | – | 1.20 |
| Diboson | | | | |
| 5985-5987 | HERWIG + HERWIG | WW/ZZ/WZ, all leptonic decays | – | – |

Table 5.3: List of MC samples relevant for this analysis [142]. The dataset numbers, cross sections and $k$-factors are presented for various samples. The $k$-factor is used for scaling the cross section for the respective MC sample to the most accurate theoretically calculated value. Cross sections and/or $k$-factors for some samples are omitted here because the number is different for each exclusive sample in a specific jet multiplicity bins or leptonic decay channel. The omitted numbers can be found in [142].

respective generators.

The default top quark mass used for the $t\bar{t}$ simulation is 172.5 $GeV$. Mass-variation samples are also generated for use in template method for top quark mass measurement and so on. These samples are not used in this analysis.

The major parameters used for simulation of the $t\bar{t}$ signal are summarized in Table 5.4. Parameter variations in PYTHIA used for ISR/FSR samples are listed in Table 5.5.

| **Parameter** | **Value** | | | |
|---|---|---|---|---|
| | MC@NLO + HERWIG/JIMMY | POWHEG + HERWIG/JIMMY | POWHEG + PYTHIA | ACERMC + PYTHIA |
| NLO ME PDF | CTEQ66 | CTEQ66 | CTEQ66 | MRST2007lomod |
| PS/UE PDF | CTEQ66 | MRST2007lomod | MRST2007lomod | MRST2007lomod |
| $Q^2$ | $m_t^2$ | $m_t^2$ | $m_t^2$ | $m_t^2$ |
| Underlying event | AUET1 | AUET1 | AMBT1 | AMBT1 |

Table 5.4: Major MC generator parameters for $t\bar{t}$ signal samples [127, 16]. $Q^2$ refers to the squared renormalization/factorization scale.

#### 5.2.3.2 Simulation of the $W + jets$ Background

For the nominal analysis, the $W + jets$ background is simulated with ALPGEN 2.13 interfaced with HERWIG/JIMMY. Additional samples are generated using SHERPA 1.1.3 for both matrix element generation and parton shower, which are not used in this analysis. Sam-

| **Parameter** | **Value** | | | | |
|---|---|---|---|---|---|
| | ISR $\downarrow$ | ISR $\uparrow$ | Baseline | FSR $\downarrow$ | FSR $\uparrow$ |
| `PARP(64)` | 4.0 | 0.25 | 1.0 | 1.0 | 1.0 |
| `PARP(67)` | 0.5 | 6.0 | 4.0 | 4.0 | 4.0 |
| `PARP(72)` [GeV] | 0.192 | 0.192 | 0.192 | 0.096 | 0.384 |
| `PARJ(82)` [GeV] | 1.0 | 1.0 | 1.0 | 2.0 | 0.5 |

Table 5.5: Parameter variations in PYTHIA used for ISR/FSR samples [127, 16]. `PARP(64)` adjusts the scale used for running $\alpha_S$ in space-like parton showers, `PARP(67)` controls the maximum parton virtuality in space-like parton showers, `PARP(72)` is the scale used for running $\alpha_S$ in time-like parton showers, and `PARJ(82)` is the FSR infra-red cut off [136, 16].

ples produced by SHERPA are inclusive of all the jet multiplicity bins and all the heavy flavor processes. In order to ensure sufficient statistics in higher jet multiplicity bins, *enhancement factors* of 2.5 are used for events with two or more jets [16]. On the other hand, samples generated by ALPGEN are exclusive samples for $W$+0, 1, 2, 3, 4 and $\geq$ 5 jets, where double counting of multijet final states is removed by the MLM matching approach incorporated in ALPGEN. Separate ALPGEN samples are also generated for heavy flavor and light jet events, including

- $W + N$ partons ($W + Np$), where $N = 0, 1, 2, 3, 4$, or $N \geq 5$.
- $W + b\bar{b} + N$ partons ($W + b\bar{b} + Np$), where $N = 0, 1, 2$, or $N \geq 3$.
- $W + c\bar{c} + N$ partons ($W + c\bar{c} + Np$), where $N = 0, 1, 2$, or $N \geq 3$.
- $W + c(\bar{c}) + N$ partons ($W + c(\bar{c}) + Np$), where $N = 0, 1, 2, 3$, or $N \geq 4$.

$W + Np$ is the so-called "W+light jets" samples, or simply referred to as the $W + jets$ samples. In these samples the final-state partons from the ME generator include gluons, $u$, $d$, $s$ and $c$ quarks (all treated as massless). Any $b$ quark in these samples is produced via the parton shower. $b$ quarks from the ME generator are included in the $W + b\bar{b} + jets$ samples. For similar reasons as for the double counting of multijet final states, there is also a small overlap between the light jet samples and the $W + b\bar{b} + jets$ samples. The $W + c(\bar{c}) + Np$ and $W + c\bar{c} + Np$ samples are generated with the $c$ quark treated as massive. In principle the light jet samples already contains the full contribution for these processes, with the $c$ quark treated as massless.

The major parameters used in ALPGEN + HERWIG/JIMMY for simulation of the light flavor $W + jets$ samples are summarized in Table 5.6. The heavy flavor samples are generated with the same settings, except that no $p_{T_{min}}$ or $\Delta R_{min}$ requirements are applied on the $b\bar{b}$ or $c\bar{c}$ system.

When combining light flavor jet samples with heavy flavor jet samples, the overlap can be removed using the heavy flavor overlap removal (HFOR) tool [16, 143]. Three approaches are provided by the tool for the overlap removal: the "MC08" procedure, the "jet-based" scheme and the "angular-based" scheme. This analysis uses the recommended

| Parameter | Value | |
|---|---|---|
| | $W + jets$ | $Z + jets$ |
| PDF | CTEQ6L1 | CTEQ6L1 |
| $Q^2$ | $m_W^2 + \sum p_T^2(jet)$ | $m_W^2 + \sum p_T^2(jet)$ |
| Underlying event | AUET1 | AUET1 |
| $p_{T\,min}(parton)$ [GeV] | 15.0 | 15.0 |
| $\eta_{max}(parton)$ | 6.0 | 6.0 |
| $\Delta R_{min}(parton, parton)$ | 0.70 | 0.70 |

Table 5.6: Major MC generator parameters for ALPGEN $W/Z + jets$ samples [127, 16]. $Q^2$ is the squared renormalization/factorization scale.

approach: the angular-based method with a cone of size $\Delta R = 0.4$. In the angular-based method, events in the light and heavy flavor $W + jets$ samples are regrouped according to the distance between the two quarks in a heavy quark pair. The exact procedure is documented in [16].

#### 5.2.3.3 Small Additional Background Simulation

The $Z + jets$ background is simulated with ALPGEN + HERWIG/JIMMY, or SHERPA, similar as the $W + jets$ background. No *enhancement factors* are used for the SHERPA $Z + jets$ sample. The major parameters used in ALPGEN + HERWIG/JIMMY for simulation of the light flavor $Z + jets$ samples are summarized in Table 5.6. The light flavor samples are generated with invariant mass of the $ll$ system in the range $40 < M_{ll} < 2000 GeV$. For the heavy flavor samples, the invariant mass lies in a slightly different range $30 < M_{ll} < 1000 GeV$.

The Single Top background is simulated using MC@NLO + HERWIG/JIMMY, similar as the $t\bar{t}$ signal. Separate samples are generated for $s$, $t$, and $Wt$ production channels.

The vector boson pair production (diboson) background, including $WW$, $ZZ$ and $WZ$, is simulated with HERWIG standalone as well as ALPGEN + HERWIG. Samples are simulated for $WW$ with both $W$s decaying leptonically, $WZ$ with inclusive $W$ decays and $Z \to ll$, and $ZZ$ with one $Z \to ll$ and the other Z with inclusive decays. By default the HERWIG samples are used. They are inclusive of all jet bins.

# Chapter 6

# Event Selection

In this chapter we discuss the event selection criteria used to select candidate $t\bar{t}$ events in the $e + jets$ and $\mu + jets$ decay channel. As much as possible we followed the common procedures recommended by the ATLAS Top physics group [144, 145]. The triggering requirements are described in Section 6.1 and the offline event selection in Section 6.2. The selection efficiency for $t\bar{t}$ events ($\epsilon_{t\bar{t}}$) is determined from a combination of measurements in Monte Carlo (MC) samples and data/MC corrections. The method and the results are presented in Section 6.3.

The event selection criteria select from data not only $t\bar{t}$ signal events, but also events from physics processes with final-state signatures similar to that of $t\bar{t}$. These other processes are referred to as background. The selection criteria have been optimized to increase the significance $S/\sqrt{S+B}$ where $S$ is the number of signal events and $B$ is the number of background events. Thus the selection criteria seeks to maximize signal efficiency while retaining good background rejection. In Section 6.4 the expected signal and background contributions to the selected data sample are presented.

## 6.1 Triggering on $t\bar{t}$ Semileptonic Events

Data taken by the ATLAS detector is written out by the TDAQ system, which is capable of writing out multiple streams of Raw data. These streams include the physics data stream used for physics analysis, as well as other special-purpose streams such as the calibration stream and the express stream, which are used for detector calibration and monitoring respectively. The physics data stream is further separated at the Event Filter (EF) subfarm outputs (SFOs) into several inclusive Raw data streams, each containing events satisfying any trigger from a defined set of physics triggers. Reconstruction is carried out on these streams separately. Each stream is useful for different types of physics studies. This analysis is done on the physics electron and muon streams. In addition, we require events passing specific electron or muon trigger requirements in the offline analysis.

The triggers for this analysis use the lepton in the $t\bar{t}$ semileptonic final state. An event is only considered for the analysis if it causes the single electron or muon trigger of our choice to fire. In addition, the offline electron or muon is required to match the trigger ROI (Region of Interest), also called the trigger feature, within $\Delta R = \sqrt{\Delta\eta^2 + \Delta\phi^2} = 0.15$. EF triggers were used for all of the run periods we considered.

Events that pass specified EF triggers must pass each of the L1, L2, and EF triggers in the chain. In the earliest run periods (A–E3), L2 and EF triggers were not yet in operation. Furthermore, data from these periods was affected by problematic muon trigger timing at L1. Because the fraction of data in these running periods amounted to only 2% of the total, it was decided to exclude this data from this analysis.

Table 6.1 shows the triggers used for the remaining run periods, as well as for the MC samples. One can see that the $p_T$ and quality threshold for the muon triggers increased with time. This was needed to reduce the trigger rate in the face of increasing accelerator luminosity.

| **Sample** | **Trigger** | |
|---|---|---|
| | $e + jets$ | $\mu + jets$ |
| Data period E4–F | EF_e15_medium | EF_mu10_MSonly |
| Data period G1–G5 | EF_e15_medium | EF_mu13 |
| Data period G6–I2 | EF_e15_medium | EF_mu13_tight |
| MC | EF_e15_medium | EF_mu13_tight |

Table 6.1: Triggers used for data collected in different run periods and for MC samples. EF_e15_medium is a single electron trigger with transverse energy ($E_T$) threshold $E_T \geq 15$ $GeV$ at EF. The term "medium" refers to the quality of the electron, which is defined similarly as in offline identification (Id). EF_mu13_tight is a single muon trigger with transverse momentum ($p_T$) threshold $p_T \geq 13$ $GeV$ at EF. The term "tight" means a tighter cut is applied at L1 on the geometrical "roads" from which the muon $p_T$ is estimated, compared to the standard EF_mu13. For EF_mu10_MSonly, "MSonly" indicates only the Muon Spectrometer (MS) is used for the trigger. EF_mu10_MSonly was used during the phase when combination of the MS and Inner Detector (ID) inputs to the trigger were not fully commissioned.

The measurement of the trigger efficiencies is discussed in Section 6.3, as part of the procedure for measuring the total $t\bar{t}$ selection efficiency.

## 6.2 Offline Event Selection

The final-state signature of the $t\bar{t}$ semileptonic decay channel is illustrated in Figure 6.1. The signature is characterized by one isolated lepton ($e$ or $\mu$) with high transverse energy ($E_T$) from a leptonic $W$ decay, large missing $E_T$ from the neutrino emission in the leptonic $W$ decay, two $b$-jets with high transverse momentum ($p_T$) from the top decays, and two jets with $p_T$ from a hadronic W decay. Additional jets could be produced due to initial and final state radiation (ISR/FSR), which are generally softer than the jets from top and W decays. The $b$ jets in general are more energetic than the jets from the hadronic $W$ decay.

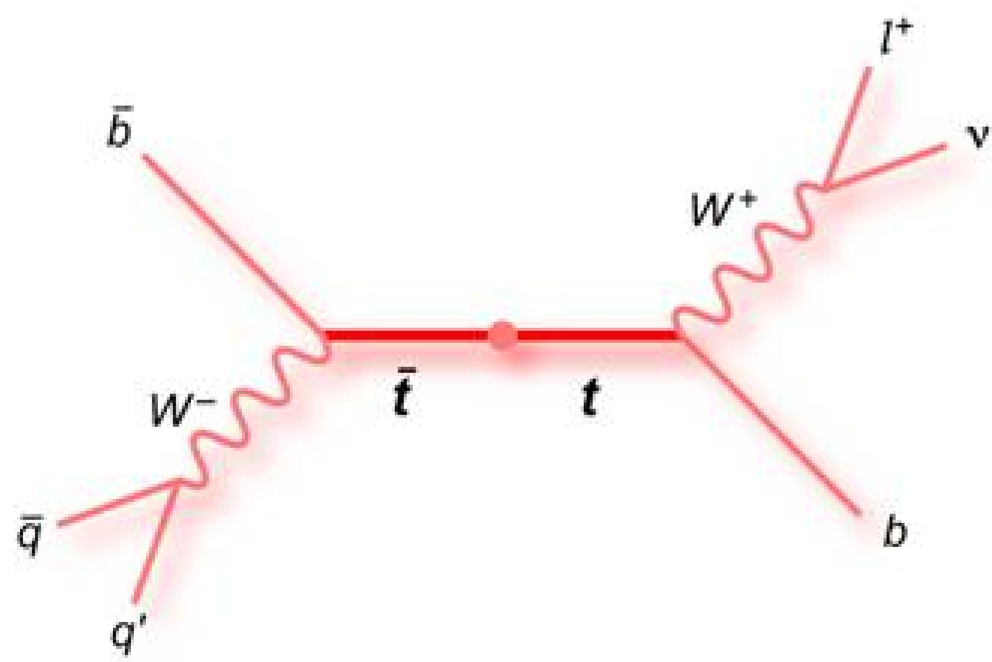


Figure 6.1: Sketch of a semileptonic $t\bar{t}$ event

The offline event selection is based on the $t\bar{t}$ semileptonic signature. The selection criteria are divided by their purpose into object identification (Id) and event-level selection.

### 6.2.1 Object Identification Criteria

Object identification selects good quality electrons, muons, and jets for use in the event-level selection and in the to likelihood analysis presented in Chapter 7. The object identification criteria used in this analysis is summarized in Table 6.2 and discussed in this section. Note that natural units are used here as well as other places in this dissertation, which means $\hbar = c = 1$ and mass has the same unit as energy. Before the application of any selection cut, energy/momentum scale correction and/or resolution smearing are applied to all electrons, muons and jets in the chosen collection above a loose threshold. The threshold is typically $\sim 10\ GeV$ for the leptons and $7\ GeV$ for the jets.

Most of the scale and resolution corrections are applied to Monte Carlo distributions. One exception is the electron energy scale offset, which is applied to data to correct for residual miscalibration in data [146]. For jets, no energy scale correction is needed because the jet energy scale (JES) has already been calibrated during reconstruction with the process described in Chapter 4. For each of the correction, missing $E_T$ is corrected accordingly. No additional correction is applied on missing $E_T$ itself.

#### 6.2.1.1 Electron Identification Criteria

We use electrons from the "ElectronAODCollection" that are found by the standard "egammaBuilder" algorithm ($author = 1 \,\|\, author = 3$). Their four momenta are reconstructed using the method outlined in Section 4.2 of Chapter 4. The analysis is restricted to the $\eta$ coverage of the precision electromagnetic (EM) calorimeters, excluding the calorimeter crack area. Only electrons with $E_T \geq 20\ GeV$ are considered, given that electrons from $t\bar{t}$ decays are usually quite energetic. The cut on the electron $E_T$ also ensures that the analysis is performed in the plateau region of the trigger.

For rejection against jets, the quality type "ElectronTight_WithTrackMatch" is required, which is defined in Table 4.1 in Chapter 4. In addition, the electrons are required to be well isolated, so as to reject electrons from photon conversions, and heavy flavor decays. A cut is applied on the corrected calorimetric isolation with a cone of size 0.2. The corrected calorimetric isolation variables are obtained by applying leakage and soft

| Category | Cuts | Smearing | Scale factors |
|---|---|---|---|
| **Electron Id** | | | ✓ |
| | ElectronAODCollection | | |
| | *author* == 1 ‖ *author* == 3 | | |
| | $E_T \geq 20\ GeV$ | ✓ | |
| | $\lvert\eta_{cluster}\rvert < 2.47$,<br>excluding $1.37 < \lvert\eta\,(cluster)\rvert < 1.52$ | | |
| | ElectronTight_WithTrackMatch | | |
| | $etcone20_{corrected} < 4\ GeV$ | | |
| | egamma object quality cuts | | |
| **Muon Id** | | | ✓ |
| | MuidMuonCollection | | |
| | $p_T \geq 20\ GeV$ | ✓ | |
| | $\lvert\eta\rvert < 2.5$ | | |
| | Tight quality level | | |
| | *author* ==MuonParameters::MuidCo | | |
| | Pass ID hit requirements | | |
| | $ptcone30 < 4\ GeV$<br>$etcone30 < 4\ GeV$<br>Remove muons within $\Delta R < 0.4$ in the $\eta$-$\phi$ plane from any jet with $p_T \geq 20\ GeV$ | | |
| **Jet Id** | | | |
| | CorrectedAntiKt4TopoEMJets | | |
| | $p_T \geq 25\ GeV$ | ✓ | |
| | $\lvert\eta_{EM}\rvert < 2.5$ | | |
| | Remove jets with negative energy | | |
| | Remove the jet closest to each accepted electron, if $\Delta R < 0.2$ in the $\eta$-$\phi$ plane | | |

Table 6.2: $t\bar{t} \rightarrow l + jets$ offline object identification criteria. Selection cuts with scale correction and/or resolution smearing and selection cuts with data/MC scale factors correcting their efficiencies are signified with a check mark in respective columns.

physics corrections to the variables provided by the Electron/Gamma group, with the "PAUcaloIsolationTool" [147].

Lastly, Electron/Gamma object quality cuts are applied to data, using the appropriate run-dependent map [148]. Electrons are rejected if they are adjacent to a region with a major hardware problem. To simulate the effect in data, the Electron/Gamma object quality cuts are also applied to Monte Carlo datasets, using a single map from the run with the highest integrated luminosity (run 167521 for 2010 data).

#### 6.2.1.2 Electron Energy Scale Offset and Resolution Smearing

The electron energy scale and resolution have been measured from the di-electron invariant mass in $Z \to ee$ decays [146, 149]. The electron energy scale is quantified by a dimensionless parameter $\alpha$ which represents the offset from a perfect calibration:

$$E_{corr} = \frac{E}{1+\alpha} \tag{6.1}$$

where $E$ is the measured energy and $E_{corr}$ is the energy after the offset correction. The energy scale offset parameter $\alpha$ is determined using the PDG (Particle Data Group) average $Z$ mass as a constraint on the peak position of the $Z \to ee$ mass distribution. It is measured for the full 2010 data as a function of electron cluster pseudorapidity ($\eta_{clus}$) using 50 bins for central electrons and eight bins for forward electrons. In the central region ($|\eta_{clus}| < 2.47$), an offset of less than 2% is observed, with a systematic error within $2-3\%$ except for the calorimeter crack region [146, 150]. Both the offset and its systematic error are larger outside the central region [146, 150]. Since corrections for the offsets are not yet included in the calibration process during the reconstruction, they are applied by hand to data.

The electron energy resolution at ATLAS is commonly written in the following form:

$$\frac{\sigma_E}{E} = \frac{a}{\sqrt{E}} \oplus \frac{b}{E} \oplus c \tag{6.2}$$

where the first term is due to sampling fluctuations, the second term is the noise term which has a significant contribution only at low energies, and the last term is the constant term caused by calibration errors and other systematic effects. An assumption is made that the sampling term is well modelled by MC. The is justified by the good data/MC agreement of the $J/\psi$ mass distribution and by the fact that at low energies the electron energy resolution is dominated by the sampling term [149]. As such, the difference between the resolution in data and MC is measured in terms of the constant term, $c$ [149]. The values of the constant term in data for different detector regions are shown in Table 6.3.

| Region | Constant term |
|---|---|
| Barrel | 1.1±0.2(stat+syst)% |
| EMEC outer-wheel | 1.8±0.2(stat+syst)% |
| EMEC inner-wheel | 4.0±0.4(stat+syst)% |
| FCAL | 2.0±0.6(stat+syst)% |

Table 6.3: The constant term of the electron energy resolution in data [150]

The electron $E_T$ in MC is smeared by adding a correction sampled event by event from a Gaussian distribution. The width of the Gaussian distribution is calculated as

$$\sigma_{smear} = \sqrt{c_{data}^2 - c_{MC}^2} \tag{6.3}$$

where $c_{data}$ is the constant term in data and $c_{MC}$ is the constant term in MC. The values for $c_{data}$ are taken from Table 6.3 and a value of 0.7% is used for $c_{MC}$ [150].

#### 6.2.1.3 Muon Identification Criteria

We use muons from the “MuidMuonCollection”, and restrict the analysis to the inner detector coverage ($|\eta| < 2.5$). For the same reasons as for the electrons, we require good muons to have a $p_T \geq 20\ GeV$. Muons with quality type “Tight” are used and are required to be combined ($author$ ==MuonParameters::MuidCo). On top of the quality type selection, the muons are required to pass all the ID hit requirements as given in Table 4.6 of Chapter 4. Two isolation cuts are applied: the first cut requires that the calorimetric isolation with a cone of size 0.3 is less than 4 $GeV$, and the second requires that the track-based isolation with a cone of size 0.3 is less than 4 $GeV$.

To further reduce muons coming from heavy flavor decays, if a muon overlaps any jet with $p_T \geq 20\ GeV$ within a cone of $\Delta R = 0.4$ in the $\eta$-$\phi$ plane, it is removed from the selected muons.

#### 6.2.1.4 Muon Momentum Scale Correction and Resolution Smearing

The momentum scale for combined muons (CB) has been determined by measuring the average deviation of the measured $Z \to \mu\mu$ invariant mass with respect to the PDG value of the $Z$ mass. The momentum resolution for combined muons has been measured from the width of the invariant mass distribution of $Z \to \mu\mu$ decays and from the difference of the individual ID and MS measurement for muons from $W \to \mu\nu$ decays. These measurements are initially based on the first pass reconstruction of 2010 data in Athena Release 15 [146, 151].

In order to measure the resolution for combined muons, the relative resolution $\sigma(p_T)/p_T$ is parametrized separately for the Muon Spectrometer:

$$\frac{\sigma(p_T)}{p_T} = \frac{p_0^{MS}}{p_T} \oplus p_1^{MS} \oplus \left(p_2^{MS} \cdot p_T\right) \tag{6.4}$$

and for the Inner Detector:

$$|\eta| < 1.9: \ \frac{\sigma(p_T)}{p_T} = p_1^{ID} \oplus \left(p_2^{ID} \cdot p_T\right) \tag{6.5}$$

$$|\eta| \geq 1.9: \ \frac{\sigma(p_T)}{p_T} = p_1^{ID} \oplus \left(p_2^{ID} \cdot \frac{p_T}{\tan^2(\theta)}\right) \tag{6.6}$$

where $p_2$ is the coefficient of the intrinsic resolution term, $p_1$ is the coefficient of the resolution term related to multiple scattering, and $p_0$ is the coefficient of the resolution terms related to calorimeter energy loss. The transverse momentum $p_T$ here refers to the $p_T$ from the MS or ID measurements alone.

The overall resolution and the corrections needed for tuning MC resolution to data are determined in terms of the parametrizations above. The final results are extracted through a combined fit which uses as input the resolution results for data and MC using $Z \to \mu\mu$ and $W \to \mu\nu$ events [151]. The extracted data/MC corrections to the parameters are shown in Table 6.4 for four different $\eta$ regions. The data/MC correction factors for muon momentum scale are shown in Table 6.5 for the same four regions. All the numbers listed are updated using Release 16 reconstruction [152].

| $\eta$ region | $\Delta p_1^{MS}$ [%] | $\Delta p_2^{MS}$ [$TeV^{-1}$] | $\Delta p_1^{MS}$ [%] | $\Delta p_2^{ID}$ [$TeV^{-1}$] ($\lvert\eta\rvert < 1.9$) | ($\lvert\eta\rvert \geq 1.9$) |
|---|---|---|---|---|---|
| barrel | 2.428±0.088 ±0.019 | 0.191±0.028 ±0.009 | 0.02±0.37 ±0.00 | 0.255±0.037 ±0.015 | – |
| transition | 6.78±0.27 ±0.16 | 0.19±0.12 ±0.04 | 0.18±0.62 ±0.02 | 0.53±0.13 ±0.14 | – |
| end-caps | 3.62±0.19 ±0.028 | 0.12±0.11 ±0.08 | 0.06±0.57 ±0.00 | 0.819±0.071 ±0.144 | – |
| CSC/no TRT | 2.37±0.45 ±0.108 | 0.669±0.091 ±0.167 | 0.00±0.71 ±0.00 | 1.177±0.050 ±0.14 | 0.0593±0.0032 ±0.0072 |

Table 6.4: Set of corrections to be applied to the $p_T$ parameterization of the MC resolution in the MS and ID to reproduce that of data. The first uncertainty is statistical, the second one systematic. For parameters not listed in the table, no correction is applied. The $\eta$ ranges for the corresponding regions can be found in Table 6.5.

| $\eta$ region | $\eta$ range | scale$_{data}$/scale$_{MC}$ |
|---|---|---|
| barrel | $0 \leq \lvert\eta\rvert < 1.05$ | 1.0000±0.0006 |
| transition | $1.05 \leq \lvert\eta\rvert < 1.7$ | 0.9933±0.0013 |
| end-caps | $1.7 \leq \lvert\eta\rvert < 2.0$ | 1.0037±0.0021 |
| CSC/no TRT | $2.0 \leq \lvert\eta\rvert < 2.5$ | 1.0033±0.0022 |

Table 6.5: Data/MC correction factors for muon momentum scale. The uncertainty is systematic only.

The muon $p_T$ in MC has to be scaled and smeared, in order to match the muon $p_T$ distribution in data. The scale correction and the smearing for the combined muons are performed according to the following formula:

$$p'_T(CB) = p_T(CB) \times \frac{\text{scale}_{data}}{\text{scale}_{MC}} \times \left[ 1 + \frac{\dfrac{\Delta(MS)}{\sigma^2(MS)} + \dfrac{\Delta(ID)}{\sigma^2(ID)}}{\dfrac{1}{\sigma^2(MS)} + \dfrac{1}{\sigma^2(ID)}} \right] \tag{6.7}$$

where $p_T(CB)$ and $p'_T(CB)$ refer to the $p_T$ of combined muons in MC before and after the corrections. The momentum scale is corrected by the term scale$_{data}$/scale$_{MC}$. The momentum smearing is applied through the last term on the right side of the formula. First, Gaussian smearing is carried out separately for $p_0$, $p_1$ and $p_2$ in Equation 6.4 to 6.6. The widths of the Gaussian distributions are taken from Table 6.4. For each event the total correction for the MS measurement, $\Delta(MS)$, is calculated by summing up contributions from different parameters:

$$\Delta(MS) = \sqrt{\Delta^2_{p_0}(MS) + \Delta^2_{p_1}(MS) + \Delta^2_{p_2}(MS)} \quad (6.8)$$

The total correction for the ID contribution, $\Delta(ID)$, is calculated similarly. Finally a weighted average is calculated from the separate corrections for the MS and ID measurements ($\Delta(MS)$, $\Delta(ID)$) and the expected resolution in MS and ID ($\sigma(MS)$, $\sigma(ID)$). The weighted average is added to $p_T(CB)$ for smearing.

#### 6.2.1.5 Jet Identification Criteria

As mentioned in Chapter 4, we use jets from the "CorrectedAntiKt4H1TopoEMJets" collection. The analysis is restricted to jets with $p_T \geq 25\ GeV$ in the central calorimeter region ($|\eta_{EM}| < 2.5$). Here $\eta_{EM}$ refers to the EM scale jet pseudorapidity with respect to the origin. It is used for all acceptance and overlap cuts involving the jet direction, instead of the pseudorapidity of the calibrated jet $\eta$, which has been corrected to point to the primary vertex. The jets are checked not to have negative energies, although in principle the problem should have already been fixed by the removal of the problematic pile-up correction (see Section 4.4).

Since electrons from $W$ and $Z$ decays automatically enter the jet list during reconstruction, the jet closest to each accepted electron is removed, if the distance between them in $\eta$-$\phi$ plane is less than 0.2 [146].

#### 6.2.1.6 Jet Energy Resolution Smearing

The jet energy resolution (JER) has already been discussed in Chapter 4. At present, only preliminary results in Athena Release 15 are available for in-situ measurements of JER. As a result, the recommendation by the Jet/ETmiss group is to take the resolution measured using MC truth information as baseline for the Monte Carlo sample, and smear it using the data/MC difference measured with in-situ techniques. The Gaussian smearing is carried out using a width $\sigma_{smear}$ calculated as:

$$\sigma_{smear} = \sqrt{(\sigma_{MC} + \Delta\sigma)^2 - \sigma_{MC}^2} \tag{6.9}$$

where $sigma_{MC}$ is the resolution measured in MC and $\Delta\sigma$ is the data/MC difference measured with in-situ techniques. The smeared sample is taken as the default for physics analyses and the difference between smeared and unsmeared sample is used for systematic uncertainty estimation.

The JER results needed for the recommended procedure are provided in a root file in terms of parametrised functions, together with a tool for accessing the information, currently available in [153]. The functions for anti-$k_T$ EM+JES jets with a cone size of 0.4 are shown in Figure 6.2, for four different $\eta$ regions.

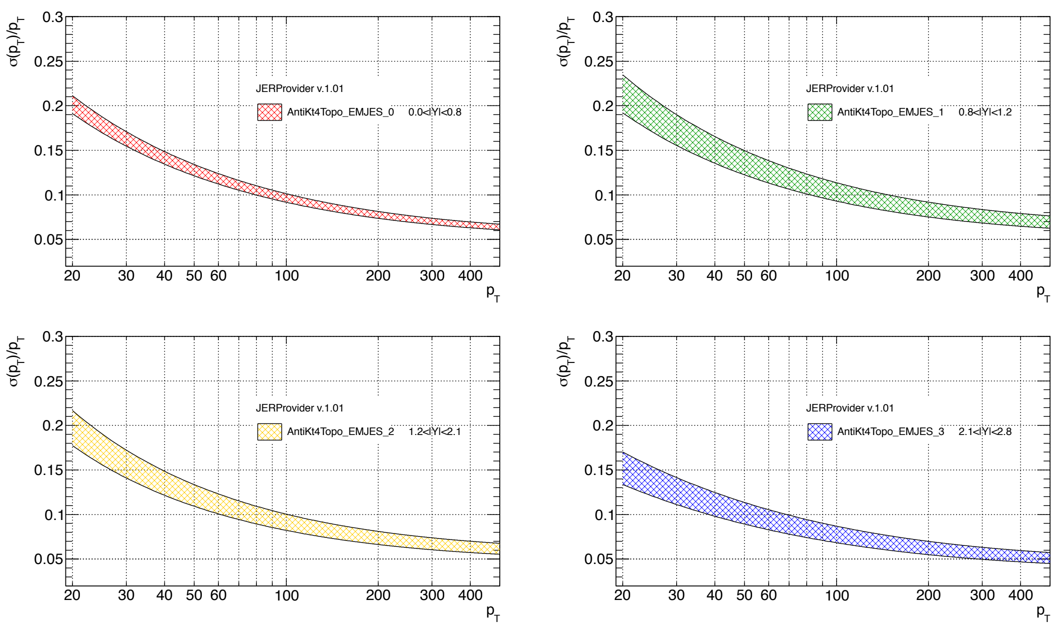


Figure 6.2: Jet Energy Resolution used in this analysis. The lower line is the JER measured in MC and the shaded area between two lines denotes the difference between data and MC.

### 6.2.2 Event-Level Selection Criteria

The event-level selection criteria include all the cuts listed in Table 6.6. The basic requirements are exactly one selected lepton (electron or muon), missing $E_T$ above threshold and at least four selected jets. In addition, a cut is placed on the leptonic $W$ transverse mass, defined as:

$$m_T^W = \sqrt{\left(p_T^{lep} + \not{E}_T\right)^2 - \left(p_x^{lep} + \not{E}_x\right)^2 - \left(p_y^{lep} + \not{E}_y\right)^2} \tag{6.10}$$

in order to suppress the QCD background (see Section 6.4.2). The $m_T^W$ cut is combined with the missing $E_T$ cut and optimized separately for the $e + jets$ and $\mu + jets$ channels to reduce the QCD fraction in the selected data sample [85]. In the $e + jets$ channel separate cuts on missing $E_T$ and $m_T^W$ are used, while in the $\mu + jets$ channel a so-called triangular cut is used in addition to the cut on missing $E_T$.

| **Category** | **Cuts** | | **Scale factors** |
|---|---|---|---|
| | $e + jets$ | $\mu + jets$ | |
| Lepton number | = 1 selected electron | = 1 selected muon | ✓ |
| Channel orthogonality | = 0 selected muon | = 0 selected electron | |
| $\not{E}_T$ and $m_T^W$ cuts | $\not{E}_T > 35\ GeV$<br>$m_T^W > 25\ GeV$ | $\not{E}_T > 20\ GeV$<br>$\not{E}_T + m_T^W > 60\ GeV$ | |
| Jet multiplicity | ≥ 4 selected jets | | |
| Jet cleaning | Remove events containing Loose bad jets with $p_T > 20\ GeV$ and $E > 0$ | | |
| Non-collision background rejection | ≥ 1 primary vertices with $N_{tracks} > 4$ | | |
| Trigger | EF_e15_medium<br>≥ 1 selected electron/muon matches trigger feature | EF_mu13_tight | ✓<br>✓ |
| $e/\mu$ overlap | Remove events tagged as $e/\mu$ overlap | | |

Table 6.6: Offline event-level selection criteria for $t\bar{t} \to e + jets$ and $t\bar{t} \to \mu + jets$ channels. The triggers listed in the table are for Selection cuts with a data/MC correction scale factor are signified with a check mark. The order of the event-level cuts reflects the order in which the cumulative signal selection efficiency is evaluated.

The event-level selection also includes a jet cleaning cut for jet quality and a cut on the number of tracks associated with primary vertices. The trigger requirements as described earlier in Section 6.1 are also enforced. The jet cleaning cut takes care of bad jets from detector effects in the 2010 data and should not be applied to Monte Carlo since most of the cleaning variables are not very well modelled. The definitions of Loose, Medium, and Tight bad jets for data reconstructed using Athena Release 16 are given in Figure 6.3. For this analysis Loose bad jets are used. The discriminating variables used in bad jet definitions are given in Table 6.7.

| | **Loose** | **Medium = Loose OR** | *****under discussion*** Tight = Medium OR** |
|---|---|---|---|
| **HEC spikes** | HECf>0.5 && \|HECQ\|>0.5<br>or<br>\|neg. E\|>60GeV | HECf>1-\|HECQ\| | |
| **EM coherent noise** | EMf>0.95 &&\|LArQ\|>0.8 && \|eta\|<2.8 | EMf>0.9 && \|LArQ\|>0.8 && \|eta\|<2.8 | \|LArQ\|>0.95<br>or<br>EMf>0.98 && \|LArQ\|>0.05 |
| **Non-collision background & Cosmics** | \|t\|>25ns<br>or<br>EMf<0.05 && Chf<0.05 && \|eta\|<2<br>or<br>EMf<0.05 && \|eta\|>=2<br>or<br>FMax>0.99 && \|eta\|<2 | \|t\|>10ns<br>or<br>EMf<0.05 && Chf<0.1 && \|eta\|<2<br>or<br>EMf>0.95 && Chf<0.05 && \|eta\|<2 | EMf<0.1 && Chf<0.2 && \|eta\|<2<br>or<br>EMf<0.1 && \|eta\|>=2<br>or<br>EMf>0.9 && Chf<0.02 && \|eta\|<2 |

Figure 6.3: Definitions of Loose, Medium, and Tight bad jets for data reconstructed in Athena Release 16 [85, 154]

| Variable name | Definition |
|---|---|
| EMf (aka emfrac) | electromagnetic fraction |
| fmax (aka fracSamplingMax) | maximum energy fraction in one calorimeter layer |
| HECf | energy fraction in the HEC |
| LArQ (aka LArQuality) | the fraction of LAr cells with a cell Q-factor greater than 4000 |
| HECQ (aka HECQuality) | same as the LArQ except calculated only with the HEC |
| negative E | negative energy in the jet |
| t (aka Timing) | jet time computed as average time using cells weighted by $E^2$ |
| n90 | minimum number of cells containing $\geq 90\%$ of the jet energy |
| eta | is the eta at the emscale (aka emscale_eta) |
| chf | is the jet charged fraction: $\sum p_T^{track}/p_T^{jet}$ |

Table 6.7: Discriminating variables used in bad jet definitions [154]. The cell Q-factor, used for calculating LArQ and HECQ, measures the difference between the measured pulse shape ($a_i^{meas}$) and the predicted pulse shape ($a_i^{pred}$) that is used to reconstruct the cell energy. It is computed as $\sum_{sample}\left(a_i^{meas} - a_i^{pred}\right)^2$ and it is stored as 16-bit integer.

The last cut in the event selection is to remove events where there is electron-muon overlap, in order to reject muons reconstructed as electrons. A muon and an electron are considered to be overlapping if they share the same track in the inner detector.

### 6.3 $t\bar{t}$ Efficiency Measurement

The total selection efficiency for the $t\bar{t}$ signal, $\epsilon_{t\bar{t}}$, is a product of the geometrical acceptance for $t\bar{t}$ events, $\mathcal{A}_{t\bar{t}}$, the lepton trigger efficiency, $\epsilon^{lepTrig}$, the lepton reconstruction (Reco) and Id efficiency, $\epsilon^{lepRecoId}$, the jet Reco and Id efficiency, $\epsilon^{jetRecoId}$, and other selection efficiencies, $\epsilon^{other}$:

$$\epsilon_{t\bar{t}} \quad = \quad \epsilon^{lepTrig}\epsilon^{lepRecoId}\epsilon^{jetRecoId}\epsilon^{other}\mathcal{A}_{t\bar{t}} \tag{6.11}$$

where the acceptance can be understood as the fraction of events passing selection if the reconstruction efficiency is unity. In principle, the acceptance can be determined using Monte Carlo truth particles.

Each efficiency term on the right side of Equation 6.11 can be measured in Monte Carlo, and then corrected for data using a data/MC scale factor (SF) measured with in-situ methods:

$$\epsilon = \epsilon_{MC} * \frac{\epsilon_{data}}{\epsilon_{MC}} = \epsilon_{MC} * \mathrm{SF} \tag{6.12}$$

Applying this method to $\epsilon^{lepTrig}$ and $\epsilon^{lepRecoId}$, the total efficiency can be rewritten as:

$$\epsilon_{t\bar{t}} \quad = \quad \left(\epsilon_{MC}^{lepTrig}\epsilon_{MC}^{lepRecoId}\epsilon^{jetRecoId}\epsilon^{other}\mathcal{A}_{t\bar{t}}\right) \times \left(\mathrm{SF}^{lepTrig} * \mathrm{SF}^{lepRecoId}\right) \tag{6.13}$$

The efficiency and acceptance terms are not measured separately. Rather, the terms inside the first parenthesis are measured together by measuring cumulative selection efficiency in MC. The data/MC correction scale factors for $\epsilon^{lepTrig}$ and $\epsilon^{lepRecoId}$ are measured using in-situ methods, which are described below in dedicated sections. No data/MC correction is applied to $\epsilon^{jetRecoId}$. Instead, a systematic error is attributed to it. $\epsilon^{other}$ and $\mathcal{A}_{t\bar{t}}$ are treated similarly. The total $t\bar{t}$ selection efficiency presented in Section 6.3.5 is extracted from the cumulative efficiency measured in MC and the data/MC scale factors.

### 6.3.1 Electron Trigger Efficiency

Trigger efficiencies for high $E_T$ electrons are measured within the Electron/Gamma working group, using the tag-and-probe method with samples of $W \to e\nu$ and $Z \to ee$ decays [146, 155]. The $W \to e\nu$ events are tagged by the neutrino while the $Z \to ee$ events are tagged by one of the electrons. Events and Details of the method are documented in [155]. The efficiency results using $W \to e\nu$ and $Z \to ee$ samples are consistent with each other, given the difference between the two methodologies and between the kinematics of the electrons from $W$ and $Z$ decays. The efficiency for the e15_medium trigger, used in this analysis, shows negligible dependence on $\eta$ and $\phi$ of the electron. It is also observed to have a sharp turn-on, a stable plateau, and an efficiency above 99% if the electron $E_T$ is around 5 $GeV$ above the trigger threshold. A single data/MC scale factor of:

$$\mathrm{SF}^{eleTrig} = 0.995 \pm 0.005 \text{ (stat + syst)} \tag{6.14}$$

is recommended for electrons with $E_T$ on the plateau of the trigger (5 $GeV$ or more above the threshold) [146, 156].

### 6.3.2 Electron Reconstruction and Identification Efficiency

The electron reconstruction, identification, and isolation efficiency are measured separately using the tag-and-probe method [146, 157]. The reconstruction efficiency is measured with a sample of $Z \to ee$ events, and the details of the method are documented in [157]. Preliminary studies have measured the data/MC scale factor for the reconstruction efficiency to be [146, 156]:

$$\mathrm{SF}^{eleReco} = 1.000 \pm 0.015 \text{ (stat + syst)} \tag{6.15}$$

The identification efficiency for high $E_T$ electrons is measured using both $W \to e\nu$ and $Z \to ee$ decays, with the details of the method documented in [156, 157]. Results from the two independent measurements using $W \to e\nu$ and $Z \to ee$ decays are combined statistically assuming uncorrelated systematic uncertainties. To take into account the kinematic dependence of the efficiency, the data/MC scale factors are derived for a 2D array in eight bins of electron cluster $\eta$ and six bins of $E_T$. Due to the limited statistics, the scale factors are not measured directly for $N^{\eta}_{bins} \times N^{E_T}_{bins}$ bins. Rather, they are first measured as a function of $\eta_{clus}$ inclusive of all $E_T$, and separately as a function of electron $E_T$ inclusive of all $\eta_{clus}$. The final result in a 2D array is obtained by multiplying $\eta_{clus}$ dependent scale factors with $E_T$ dependent corrections for the scale factors [157]. The results can be used by retrieving the number from the 2D array corresponding to the $\eta_{clus}$ and $E_T$ for a given electron.

The isolation efficiency is measured within the top physics group for the group-specific isolation cuts, using a sample of $Z \to ee$ decays [146]. The scale factors are studied as a function of the isolation cut, for different $\eta_{clus}$ using the same binning as for the identification SF's. The combined identification and isolation SF's, determined as a product of the individual SF's, are shown Table 6.8. For convenience, we will refer to the combined SF as SF$^{eleId}$.

| $E_T$ region | $\eta_{clus}$ in | | | | | | |
|---|---|---|---|---|---|---|---|
| [GeV] | [-2.47, -2.01] | [-2.01, -1.52] | [-1.37, -0.8] | [-0.8,0] | [0, 0.8] | [0.8, 1.37] | [1.52, 2.01] | [2.01, 2.47] |
| [20, 25] | 0.917 ± 0.082 | 0.946 ± 0.084 | 0.968 ± 0.083 | 0.907 ± 0.082 | 0.912 ± 0.082 | 0.970 ± 0.082 | 0.961 ± 0.086 | 0.953 ± 0.086 |
| [25, 30] | 0.960 ± 0.028 | 0.990 ± 0.032 | 1.013 ± 0.029 | 0.949 ± 0.027 | 0.955 ± 0.027 | 1.016 ± 0.028 | 1.006 ± 0.038 | 0.998 ± 0.036 |
| [30, 35] | 0.998 ± 0.027 | 1.029 ± 0.030 | 1.053 ± 0.027 | 0.987 ± 0.025 | 0.993 ± 0.025 | 1.056 ± 0.026 | 1.046 ± 0.037 | 1.037 ± 0.035 |
| [35, 40] | 0.996 ± 0.024 | 1.027 ± 0.028 | 1.051 ± 0.025 | 0.985 ± 0.023 | 0.991 ± 0.023 | 1.054 ± 0.024 | 1.044 ± 0.035 | 1.035 ± 0.034 |
| [40, 45] | 0.998 ± 0.025 | 1.029 ± 0.029 | 1.053 ± 0.026 | 0.987 ± 0.024 | 0.993 ± 0.024 | 1.056 ± 0.024 | 1.046 ± 0.036 | 1.037 ± 0.034 |
| [45, inf] | 1.007 ± 0.033 | 1.038 ± 0.037 | 1.062 ± 0.034 | 0.995 ± 0.032 | 1.002 ± 0.032 | 1.065 ± 0.033 | 1.055 ± 0.042 | 1.046 ± 0.041 |

Table 6.8: The combined identification and isolation scale factors in $\eta_{clus}$ and $E_T$ bins [146]

### 6.3.3 Muon Trigger Efficiency

Efficiencies for the muon triggers used in this analysis are measured in data and Monte Carlo samples for muons passing all the muon identification cuts listed in Table 6.2, using the tag-and-probe method with a sample of $Z \to \mu\mu$ decays [146]. The data sample used is the same as what is used in this analysis, while the MC sample used is the ALPGEN $Z \to \mu\mu + jets$ datasets in the MC10 production [142]. Both the tag and probe muons are required to pass the muon ID cuts in Table 6.2. In addition, the tag muon is required to match an EF trigger ROI within $\Delta R = 0.2$ in the $\eta$-$\phi$ plane. In order to select the $Z \to \mu\mu$ sample, the tag and probe muons are required to have opposite charges and their invariant mass is required to lie within a window of 12 $GeV$ from the mass of the $Z$ boson:

$$\left|M_{tag+probe} - M_Z\right| \leq 12\ GeV \tag{6.16}$$

The muon trigger efficiency, defined as the fraction of probe muons that are matched to a trigger ROI,

$$\epsilon^{muonTrig} = \frac{N_{probes}^{matched}}{N_{probes}}, \tag{6.17}$$

is studied as a function of $\eta(\mu)$ and $\phi(\mu)$. It is also studied as functions of $p_T(\mu)$ and $\Delta R(\mu, closest\ jet)$. Visible $\eta$ and $\phi$ dependent disagreements between data and MC are observed and attributed to local residual miscalibration of the Level-1 Barrel trigger. In order to isolate these problems, the data/MC correction scale factors are evaluated in 10 $\eta$-$\phi$ bins. The results are shown in Table 6.9.

| Bin name | $\eta$ range | $\phi$ range | SF |
|---|---|---|---|
| EC | $\lvert\eta\rvert > 1.05$ | any $\phi$ | $0.987 \pm 0.003$ (stat) $^{+0.001}_{-0.001}$ (syst) |
| B1P1 | [-1.05, 0.6] | $[-\pi, 5\pi/16] \bigcup [11\pi/16, \pi]$ | $1.026 \pm 0.010$ (stat) $^{+0.003}_{-0.002}$ (syst) |
| B1P2 | $[-1.05, 0.6] \bigcup [-0.6, -0.5]$ $\bigcup [-0.4, 0.2] \bigcup [0.3, 0.6]$ | $[5\pi/16, \pi/2]$ | $0.919 \pm 0.017$ (stat) $^{+0.007}_{-0.000}$ (syst) |
| B1P3 | [-1.05, 0.6] | $[\pi/2, 11\pi/16]$ | $0.952 \pm 0.030$ (stat) $^{+0.002}_{-0.003}$ (syst) |
| B2P1 | [-0.6, 0.6] | $[-\pi, 5\pi/16] \bigcup [11\pi/16, \pi]$ | $1.009 \pm 0.006$ (stat) $^{+0.001}_{-0.002}$ (syst) |
| B2P2 | $[-0.5, -0.4] \bigcup [0.2, 0.3]$ | $[5\pi/16, \pi/2]$ | $0.657 \pm 0.050$ (stat) $^{+0.010}_{-0.000}$ (syst) |
| B2P3 | [-0.6, 0.6] | $[\pi/2, 11\pi/16]$ | $0.906 \pm 0.019$ (stat) $^{+0.000}_{-0.004}$ (syst) |
| B3P1 | [0.6, 1.05] | $[-\pi, 5/16\pi] \bigcup [11\pi/16, \pi]$ | $1.005 \pm 0.010$ (stat) $^{+0.002}_{-0.003}$ (syst) |
| B3P2 | [0.6, 1.05] | $[5\pi/16, \pi/2]$ | $0.843 \pm 0.053$ (stat) $^{+0.000}_{-0.013}$ (syst) |
| B3P3 | [0.6, 1.05] | $[\pi/2, 11\pi/16]$ | $1.046 \pm 0.029$ (stat) $^{+0.011}_{-0.009}$ (syst) |

Table 6.9: Muon trigger scale factors in different $\eta - \phi$ bins [146]

### 6.3.4 Muon Reconstruction and Identification Efficiency

Like the trigger efficiency, the muon offline reconstruction and identification efficiency is measured using the tag-and-probe method with a sample of $Z \rightarrow \mu\mu$ decays [146]. The data and MC samples used are the same as for the trigger efficiency measurement. The tag muon is defined using all requirements as in the trigger efficiency measurement, plus an additional cut on the transverse impact parameter (IP) of the muon track: $|d_0\,(\mu, \mathrm{PV})| \leq 0.05\ mm$.

The reconstruction efficiency is defined as:

$$\epsilon^{muonReco} = \frac{N^{matched\ to\ combined}_{ID\ probes}}{N_{ID\ probes}} \tag{6.18}$$

where ID probes are muon tracks reconstructed with ID only, selected by cuts listed in Table 6.10. Note that the $p_T$ cut is slightly different from the standard $p_T$ cut, so as to allow for MS-ID mismatches due to tracking resolution effects and to avoid boundary effects around $p_T = 20\ GeV$. A combined muon with $p_T > 20\ GeV$ is counted for $N^{matched\ to\ combined}_{ID\ probes}$ if it is within $\Delta R = 0.05$ of a ID probe muon.

| Category | Cut |
|---|---|
| ID hit requirement | Pass ID hit requirements |
| $p_T$ cut | $p_T \geq 22\ GeV$ |
| Transverse IP | $\lvert d_0\,(\mu, PV)\rvert \leq 0.05\ mm$ |
| $Z$ mass constraint | $\left\lvert M_{tag+probe} - M_Z \right\rvert \leq 10\ GeV$ |
| Angular separation | $\Delta\phi\,(tag, probe) \geq 1.5$ |
| Charge | Opposite electric charge with respect to the tag muon |

Table 6.10: Selection cuts for ID probes used in the tag-and-probe measurement of the muon reconstruction efficiency

The identification efficiency is defined as:

$$\epsilon^{muonID} = \frac{N^{matched\ to\ selected}_{combined\ probes}}{N_{combined\ probes}} \tag{6.19}$$

where combined probes are selected by the cuts listed in Table 6.11.A combined probe muon is counted for $N^{matched\ to\ selected}_{combined\ probes}$ if it is also selected by criteria listed in Table 6.2.

| Category | Cut |
|---|---|
| Quality type | Tight |
| Author | *author* ==MuonParameters::MuidCo |
| $p_T$ cut | $p_T \geq 20\ GeV$ |
| $Z$ mass constraint | $\left\|M_{tag+probe} - M_Z\right\| \leq 10\ GeV$ |
| Angular separation | $\Delta\phi\,(tag, probe) \geq 1.5$ |
| Charge | Opposite electric charge with respect to the tag muon |

Table 6.11: Selection cuts for ID probes used in the tag-and-probe measurement of the muon reconstruction efficiency

The combined Reco+Id efficiency is measured by selecting tag and probes as for the reconstruction efficiency, and then matching it to a muon passing all muon Id criteria in Table 6.2. The data/MC correction scale factors for muon reconstruction and identification efficiencies, separately and combined, are given in Table 6.12. The scale factors are not binned as they are observed to be stable for different kinematics regions.

| Reconstruction | Identification | Reco+Id |
|---|---|---|
| 0.997 ± 0.001 (stat) ±0.003 (syst) | 1.002 ± 0.001 (stat) ±0.001 (syst) | 0.999 ± 0.002 (stat) ±0.003 (syst) |

Table 6.12: Muon reconstruction and identification scale factors [146]

### 6.3.5 Total $t\bar{t}$ Selection Efficiency

The object identification and event-level selection criteria as shown in Table 6.2 and 6.6 are applied to the default MC sample of $t\bar{t}$ (see Chapter 5). The exclusive and cumulative efficiencies for each event-level cut are extracted, in the same order as in Table 6.6. The scale factors (SFs) discussed in Section 6.3.1 to 6.3.4 are applied to the selected events as multipliable event weights dependent on the event kinematics. These event weights are applied on top of physics weights from the Monte Carlo generation, if any. An overall scale factor is derived as the ratio of the total number of events with the SF's and without the SF's. The total efficiency, after applying all the SF's, is:

$$e + jets \text{ channel: } \epsilon_{t\bar{t}} = 5.972 \pm 0.027(\text{stat})\ \% \tag{6.20}$$

$$\mu + jets \text{ channel: } \epsilon_{t\bar{t}} = 8.572 \pm 0.032(\text{stat})\ \% \tag{6.21}$$

where the statistical uncertainty comes from the limited statistics of the Monte Carlo dataset. The individual efficiencies of each cut and the data/MC scale factors are listed in Table 6.13 and 6.14.

| Cut or Scale Factor | Exclusive efficiency | Cumulative efficiency |
|---|---|---|
| Lepton number | (19.83±0.05)% | (19.83±0.05)% |
| Channel orthogonality | (91.33±0.07)% | (18.11±0.04)% |
| $\not{E}_T$ cut | (75.23±0.12)% | (13.63±0.04)% |
| $m_T^W$ cut | (88.17±0.10)% | (12.02±0.04)% |
| Jet multiplicity | (50.11±0.16)% | (6.021±0.027)% |
| Jet cleaning | (99.60±0.03)% | (5.997±0.027)% |
| Good PV number | (100±0)% | (5.997±0.027)% |
| Trigger passing | (99.57±0.03)% | (5.971±0.027)% |
| Trigger matching | (99.99±0.00)% | (5.971±0.027)% |
| $e/\mu$ overlap | (100±0)% | (5.971±0.027)% |
| $\mathrm{SF}^{lepTrig} * \mathrm{SF}^{lepRecoId}$ | 1.0001 | (5.972±0.027)% |

Table 6.13: Summary of the $t\bar{t} \to e + jets$ selection efficiencies and the data/MC scale factors, if applicable. The uncertainty shown is statistical uncertainties from the limited MC statistics.

### 6.4 Expected Data Sample Composition

The event selection, as described in Section 6.1 and 6.2, selects not only $t\bar{t}$ events but also non-$t\bar{t}$ events with similar final-state signatures. These background processes may have a significant contribution to the selected data sample. In this section the expected number of $t\bar{t}$ signal and background events in the data are discussed.

The backgrounds can be subdivided into either physics backgrounds and instrumental backgrounds. Physics backgrounds share the same final-state signature as the signal events, with one isolated lepton, four jets, and missing $E_T$ from the neutrino. The dominant physics background to $t\bar{t}$ semileptonic decay is the $W + jets$ background. By contrast, the QCD background is an instrumental background. Its final-state signature differs from the $t\bar{t}$ signature in that there is neither a real isolated lepton nor real missing $E_T$. However, event misreconstruction may give rise to misidentified leptons and missing $E_T$, allowing

| Cut or Scale Factor | Exclusive efficiency | Cumulative efficiency |
|---|---|---|
| Lepton number | (25.86±0.05)% | (25.86±0.05)% |
| Channel orthogonality | (93.33±0.06)% | (24.13±0.05)% |
| $\not{E}_T$ cut | (91.62±0.06)% | (22.11±0.05)% |
| Triangular cut | (94.51±0.06)% | (20.90±0.05)% |
| Jet multiplicity | (51.10±0.12)% | (10.68±0.04)% |
| Jet cleaning | (99.57±0.02)% | (10.63±0.04)% |
| Good PV number | (100±0)% | (10.63±0.04)% |
| Trigger passing | (83.00±0.13)% | (8.825±0.032)% |
| Trigger matching | (98.20±0.05)% | (8.666±0.032)% |
| $e/\mu$ overlap | (100±0)% | (8.666±0.032)% |
| $\mathrm{SF}^{lepTrig}*\mathrm{SF}^{lepRecoId}$ | 0.9890 | (8.572±0.032)% |

Table 6.14: Summary of the $t\bar{t} \to \mu + jets$ selection efficiencies and the data/MC scale factors, if applicable. The uncertainty shown is statistical uncertainties from the limited MC statistics.

for these events to pass the selection criteria.

Each of the background processes to the $t\bar{t}$ semileptonic channel are described below. In Section 6.4.6 the event yields are estimated for the signal and the backgrounds. In Section 6.4.7, data and Monte Carlo comparison plots are displayed to check consistency with data. Additional corrections are applied to MC to correct for remaining differences with data.

### 6.4.1 $W + jets$ background

The dominant physics background to the $t\bar{t}$ semileptonic channel arises from the direct production of W bosons via electroweak interaction. Jets can be produced in association with the W boson through QCD bremsstrahlung (i.e. emission of gluons) and gluon to $q\bar{q}$ splitting. The Feynman diagram of the $W+0$ parton process is shown in Figure 6.4. Some examples of Feynman diagrams for the $W + 1$ and $W + 2$ parton processes are shown in Figure 6.5 and 6.6. The signature of the $W+ \geq 4$ parton production with a subsequent $W$ leptonic decay is identical to the semileptonic $t\bar{t}$ signature.

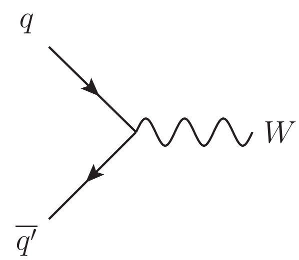


Figure 6.4: Feynman diagram for the *w* + 0 parton process

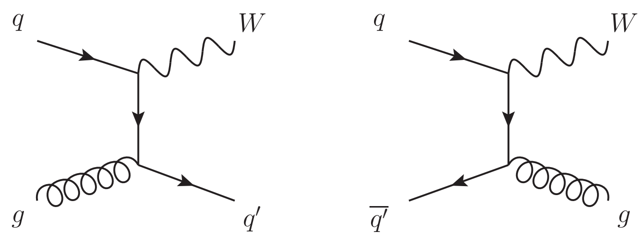


Figure 6.5: Some examples of Feynman diagrams for the *W* + 1 parton processes

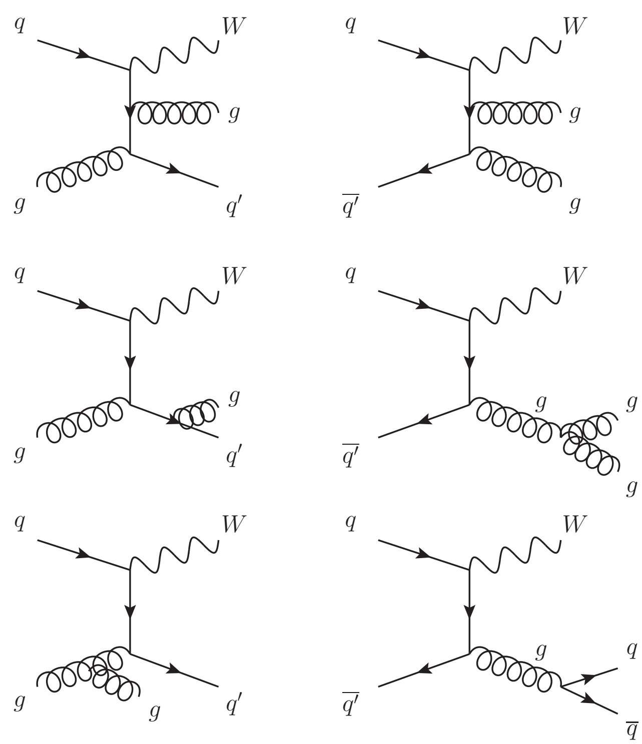


Figure 6.6: Some examples of Feynman diagrams for the *W* + 2 parton processes

### 6.4.2 QCD Multijet Background

The QCD multijet background, or more simply, the QCD background, comes from the strong production of four or more jets. If one of the jets is misreconstructed as an isolated electron and there is enough missing $E_T$ from fake or instrumental sources, the QCD events can also pass the $t\bar{t}$ selection criteria. A major source of fake leptons in the QCD background arise from non-isolated leptons produced through semileptonic decays of heavy flavor hadrons. Additionally, jets that are misidentified as electrons can also produce electromagnetic clusters that pass isolation tests.

Although the selection efficiency of the QCD background is low, it is still one of the major backgrounds to the $t\bar{t}$ signal. This is due to its large cross section at hadron colliders like LHC.

### 6.4.3 $Z + jets$ Background

The $Z/\gamma^{\star}+jets$ background, or more simply, the $Z + jets$ background, is produced similarly as the $W + jets$ background. The Feynman diagrams of these processes can be obtained from Figure 6.4 to 6.6 by replacing the W by a $Z/\gamma^{\star}$. The $Z + jets$ production is the major background to the $t\bar{t}$ di-lepton decay channel, because the $Z$ boson can decay to two leptons ($ee$, $\mu\mu$). In cases where one of the two leptons is not detected due to limited detector acceptance, $Z + jets$ can fake $t\bar{t}$ semileptonic events too.

### 6.4.4 Single Top Background

Single tops can be produced via electroweak interaction in several channels. In the $t$-channel, the top quark is produced from an intermediate $W$ boson decaying into a pair of $t$ and $b$ quarks. In the $s$-channel, a bottom quark transforms into a top quark by exchanging a virtual $W$ boson with a light quark. In addition, single tops can also be produced in association with a $W$ boson. The Feynman diagrams for the different channels of single top production are shown in Figure 6.7. The final-state signature of the $s$-channel where the $W$ boson subsequently decays leptonically, is one lepton, missing $E_T$ from the neutrino, and two $b$ jets. In the $t$-channel production, there is an additional light jet. For the $Wt$

channels where one of the $W$'s decays leptonically, the final state signature is one lepton, one $b$-jet, and two light jets. Due to ISR and FSR more jets can be produced, which leads to the same signature as the $t\bar{t}$ semileptonic decay channel.

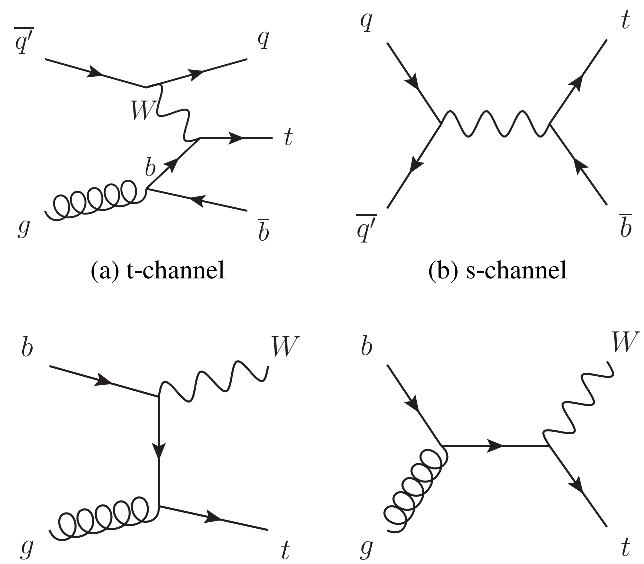


(a) t-channel (b) s-channel

(c) $Wt$ t-channel (d) $Wt$ s-channel

Figure 6.7: Leading order Feynman diagrams for the single top production in different production channels

The selection efficiency on the single top background is high due to its high degree of similarity to the $t\bar{t}$ signal. However, the production cross section for single top is relatively low. Therefore it is considered a small background to the signal $t\bar{t}$ process.

### 6.4.5 DiBoson Background

Another small background to the $t\bar{t}$ semileptonic channel is the vector boson pair production ($WW$, $ZZ$, and $WZ$), collectively known as the diboson background. Production of $WW$ pairs occurs primarily through interactions represented by diagrams in Fig 6.8. $WZ$ and $ZZ$ pairs are produced similarly. Semileptonic decay modes of the vector boson pairs can lead to similar final-state signatures as that of the signal $t\bar{t}$ process.

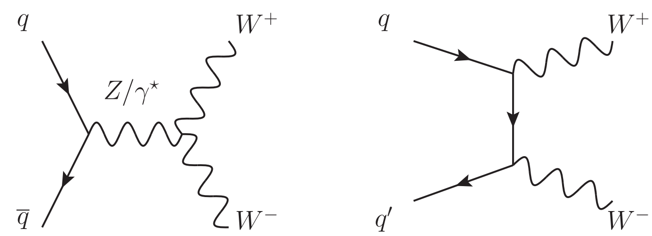


Figure 6.8: Some examples of Feynman diagrams for the $WW$ pair production

### 6.4.6 Expected Event Yields

The expected event yields for $t\bar{t}$ signal and backgrounds for an integrated luminosity of 35.3 $pb^{-1}$ are summarized in Table 6.15. The number of QCD background events is measured using data driven methods, which will be described in Chapter 8, while for all other processes it is determined by normalizing the number of MC events to 35.3 $pb^{-1}$. The normalization is imposed by weighting the events in different MC samples according to their theoretical cross sections. The event weight is calculated as:

$$w = \frac{\sigma \times \mathrm{BR} \times \int \mathcal{L}\, dt}{N} \tag{6.22}$$

where $\sigma$ and BR are the theoretical cross section and branching ratio for a certain Monte Carlo sample, $\int \mathcal{L}\, dt$ is the integrated luminosity, and $N$ is the total number of events in the MC sample. The cross sections used in the calculation can be found in Table 5.3 in Chapter 5.

The expected event yields that are presented in Table 6.15 also include an estimation of the signal over background ($S/B$) ratio and a comparison of the total expected number of events with the number of observed data events. The total expected number is consistent with the total observed number, if all statistical and systematic uncertainties are taken into account [158].

The background in the selected sample is dominated by the $W + jets$ events, the size of this background and the $t\bar{t}$ signal being approximately equal. The $S/B$ ratio can be enhanced by making further cuts such as increasing the jet $p_T$ threshold, requiring one or more $b$-tagged jets, or utilizing $W$ and top mass constraints. On the other hand, these cuts will reduce the number of selected data events and thus increase the statistical uncertainty.

| Process | Event yield | |
|---|---|---|
| | $e + jets$ channel | $\mu + jets$ channel |
| $t\bar{t}$ (MC) | 188.5±1.0 | 271.4±1.2 |
| $W + jets$ (MC) | 178.6±2.1 | 317.5±2.8 |
| QCD (DD) | 21.78±7.92 | 51.3±5.5 |
| $Z + jets$ (MC) | 16.2±1.2 | 24.4±1.4 |
| single top (MC) | 10.5±0.2 | 14.9±0.2 |
| dibosons (MC) | 2.5±0.1 | 4.0±0.1 |
| Total background | 229.5±8.3 | 411.2±6.3 |
| $S/B$ | 0.82 | 0.66 |
| Total expected | 418.0±8.3 | 681.6±6.4 |
| Observed | 396 | 653 |

Table 6.15: Number of data and MC events passing the event selection criteria. The MC events are normalized to 35.3 $pb^{-1}$. The methods used to extract the number for $t\bar{t}$ and backgrounds sample are shown in parentheses: MC means MC normalization, and DD means data-driven methods. Uncertainties in the table are from the limited MC statistics, or from uncertainties with the data-driven method in the case of QCD.

This is undesirable with the limited integrated luminosity of the data set used in this dissertation. The top likelihood method used in this thesis preserves statistics in that it does not require further cuts to reduce the backgrounds. In addition, the top likelihood method requires enough MC statistics after selection for both $t\bar{t}$ signal and backgrounds, so as to model their distributions reliably. As a result, it is decided not to apply any further cuts on the selected sample.

### 6.4.7 Additional Data/MC Corrections

In order to reliably model the physics distributions in data, additional data/MC corrections need to be applied to the MC samples after selection. As illustrated in Figure 6.9(a) and 6.9(b), the number of collision vertices (pile-up) is different in MC and data. The pile-up distribution in MC is adjusted to that observed in data by re-weighting MC events accordingly as a function of the number of vertices in each event. The weights used are given in Table 6.16. After the re-weighting, good Figure 6.9(c) and 6.9(d) show good agreement between data and MC after the re-weighting procedure is applied.

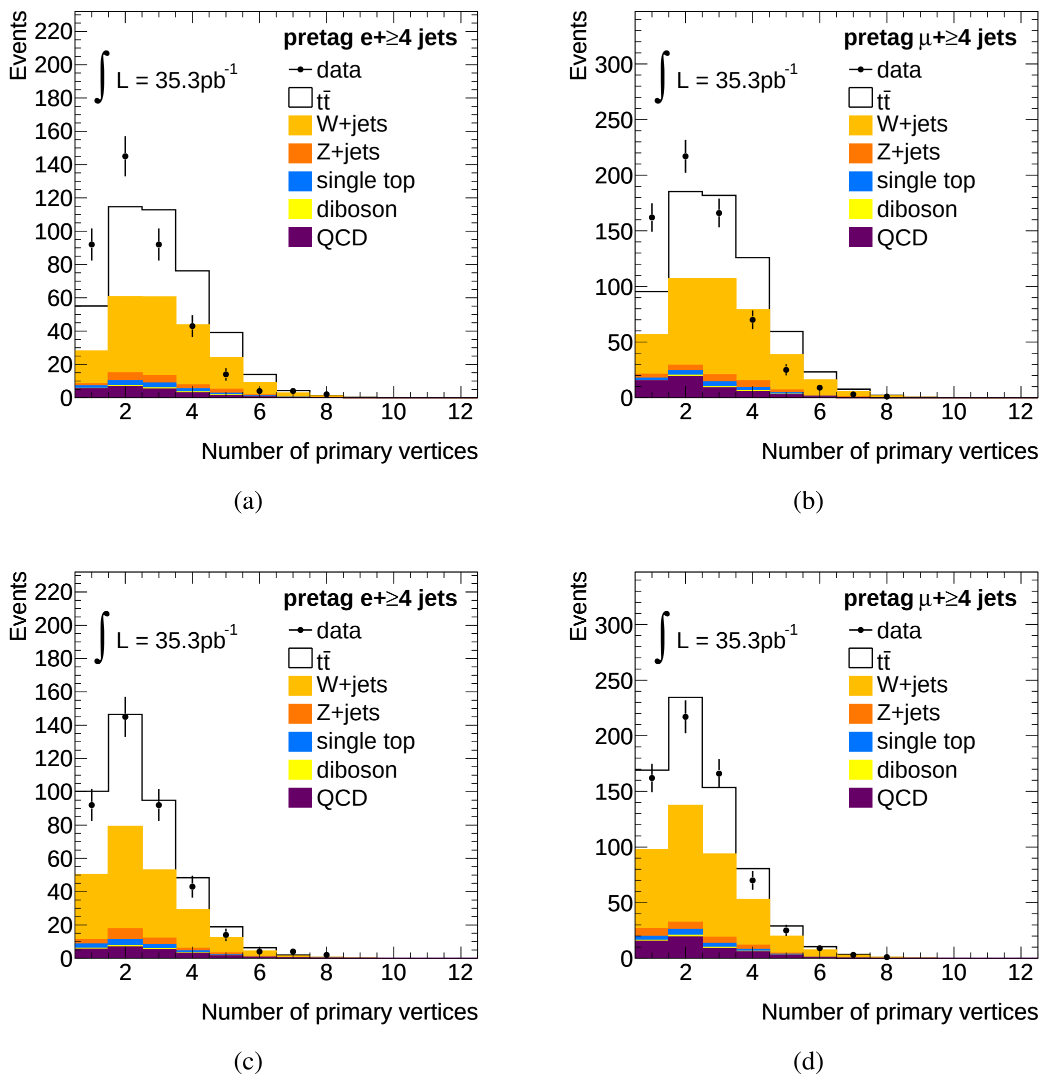


Figure 6.9: Distribution of the number of good primary vertices ($N_{tracks} > 4$) for events passing all selection criteria before (top) and after (bottom) pile-up vertex number correction in the $e + jets$ channel (left) and the $\mu + jets$ channel (right)

| Number of vertices | 1 | 2 | 3 | 4 | 5 | $\geq 6$ |
|---|---|---|---|---|---|---|
| Weight | 1.929 | 1.3029 | 0.838 | 0.6225 | 0.4635 | 0.4345 |

Table 6.16: Weights for re-weighting the MC vertex number distribution to match the data [159]. The weights are obtained for $l+ \geq 3\,jets$ averaged over electron and $\mu + jets$ channels. The values are compatible with values for electron only and muon only. The values are also compatible before and after selection.

Since the top likelihood analysis in this dissertation makes use of the $b$-tagging SV0 weight, it is important to apply the $b$-tagging calibration correctly, as well as have an accurate estimation of the $W + jets$ HF (heavy flavor) fractions. The theoretical prediction of $W + jets$ HF fractions has a large uncertainty because it relies on HF flavor Parton Distribution Functions (PDFs). As a result, the HF fractions in the $W + jets$ events are determined using in-situ methods [103]. The fractions are measured in data in the $W + 2jets$ control region and then projected into the signal region. The projection factor and its uncertainties are determined from MC studies [103]. Based on the preliminary results of the in-situ measurement, it is recommended to scale the fractions of $Wbb$ and $Wcc$ together by 1.3 from the Alpgen prediction. No correction should be applied to the $Wc$ events. The fractions are scaled via event weights.

The $b$-tagging calibration is applied by re-weighting MC events [103, 160]. The starting point is the per-jet scale factor provided in Table 4.9 and 4.10. If a jet is tagged, the jet weight is:

$$w_{jet} = \mathrm{SF}_{flavor}(p_T, \eta), \tag{6.23}$$

whereas if the jet is not tagged,

$$w_{jet} = \frac{1 - \epsilon^{data}_{flavor}(p_T, \eta)}{1 - \epsilon^{MC}_{flavor}(p_T, \eta)} = \frac{1 - \mathrm{SF}_{flavor}(p_T, \eta)\,\epsilon^{MC}_{flavor}(p_T, \eta)}{1 - \epsilon^{MC}_{flavor}(p_T, \eta)} \tag{6.24}$$

where the flavor of the jets are decided by matching them with MC truth jets. The event weight is then given by the product of the jet weights for all selected jets:

$$w_{event} = \prod_{jets} w_{jet} \tag{6.25}$$

Figure 6.10 shows the data/MC comparison plot of the number of $b$-tagged jets, after all data/MC corrections are applied to MC.

Agreement between data and Monte Carlo can be checked by examining other kinematic distributions. Comparison plots for the lepton $p_T$, missing $E_T$, jet multiplicity, and the leading jet $p_T$ are shown from Figure 6.11 to 6.14. The data and MC distributions are after all selection criteria and MC weights have been applied.

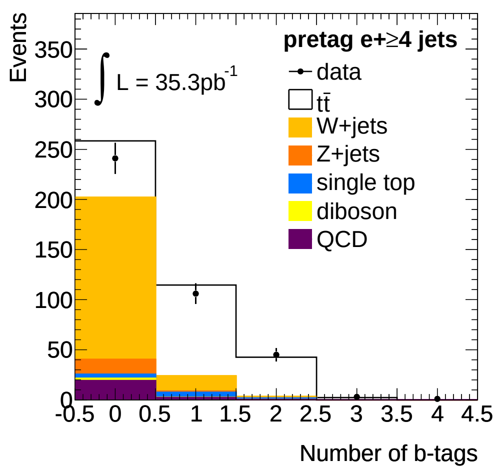


(a)

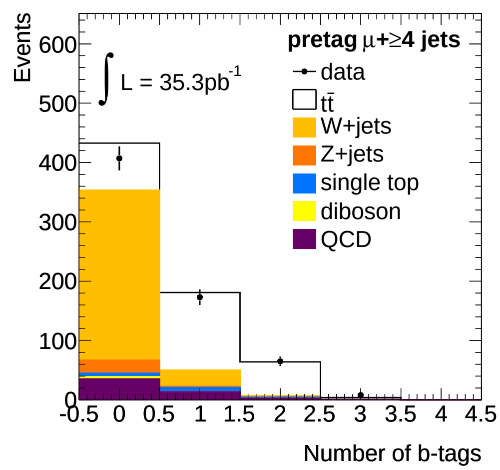


(b)

Figure 6.10: Number of jets tagged as $b$-jets for the events passing all selection criteria in the $e + jets$ channel (left) and the muon channel (right)

One can reconstruct $W$ bosons and top quarks after the selection criteria have been applied. The hadronic top is reconstructed from the three jets with the highest total $p_T$ out of the four leading jets. Its invariant mass distribution is shown in Figure 6.15. The hadronic $W$ is reconstructed by comparing the invariant mass of each pair of jets in the hadronic top with the PDG value of the $W$ mass. Its invariant mass distribution is shown in Figure 6.16. The leptonic top is reconstructed using the remaining one jet, the lepton, and the missing $E_T$. The kinematics of the neutrino is solved from the lepton and missing $E_T$ using the PDG mass of the $W$ boson as a constraint. In case no solution can be found, the missing $E_T$ is scaled by a factor of $m^W/m_T^W$ and an approximate solution is found. The invariant mass of the leptonic top is shown in Figure 6.17. In all the plots a good agreement between data and MC is observed.

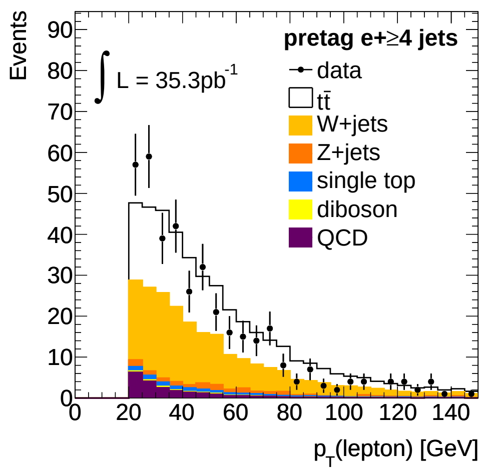


(a)

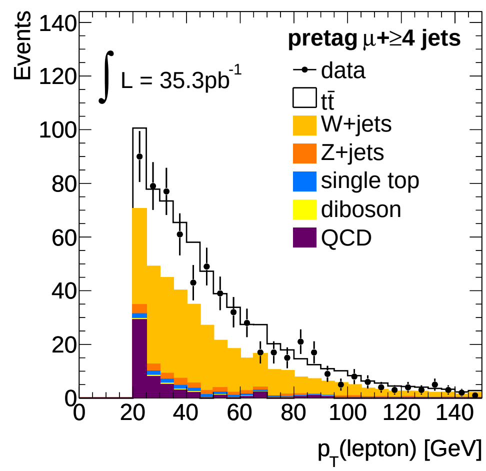


(b)

Figure 6.11: Distribution of $p_T$ of the selected lepton ($e$ or $\mu$) for the events passing all selection criteria in the $e$ + *jets* channel (left) and the $\mu$ + *jets* channel (right)

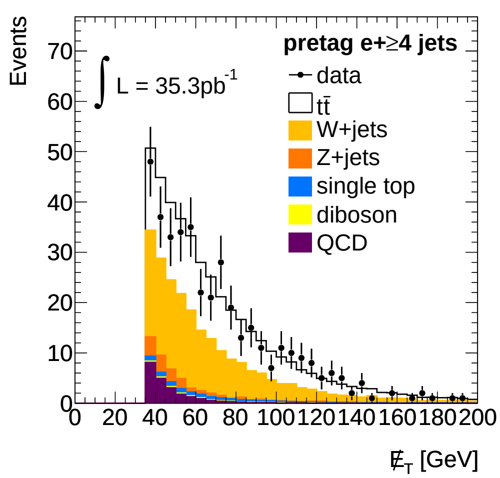


(a)

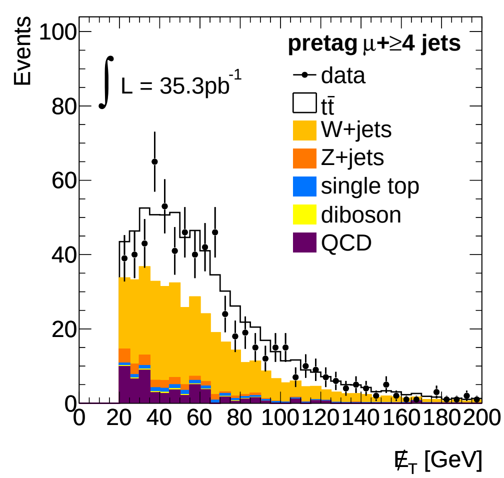


(b)

Figure 6.12: Distribution of $\not\!\!E_T$ for the events passing all selection criteria in the $e$ + *jets* channel (left) and the $\mu$ + *jets* channel (right)

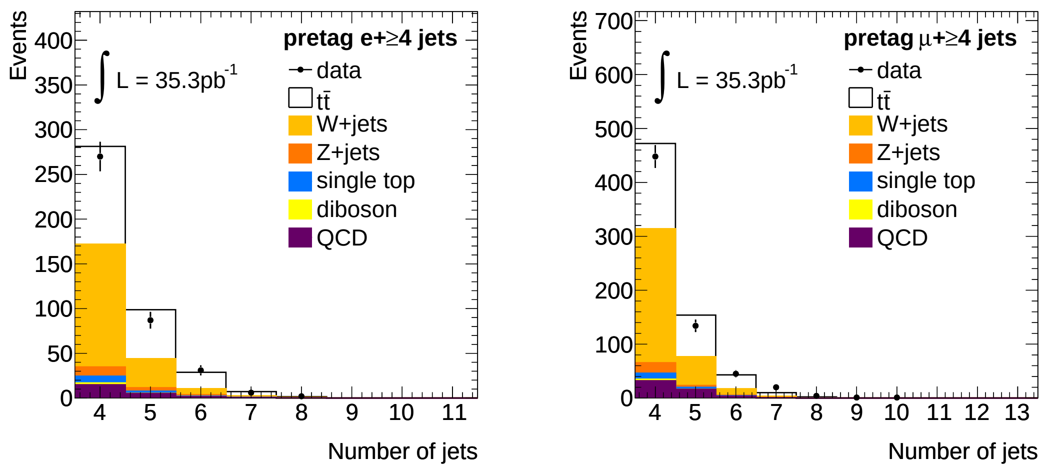


(a) (b)

Figure 6.13: Jet multiplicity (i.e., number of selected jets) distribution for events passing all selection criteria in the $e + jets$ channel (left) and the $\mu + jets$ channel (right)

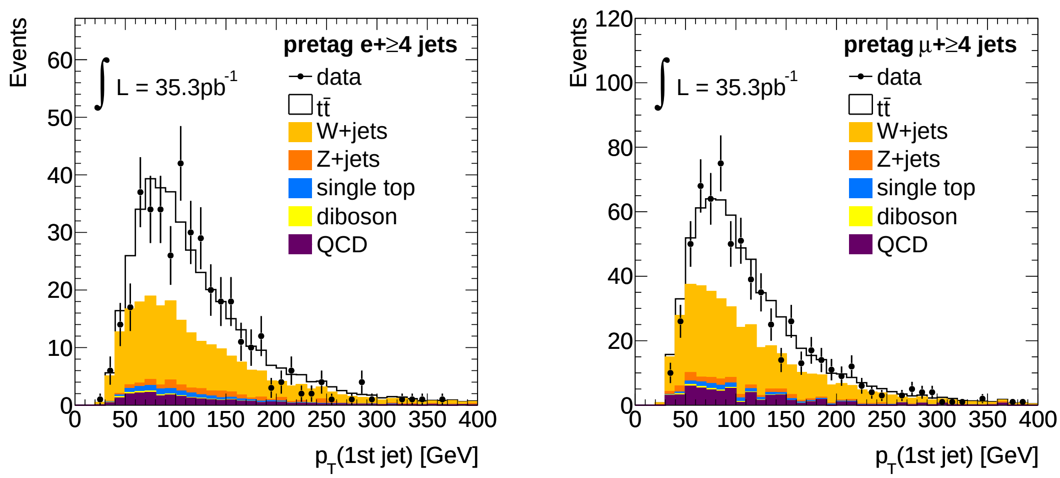


(a) (b)

Figure 6.14: Distribution of $p_T$ of the leading jet for the events passing all selection criteria in the $e + jets$ channel (left) and the muon channel (right)

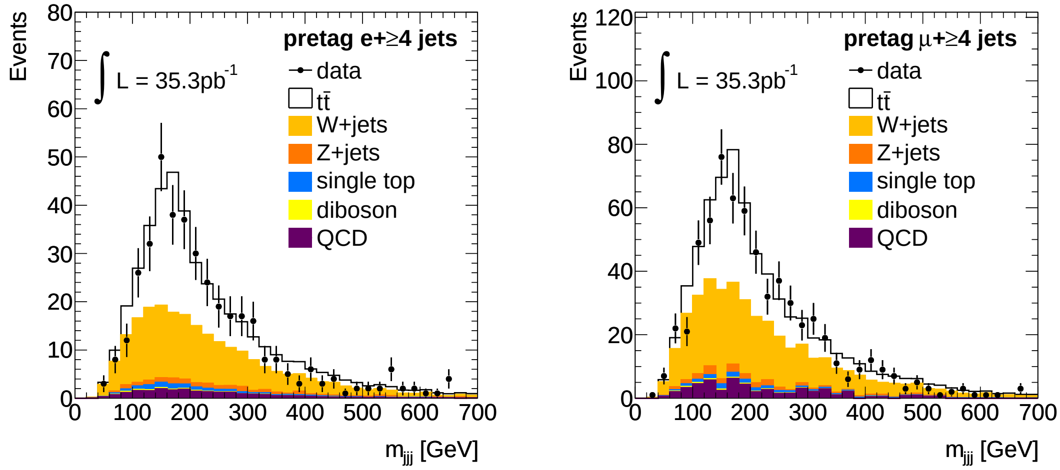


(a) (b)

Figure 6.15: Distribution of the invariant mass of the hadronic top, reconstructed as the three jets with the highest total $p_T$ out of the four leading jets, for the events passing all selection criteria in the $e + jets$ channel (left) and the $\mu + jets$ channel (right)

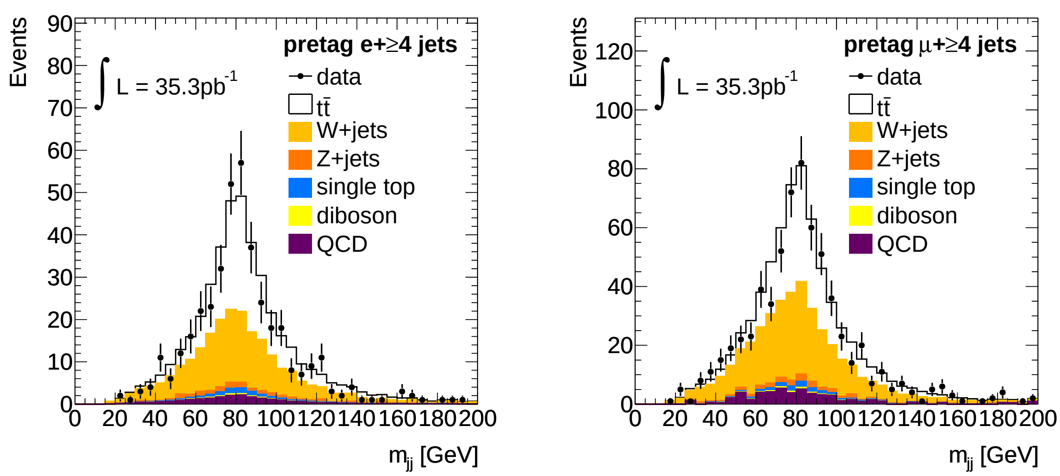


(a) (b)

Figure 6.16: Distribution of the invariant mass of the hadronic $W$, reconstructed as the two jets out of the three jets in hadronic top with mass closest to the PDG $W$ mass, for the events passing all selection criteria in the $e + jets$ channel (left) and the muon channel (right)

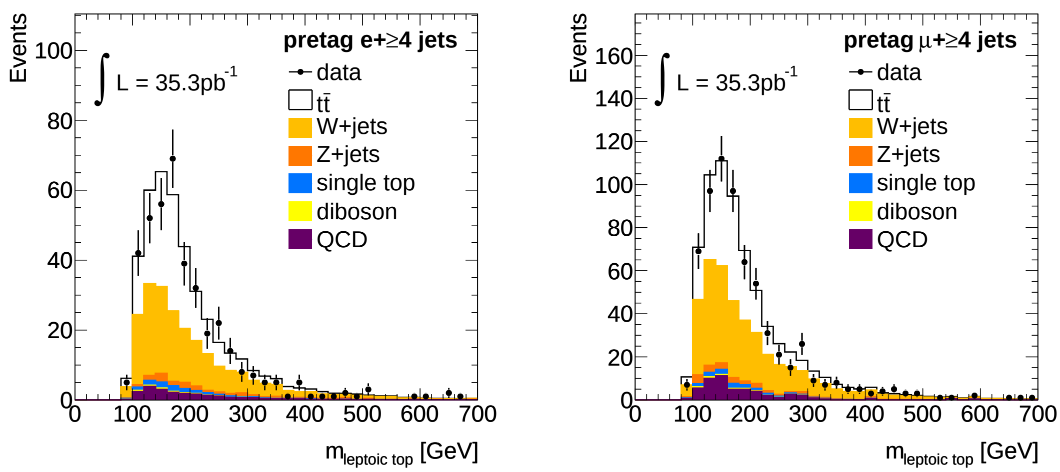


(a) (b)

Figure 6.17: Distribution of the invariant mass of the leptonic top, reconstructed from the lepton, the missing $E_T$, and the jet in the leading four jets which is not part of the hadronic top, for the events passing all selection criteria in the $e+jets$ channel (left) and the $\mu+jets$ channel (right)

# Chapter 7

# Top Likelihood Analysis

After the event selection, the $t\bar{t}$ production cross section can be measured using several different approaches. The first approach is the cut-and-count method, in which the number of background events is subtracted from the number of selected data events [158, 161]. This method is simple but currently it relies on Monte Carlo (MC) for determination of all the backgrounds except QCD. The background contribution from $W+jets$ is not predicted accurately and has a large uncertainty. This translates to a large systematic error on the $t\bar{t}$ cross section measurement.

The $t\bar{t}$ cross section can also be measured using approaches based on the fitting of kinematic variables with different probability distribution functions (pdfs) for signal and background. A maximum likelihood fit to data can be performed using signal and background templates for any such variables to extract the number of $t\bar{t}$ events in data. The number of background events is also extracted directly from the fit. This lessens the dependence on Monte Carlo for determination of background but there is still some Monte Carlo dependence on the shapes of the kinematic variable distributions. Examples of analyses that have used this approach include fitting the hadronic top quark mass and fitting the lepton pseudorapidity [162, 163].

This analysis exploits a multivariate top likelihood approach for the discrimination of the $t\bar{t}$ signal and its backgrounds. Compared to single variable analyses, the sensitivity can be largely improved because several variables are combined to build a likelihood discriminant with high separation power. Variables considered for the likelihood discriminant include lepton charge asymmetry, $b$-tagging SV0 weight, as well as kinematic and topological variables.

## 7.1 Top Likelihood Discriminant

Since the dominant background after selection criteria is $W + jets$ events, a two-class likelihood with $t\bar{t}$ as signal and $W + jets$ as background is adopted. The likelihood discriminant $\mathcal{L}$ has the following general form:

$$\mathcal{L} = \frac{S\,(x_1, x_2, ..., x_N)}{S\,(x_1, x_2, ..., x_N) + B\,(x_1, x_2, ..., x_N)} \tag{7.1}$$

where $x_1, x_2, ..., x_N$ is a set of $N$ input variables. The functions $S\,(x_1, x_2, ..., x_N)$ and $B\,(x_1, x_2, ..., x_N)$ are the pdfs for observing a particular set of values of $(x_1, x_2, ..., x_N)$ in signal and background events respectively. Neglecting the correlations between the input variables, the likelihood discriminant can be approximated by:

$$\mathcal{L} = \frac{\prod_i S_i\,(x_i)}{\prod_i S_i\,(x_i) + \prod_i B_i\,(x_i)} = \frac{\prod_i S_i\,(x_i)\,/B_i\,(x_i)}{\prod_i S_i\,(x_i)\,/B_i\,(x_i) + 1} \tag{7.2}$$

where $i$ goes from 1 to $N$. The functions $S\,(x_i)$ and $B_i\,(x_i)$ are the pdfs of each individual variable $x_i$ for signal and background events respectively. In this analysis, we express the likelihood discriminant as:

$$\mathcal{L} = \frac{exp\left(\sum_i \left(\ln \frac{S_i\,(x_i)}{B_i\,(x_i)}\right)\right)}{exp\left(\sum_i \left(\ln \frac{S_i\,(x_i)}{B_i\,(x_i)}\right)\right) + 1} = \frac{exp\left(\sum_i \left(\ln \frac{S_i\,(x_i)}{B_i\,(x_i)}\right)^{fitted}\right)}{exp\left(\sum_i \left(\ln \frac{S_i\,(x_i)}{B_i\,(x_i)}\right)^{fitted}\right) + 1} \tag{7.3}$$

where $\left(\ln \frac{S_i(x_i)}{B_i(x_i)}\right)^{fitted}$ is a fit to the logarithm of the ratio of the signal and background pdfs for variable $x_i$. It is a function of the variables $x_i$. The fit reduces the influence of individual events on the likelihood output and dilutes the statistical dependence between the training and evaluation of the likelihood.

The word "training" and "evaluation" refer to different steps in building the likelihood discriminant. During the training, the log ratio fits, $\left(\ln \frac{S_i(x_i)}{B_i(x_i)}\right)^{fitted}$, are derived from the signal and background pdfs. During the evaluation, the log ratio fits are used to evaluate the likelihood discriminant for a sample of input events ($t\bar{t}$, $W+jets$, other backgrounds, or data). In order to detect and avoid overtraining (or undertraining), it is convenient to have two independent samples of $t\bar{t}$ and $W+jets$ events. Only one of the two samples is used for training, and then the likelihood is evaluated for both samples separately. A comparison between the likelihood outputs for the two samples can be used for overtraining detection. Another approach to detect overtraining is to study the goodness of the log ratio fits, which doesn't require two independent event samples.

In this analysis, full available MC statistics for $t\bar{t}$ and $W+jets$ are used both for training and for evaluation. The goodness of the log ratio fits are used for overtraining detection and prevention. A sanity check was performed using half events for training and the other half for testing. No significant difference in the likelihood output was observed between the training and testing sample in this set-up, or between this set-up and the set-up used for this analysis.

The input variables we considered include lepton charge asymmetry, $b$-tagging SV0 weight, as well as various kinematic and topological variables. The kinematic and topological variables are transformed using nonlinear functions in order to be less sensitive to statistical fluctuations in rapidly varying regions. For energy related variables the logarithm is usually taken.

The ranges and binning for the pdf histograms of the input variables are chosen so that most bins contain many entries. Data in the tail of a distribution is consolidated including over- and underflow bins and filled into the first and last bins of the histogram. The logarithm of the ratio of the signal and background pdfs is built and fitted with a polynomial. The reduced chi square from the fit is used as a tool for evaluating the goodness of the fit. In principle a reduced chi square of $\approx 1$ indicates a good fit. However, bins with low statistics close to the histogram limits, as well as bins with large statistical fluctuations, could worsen the value of the reduced chi square. In cases like this, the histograms and fitted curve are examined carefully to decide whether the fit is good.

## 7.2 Selection of Discrimination Variables

There are two major theoretical arguments for the discrimination of the $t\bar{t}$ signal and its backgrounds. First, due to the top quark's large mass of $\sim 172\ GeV$, its decay products are highly energetic. In contrast, jets in $W + jets$, $Z + jets$, or QCD events tend to have lower energy due to jet production from QCD bremsstrahlung. Second, because of the top quark's large mass, the $t\bar{t}$ pairs are produced close to the kinematically allowed threshold. This results in an isotropic and central distribution of the decay products, whereas jet production in the $W + jets$, $Z + jets$, and QCD backgrounds tend to peak in the forward direction. This effect is not as prominent at the LHC, where the current center-of-mass energy is 7 $TeV$, as at the Tevatron, where $t\bar{t}$ pairs were produced mostly at threshold due to a lower center-of-mass energy of 1.96 $TeV$. Nevertheless, it still leads to topological differences between the $t\bar{t}$ signal and its backgrounds.

While the theoretical arguments provide guidelines for the discrimination of the $t\bar{t}$ signal and its backgrounds, Monte Carlo studies are performed to examine numerous possible discriminating variables, as well as selecting the best ones out of them. All variables with different pdfs for $t\bar{t}$ and $W + jets$ events have the ability to discriminate between the two. Preselection of variables is using experience and simply looking at the comparison plots by eye. After this step we are left with approximately two dozen possible variables. The number of variables is further reduced by removing variables with least separation power or high correlations. Variables that do not have a good data/MC agreement and variables that do not fit well are removed as well.

The separation $\left\langle \mathcal{S}^2 \right\rangle$ of a discriminating variable has the following general form:

$$\left\langle \mathcal{S}^2 \right\rangle = \frac{1}{2} \int \frac{(S\,(x) - B\,(x))^2}{S\,(x) + B\,(x)} dx \tag{7.4}$$

where $S\,(x)$ and $B\,(x)$ are the signal and background pdfs of variable x, respectively. In this analysis, since the pdfs are binned, $\left\langle \mathcal{S}^2 \right\rangle$ is written in the following form:

$$\left\langle \mathcal{S}^2 \right\rangle = \frac{1}{2} \sum_{bin} \frac{(S_{bin}\,(x) - B_{bin}\,(x))^2}{S_{bin}\,(x) + B_{bin}\,(x)} \tag{7.5}$$

Variables considered for the likelihood discriminant are ranked according to their own separation power as well as their contribution to the separation power of the likelihood discriminant.

The correlation between variable $x_i$ and $x_j$ is evaluated with the correlation coefficient $\rho$, defined by:

$$\rho\left(x_i, x_j\right) = \frac{cov\left(x_i, x_j\right)}{\sigma_{x_i}\sigma_{x_j}} \tag{7.6}$$

where $cov(x_i, x_j)$ is the covariance between variable $x_i$ and $x_j$, $\sigma_{x_i}$ is the standard deviation of variable $x_i$, and $\sigma_{x_j}$ is the standard deviation of variable $x_j$. The correlation coefficient is symmetric in $x_i$ and $x_j$ and lies within the interval $[-1, 1]$. The coefficient $\rho \sim 0$ indicates independent variables, while $\rho \sim \pm 1$ indicates highly correlated or anticorrelated variables. If two of the input variables are found to be highly correlated or anticorrelated with each other, the one with lower separation power is removed.

After removing variables with least separation power or high correlation, there are twelve variables left. The list of variables are given in Table 7.1. The second column in the table gives the polynomial functions used to fit the log ratio histograms. The third column gives the definitions of the variables. Only the leading four jets are considered in the calculation of jet related variables. This choice reduces the dependence on systematic effects from the modelling of the initial and final state radiation (ISR/FSR) as well as the underlying event (UE). Aplanarity ($\mathcal{A}$) and sphericity ($\mathcal{S}$) are calculated from the eigenvalues of the normalized momentum tensor:

$$\mathcal{M}_{\alpha\beta} = \frac{\sum_o p_\alpha^o p_\beta^o}{\sum_o \left|\vec{p^o}\right|^2} \tag{7.7}$$

where $\vec{p^o}$ is the momentum of a reconstructed object with index $o$, and $\alpha, \beta = 1, 2, 3$ refers to the $x$, $y$, and $z$ coordinates. The momentum tensor has three eigenvalues satisfying

$$\lambda_1 \geq \lambda_2 \geq \lambda_3 \text{ and } \lambda_1 + \lambda_2 + \lambda_3 = 1 \tag{7.8}$$

The formulas for calculating the aplanarity and sphericity are included in Table 7.1, as well as the definitions for all the variables.

| Variable name | Fit function | Definition |
|---|---|---|
| $\ln(H_T^3)$ | pol3 | Scalar sum of $p_T$ of jets, excluding the first two leading jets |
| $\ln(H_T^{2\prime})$ | pol2 | Scalar sum of $p_T$ of jets, excluding the leading jet, divided by the scalar sum of $p_z$ of jets, lepton and neutrino |
| $\ln(C)$ | pol2 | Centrality, defined as the scalar sum of $p_T$ of jets divided by the scalar sum of $E$ of jets |
| $\exp(-11\mathcal{A})$ | pol1 | Aplanarity, defined as $(3/2)\,\lambda_3$, calculated with jets and lepton |
| $\ln(\mathcal{S})$ | pol3 | Sphericity, defined as $(3/2)\,(\lambda_2 + \lambda_3)$, calculated with jets and lepton |
| $\ln(K_{T\,min}{}')$ | pol3 | Distance in $\eta$-$\phi$ space between the closest pair of jets, multiplied by $p_T$ of the lowest-$p_T$ jet in the pair, divided by $p_T$ of the leptonic W |
| $\ln(m_{jj_{min}})$ | pol6 | Minimum dijet mass of all jet pairs |
| $\eta_l$ | pol2 | Lepton pseudoraplity |
| $\Delta\eta(l, 1st\ j)$ | pol2 | Distance in $\eta$ between the lepton and the leading jet |
| $\Delta\eta(l, 2nd\ j)$ | pol2 | Distance in $\eta$ between the lepton and the second leading jet |
| lepton charge | pol1 | Charge of the lepton, either 1 or -1 |
| binary $SV0_{max}$ | pol1 | Derived from the $b$-tagging SV0 weight (see Section 4.5.1). = 1 if maximum SV0 in the event larger than 5.85, = 0 otherwise |

Table 7.1: The list of discrimination variables selected for the top likelihood analysis. The table includes the polynomial functions used to fit the log ratio histograms, as well as the definitions of the variables. Only the leading four jets are considered in the calculation of jet related variables. For the calculation of aplanarity and sphericity the two smaller eigenvector $(\lambda_2, \lambda_3)$ of the normalized momentum tensor are used. The momentum tensor is defined in Equation 7.8.

The selected discrimination variables include lepton charge and binary $SV0_{max}$ in addition to kinematic and topological variables. The lepton charge is symmetric for the $t\bar{t}$ signal. In contrast, for the $W + jets$ background there is an asymmetry in the lepton charge distribution. This is because at LHC where $pp$ pairs collide, since there is more up quarks than anti-up quarks in the proton, more $W^{+}$'s are produced than $W^{-}$'s. The $b$-tagging SV0 weight (see Section 4.5.1) is a good discriminating variable because there are two $b$ jets in all $t\bar{t}$ events. We used a binary variable derived from the maximum SV0 weight in the event. It is expected to be not as powerful as the continuous distribution of the SV0 weight. However, currently the SV0 tagger is only calibrated at a single working point at which SV0= 5.85, as was discussed in Section 4.5.2. Using the binary variable allows us to estimate the systematic error from the uncertainties in the $b$-tagging calibration.

The pdfs of the selected variables are shown in Figure 7.1 for the $e + jets$ channel and Figure 7.2 for the $\mu$ + $jets$ channel. The plots in the figures shows the pdfs for both the $t\bar{t}$ signal and the $W$ + $jets$ background. The matrix of the correlation coefficients of the variables are shown in Figure 7.3 for the $e$ + $jets$ channel and Figure 7.4 for the $\mu$ + $jets$ channel. Even though several of these variables are correlated with each other, including these variables in the likelihood discriminant does improve the separation power of the discriminant. Also, in theory they could have different contributions to the systematic error. As a result, these variables are kept until the next stage of optimzation.

Figure 7.5 and Figure 7.6 shows the fit to the logarithm of the ratio of the signal and background pdfs for the $e$ + $jets$ channel and $\mu$ + $jets$ channel respectively. The fitted functions are included as well as the distributions. For both channels the same set of polynomials are used. Note that instead of performing a fit to the lepton charge and the binary $SV0_{max}$, we simply take the ratio between the entris for each of the two bins. The reduced chi square ($\chi^2$/ndf) is shown on each plot as a test of the goodness of the fit. Most of the fits have a reduced chi square between approximately one to two. The fit of the variable $m_{jj_{min}}$ in $\mu$ + $jets$ returns a reduced chi square of $\sim 4$. Deviations away from a value of one can be attributed to bins with low statistics at the histogram limits, or bins with large statistical fluctuations.

The likelihood discriminants built from all twelve selected input variables are shown

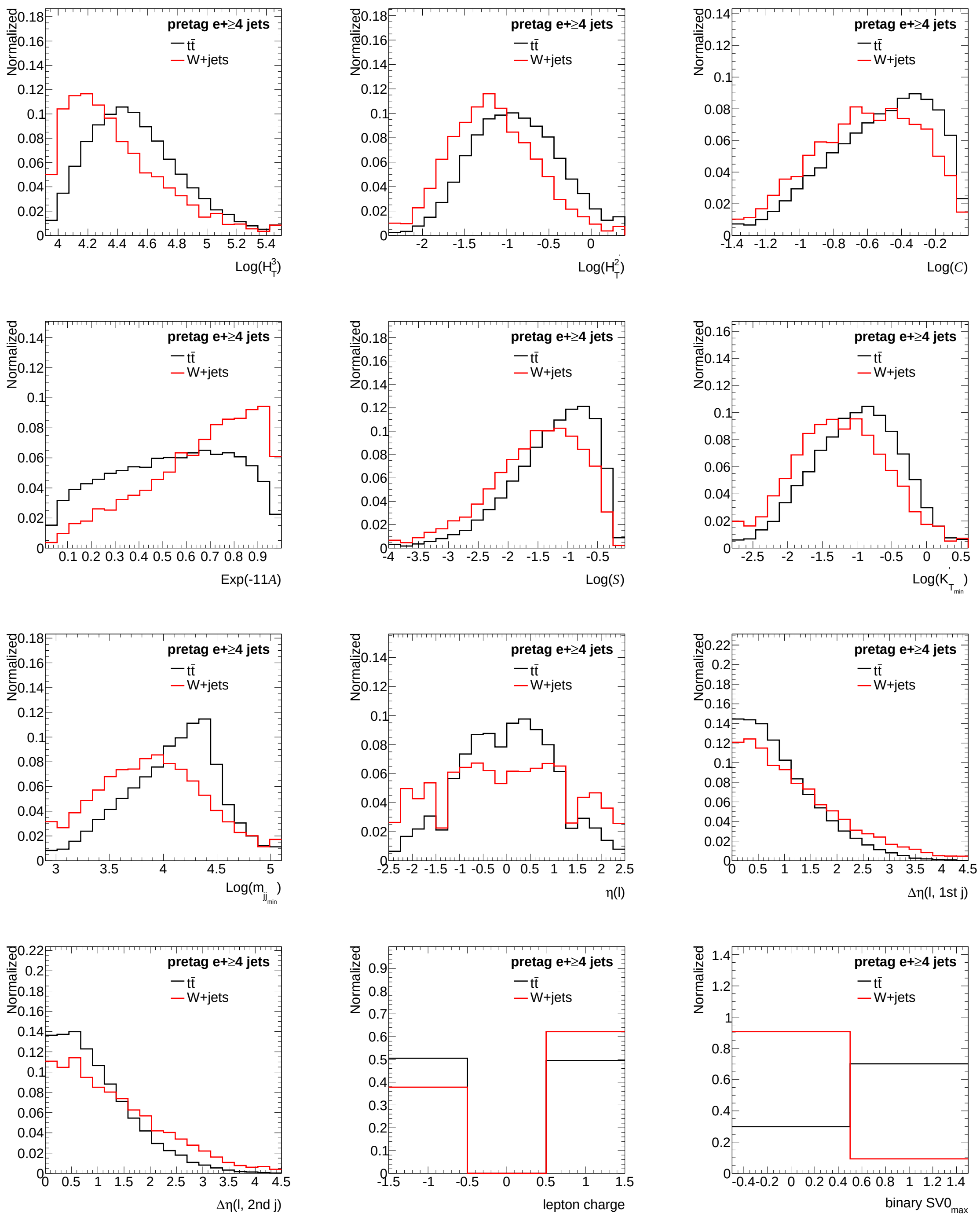


Figure 7.1: Probability density function of the selected input variables to the top likelihood analysis, in the $e + jets$ channel. All variables have been transformed according to the expressions in Table 7.1

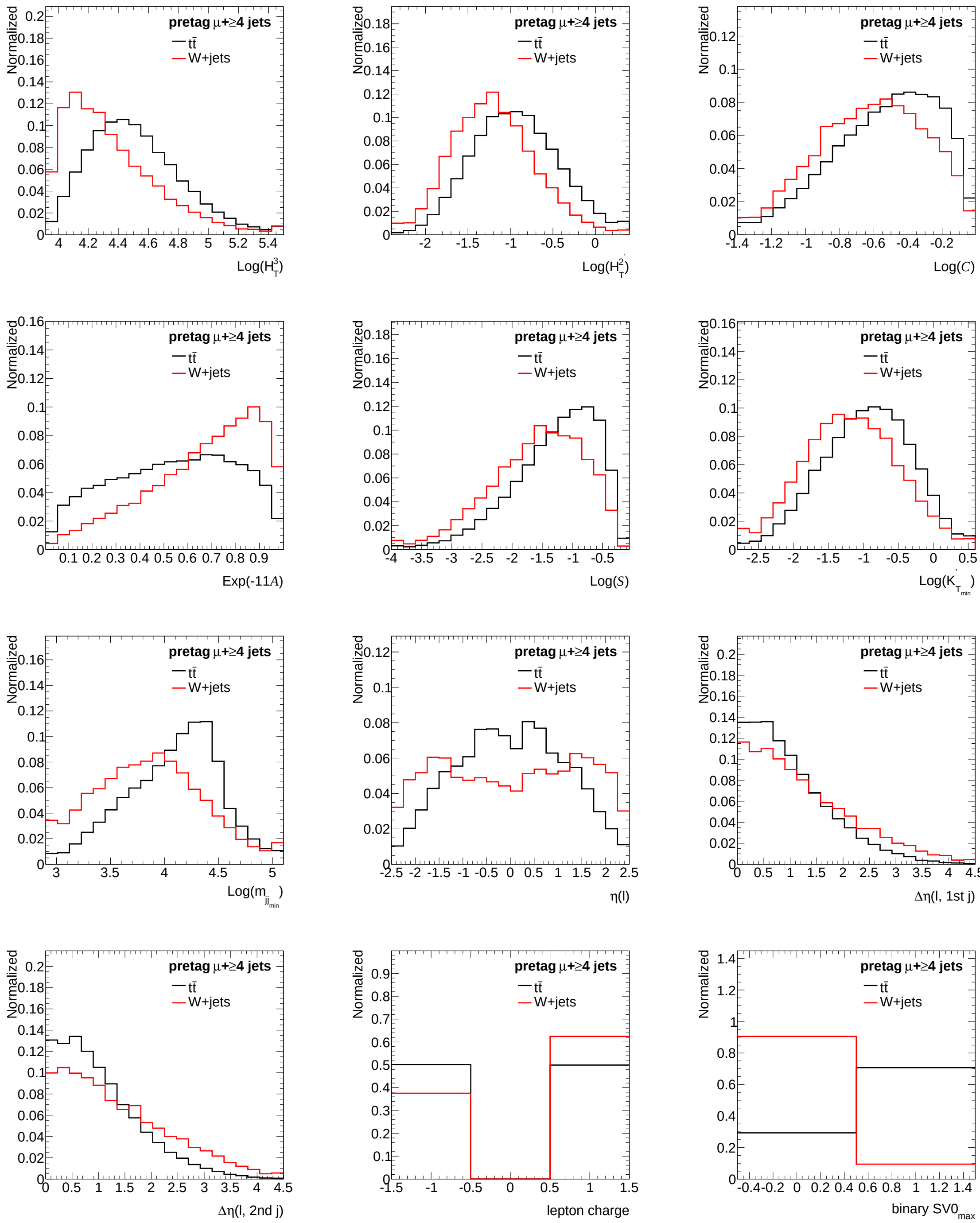

Figure 7.2: Probability density function of the selected input variables to the top likelihood analysis, in the $\mu + jets$ channel. All variables have been transformed according to the expressions in Table 7.1

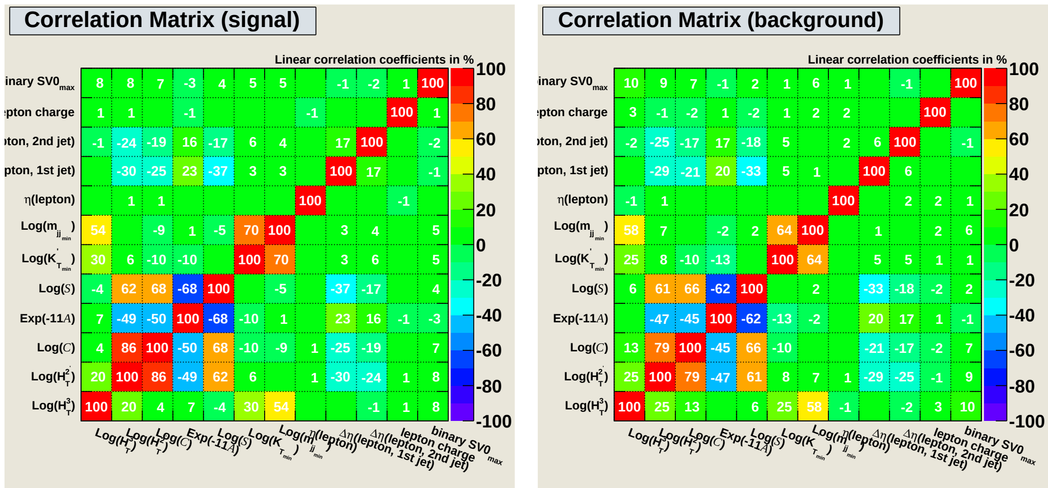


(a) (b)

Figure 7.3: Correlation matrix of the selected input variables to the top likelihood analysis in the $e + jets$ channel. Left: signal, right: background

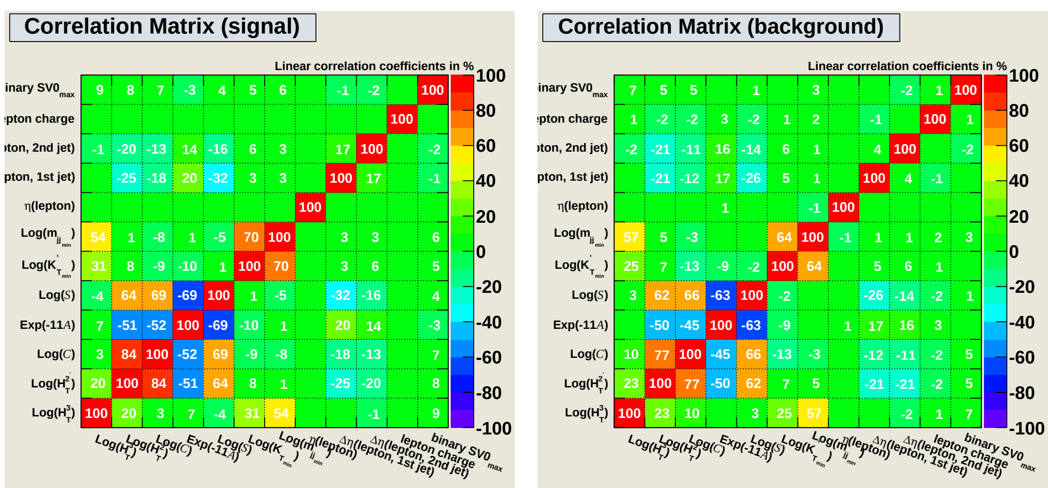


(a) (b)

Figure 7.4: Correlation matrix of the selected input variables to the top likelihood analysis in the $\mu + jets$ channel. Left: signal, right: background

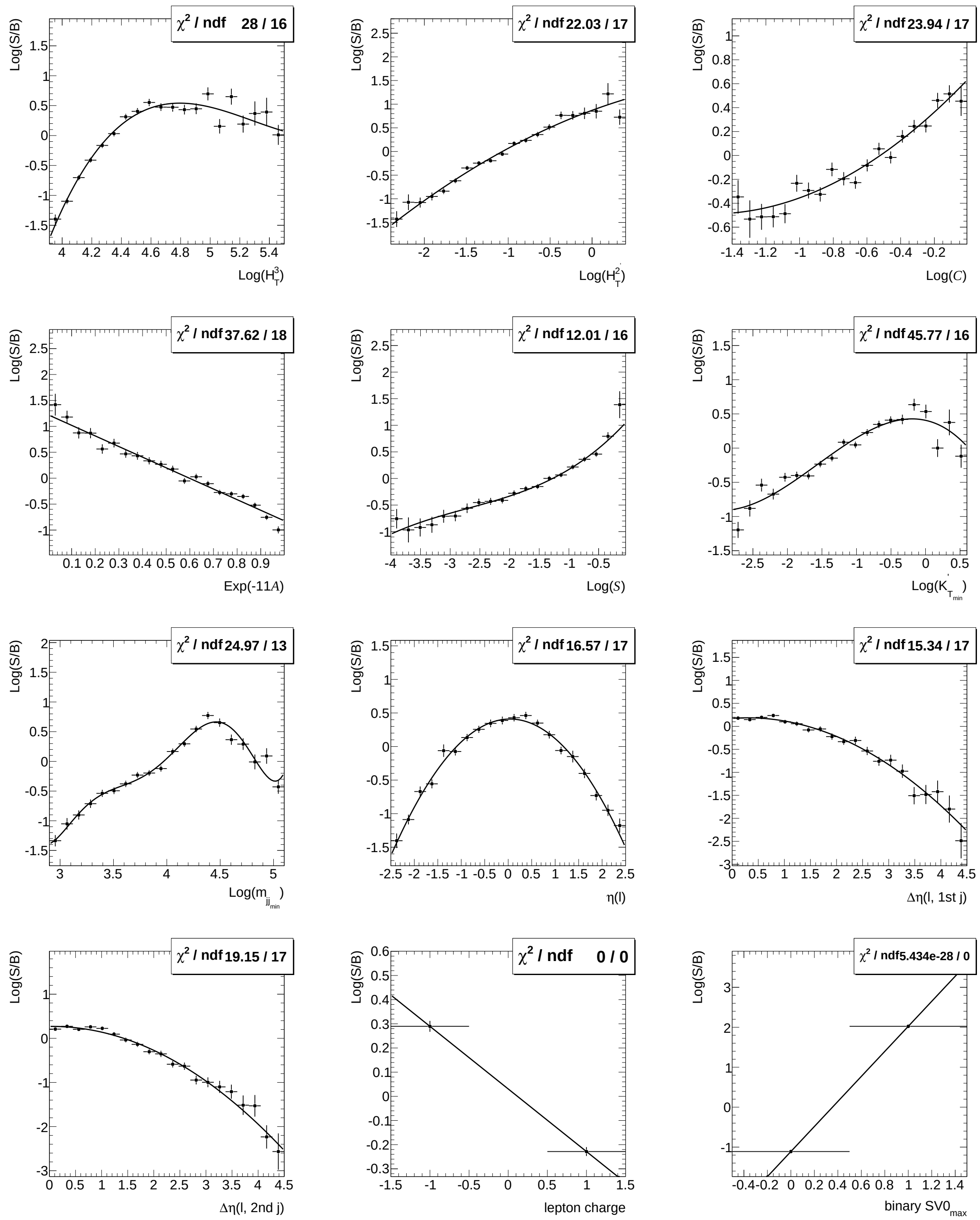


Figure 7.5: Fit of the log ratio histograms of the selected input variables to the top likelihood analysis, in the $e + jets$ channel. The polynomial functions used for the fit are listed in Table 7.1

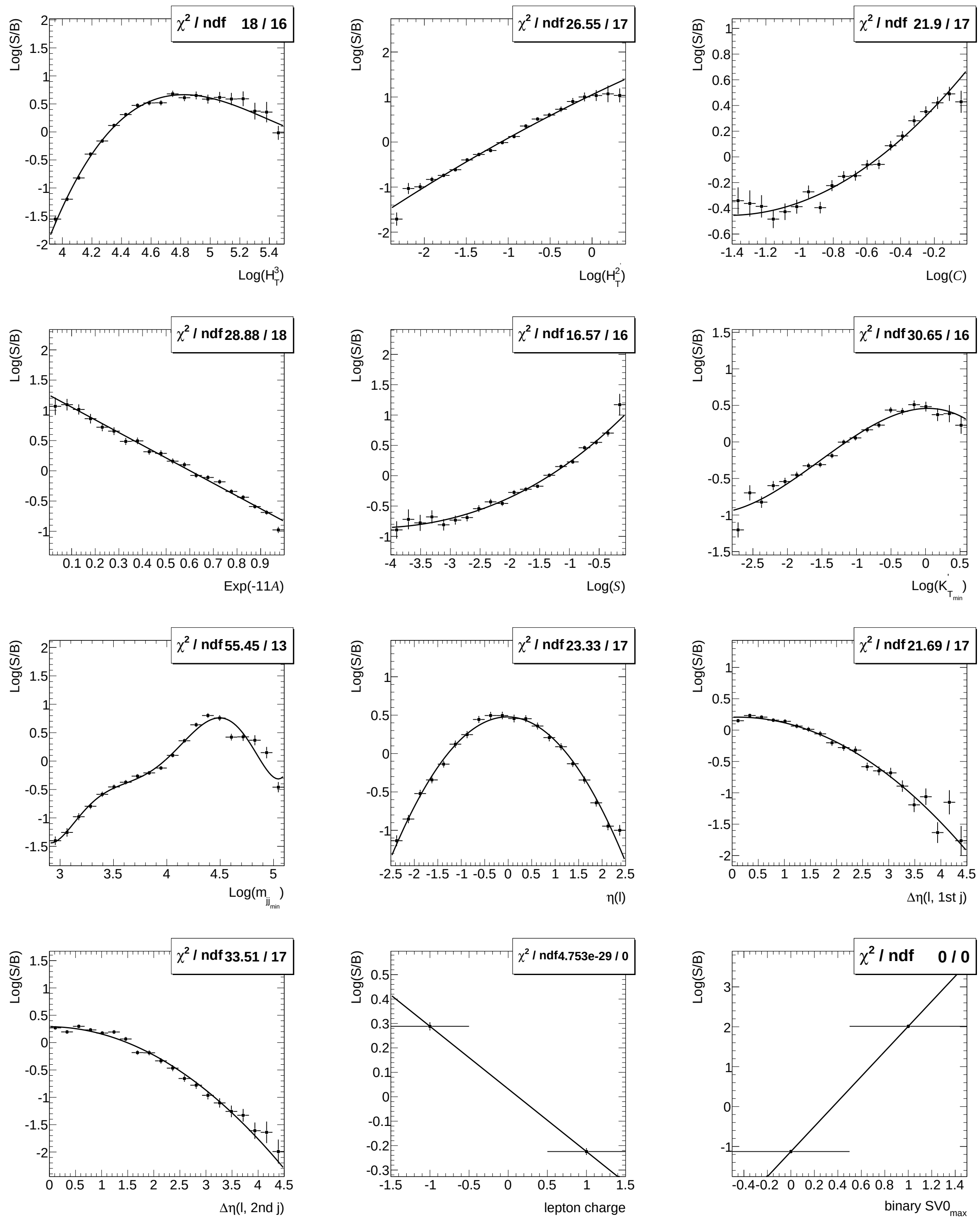


Figure 7.6: Fit of the log ratio histograms of the selected input variables to the top likelihood analysis, in the $\mu + jets$ channel. The polynomial functions used for the fit are listed in Table 7.1

in Figure 7.7 for the $e + jets$ channel and the $\mu + jets$ channel. A very good separation is observed between signal and background, with the $t\bar{t}$ signal peaking sharply at one and the $W + jets$ background peaking sharply at zero.

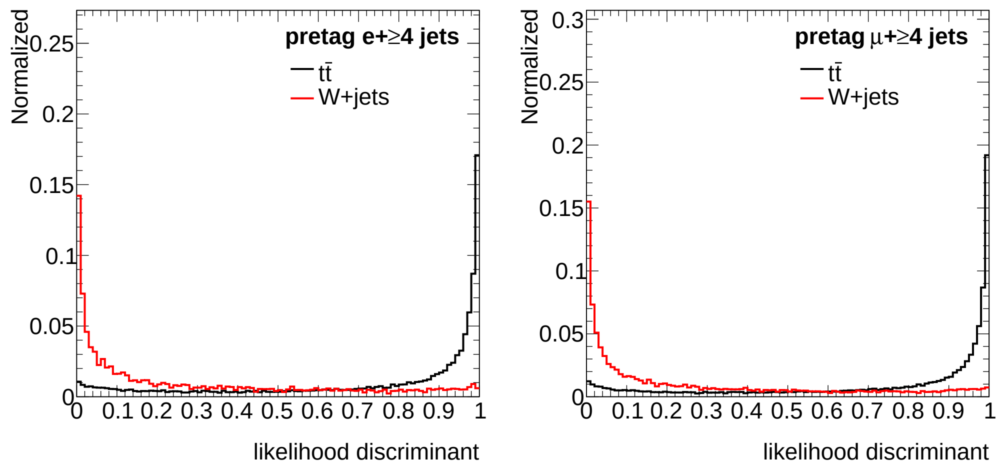


(a) (b)

Figure 7.7: Distribution of the likelihood discriminant built from all twelve selected input variables in the $e + jets$ channel (left) and the muon channel (right)

In order to test if the MC models the data reliably, data and MC comparison plots are made for the input variables and the likelihood discriminant, using the expected event yields given in Table 6.15. These plots are shown from Figure 7.8 to Figure 7.10. A Kolmogorov-Smirnov (KS) test is used to test the agreement between data and Monte Carlo for each input variable as well as the likelihood discriminant. A very small KS statistic, say < 5%, indicates a significant difference between data and MC. For all comparisons, the KS variable is sufficiently large as to merit agreement between data and MC.

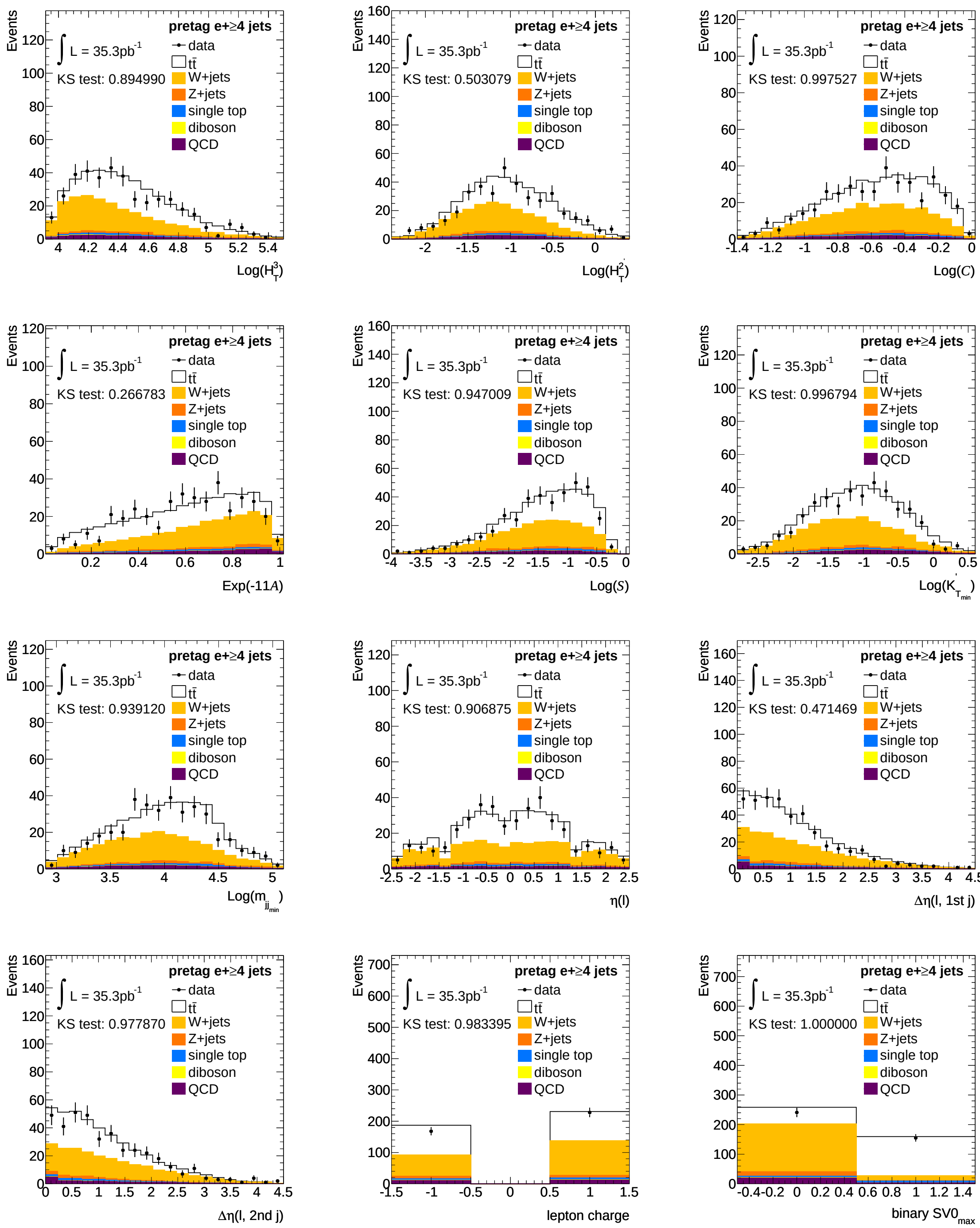


Figure 7.8: Data/MC comparison for the selected input variables to the top likelihood analysis in the $e + jets$ channel

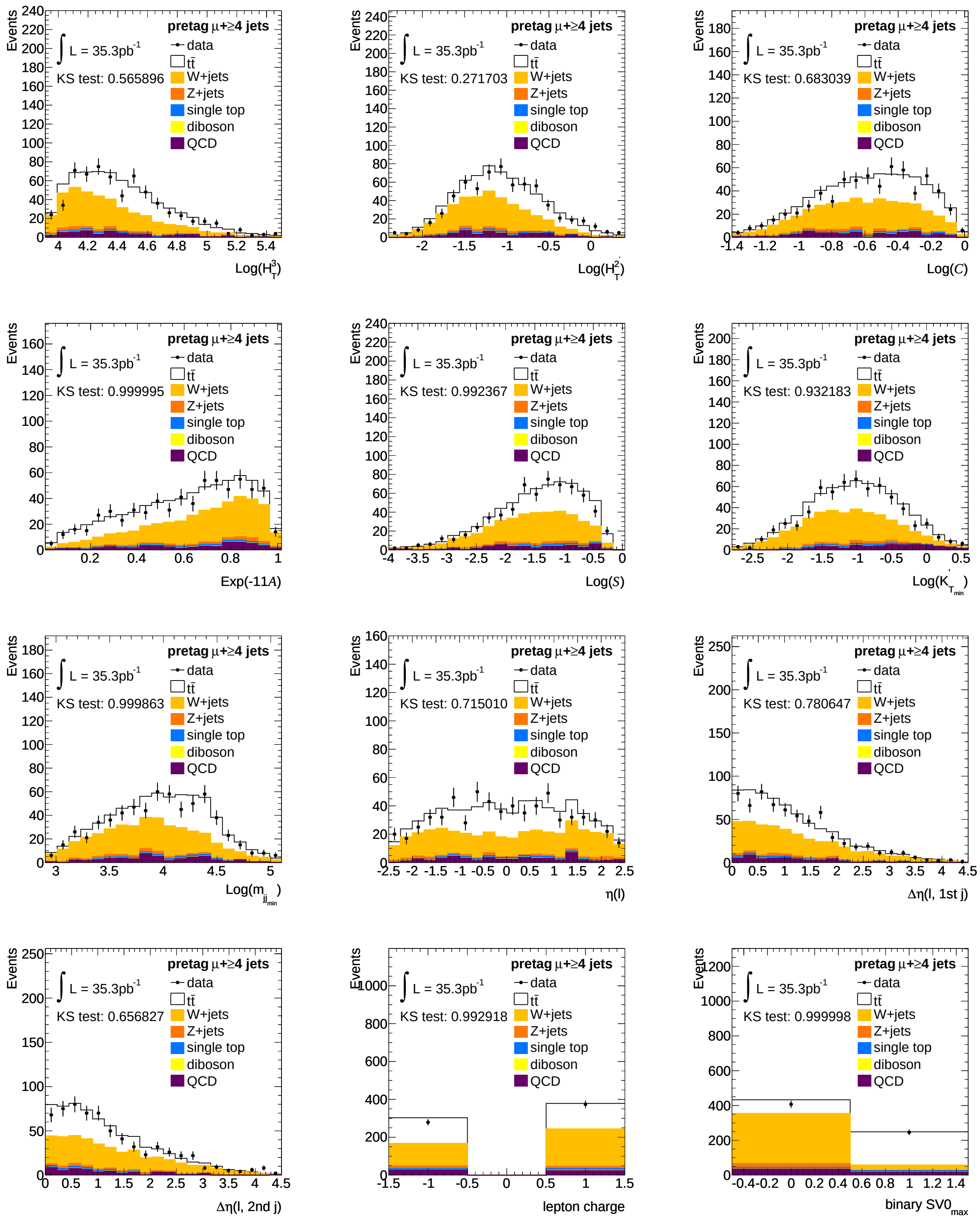


Figure 7.9: Data/MC comparison for the selected input variables to the top likelihood analysis in the $\mu + jets$ channel

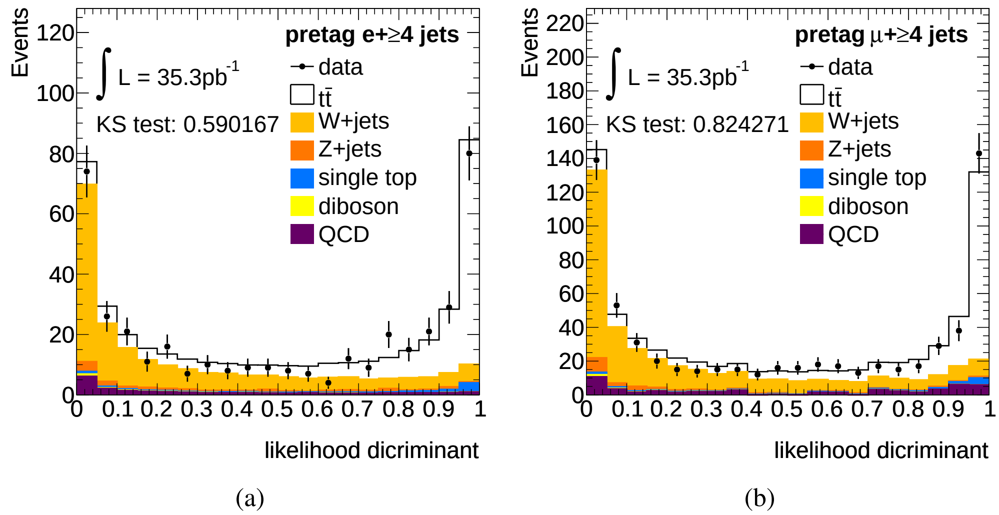


Figure 7.10: Data/MC comparison for the likelihood discriminant built from all twelve selected input variables in the $e + jets$ channel (left) and the $\mu + jets$ channel (right)

### 7.3 Optimization of the Likelihood Discriminant

The discrimination variables selected in last section are next optimized to determine the combination of variables for the final likelihood discriminant. The likelihood discriminant is optimized separately for the $e + jets$ and $\mu + jets$ channel. The optimization involves the full analysis procedure described in Chapter 8 and 9. Of particular relevance are the ensemble test procedure described in Section 8.3 and the estimation of systematic errors described in Section 9.2. One may want to read those sections first and then return to this section.

The goal of the optimization is to find the combination of variables which gives the lowest combined statistical and systematic error on the $t\bar{t}$ cross section measurement. In addition, it is desired to use a relatively small number of variables to keep the analysis simple. The expected total error ($\sigma_{tot}$) is estimated by adding the systematic errors related to Jet Energy Scale (JES) ($\sigma_{JES}$) and ISR/FSR modelling ($\sigma_{ISR/FSR}$) in quadrature to the statistical error ($\sigma_{stat}$):

$$\sigma_{tot} = \sqrt{\sigma^2_{stat} + \sigma^2_{JES} + \sigma^2_{ISR/FSR}} \tag{7.9}$$

The JES and ISR/FSR are among the largest sources of systematic uncertainties in this analysis. They are also expected to show significant variation depending on the combination of variables. For example, one would expect reduced JES and ISR/FSR systematic error using variables such as lepton $\eta$ and SV0 weight. As such, the JES and ISR/FSR are chosen among the many sources of systematic uncertainties for use in the optimization.

The expected total error $\sigma_{tot}$ is calculated for the $2^{12} - 1 = 4095$ possible likelihood discriminants built from all possible combinations of the selected 12 variables. This is achieved through running ensemble tests using 1000 mock datasets for each of the 4095 combinations of variables. The average number of $t\bar{t}$ events ($N_{t\bar{t}}$) in the mock datasets is taken from the expected value listed in Table 6.15. The number of QCD events ($N_{QCD}$) is taken from the table as well. Then the number of $W + jets$ events ($N_W$) is calculated using:

$$N_W = N^{obs} - N_{t\bar{t}} - N_{QCD} \tag{7.10}$$

where $N^{obs}$ is the observed number of data events minus the single top contribution (see Section 8.2 and 8.3). The number of $t\bar{t}$, $W$, and QCD events are subsequently Poisson fluctuated according to these means.

The likelihood discriminant is evaluated for nominal and JES and ISR/FSR shifted samples for each of the 4095 combinations of variables. Mock datasets are drawn from the nominal discriminant distribution, and the discriminant distribution in each mock dataset is fitted using both nominal and shifted templates. The statistical error is estimated by the width of the fitted $N_{t\bar{t}}$ distribution in the nominal analysis. The systematic errors are estimated by the change of the average fitted $N_{t\bar{t}}$ with respect to the nominal analysis. Then the expected total error $\sigma_{tot}$ is calculated by summing in quadrature the separate statistical and systematic errors. Note that both JES and ISR/FSR systematic error estimated this way can be asymmetric. As a result, the total error $\sigma_{tot}$ can also be asymmetric. The optimization thus takes the difference of the positive and negative total error divided by two as its figure of merit (FOM).

Figure 7.11 shows the total expected error as a function of the likelihood index, and as a function of the total number of variables used in the likelihood discriminant, in the

$e+jets$ and the $\mu+jets$ channel. In the total error versus likelihood index plots, we observe that the combinations with the $b$-tagging variable (the left half of the plot) have a much smaller total error than the combinations without the $b$-tagging variable (the right half of the plot). This can also be seen in the plots of total error versus number of variables. The top band in the plots corresponds to the combinations without the $b$-tagging variable, and the bottom band corresponds to the combinations with this variable. In addition, the plot shows that there is not much to gain using more than four variables, since the best combination of four variables, with or without the $b$-tagging variable, already gives compatible total error with likelihood built with more variables.

Table 7.2 lists the best five combinations of variables found by the optimization procedure, separately for the $e + jets$ and the $\mu + jets$ channel. For convenience, the best combination in the $\mu + jets$ channel are chosen to build the final likelihood discriminant in both channels. Four variables are used: $\ln(C)$, $\exp(-11\mathcal{A})$, $\eta_l$, and binary $\mathrm{SV0}_{max}$. We have checked that this set of variables, used in the $e + jets$ channel, gives a expected total error close to the best likelihoods found by the optimization. The likelihood discriminant built from this combination of variables also has a nicer distribution than those listed in the table for the $e + jets$ channel. This is because it only uses one discrete variable, the binary $\mathrm{SV0}_{max}$, while the combinations listed in the table all use both the binary $\mathrm{SV0}_{max}$ and the lepton charge.

Figure 7.12(a) and 7.12(b) show the likelihood discriminant built from the chosen four variables. The separation is not as good as the likelihood discriminant using all 12 selected variables, as was shown in Figure 7.7. However, signal and background separation is still good, with signal peaking at one and background peaking around zero. The data/MC comparison plots for this discriminant is shown in Figure 7.13.

The systematic error due to uncertainties in the $b$-tagging calibration was not considered in the optimization procedure. This is because it only affects the binary $\mathrm{SV0}_{max}$ varible. As will be shown in Section 9.2, this error is one of the largest systematic error on the $t\bar{t}$ cross section measurement in this analysis. We have chosen to use this variable, despite of the large systematic error associated with it. This is because of its significant signal and background separation power. As shown in in Figure 7.12(c) and 7.12(d),

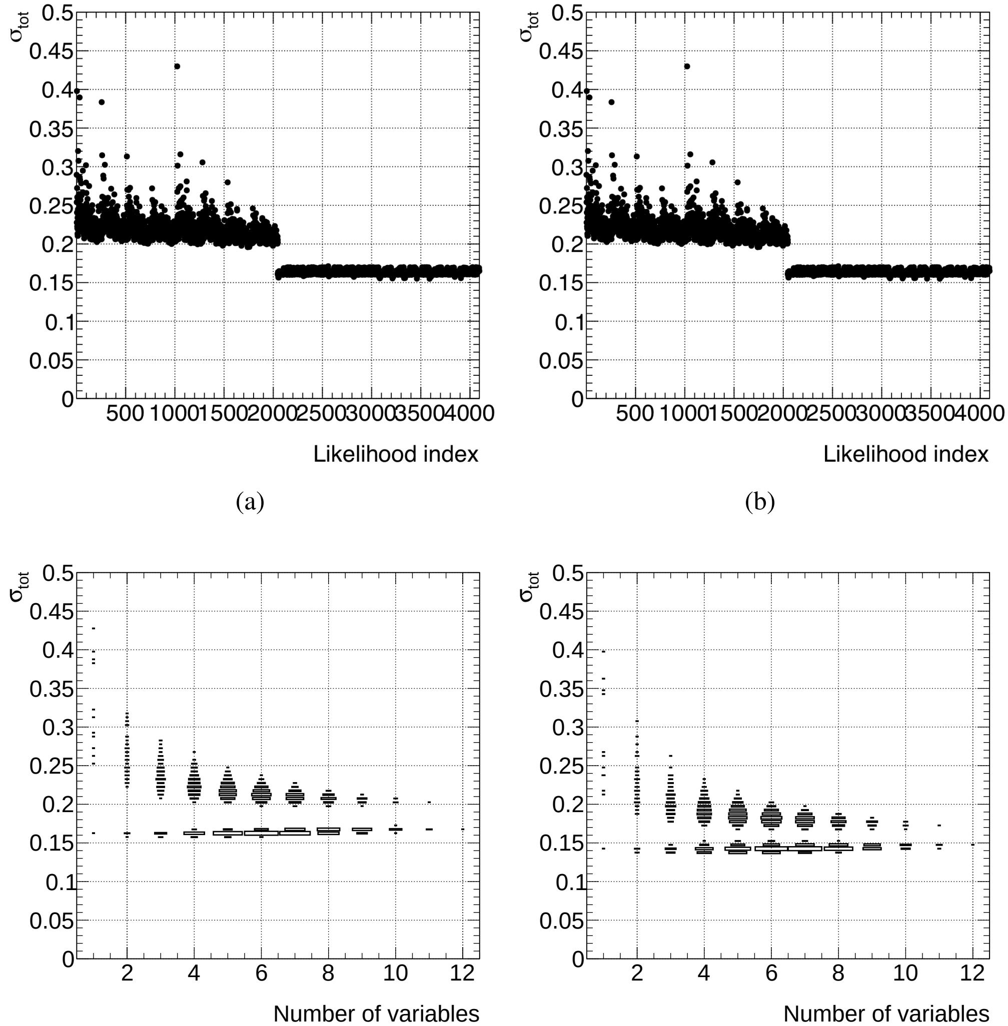


(a) (b)

(c) (d)

Figure 7.11: Top: total expected error ($\sigma_{tot}$) versus likelihood index in the $e+jets$ channel (left) and the $\mu + jets$ channel (right). Bottom: total expected error ($\sigma_{tot}$) versus number of variables used in each likelihood discriminant in the $e + jets$ channel and the $\mu + jets$ channel.

| FOM | Variables | $\sigma_{stat}$ [%] | $\sigma_{JES}$ [%] | $\sigma_{ISR/FSR}$ [%] | $\sigma_{tot}$ [%] |
|---|---|---|---|---|---|
| | $e + jets$ channel | | | | |
| 0.158592 | ln($C$), $\Delta\eta(l, 1st\ j)$, lepton charge, binary SV0$_{max}$ | ±9.9 | +7.4-7.7 | +4.6-13.7 | +13.1-18.6 |
| 0.158734 | ln($C$), $\Delta\eta(l, 1st\ j)$, lepton charge, binary SV0$_{max}$ | ±9.9 | +7.4-7.5 | +4.6-13.8 | +13.2-18.6 |
| 0.158853 | ln($C$), $\Delta\eta(l, 1st\ j)$, $\Delta\eta(l, 2nd\ j)$, lepton charge, binary SV0$_{max}$ | ±9.8 | +7.5-7.6 | +4.7-13.7 | +13.3-18.5 |
| 0.158921 | ln($H_T^{2\prime}$), lepton charge, binary SV0$_{max}$ | ±9.9 | +7.3-7.8 | +4.8-13.7 | +13.2-18.6 |
| 0.159006 | ln($C$), ln$\mathcal{S}$, $\Delta\eta(l, 2nd\ j)$, lepton charge, binary SV0$_{max}$ | ±9.9 | +7.3-7.6 | +4.8-13.7 | +13.2-18.6 |
| | $\mu + jets$ channel | | | | |
| 0.136195 | ln($C$), exp($-11\mathcal{A}$), $\eta_l$, binary SV0$_{max}$ | ±8.4 | +6.3-6.5 | +3.2-12.3 | +11.0-16.3 |
| 0.136261 | ln($C$), exp($-11\mathcal{A}$), $\eta_l$, lepton charge, binary SV0$_{max}$ | ±8.4 | +7.6-7.9 | +2.8-12.4 | +10.9-16.3 |
| 0.136681 | ln($H_T^{2\prime}$), ln($C$), exp($-11\mathcal{A}$), $\Delta\eta(l, 2nd\ j)$, lepton charge, binary SV0$_{max}$ | ±8.6 | +6.0-6.6 | +2.5-12.4 | +10.8-16.5 |
| 0.136827 | ln($C$), exp($-11\mathcal{A}$), $\eta_l$, $\Delta\eta(l, 2nd\ j)$, binary SV0$_{max}$ | ±8.4 | +6.5-6.3 | +3.2-12.4 | +11.0-16.3 |
| 0.136872 | ln($H_T^{2\prime}$), ln($C$), exp($-11\mathcal{A}$), $\Delta\eta(l, 2nd\ j)$, binary SV0$_{max}$ | ±8.7 | +6.0-6.6 | +2.7-12.4 | +10.9-16.5 |

Table 7.2: The five best likelihood discriminants found by the optimization procedure in the $e + jets$ channel and the $\mu + jets$ channel, ordered by the figure of merit (FOM). The expected total error, as well as separate statistical and systematic errors are shown for each discriminant

removal of the binary SV0$_{max}$ variable decreases the separation power of the likelihood significantly. Including the variable in the likelihood discriminant also suppresses other systematic errors such as from JES and ISR/FSR, because this variable is independent of these uncertainties.

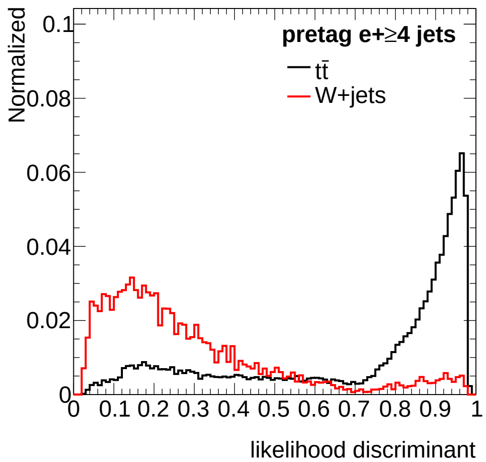


(a)

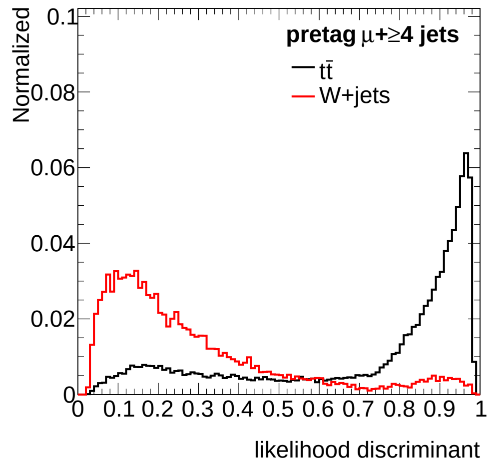


(b)

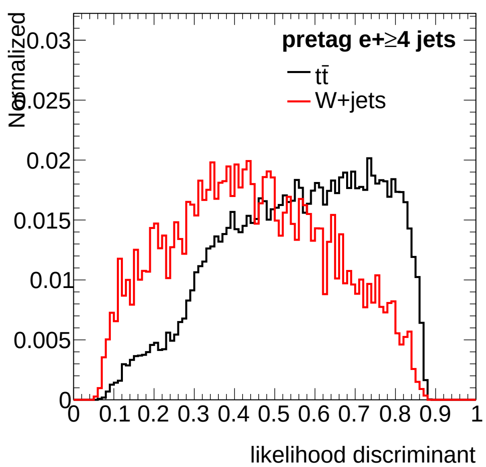


(c)

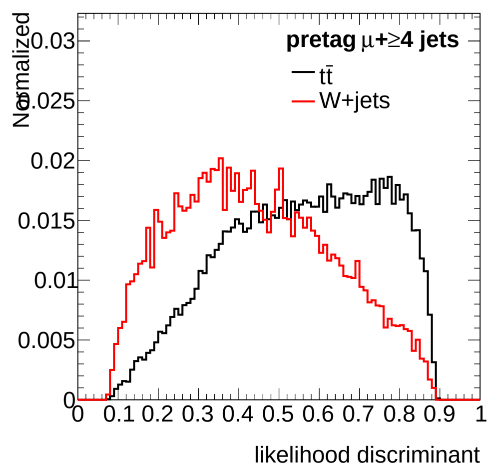


(d)

Figure 7.12: Top: Distribution of the likelihood discriminant built from chosen set of four variables: $\ln(C)$, $\exp(-11\mathcal{A})$, $\eta_l$, and binary $\mathrm{SV0}_{max}$, in the $e + jets$ channel (left) and the $\mu + jets$ channel (right). Bottom: the likelihood discriminant built with the variable binary $SV0_{max}$ removed from the chosen set of four variables

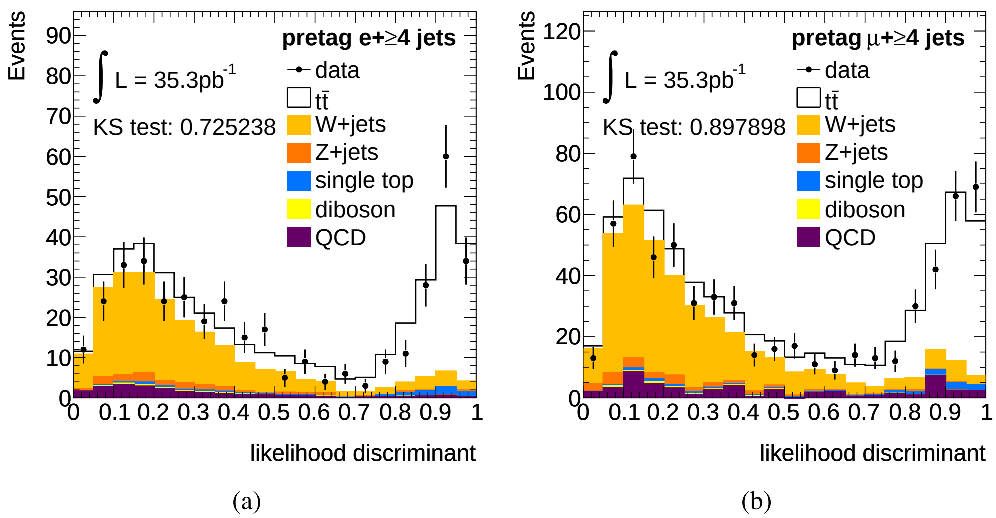


Figure 7.13: Data/MC comparison of the likelihood discriminant built from the optimized set of four variables: $\ln(C)$, $\exp(-11\mathcal{A})$, $\eta_l$, and binary $SV0_{max}$, in the $e + jets$ channel (left) and the $\mu + jets$ channel (right)

# Chapter 8

# Signal Determination

In order to measure the $t\bar{t}$ production cross section, it is necessary to measure or extract $N_{t\bar{t}}$, the number of $t\bar{t}$ events in the data sample passing the event selection (see Equation 1.2). This is achieved by performing a maximum likelihood (ML) fit to the distribution of the likelihood discriminant in data, using the likelihood discriminant templates for the $t\bar{t}$ signal, the $W + jets$ background, and the QCD background. The $t\bar{t}$ and $W + jets$ likelihood templates are built from Monte Carlo (MC) samples passing the selection, with data/MC corrections applied. The QCD background, on the other hand, can not be modelled reliably by MC. Therefore, its likelihood template is provided by data driven methods. Also provided by the data driven methods is the number of QCD events, or the QCD normalization, in the selected data sample. This results is subsequently used in the ML fit itself, appearing as an additional constraint.

In this chapter the procedure for determining the number of selected $t\bar{t}$ events, $N_{t\bar{t}}$, in data is described. Section 8.1 describes the data driven methods used for QCD background evaluation in the $t\bar{t} \to e + jets$ and the $t\bar{t} \to \mu + jets$ channel. Section 8.2 describes the maximum likelihood fit and applies it to data in order to determine the number of selected $t\bar{t}$ events. Different constraints are applied on the QCD normalization in the $e + jets$ and $\mu + jets$ channel depending on the data driven method used in the channel. Section 8.3 describes the validation of this method through the use of ensemble tests. It also describes how ensemble tests can be used to estimate various systematic errors. This procedure is used in Chapter 9 of this dissertation for evaluation of the systematics, as well as in Chapter 7 for optimization of the likelihood discriminant.

## 8.1 Evaluation of the QCD Background

There are two complementary methods for estimating the QCD background in the $t\bar{t} \to l + jets$ channels, the matrix method (MM) and the template fit method. Both types of methods can provide measurement of the QCD normalization and modelling of the QCD shape. For this analysis the QCD background in the $\mu + jets$ channel is evaluated using the matrix method method, while in the $e + jets$ channel it is measured using the template fit method based on the anti-electron modelling of the QCD [164].

### 8.1.1 The Matrix Method

The matrix method is used to estimate the QCD background in the $\mu + jets$ decay sample. It exploits the difference in lepton identification (Id) efficiency between isolated leptons from $W$ or $Z$ decays and non-isolated leptons from heavy flavor decays. Two data samples are used to estimate the number of QCD events: a sample with loose lepton selection (isolation) criteria and a sample with tight lepton selection criteria. In particular, the loose sample in the $\mu + jets$ channel is obtained by dropping the calorimetric and track isolation requirements ($etcone30 < 4\ GeV$ and $ptcone30 < 4\ GeV$) in the standard muon Id cuts in Table 6.2.

The number of events in the loose sample ($N^l$) and the number of events in the tight sample ($N^t$) can be expressed as a linear combination of the number of signal events with a real lepton ($N^t_{sig}$) and the number of QCD events ($N^t_{QCD}$) in the tight sample:

$$\begin{aligned} N^l &= \frac{1}{\epsilon_{sig}} N^t_{sig} + \frac{1}{\epsilon_{QCD}} N^t_{QCD} \\ N^t &= N^t_{sig} + N^t_{QCD} \end{aligned} \tag{8.1}$$

where $\epsilon_{sig}$ and $\epsilon_{QCD}$ are the efficiencies of the loose to tight selection cuts, for the signal and the QCD background respectively. Note by signal here we mean any real isolated muon regardless of its physics source. By solving the above equation, we obtain the number of signal and QCD events in the signal data sample in terms of $N^l$, $N^t$, and the efficiencies:

$$
\begin{aligned}
N^t_{sig} &= \frac{\epsilon_{sig}}{\epsilon_{sig} - \epsilon_{QCD}} \left(N_{tight} - \epsilon_{sig} N^l\right) \\
N^t_{QCD} &= \frac{\epsilon_{QCD}}{\epsilon_{sig} - \epsilon_{QCD}} \left(\epsilon_{sig} N^l - N^t\right)
\end{aligned}
\tag{8.2}
$$

The signal efficiency $\epsilon_{sig}$ in the $\mu + jets$ channel is measured using tag-and-probe method with a sample of $Z \rightarrow \mu\mu$ events. The QCD fake rate $\epsilon_{QCD}$ is estimated by measuring the tight/loose ratio in a control region and extrapolated for application in the signal region. The control region is defined so that it is rich in QCD events and orthogonal to the selected analysis sample. Two control regions are used, both requiring exactly one muon, no electron and at least one jet. In addition, the first control region requires low $W$ transverse mass ($m_T^W < 20\ GeV$) and uses a reversed triangular cut ($\not{E}_T + m_T^W < 60\ GeV$). The second control region uses a reversed missing $E_T$ cut ($\not{E}_T < 10\ GeV$).

Both $\epsilon_{sig}$ and $\epsilon_{QCD}$ are analyzed for their dependence on the muon kinematics ($p_T$, $\eta$ and $\phi$). No significant dependence on $p_T$ and $\phi$ is observed. Hence the efficiencies are measured in several bins of $\eta$. The results are taken from a top group common tool and given in Table 8.1.

| Muon $\eta$ region | $\epsilon_{sig}$ | $\epsilon_{QCD}$ |
|---|---|---|
| $0 \leq \|\eta\| < 0.3$ | 0.988 | 0.348 |
| $0.3 \leq \|\eta\| < 0.6$ | 0.990 | 0.348 |
| $0.6 \leq \|\eta\| < 0.9$ | 0.989 | 0.345 |
| $0.9 \leq \|\eta\| < 1.2$ | 0.990 | 0.372 |
| $1.2 \leq \|\eta\| < 1.5$ | 0.993 | 0.398 |
| $1.5 \leq \|\eta\| < 1.8$ | 0.991 | 0.351 |
| $1.8 \leq \|\eta\| < 2.1$ | 0.985 | 0.305 |
| $2.1 \leq \|\eta\| < 2.5$ | 0.991 | 0.285 |

Table 8.1: Signal efficiency and QCD fake rate for the matrix method in the $\mu + jets$ channel

Since the efficiencies are different in different lepton $\eta$ bins, Equation 8.2 has to be applied separately to events in different lepton $\eta$ bins. Also, the matrix method has to be applied bin-by-bin to the likelihood discriminant histogram in order to extract the QCD likelihood template. Therefore it is convenient to rewrite Equation 8.2 to express the number of QCD events as a sum of event weights:

$$
\begin{aligned}
N^t_{QCD} &= \frac{\epsilon_{QCD} * \epsilon_{sig}}{\epsilon_{sig} - \epsilon_{QCD}} \left(N^l - N^t\right) + \frac{\epsilon_{QCD} * \left(\epsilon_{sig} - 1\right)}{\epsilon_{sig} - \epsilon_{QCD}} N^t \\
&= \sum_{i=1}^{N^l - N^t} w^l_i + \sum_{j=1}^{N^t} w^t_i
\end{aligned}
\tag{8.3}
$$

where

$$
\begin{aligned}
w^l &= \frac{\epsilon_{QCD} * \epsilon_{sig}}{\epsilon_{sig} - \epsilon_{QCD}} \\
w^t &= \frac{\epsilon_{QCD} * \left(\epsilon_{sig} - 1\right)}{\epsilon_{sig} - \epsilon_{QCD}}
\end{aligned}
\tag{8.4}
$$

The weights can be calculated event by event from the signal and QCD efficiencies. As such, they are functions of the $\eta$ of muon. By calculating these weights for all events in the loose sample and then summing over them, we get the number of QCD events in the tight sample. The results of the matrix method for the $\mu + jets$ channel is given in Table 8.2. The QCD likelihood template is obtained by filling the likelihood histogram with entries weighted by weights given in Equation 8.4. Kinematic distributions of the QCD background can be found by similar use of the weights.

| Quantity | $N^l_{sig}$ | $N^l_{QCD}$ | $N^t_{sig}$ | $N^t_{QCD}$ |
|---|---|---|---|---|
| Value | 608.0 | 146.0 | 601.7 | 51.3 |

Table 8.2: Outputs of the matrix method in the $\mu + jets$ channel. $N^l_{sig}$, $N^l_{QCD}$, and $N^t_{sig}$ are extracted in similar way as $N^t_{QCD}$. All four numbers are needed to construct the matrix method constraint in the maximum likelihood fit.

### 8.1.2 The Template Fit Method

While the QCD background in the $\mu + jets$ channel is dominated by muons from heavy flavor decays, the QCD background in the $e + jets$ channel contains additional contributions such as photon conversions and Dalitz decays as well as jets with high EM fraction faking electrons. This makes application of the matrix method method to the $e + jets$

channel more difficult. For example, the composition of the QCD background may be different in the control region and the signal region, biasing the extrapolation of the fake rate. As such, an alternative method utilizing a binned likelihood fit to extract the QCD normalization is used for the evaluation of QCD background in the $e + jets$ channel. The kinematic distributions of QCD are taken from a data sample selected to include mostly fake electrons. Missing $E_T$ is chosen as the fit variable most sensitive to the contribution from electron fakes.

The "anti-electron" method is used for modelling of the QCD background. In this method, a data sample containing predominantly fake electrons is obtained by inverting part of the identification (Id) cuts designed to reject fake electrons. The electrons are required to fail the Id cuts chosen for inversion and pass the rest of the kinematics and Id requirements. Electrons selected this way are called anti-electrons. In the standard top missing $E_T$ reconstruction the selected anti-electrons are considered as jets. Hence missing $E_T$ is recalculated by treating anti-electrons as electrons. Events in the data sample are required to have exactly one anti-electron, no good electron or muon, and satisfy the remaining event selection cuts.

Several different combinations of electron Id cuts can be reversed for selecting anti-electrons. The hadronic leakage requirements (see Table 4.1) is chosen for the best agreement with data. A binned likelihood fit to the missing $E_T$ distribution in data is performed in the missing $E_T$ sideband ($\not{E}_T < 35\,GeV$) separately for several jet multiplicity bins. The signal templates are derived from MC and the QCD templates are from the anti-electron sample [164]. The results of the fits are shown in Figure 8.1. And then, the fit results in the control region are extrapolated to extract the QCD normalizations in the signal region. The results from the extrapolation are shown in Table 8.3 for the different jet multiplicity bins.

An alternative selection for anti-electrons is used to provide a second modelling of the QCD background. This proves useful in the estimation of systematic error from the QCD shape uncertainties. The alternative combination of electron id cuts are chosen so as to give the largest difference in the QCD distributions from the default selection described above. The cuts used in the alternative selection are given in Table 8.4. The

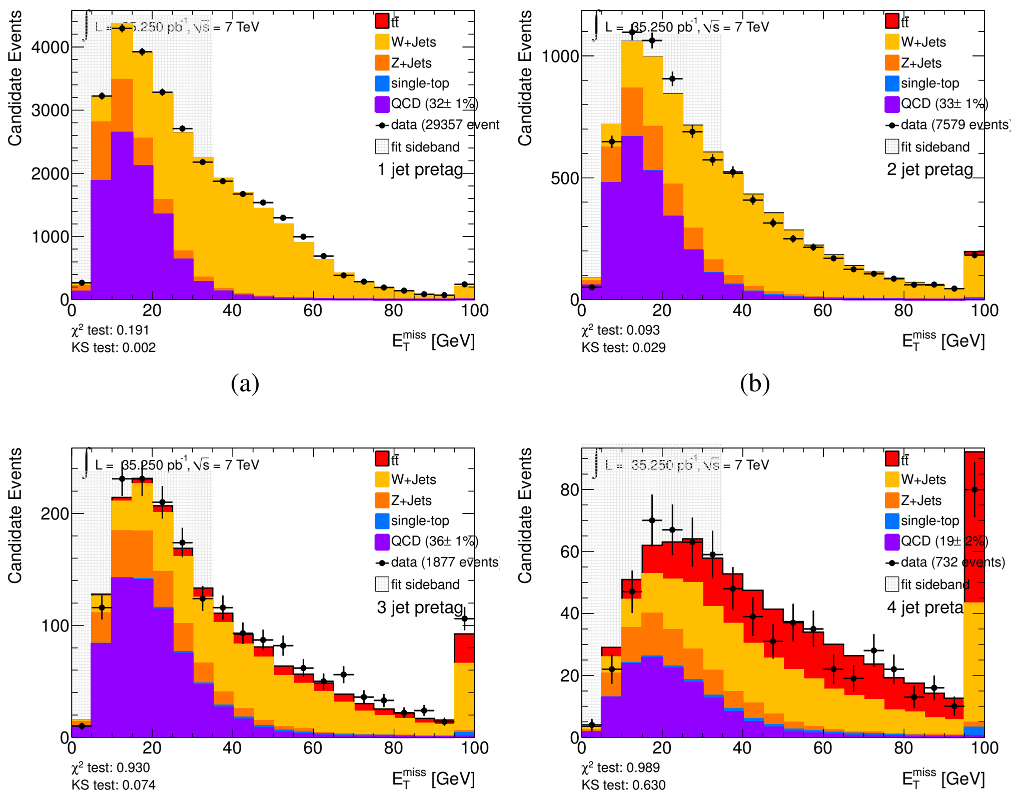


(a) (b) (c) (d)

Figure 8.1: Fitted QCD fractions for the pretag selected data for different jet multiplicity bins. The fit is performed only in the missing $E_T$ side band (the shaded area). After the fit in the control region, the result is extrapolated to the signal region. The QCD fraction marked on the plot is for the entire region. The uncertainty of the QCD fraction is statistical only.

| Jet multiplicity bin | $N_{data}$ | $N_{QCD}$ |
|---|---|---|
| 1-jet | 9479 | 287±95.7 |
| 2-jet | 2551 | 123±25.6 |
| 3-jet | 781 | 62±11.0 |
| ≥4-jet | 396 | 21.78±7.92 |

Table 8.3: QCD normalization in the signal region from the template fit method using anti-electron model for the $e + jets$ channel

shape differences for missing $E_T$ and $W$ transverse mass are shown in Figure 8.4.

| Electron Id cut type | Requirement |
|---|---|
| Id level | Requires ElectronLoose<br>Fails ElectronTight_WithTrackMatch |
| Track quality | Requires the cut on number of pixel hits<br>Requires the cut on number of silicon hits |
| Track matching | Requires tight cuts on track $\Delta\eta$ matching |
| isolation | Fails the default (95%) electron cluster isolation cut<br>Fails the default (95%) electron track isolation cut |

Table 8.4: Cuts used in the alternative anti-electron model. More details of the cuts have been presented in Section 4.2.1.

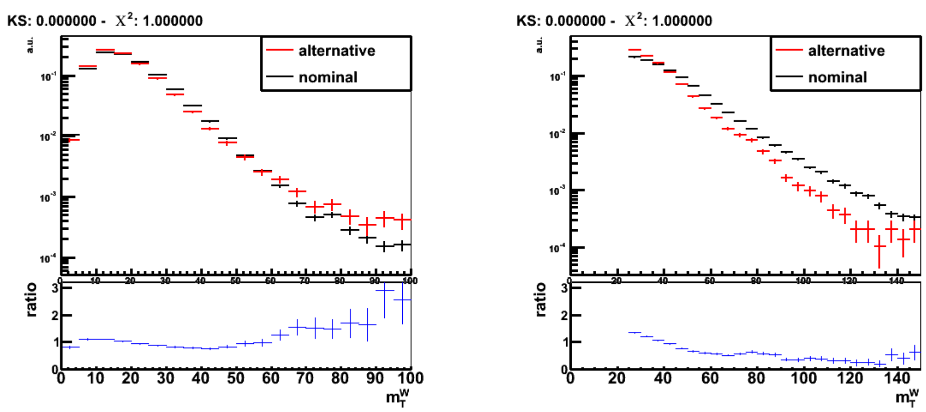


(a) (b)

Figure 8.2: Shape difference between the nominal anti-electron model and the alternative one for the $\not{E}_T$ and the $m_T^W$ distributions in the 2-jet bin

### 8.2 Maximum Likelihood Fit

The number of $t\bar{t}$ events ($N_{t\bar{t}}$) in the selected data sample is determined via a binned maximum likelihood (ML) fit to the top likelihood discriminant in data using the likelihood templates for $t\bar{t}$, $W + jets$, and QCD. Twenty bins are used for the fit. Figure 8.3 shows the likelihood templates for the $t\bar{t}$ signal and all its backgrounds, built from the set of four variables determined through optimization (see Chapter 7). The templates for the $Z + jets$ and the diboson backgrounds are found to be similar to the $W + jets$ template. Also considering that the fractions of these backgrounds in data are expected to be small, they are represented by the $W + jets$ template in the fit. However, the template for the single top background looks quite like the signal. As its fraction in data is expected to be small, we choose to subtract its likelihood discriminant distribution from the data discriminant distribution before the fit. The single top discriminant distribution is normalized to the expectation for an integrated luminosity of 35.3 $pb^{-1}$ before the subtraction.

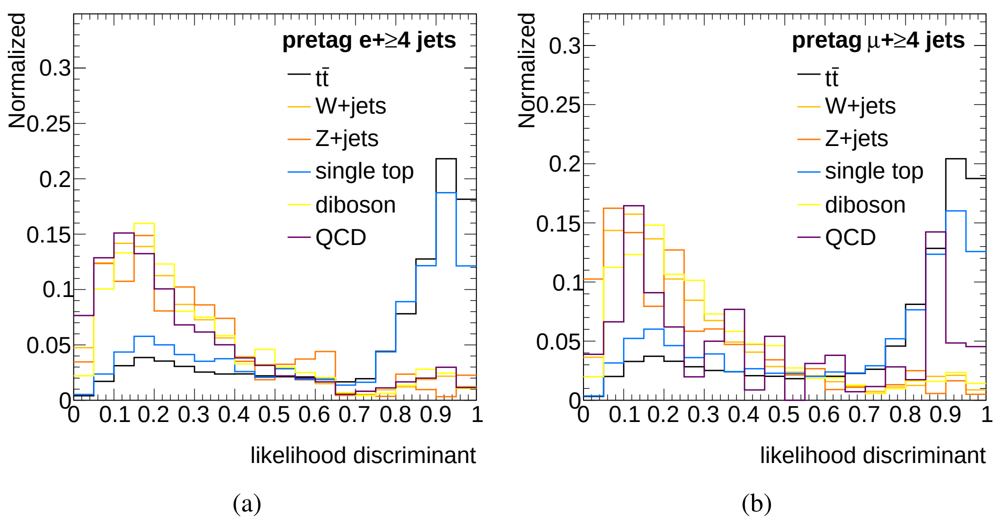


Figure 8.3: Likelihood templates for the $t\bar{t}$ signal and all its backgrounds for the $e + jets$ channel (left) and the $\mu + jets$ channel (right)

As mentioned at the beginning of this chapter, the QCD normalization is constrained by results from data driven measurements. Thus the likelihood function used for the ML fit is the product of the Poisson terms for each bin of the discriminant histogram, multiplied by the constraint term on the QCD normalization.

In the $\mu + jets$ channel the constraint on the QCD normalization is effectively implemented by a Poisson constraint on the number of events in the loose minus tight selection sample ($N_{l-t}$). The likelihood function is given by the following formula:

$$L\left(N_t^{t\bar{t}}, N_t^W, N_t^{QCD}\right) = \left[\prod_i P\left(n_i^{obs}, \mu_i\right)\right] \cdot P\left(N_{l-t}^{obs}, N_{l-t}\right) \tag{8.5}$$

where $N_t^{t\bar{t}}$, $N_t^W$, and $N_t^{QCD}$ are respectively the numbers of $t\bar{t}$, $W + jets$, and QCD events in the selected data sample. The subscript "$t$" denotes "tight" sample. In general, $P(n, \mu)$ denotes the Poisson probability distribution function (pdf) for $n$ observed events given an expected value of $\mu$. In the first term in Equation 8.8, $i$ runs over all bins of the discriminant histogram. $n_i^{obs}$ is the observed number of events of bin $i$ in data, and $\mu_i$ is the expected number in bin $i$. The expectation in bin $i$, $\mu_i$, is a function of $N_t^{t\bar{t}}$, $N_t^W$, and $N_t^{QCD}$:

$$\mu_i\left(N_t^{t\bar{t}}, N_t^W, N_t^{QCD}\right) = f_i^{t\bar{t}} N_t^{t\bar{t}} + f_i^W N_t^W + f_i^{QCD} N_t^{QCD} \tag{8.6}$$

where $f_i^{t\bar{t}}$, $f_i^W$, and $f_i^{QCD}$ represent the fractions of events in bin $i$ of the $t\bar{t}$, $W$, and QCD templates, respectively. The second term of Equation 8.8 is a constraint on the number of events in the loose minus tight sample ($N_{l-t}$) and effectively implements the constraint on the QCD normalization. Constraining $N_{l-t}$ ensures that the first term and the second term in Equation 8.8 are uncorrelated by construction, because the first term implicitly constrains the number of tight events ($N_t$). The number $N_{l-t}$ is expressed as a function of $N_t^{t\bar{t}}$, $N_t^W$ and $N_t^{QCD}$:

$$N_{l-t} = \frac{1-\epsilon_{sig}}{\epsilon_{sig}} N_t^{t\bar{t}} + \frac{1-\epsilon_{sig}}{\epsilon_{sig}} N_t^W + \frac{1-\epsilon_{QCD}}{\epsilon_{QCD}} N_t^{QCD} \tag{8.7}$$

In the $e + jets$ channel a Gaussian constraint is applied on the QCD normalization, with the mean and the standard deviation given by the result from the anti-electron template fit method (see Table 8.3). The likelihood function is:

$$L\left(N_t^{t\bar{t}}, N_t^W, N_t^{QCD}\right) = \left[\prod_i P\left(n_i^{obs}, \mu_i\right)\right] \cdot exp\left(-\left(N_t^{QCD} - \overline{N_t^{QCD}}\right)^2 / 2\sigma_t^{QCD^2}\right) \tag{8.8}$$

where the first term is the same as for the $\mu + jets$ channel. The second term is a Gaussian constraint on the number of QCD events $N_t^{QCD}$. The mean of the Gaussian is $\overline{N_t^{QCD}}$ and the standard deviation is $\sigma_t^{QCD}$. Note that for the $e + jets$ channel, the matrix method was not used. Therefore there is no loose and tight selection defined. Here the subscript $t$ in $N_t^{t\bar{t}}$, $N_t^W$, $N_t^{QCD}$ is only added for consistency with the $\mu + jets$ channel.

The task of the ML fit is to maximize the likelihood function in Equation 8.5 and 8.8.

Equivalently, it is to minimize the negative log-likelihood function,

$$-\,logL\left(N_t^{t\bar{t}}, N_t^{W}, N_t^{QCD}\right) = -\sum_i n_i^{obs} log\mu_i + \mu_i - N_{l-t}^{obs} logN_{l-t} + N_{l-t} \tag{8.9}$$

in the $\mu + jets$ channel, and

$$-\,logL\left(N_t^{t\bar{t}}, N_t^{W}, N_t^{QCD}\right) = -\sum_i n_i^{obs} log\mu_i + \mu_i + \left(N_t^{QCD} - \overline{N_t^{QCD}}\right)^2 / 2\sigma_t^{QCD^2} \tag{8.10}$$

in the $e + jets$ channel. Any terms independent of the fit parameters ($N_t^{t\bar{t}}$, $N_t^{W}$, and $N_t^{QCD}$) are dropped.

The fitted number of $t\bar{t}$, $W + jets$, and QCD events ($N_t^{t\bar{t}}$, $N_t^{W}$, and $N_t^{QCD}$) are given by their values at the minimum of the negative log-likelihood function. Their uncertainties are obtained by raising the negative log-likelihood by one half unit above the minimum while allowing the fit parameters to float. The values and the uncertainties of the fit parameters are listed in Table 8.5. The result of the fit to the discriminant distribution is shown in Figure 8.4. The Kolomogorov-Smirkov (KS) test result between the data and the sum of signal and backgrounds, estimated with their fitted contributions, is printed on the plot. The test result shows an improvement of data/MC agreement compared to the result using the expected event yields. Data/MC comparison plots are shown in Figure 8.5 and Figure 8.6 for the input variables to the likelihood discriminant. In general the KS test results have been improved by the fit.

| Parameter | Channel | |
|---|---|---|
| | $e + jets$ | $\mu + jets$ |
| $N_t^{t\bar{t}}$ | $188.2^{+18.5}_{-17.6}$ | $275.8^{+22.9}_{-22.0}$ |
| $N_t^{W}$ | $175.6^{+20.2}_{-19.6}$ | $312.5^{+24.2}_{-23.5}$ |
| $N_t^{QCD}$ | $22.0^{+7.9}_{-7.9}$ | $50.8^{+5.6}_{-5.2}$ |

Table 8.5: Fitted number of $t\bar{t}$, $W + jets$, and QCD background events in the selected data sample in the $e + jets$ and $\mu + jets$ channel. $N_t^{W}$ includes contributions from the $Z + jets$ and diboson background.

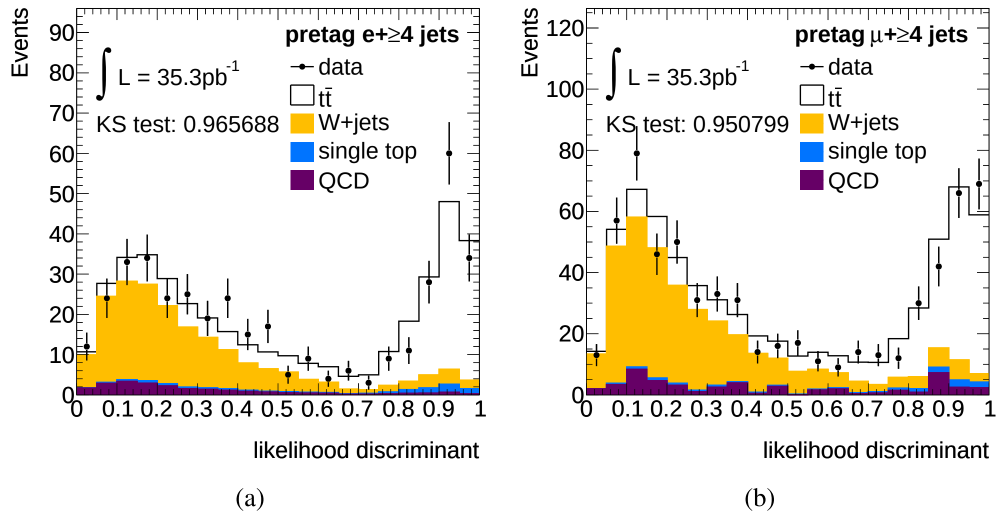


Figure 8.4: Result of the ML fit to data in the $e + jets$ channel (left) and the $\mu + jets$ channel (right)

## 8.3 Ensemble Test for the Maximum Likelihood Fit

The top likelihood fit method described in last section is validated through ensemble tests using mock datasets. A mock dataset is generated by mixing events randomly sampled from signal and background distributions of the likelihood discriminant. The number of events sampled from each distribution is fluctuated according to the Poisson distribution. The ML fit can be performed on the mock dataset in the same way as on real data, using the likelihood templates for $t\bar{t}$, $W + jets$, and $QCD$. The parameter of the QCD constraint ($N_{l-t}^{obs}$ or $\overline{N_t^{QCD}}$) is also fluctuated according the type of constraint used.

In principle, the event sample used for deriving the templates, and the event sample used for deriving the parent distributions for mock data generation, should be independent to each other. In this analysis, full available statistics are used for both. A sanity check was done using half MC events of $t\bar{t}$ and $W + jets$ for the templates and the other half events for the parent distributions. The validation procedures described below were repeated. No significant changes were observed.

In the first validation test, we test if the ML fit is unbiased and if the fit error is a correct estimate of the statistical error. Mock datasets are generated with on average the

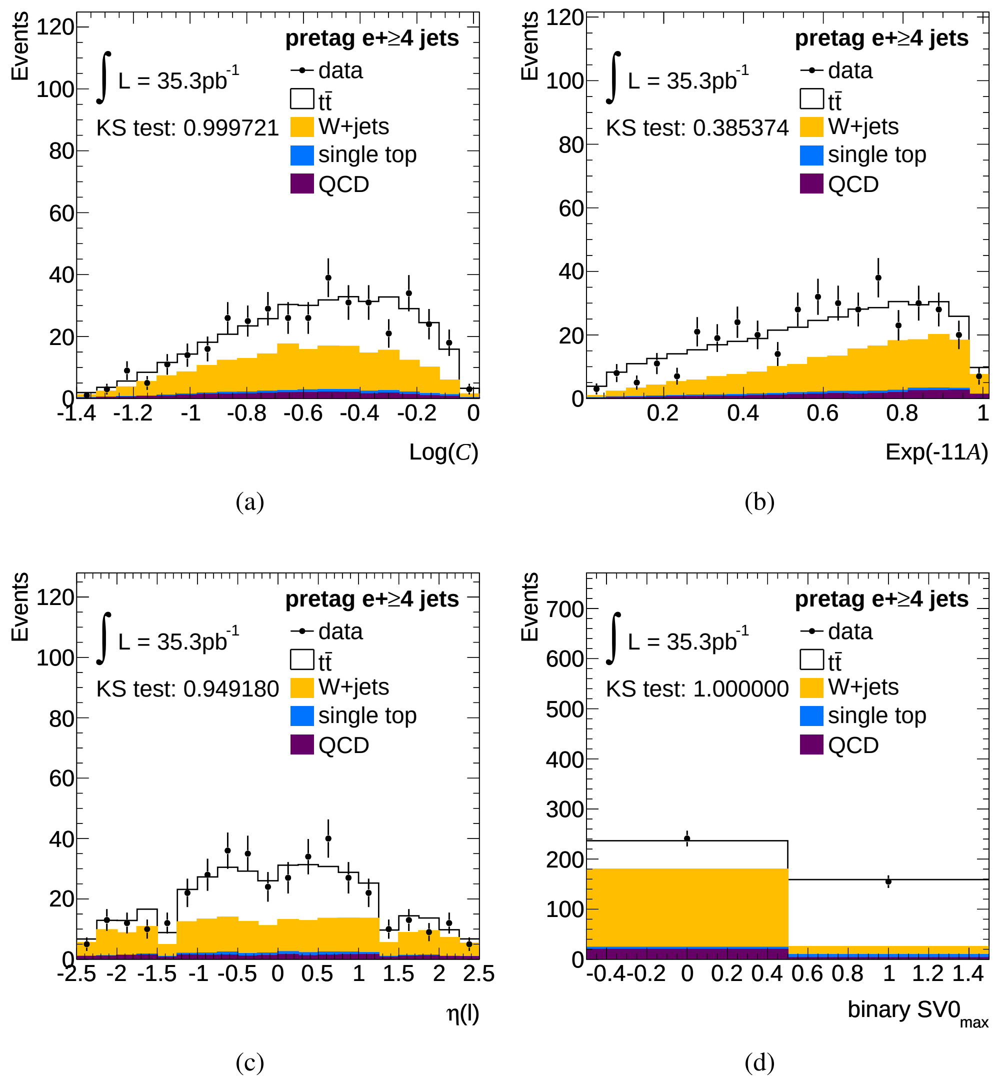


Figure 8.5: Data/MC comparison of the optimized set of variables ($\ln(C)$, $\exp(-11\mathcal{A})$, $\eta_l$, and binary SV0$_{max}$) using the fitted number of events in the $e + jets$ channel

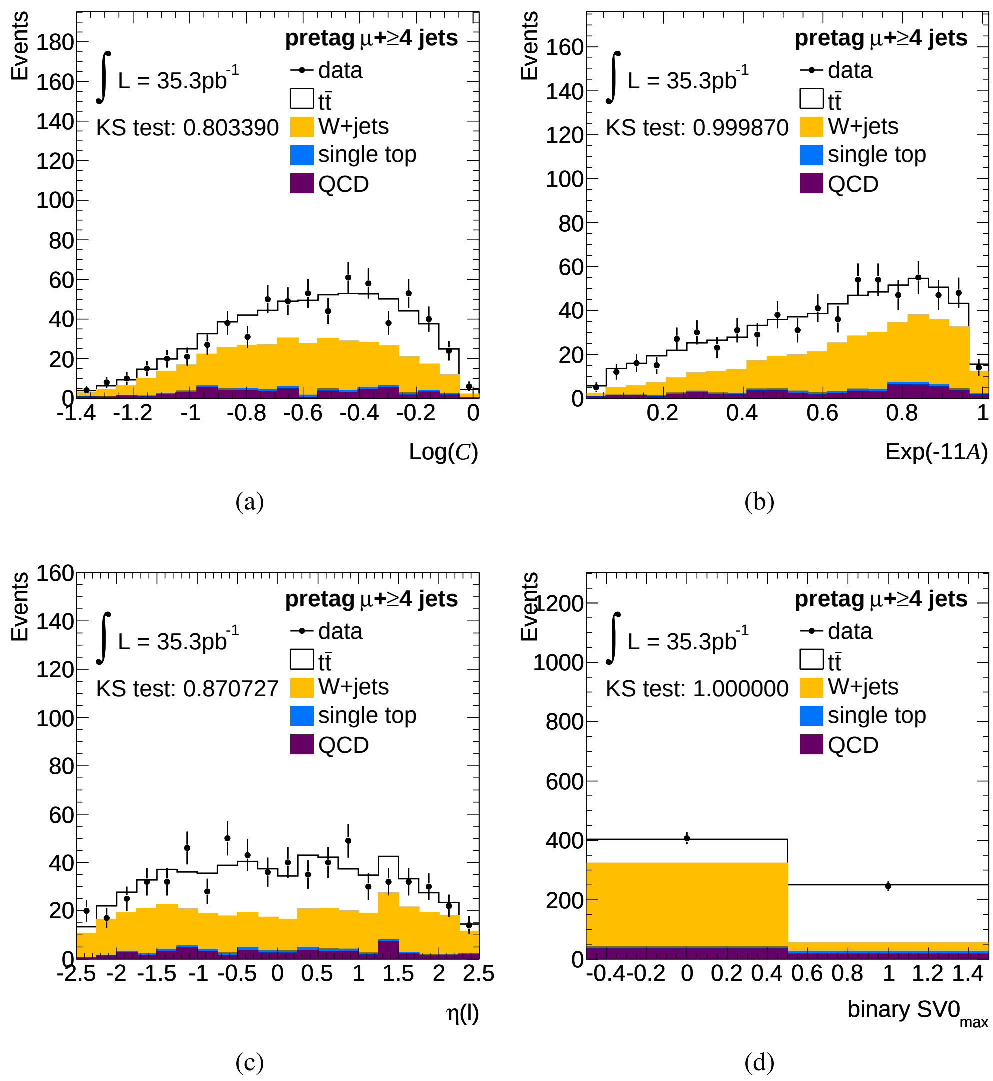


Figure 8.6: Data/MC comparison of the optimized set of variables ($\ln(C)$, $\exp(-11\mathcal{A})$, $\eta_l$, and binary $SV0_{max}$) using the fitted number of events in the $\mu + jets$ channel

same signal and background composition as given by the fit to real data. The number of signal and background events in each mock data are Poisson fluctuated with respect to their average values. The parameter of the QCD constraint in each channel is fluctuated according to the type of the constraint. For this test, as well as all other ensemble tests in this analysis, we used 1000 mock datasets.

The ML fit is performed on each of the 1000 mock datasets. Histograms of the fitted number of $t\bar{t}$, $W + jets$, and QCD events are shown in Figure 8.7. Each entry in the histograms corresponds to one mock dataset. Histograms of the associated fit errors are shown in Figure 8.8. The pull distributions of the fit parameters ($N_t^{t\bar{t}}$, $N_t^W$, and $N_t^{QCD}$) are used as a test of the validity of the ML fit. In this context the pull $g$ of a variable $x$ is generally defined as:

$$g_x = \frac{x^{fit} - x^{true}}{\sigma_x^{fit}} \tag{8.11}$$

where $x_{fit}$ is the fitted value of the observable, $x_{true}$ is the true value, and $\sigma_x^{fit}$ is the error from the fit.

The pull distributions of the ML fit parameters ($N_t^{t\bar{t}}$, $N_t^W$, and $N_t^{QCD}$) are shown in Figure 8.9. The distributions are observed to have a mean of $\sim 0$ and a width of $\sim 1$, i.e., they are observed to be standard normal distributions. The mean of 0 indicates that the fit gives on average the correct answer, i.e., it is unbiased. The width of 1 indicates the error from fit is a correct estimate of the statistical error.

The linearity of the ML fit is validated through ensemble tests using mock datasets generated with a few different fractions of $t\bar{t}$ events. The average number of $t\bar{t}$ events ($N_t^{t\bar{t}}$) in the mock datasets is calculated from an assumed input $t\bar{t}$ cross section ($\sigma_{t\bar{t}}$). The input $\sigma_{t\bar{t}}$ is varied between 120 $pb$ and 200 $pb$ in steps of 10 $pb$. The number of QCD events ($N_t^{QCD}$) is taken from the fit to data. Then the number of $W + jets$ events ($N_t^W$) is calculated using:

$$N_t^W = N^{obs} - N_t^{t\bar{t}} - N_t^{QCD} \tag{8.12}$$

where $N^{obs}$ is the observed number of data events, with the single top contribution already subtracted. 1000 mock experiments are performed for each assumed cross section. The

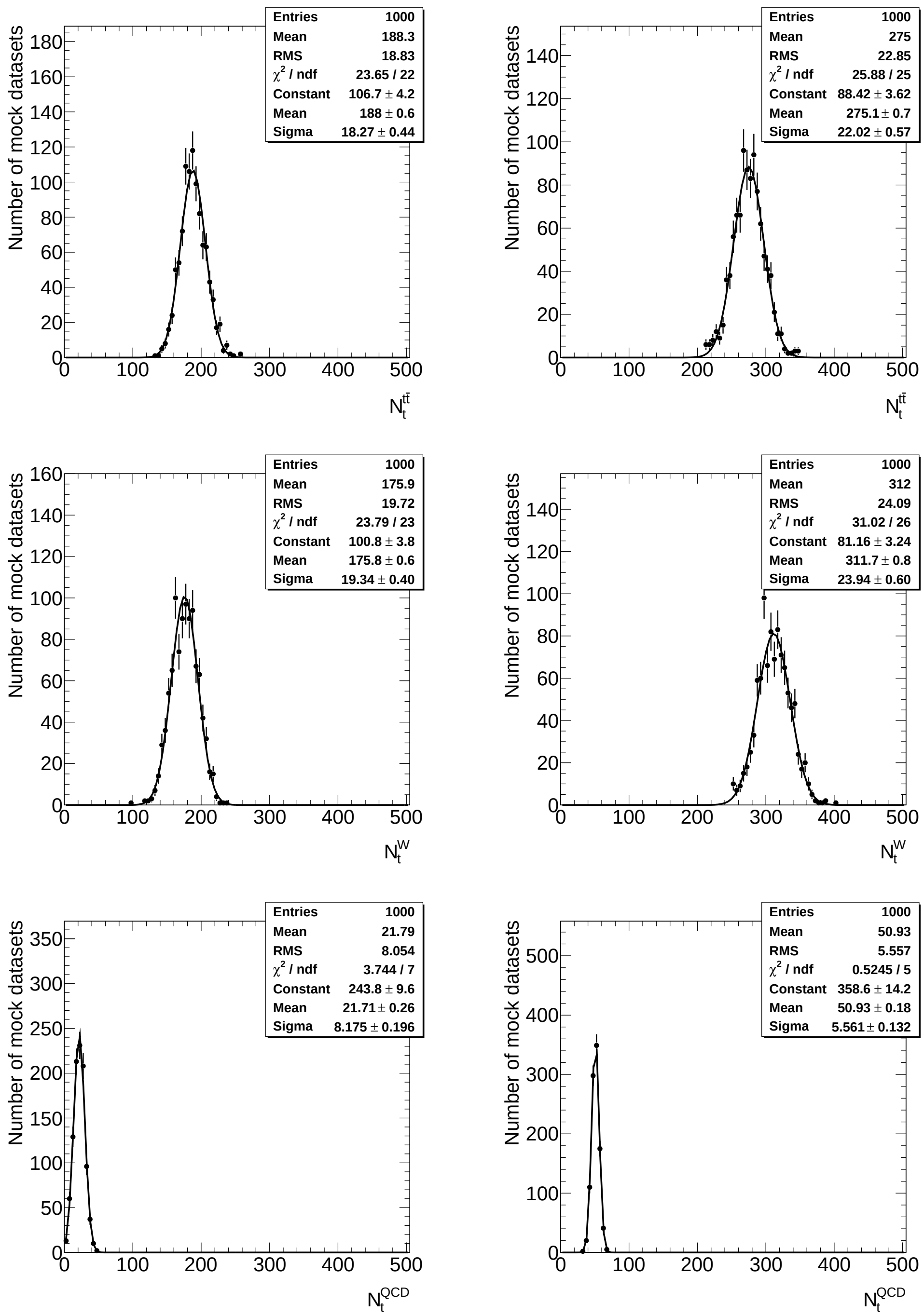


Figure 8.7: Distributions of the fitted number of $t\bar{t}$, $W$ + *jets*, and QCD events ($N_t^{t\bar{t}}$, $N_t^W$, and $N_t^{QCD}$) in the $e$ + *jets* channel (left) and the $\mu$ + *jets* channel (right)

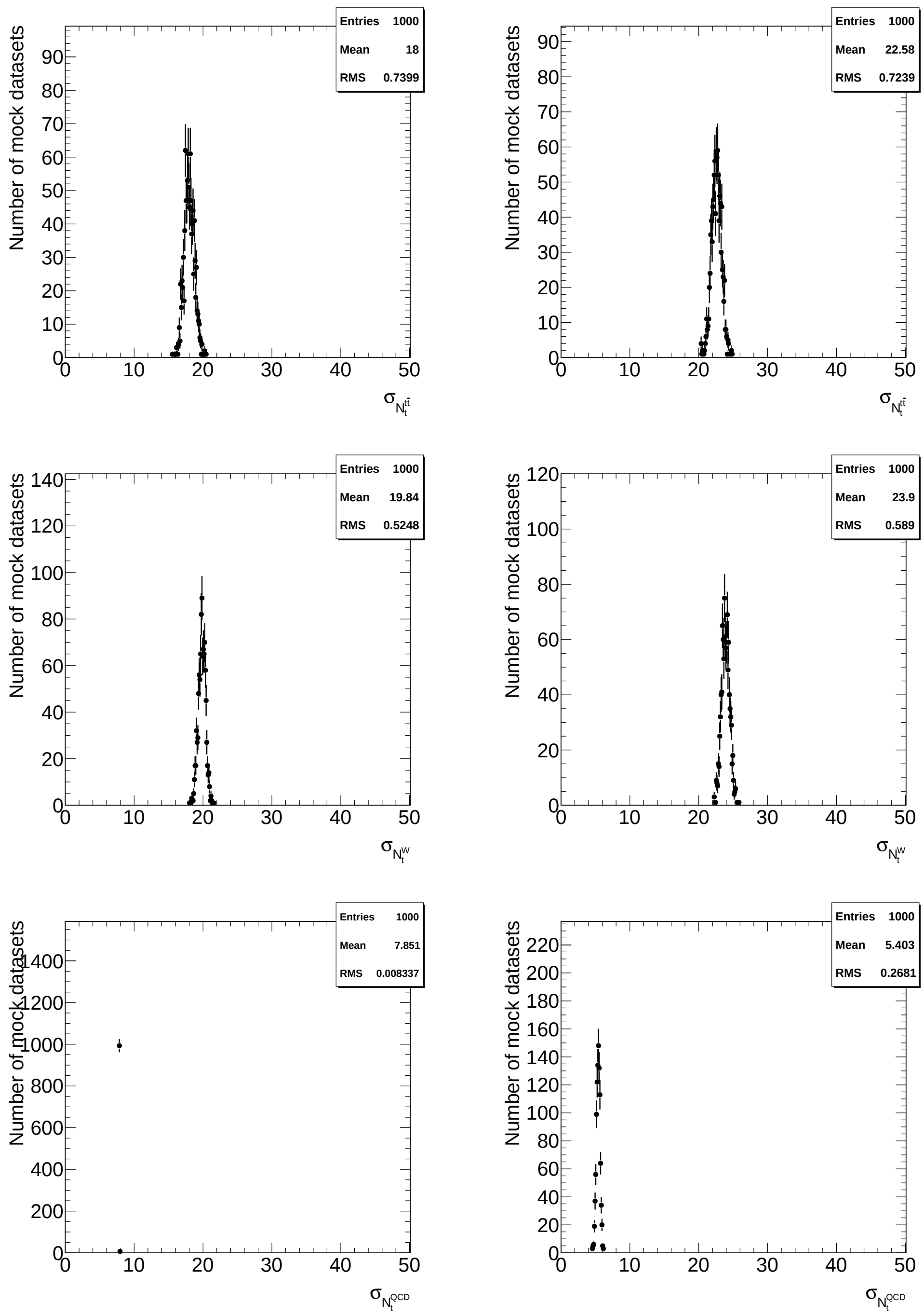


Figure 8.8: Distributions of the fit errors for number of $t\bar{t}$, $W + jets$, and QCD events ($\sigma_{N_t^{t\bar{t}}}$, $\sigma_{N_t^W}$, and $\sigma_{N_t^{QCD}}$) in the $e + jets$ channel (left) and the muon channel (right)

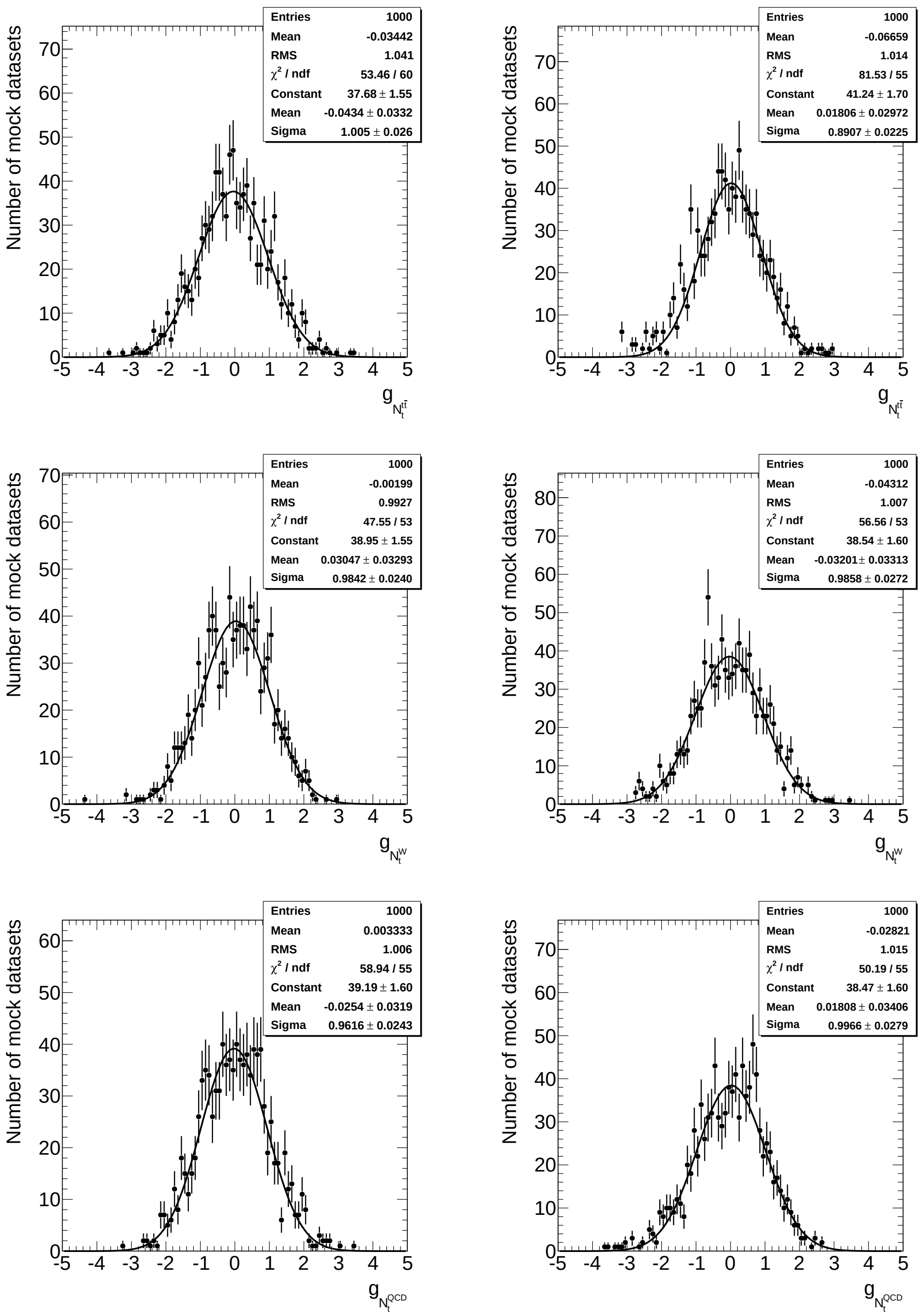


Figure 8.9: Pull distributions of the fitted number of $t\bar{t}$, $W + jets$, and QCD events ($N_t^{t\bar{t}}$, $N_t^{W}$, and $N_t^{QCD}$) in the $e + jets$ channel (left) and the $\mu + jets$ channel (right)

linearity of the fit is illustrated in Figure 8.10, showing the average $\sigma_{t\bar{t}}$ from the fit versus the input $\sigma_{t\bar{t}}$. The straight line fitted to the data points shows no significant offset or departure from unit slope.

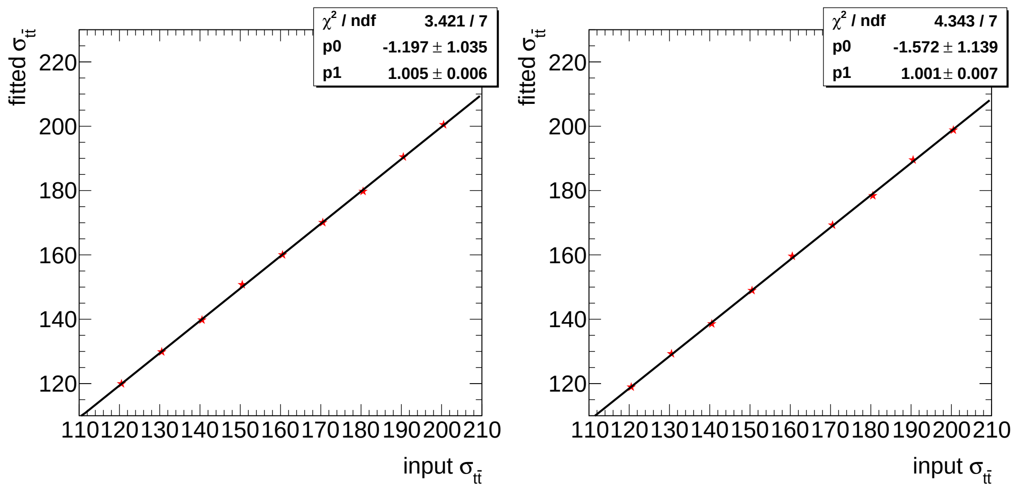


Figure 8.10: Result of the linearity test of the ML fit in the $e + jets$ channel (left) and the $\mu + jets$ channel (right)

The ensemble test procedure as described above can also be used to estimate various systematic errors associated with the likelihood template shape (see Section 9.2). The likelihood discriminant is evaluated for the shifted $t\bar{t}$, $W + jets$, or QCD samples, as well as for the nominal samples. Note that for simplicity, the training (see Section 7.1) is only performed once, with the nominal samples, and then the evaluation is performed with all the samples. The systematic error from a certain source of uncertainties can be estimated either by changing the likelihood templates used for the ML fit or changing the mock datasets generated for the ensemble test.

In the first method, mock datasets are drawn from nominal discriminant distributions. Then the discriminant distribution in each nominal mock dataset is fitted to the shifted templates. In the second method, mock datasets are drawn from shifted discriminant distributions. Then the discriminant distribution in each shifted mock dataset is fitted to the nominal templates. For both methods, the average value of fitted number of $t\bar{t}$ events ($N_{t\bar{t}}$) is compared with that from the nominal analysis. The fractional change of $N_{t\bar{t}}$

with respect to the nominal analysis is taken as the systematic error associated with the likelihood template shape.

We have verified that both of the two methods give compatible results. For simplicity, the first method was chosen for this analysis. Here we give an example of applying the method to extract the systematic error from the Jet Energy Scale uncertainty. To estimate this error, the jet energies are varied by $\pm 1\sigma$. The event selection is repeated with the varied jet energies, which gives us the shifted samples for JES. Then likelihood discriminant is evaluated for these shifted samples. Then these shifted discriminant distribution is used as shifted templates for the ML fit. 1000 mock datasets are drawn from the nominal discriminant distribution and fitted with both the nominal templates and the shifted templates. The fractional change of average fitted $N_{t\bar{t}}$ is taken as the JES systematic error associated with the likelihood template shapes.

The above procedure is used in Chapter 9 for evalution of the systematic errors, as well as in Chapter 7 for optimization of the likelihood template.

# Chapter 9

# Cross Section Results

In this chapter we present the final $t\bar{t}$ cross section results. In Section 9.1, the cross section results and statistical errors are given separately for the $e + jets$ and $\mu + jets$ channel. In Section 9.2, the systematic uncertainties associated with the measurement are discussed. A summary of all the uncertainties is given in Section 9.3. In Section 9.4, a combined cross section result is given for the $l + jets$ channel. The $e + jets$ and $\mu + jets$ channel are combined through the use of a combined maximum likelihood (ML) fit which minimizes the sum of the negative log-likelihoods of the two channels. The systematic uncertainties are combined taking into account their correlations.

## 9.1 $t\bar{t}$ Cross Section in Individual Channels

In the previous chapter, the number of $t\bar{t}$ signal events ($N_{t\bar{t}}$) was extracted via a maximum likelihood (ML) fit to the likelihood discriminant distribution in data using likelihood templates representing $t\bar{t}$ signal and background. The total efficiency for signal ($\epsilon_{t\bar{t}}$) was determined in Chapter 6 using Monte Carlo (MC) samples and data/MC corrections. The value of the integrated luminosity ($\int \mathcal{L}\, dt$) was given and discussed in Chapter 5. The branching ratios (BR) for $t\bar{t}$ decay channels were given in Chapter 2. The $t\bar{t}$ cross section is given by:

$$\sigma_{t\bar{t}} = \frac{N_{t\bar{t}}}{\epsilon_{t\bar{t}} \times \mathrm{BR} \times \int \mathcal{L}\, dt} \tag{9.1}$$

where BR is the branching ratio for $t\bar{t}$ non-hadronic final states because the MC sample we used is inclusive of all $t\bar{t}$ non-hadronic final states. The values of $N_{t\bar{t}}$, $\epsilon_{t\bar{t}}$, $BR$ and $\int \mathcal{L}\, dt$ for the two individual channels are summarized in Table 9.1.

The $t\bar{t}$ cross section can be calculated using Equation 9.1 and the values from Table 9.1. In this way the statistical error of $N_{t\bar{t}}$ is converted to the statistical error of $\sigma_{t\bar{t}}$. An

| Channel | $N_{t\bar{t}}$ | $\epsilon_{t\bar{t}}$ [%] | BR [%] | $\int \mathcal{L}\,dt$ [$pb^{-1}$] |
|---|---|---|---|---|
| $e + jets$ | $188.2^{+18.5}_{-17.6}$ | 5.972 | 54.30 | 35.3 |
| $\mu + jets$ | $275.8^{+22.9}_{-22.0}$ | 8.572 | 54.30 | 35.3 |

Table 9.1: The inputs to the cross section formula in the $e + jets$ and $\mu + jets$ channels. The error on $N_{t\bar{t}}$ is the statistical only, evaluated from the ML fit.

alternative method is to write $N_{t\bar{t}}$ in terms of $\sigma_{t\bar{t}}$ according to Equation 9.1:

$$N_{t\bar{t}} = \sigma_{t\bar{t}}\left(\epsilon_{t\bar{t}} \cdot \mathrm{BR} \cdot \int \mathcal{L}\,dt\right) \tag{9.2}$$

and substitute it in the likelihood functions (Equation 8.8 and Equation 8.5) used for the ML fit. The fit can then be performed to extract directly the cross section and its statistical error.

Both methods give the same cross section results for the individual channels:

$$e + jets \text{ channel: } \sigma_{t\bar{t}} = 164.4^{+16.2}_{-15.4}(\text{stat})\ pb \tag{9.3}$$

$$\mu + jets \text{ channel: } \sigma_{t\bar{t}} = 167.8^{+14.0}_{-13.4}(\text{stat})\ pb \tag{9.4}$$

### 9.2 Systematic Uncertainties

In determining the systematic errors, common procedures adopted by the ATLAS top physics group were followed closely [159]. In this analysis, systematic uncertainties arise into two main areas: uncertainties associated with the $t\bar{t}$ signal selection efficiency and uncertainties associated with the likelihood template shapes, and therefore with the extracted number of $t\bar{t}$ events. The uncertainties in the object selection and signal modelling are associated with both areas, while uncertainties in the background modelling as well as other sources are only associated with the likelihood template shapes. A final systematic error is associated with the uncertainty of the integrated luminosity.

Equation 9.5 shows how the systematic errors associated with the $t\bar{t}$ signal selection efficiency $\epsilon$ and the number of extracted $t\bar{t}$ events $N$ propagate to errors on the $t\bar{t}$ cross section.

$$\frac{\Delta\sigma}{\sigma} = \frac{\frac{N \pm \Delta N}{\epsilon \pm \Delta\epsilon} - \frac{N}{\epsilon}}{\frac{N}{\epsilon}} \tag{9.5}$$

Depending on the signs of $\Delta N$ and $\Delta\epsilon$, they can either enhance or cancel each other's effect on $\Delta\sigma$. Equation 9.5 shows that the fractional error on the cross section due to selection efficiency uncertainties is given by:

$$\left(\frac{\Delta\sigma}{\sigma}\right)_{\epsilon} = \frac{\frac{1}{\epsilon \pm \Delta\epsilon} - \frac{1}{\epsilon}}{\frac{1}{\epsilon}} \tag{9.6}$$

And the error on the cross section from the likelihood template shapes is:

$$\left(\frac{\Delta\sigma}{\sigma}\right)_{N} = \frac{\Delta N}{N} \tag{9.7}$$

The error on the selection efficiency can be extracted by rerunning the event selection with shifted MC samples for $t\bar{t}$ events and comparing the measured efficiency with that from the nominal analysis. By shifted MC samples we mean MC samples that have been generated or processed with varied parameters associated with a certain source of uncertainties.

Likewise the error on the cross section due to uncertainties in the likelihood shapes ($\Delta N/N$) is given by running ensemble tests with nominal and varied parameters and comparing the results. The ensemble test procedure and its usage in estimating systematic errors is described in Section 8.3.

The systematic error on $\sigma_{t\bar{t}}$ can be calculated using Equation 9.5 using the error on $\epsilon_{t\bar{t}}$ and $N_{t\bar{t}}$ alone. As already mentioned in the previous section, alternatively, the ML fit can be made to produce $\sigma_{t\bar{t}}$ directly in a single step (rather than $N_{t\bar{t}}$). The systematic error on $\sigma_{t\bar{t}}$ can be found in this manner as well. Both methods give the same result for $\Delta\sigma/\sigma$ but the latter proves more useful when combining the $e + jets$ and $\mu + jets$ channels.

In the following sections, we apply the first method described above to extract the systematic error from each of the many sources we have considered. The sources contributing the largest systematic errors arise from the Jet Energy Scale (JES) uncertainties, the Initial/Final State Radiation (ISR/FSR) modelling, the signal Monte Carlo (MC) generators, and the $b$-tagging calibration uncertainties. For each of the sources that vary kinematics of leptons or jets, missing $E_T$ is changed accordingly. No additional uncertainty on missing $E_T$ itself is considered.

### 9.2.1 Lepton RecoId and Trigger Efficiencies

The uncertainties of the electron reconstruction and identification (RecoId) efficiencies were presented in Section 6.3.2, and the uncertainty of the electron trigger efficiency was presented in Section 6.3.1. The corresponding uncertainties for muon RecoId and trigger efficiencies were documented in Section 6.3.4 and 6.3.4. For both lepton flavors, the RecoId and trigger uncertainties are summed in quadrature to form a total uncertainty $\sigma$. The total lepton scale factor $\mathrm{SF}^{lepTrig} * \mathrm{SF}^{lepRecoId}$ is varied by $\pm\sigma$, and Equation 6.13 is used to calculate the systematic error on the signal selection efficiency from these uncertainties.

Since some of the lepton efficiencies are binned in certain kinematic variables, the variation of the total SF is applied event by event, with its value dependent on the event kinematics. As a result, the uncertainty of the lepton RecoId and trigger efficiencies also affects the signal and background template shapes. The systematic error on templates shapes is estimated using the procedure described in Section 8.3. Equation 9.5 is then used to estimate the total systematic error on the cross section. The systematic error on the signal selection efficiency, on the number of $t\bar{t}$ events, and the total systematic error on the $t\bar{t}$ cross section combining these two are summarized in Table 9.2.

This systematic error is observed to be larger in the $e + jets$ channel than in the $\mu + jets$ channel due to a larger RecoId uncertainty in the $e + jets$ channel.

### 9.2.2 Jet Energy Scale

The Jet Energy Scale (JES) is one of the most important sources of systematic error for this measurement. The JES uncertainty was discussed in Section 4.4.2. It affects both the signal selection efficiency and the signal and background template shapes. The JES

| Source | relative uncertainty [%] | | | |
|---|---|---|---|---|
| | $\Delta\epsilon/\epsilon$ | $(\Delta\sigma/\sigma)_{\epsilon}$ | $(\Delta\sigma/\sigma)_{N_{t\bar{t}}}$ | $\Delta\sigma/\sigma$ |
| | | $e + jets$ | | |
| Lepton reco,Id,Trigger SF ↑↓ | +4.0-4.0 | +4.2-3.9 | +0.0-0.0 | +4.1-3.8 |
| | | $\mu + jets$ | | |
| Lepton reco,Id,Trigger SF ↑↓ | +0.9-0.9 | +0.9-0.9 | +0.1-0.1 | +1.0-1.0 |

Table 9.2: Systematics from uncertainties in lepton reconstruction, identification and trigger scale factors

uncertainty includes many terms. The base term corresponds to the values in Table 4.7. To account for close-by jet effect, a conservative approach is used which adds an additional uncertainty of 5% for every jet not overlapping an electron and with a close-by jet of $p_T \geq 10\ GeV$ within $\Delta R = 0.6$. Within the MultijetJESUncertainty (see Section 4.4.2) provider tool, the JES uncertainty is corrected for quark/gluon content fractions in semileptonic $t\bar{t}$ sample, using as input the fraction of the gluon jets, the uncertainty on the gluon fraction, as well as the average jet response in the sample of interest [85, 165, 166]. The uncertainty from the $b$-jet fraction has not been included yet, which has been shown by very preliminary studies to be an additional $\sim 2\%$ uncertainty for each jet tagged as a $b$-jet [85].

The MultijetJESUncertainty tool is used to vary the jet energies by $\pm 1\sigma$. The entire analysis is repeated and the results compared with nominal analysis. The systematic error on the signal selection efficiency is extracted by comparing the efficiency measured in the nominal analysis and the shifted analysis. The systematic error on the likelihood template shapes is estimated using the procedure described in Section 8.3. Note that the JES was used as an example in the description of the procedure. The error on the selection efficiency and the template shapes are added using Equation 9.5. The results of systematic error from the JES uncertainties are summarized in Table 9.3.

| Source | relative uncertainty [%] | | | |
|---|---|---|---|---|
| | $\Delta\epsilon/\epsilon$ | $(\Delta\sigma/\sigma)_\epsilon$ | $(\Delta\sigma/\sigma)_{N_{t\bar{t}}}$ | $\Delta\sigma/\sigma$ |
| | | *e + jets* | | |
| JES ↑↓ | +10.0-8.1 | +8.9-9.1 | +1.3-1.3 | +7.4-8.0 |
| | | $\mu$ + *jets* | | |
| JES ↑↓ | +8.8-7.9 | +8.6-8.0 | +1.6-2.1 | +6.3-6.6 |

Table 9.3: Systematics from uncertainties in Jet Energy Scale

### 9.2.3 Jet Energy Resolution

The systematic error associated with the Jet Energy Resolution (JER) was discussed in Section 6.2.1.6. Like the JES uncertainty, the JER uncertainty affects both the selection efficiency and the template shapes. The procedure described in Section 6.2.1.6 uses the parametrised functions of JER shown in Figure 6.2. The results of the JER systematic error are given in Table 9.4. Like the JES uncertainty, the error on efficiency comes from comparing the efficiency measured in the nominal analysis and the shifted analysis. The error on the template shapes comes from the procedure described in Section 8.3. The two errors are added using Equation 9.5.

| Source | relative uncertainty [%] | | | |
|---|---|---|---|---|
| | $\Delta\epsilon/\epsilon$ | $(\Delta\sigma/\sigma)_\epsilon$ | $(\Delta\sigma/\sigma)_{N_{t\bar{t}}}$ | $\Delta\sigma/\sigma$ |
| | | *e + jets* | | |
| JER | +0.1-0.1 | +0.1-0.1 | +0.2-0.2 | +0.1-0.1 |
| | | $\mu$ + *jets* | | |
| JER | +0.5-0.5 | +0.5-0.5 | +0.6-0.6 | +0.1-0.1 |

Table 9.4: Systematics from uncertainties in Jet Energy Resolution

The systematic error on the selection efficiency is observed to be small, which is expected because the smearing does not change the average Jet Energy Scale. The error on the number of fitted $t\bar{t}$ events is observed to be small as well.

### 9.2.4 Jet Reconstruction Efficiency

The jet reconstruction efficiency (JEF) and its associated uncertainties have been measured using two different methods, as described in Section 4.4.4. As the results from both methods need further investigation, a conservative JEF uncertainty of a 2% is used to estimate the systematic error associated with it.

The systematic error associated with the jet reconstruction efficiency is estimated by randomly dropping jets using a probability of 2%, repeating the entire analysis, and comparing results with the nominal analysis. The systematic error on the signal selection efficiency, on the likelihood template shapes, and on the cross section, are estimated in the same way as for JES and JER. The results given in Table 9.5.

| Source | relative uncertainty [%] | | | |
|---|---|---|---|---|
| | $\Delta\epsilon/\epsilon$ | $(\Delta\sigma/\sigma)_{\epsilon}$ | $(\Delta\sigma/\sigma)_{N_{t\bar{t}}}$ | $\Delta\sigma/\sigma$ |
| | | $e + jets$ | | |
| JEF | +4.5-4.5 | +4.8-4.8 | +0.4-0.4 | +5.2-5.2 |
| | | $\mu + jets$ | | |
| JEF | +4.8-4.8 | +5.0-5.0 | +0.7-0.7 | +5.7-5.7 |

Table 9.5: Systematics from uncertainties in jet reconstruction efficiency

The 2% uncertainty of the jet reconstruction efficiency transforms to a quite large error on the $t\bar{t}$ signal selection efficiency. This is because of the large number of jets in the $t\bar{t}$ final state.

### 9.2.5 Initial and Final State Radiation Modelling

ISR/FSR modelling affects the signal acceptance by increasing or decreasing the number of jets and by changing the jet energy and transverse momentum ($p_T$) in the event. To estimate the systematic error associated with this uncertainty, several $t\bar{t}$ samples are generated varying the parameters that control ISR and FSR using the maximum range allowed by the current underlying event (UE) tuning. These parameters are documented in Chapter 5.

Both the nominal and the variation samples are generated using the LO generator AcerMC, coupled with Pythia, because currently there is no accepted way in ATLAS to vary ISR and FSR with NLO MC generators. Six variation samples are available, with maximum or minimum ISR, maximum or minimum FSR, and with ISR and FSR varied up and down together. Systematic error on signal selection efficiency is estimated by comparing the acceptance of the variation samples with respect to the ISR/FSR nominal sample. ISR/FSR modelling also changes the shape of the signal likelihood template. This error is estimated by fitting MC@NLO nominal mock datasets with nominal and varied ISR/FSR templates and comparing the results. After combining the error from the efficiency and the shape for the six samples, the largest error in the positive and negative direction is quoted as the systematic error from ISR/FSR modelling. The results are shown in detail in Table 9.6.

| Source | relative uncertainty [%] | | | |
|---|---|---|---|---|
| | $\Delta\epsilon/\epsilon$ | $(\Delta\sigma/\sigma)_\epsilon$ | $(\Delta\sigma/\sigma)_{N_{t\bar{t}}}$ | $\Delta\sigma/\sigma$ |
| | | $e + jets$ | | |
| ISR ↑↓ | +16.0-2.0 | +2.0-13.8 | -0.1-2.0 | +0.1-13.9 |
| FSR ↑↓ | +12.8-2.8 | +2.9-11.3 | +1.9-1.1 | +4.8-12.3 |
| ISR ↑↓ FSR ↑↓ | +9.9+0.7 | -0.6-9.0 | +1.9-2.6 | -3.3-7.2 |
| Result | – | – | – | +4.8-13.9 |
| | | $\mu + jets$ | | |
| ISR ↑↓ | +13.4-1.5 | +1.5-11.8 | -0.6-2.0 | -0.5-12.3 |
| FSR ↑↓ | +12.5-1.2 | +1.2-11.1 | +2.0-1.3 | +3.2-12.2 |
| ISR ↑↓ FSR ↑↓ | +9.6+1.5 | -1.5-8.8 | +1.3-2.6 | -4.1-7.5 |
| Result | – | – | – | +3.2-12.3 |

Table 9.6: Systematics from modelling of the initial/final state radiation

### 9.2.6 Monte Carlo Generators

Another source of systematic error is associated with Monte Carlo modelling of $t\bar{t}$ signal events. To estimate this error, results are compared using two different NLO ME (next to leading order matrix element) generators: MC@NLO and Powheg with both using

Herwig for parton shower generation. The MC@NLO generator is used as the nominal in this comparison. Additionally, two different parton shower (PS) generators, Pythia and Herwig, are sampled, with both using Powheg for the initial generation. The Herwig generator is used as the nominal in the comparison.

The uncertainty in MC modelling of the signal affects both the signal selection efficiency and the signal template shape. As previously, this is a two step process. Errors on the selection efficiency are found by comparing the efficiency measured in the variation samples to the nominal samples. Errors on the likelihood template shapes are found by fitting nominal mock datasets with nominal and shifted templates and comparing the results. The results are shown in Table 9.7, separately for the NLO generators and the parton shower generators.

| Source | relative uncertainty [%] | | | |
|---|---|---|---|---|
| | $\Delta\epsilon/\epsilon$ | $(\Delta\sigma/\sigma)_\epsilon$ | $(\Delta\sigma/\sigma)_{N_{t\bar{t}}}$ | $\Delta\sigma/\sigma$ |
| | | *e + jets* | | |
| NLO generator | +6.6-6.6 | +6.2-6.2 | +0.8-0.8 | +7.0-7.0 |
| Parton Shower | +4.8-4.8 | +5.0-5.0 | +2.4-2.4 | +2.6-2.6 |
| | | *$\mu$ + jets* | | |
| NLO generator | +5.4-5.4 | +5.1-5.1 | +1.2-1.2 | +3.9-3.9 |
| Parton Shower | +3.4-3.4 | +3.5-3.5 | +2.4-2.4 | +1.0-1.0 |

Table 9.7: Systematics from signal Monte Carlo generators

### 9.2.7 Parton Distribution Functions

The systematic error due to uncertainties in the Parton Distribution Functions (PDFs) are examined via event re-weighting, instead of generating new MC samples [167]. Events are re-weighted with probability factors calculated as:

$$w = \frac{P_N(x_1, f_1, Q) * P_N(x_2, f_2, Q)}{P_0(x_2, f_2, Q) * P_0(x_2, f_2, Q)} \tag{9.8}$$

where $P_N$ and $P_0$ are respectively the variation and the nominal parton distribution functions, for two hard scattering partons of flavor $f_1$ and $f_2$ and with fractional momentum $x_1$

and $x_2$. Q is the momentum transfer in the event. $x$, $f$ and $Q$ are all derived from the MC truth information.

The nominal PDF used in this analysis is CTEQ66, which is used for most of the generation. Additional PDFs used include MSTW08, and NNPDF2.0 sets [13]. The error bands are derived for all these PDFs following recommendations in [13]. The estimation of this systematic error is based on shifting separately each of these PDFs by its uncertainty. In principle the PDFs affect not only the signal efficiency but also the signal and background template shapes. However, the effect on the shapes is expected to be small. Hence we only considered the effect on the signal efficiency, which is estimated to be 1.7% for both channels [159].

### 9.2.8 $W + jets$ Heavy Flavor Content

Another large source of systematic error for this analysis arises from the uncertainty of the $W + jets$ Heavy Flavor (HF) fractions. This affects the analysis through the use of the SV0 weight as one of the top likelihood variables. This uncertainty only affects the $W + jets$ background template shape ($N_{t\bar{t}}$).

As discussed in Section 6.4.7, the $W + jets$ HF fractions are measured in the 2-jet bin and projected into higher jet multiplicity bins [103, 159]. Based on the preliminary results of the measurements, it is recommended to assume a 50% uncertainty of the $Wb\bar{b}$ and $Wc\bar{c}$ fractions and separately a 40% uncertainty of the $Wc$ fraction in the 2-jet bin. The projection factor to the $\geq$ 4-jet bin is 2.8±0.8 and 3.1±0.9 for the $e + jets$ and $\mu + jets$ channels respectively. The uncertainties in the $\geq$ 4-jet bin is extracted by combining the uncertainty in the 2-jet bin and the uncertainty from the projection factors, and are given in Table 9.8.

| HF type | $\Delta f/f$ [%] | |
|---|---|---|
| | $e + jets$ | $\mu + jets$ |
| $Wb\bar{b}$,$Wc\bar{c}$ | ±58% | ±58% |
| $Wc$ | ±49% | ±49% |

Table 9.8: Uncertainties of the $W + jets$ HF content in the $\geq$ 4-jet bin

The shifted likelihood templates for $W + jets$ are derived by varying the HF content in $W + jets$ with respect to the nominal, using the numbers in Table 9.8. The systematic error due to these uncertainties is obtained by fitting nominal mock datasets with nominal and shifted likelihood templates and comparing the results. The results are given in Table 9.9.

| Source | $\Delta\sigma/\sigma$ [%] | |
|---|---|---|
| | $e + jets$ | $\mu + jets$ |
| $Wb\bar{b}$,$Wc\bar{c}$ fraction | +4.5-4.7 | +5.1-5.3 |
| $Wc$ fraction | +1.1-1.1 | +1.3-1.3 |

Table 9.9: Systematics from uncertainties in $W + jets$ heavy flavor content

### 9.2.9 $W + jets$ Background Shape

While the $t\bar{t}$ signal modelling uncertainties were estimated by varying the $t\bar{t}$ Monte Carlo generators, the $W + jets$ modelling uncertainties are estimated by varying appropriate parameters of the Alpgen generator. These parameters are known as `iqopt` and `ptjmin`. The variable `iqopt` controls the renormalization/factorization scale $Q$, and the variable `ptjmin` is the cut on $p_T$ of the parton jet. The nominal $W + jets$ sample uses `iqopt` = 1, corresponding to $Q^2 = m_W^2 + \sum p_T^2(jet)$. Two variations are considered: `iqopt` = 2, corresponding to $Q^2 = m_W^2$, and `iqopt` = 3, meaning $Q^2 = m_W^2 + {p_T}_W^2$. The nominal $W + jets$ sample uses `ptjmin` = 15 $GeV$. Two variations are considered: `ptjmin` = 10 $GeV$ and `ptjmin` = 20 $GeV$.

These parameters are varied through re-weighting events in the nominal $W + jets$ sample, instead of generating new samples. The events are re-weighted for each variation with probability factors calculated from the number of jets with $p_T \geq 20\ GeV$ and the $p_T$ of the leading jet in the event [168].

The $W + jets$ modelling uncertainty only affects the $W + jets$ template shape ($N_{t\bar{t}}$). The systematic error is obtained by fitting nominal mock datasets with shifted $W + jets$ likelihood templates and comparing the results with the nominal analysis. This error is estimated for all four variations. The largest error in the positive and negative direction are taken as the final results. The results are shown in Table 9.10 in detail.

| Source | $\Delta\sigma/\sigma$ [%] | |
|---|---|---|
| | $e + jets$ | $\mu + jets$ |
| `iqopt2` | -0.4 | -0.4 |
| `iqopt3` | -0.2 | -0.2 |
| `ptjmin10` | -0.2 | -0.2 |
| `ptjmin20` | +0.0 | -0.0 |
| Result | +0.0-0.4 | +0.0-0.4 |

Table 9.10: Systematics from uncertainties in $W + jets$ background shape

### 9.2.10 QCD Background Shape

As discussed in Section 8.1.2, the shifted QCD shape in the $e+jets$ channel is obtained by changing the selection criteria for the anti-electrons. The systematic error on the template shapes due to this uncertainty is obtained by fitting the nominal mock data with the shifted QCD template and comparing the result with the nominal analysis. In the $\mu+jets$ channel, there is no variation sample available to produce the shifted template. Given that using the anti-electron modelling of the QCD background shape to fit the muon channel gives fractions from the fit method consistent with the matrix method (MM), a comparison is made between QCD shape from the anti-electron sample passing muon channel selections and the default MM method shape to extract the systematic error [169]. The results are shown in Table 9.11.

| Source | $\Delta\sigma/\sigma$ [%] | |
|---|---|---|
| | $e + jets$ | $\mu + jets$ |
| qcdShape | +1.0-1.0 | +6.5-6.5 |

Table 9.11: Systematics from uncertainties in QCD background shape

### 9.2.11 *b*-Tagging Calibration

The uncertainties in $b$-tagging calibration for the SV0 tagger were given in Table 4.9 and 4.10. This uncertainty does not affect the signal selection efficiency since $b$-tagging was not used in event selection. Therefore, only the systematic error on the template shapes ($N_{t\bar{t}}$) need to be estimated. Both the $t\bar{t}$ and the $W + jets$ template shapes are affected.

The shifted templates for $b$-tagging calibration are obtained by varying the data/MC scale factors (SFs) by $\pm 1\sigma$ and applying the varied $b$-tagging event weights to MC events (see Section 6.4.7). The systematic error on the template shapes come from fitting the nominal mock data with the shifted templates and comparing the results with the nominal analysis. Two systematic errors are estimated separately, the first from the $b$,$c$-jet efficiency uncertainty, listed in Table 4.9, and the second from the light jet mis-tag rate uncertainty, listed in Table 4.10. The resulting systematic error are shown in Table 9.12.

| Source | $\Delta\sigma/\sigma$ [%] | |
|---|---|---|
| | $e + jets$ | $\mu + jets$ |
| $b$,$c$-jet efficiency | +12.5-10.2 | +12.9-10.4 |
| light jet mistag rate | +1.0-0.8 | +0.8-0.7 |

Table 9.12: Systematics from uncertainties in $b$-tagging calibration scale factors

As expected, we observe a large systematic error from the $b$-tagging efficiency. This is due to the large uncertainty of the $b$-tagging SFs. Although the uncertainty of the mis-tag rate SFs is large too, the resulted systematic error is small. This is because the mis-tag rate is very low.

### 9.2.12 Single Top Normalization

Since the single top is subtracted from data before the ML fit, we estimate the systematic error due to single top normalization by changing the amount of single top subtracted from data by ±10% and redoing the fit to data. The fraction 10% is approximately the theoretical uncertainty on the single top cross section [16]. The resulting systematic error on the $t\bar{t}$ cross section is shown in Table 9.13.

### 9.2.13 Integrated Luminosity Uncertainty

The uncertainty on the integrated luminosity was given in Chapter 5 to be 3.4%. The uncertainty is translated to an error on the $t\bar{t}$ cross section using Equation 9.1 and shown

| Source | $\Delta\sigma/\sigma$ [%] | |
|---|---|---|
| | $e + jets$ | $\mu + jets$ |
| single top normalization | +0.5-0.5 | +0.4-0.4 |

Table 9.13: Systematics from the uncertainty of single top normalization

in Table 9.14.

| Source | $\Delta\sigma/\sigma$ [%] | |
|---|---|---|
| | $e + jets$ | $\mu + jets$ |
| Integrated luminosity | +3.5-3.3 | +3.5-3.3 |

Table 9.14: Error from the uncertainty of the integrated luminosity

### 9.3 Summary of Uncertainties

Table 9.16 summarizes the individual uncertainties contributing to the cross section measurement using the multivariate top likelihood method in this analysis. Results are shown for the $e + jets$ and $\mu + jets$ channel separately, and combined. The combination of the two channels will be discussed in Section 9.4. As expected, the most important sources of systematic error in this measurement arise from uncertainties in the JES, the modelling of ISR/FSR, the signal MC generators, and the $b$-tagging calibration. We have not considered sources such as the uncertainties on the lepton energy/momentum scale correction and resolution smearing, and the those associated with limited Monte Carlo statistics. These sources are expected to have a small effect.

This analysis assumes a top mass of 172.5 $GeV$. The current PDG value of the top mass is 172.0 $GeV$ (see Table 2.2). All the top MC samples were generated with this mass. No systematic is quoted for the uncertainty associated with the top mass, and this source of uncertainty is not included in the total systematic error on this measurement. This is due to the strong preference in the theory community to quote the cross section for different mass points instead of including it as a systematic error [159]. The dependence of the theoretical $t\bar{t}$ cross section on the top mass is shown in Table 9.15.

| $m_t$ [GeV] | $\sigma_{t\bar{t}}$ [pb] | Scale [pb] | | PDF [pb] | | Total [pb] | |
|---|---|---|---|---|---|---|---|
| 160.0 | 242.39 | +6.21 | -13.64 | +9.55 | -8.84 | +11.39 | -16.25 |
| 165.0 | 206.95 | +5.38 | -11.50 | +8.44 | -7.77 | +10.01 | -13.88 |
| 167.5 | 191.64 | +4.91 | -10.87 | +7.97 | -7.32 | +9.36 | -13.10 |
| 170.0 | 177.49 | +4.53 | -9.92 | +7.53 | -6.88 | +8.79 | -12.08 |
| 172.5 | 164.57 | +4.30 | -9.27 | +7.15 | -6.51 | +8.34 | -11.33 |
| 175.0 | 152.77 | +3.99 | -8.55 | +6.75 | -6.13 | +7.84 | -10.52 |
| 177.5 | 141.93 | +3.67 | -8.02 | +6.34 | -5.74 | +7.33 | -9.87 |
| 180.0 | 131.97 | +3.41 | -7.44 | +6.04 | -5.47 | +6.94 | -9.23 |
| 190.0 | 99.32 | +2.67 | -5.58 | +4.82 | -4.31 | +5.51 | -7.05 |

Table 9.15: Top pair production cross section at approximate NNLO for several values of the top quark mass $m_t$ [16]. The values are computed for $\sqrt{s} = 7$ TeV, CTEQ66 PDFs, and a scale choice of $\mu_R = \mu_F = m_t$.

The $t\bar{t}$ cross section results for the individual channels including all systematic errors are:

$$e + jets \text{ channel: } \sigma_{t\bar{t}} = 164.4^{+16.2}_{-15.4}(\text{stat})^{+31.2}_{-36.2}(\text{syst})^{+5.8}_{-5.4}(\text{lumi})\ pb \tag{9.9}$$

$$\mu + jets \text{ channel: } \sigma_{t\bar{t}} = 167.8^{+13.9}_{-13.4}(\text{stat})^{+30.9}_{-34.8}(\text{syst})^{+5.9}_{-5.5}(\text{lumi})\ pb \tag{9.10}$$

$$\tag{9.11}$$

## 9.4 Result of the Combined $t\bar{t}$ Cross Section

The combined cross section in the $l + jets$ channel is estimated by minimizing the sum of the negative log-likelihood functions in the $e + jets$ and the $\mu$+jets channel (Equation 8.8 and 8.5). The number of $t\bar{t}$ events $N_{t\bar{t}}$ in the likelihood functions is written in terms of the $t\bar{t}$ cross section $\sigma_{t\bar{t}}$, according to Equation 9.2. There are five parameters in the combined fit: $\sigma_{t\bar{t}}$, which is common to both channels, and $N_W$ and $N_{QCD}$, separately for each channel. The combined cross section, assuming a top quark mass of 172.5 $GeV$, is:

$$e + jets \text{ and } \mu + jets \text{ combined: } \sigma_{t\bar{t}} = 166.4^{+10.5}_{-10.2}(\text{stat})^{+31.7}_{-33.6}(\text{syst})^{+5.9}_{-5.5}(\text{lumi})\ pb \tag{9.12}$$

where the statistical error is obtained by varying the combined log-likelihood function by one half unit above the minimum allowing the fit parameters to float.

| Source | $\Delta\sigma/\sigma$ [%] | | |
|---|---|---|---|
| | $e + jets$ | $\mu + jets$ | Combined |
| Statistical error | +9.9-9.4 | +8.3-8.0 | +6.3-6.1 |
| *Object selection* | | | |
| Lepton reco,Id,Trigger SF | +4.1-3.8 | +1.0-1.0 | +1.8-1.8 |
| Jet energy scale | +7.4-8.0 | +6.3-6.6 | +6.8-7.2 |
| Jet energy resolution | +0.1-0.1 | +0.1-0.1 | +0.1-0.1 |
| Jet reconstruction efficiency | +5.2-5.2 | +5.7-5.7 | +5.5-5.5 |
| *Signal modelling* | | | |
| ISR/FSR | +4.8-13.9 | +3.2-12.3 | +3.9-13.0 |
| NLO generator | +8.0-7.0 | +4.4-3.9 | +5.3-5.3 |
| Parton Shower | +2.6-2.3 | +1.0-0.9 | +1.7-1.7 |
| PDF | +1.7-1.7 | +1.7-1.7 | +1.7-1.7 |
| *Background modelling* | | | |
| $W + jets$ HF content ($Wb\bar{b}$,$Wc\bar{c}$) | +4.5-4.7 | +5.1-5.3 | +4.8-5.1 |
| $W + jets$ HF content ($Wc$) | +1.1-1.1 | +1.3-1.3 | +1.2-1.2 |
| $W + jets$ shape | +0.0-0.4 | +0.0-0.4 | +0.0-0.4 |
| QCD shape | +1.0-1.0 | +6.5-6.5 | +3.9-3.9 |
| *Other* | | | |
| $b$-tagging efficiency | +12.5-10.2 | +12.9-10.4 | +12.7-10.4 |
| $b$-tagging mistag rate | +1.0-0.8 | +0.8-0.7 | +0.9-0.8 |
| single top normalization | +0.5-0.5 | +0.4-0.4 | +0.5-0.5 |
| Sum systematics | +19.0/-22.0 | +18.4/-20.7 | +19.0-20.2 |
| Integrated luminosity | +3.5/-3.3 | +3.5/-3.3 | +3.5-3.3 |

Table 9.16: Summary of individual uncertainties contributing to the cross section measurement using the multivariate topological likelihood method. All numbers are relative errors expressed as percentage.

The systematic error on the combined cross section is estimated following the same procedure used for the individual channels, taking into account the correlations of the systematic uncertainties between the channels. The uncertainty associated with a certain source is classified as either fully correlated or uncorrelated between the channels. Systematic uncertainties affecting the two channels simultaneously are considered fully correlated, which includes most of the uncertainties we considered. However, the uncertainty in the lepton scale factors and the uncertainty in the QCD background shape, are considered as uncorrelated.

The correlated and uncorrelated uncertainties are treated differently in the ensemble test procedure. Take the JES uncertainty as an example for the correlated uncertainties. The systematic error associated with the JES uncertainty is estimated by shifting simultaneously the likelihood templates for the $e + jets$ and $\mu + jets$ channels and fitting the nominal mock data with them. The fractional change of the average fitted $\sigma_{t\bar{t}}$ with respect to the nominal analysis is taken as the systematic error. With uncorrelated uncertainties, this procedure has to be done twice. For example, the systematic error due to the uncertainty in the lepton scale factors is obtained by first estimating separately the systematic error due to the electron scale factors and the muon scale factors, and then adding the two errors quadratically.

The result of the combined $t\bar{t}$ cross section, including both the statistical and the systematical error, was presented above in Equation 9.12. The individual uncertainty contributions are summarized in Table 9.16. The statistical error has been reduced by a factor of $\sim \sqrt{2}$, while the systematic error remains approximately the same as the individual measurements.

# Chapter 10

# Summary and Discussion

This dissertation presents a measurement of the top pair ($t\bar{t}$) production cross section using the semileptonic decay final states at a center-of-mass energy ($\sqrt{s}$) of 7 $TeV$. The measurement utilized approximately 35.3 $pb^{-1}$ of data produced by the Large Hadron Collider (LHC), which currently collides proton-proton ($pp$) pairs at this center-of-mass energy. The data was collected by the ATLAS detector in 2010.

A series of event selection criteria was developed based on the $t\bar{t}$ semileptonic final state signature. The signature consists of a charged lepton ($l = e$ or $\mu$), a neutrino, and $\geq 4$ jets, all produced with high transverse energy/momentum ($E_T/p_T$). The selection cuts were optimized to select $t\bar{t}$ signal events over the $W + jets$ and QCD multijet background. After the selection, 396 events were observed in data in the $e + jets$ channel and 653 events in the $\mu + jets$ channel. However the selected data still contain a large fraction of $W + jets$ background events.

In order to preserve sample statistics, a top likelihood discriminant was built to further discriminate the $t\bar{t}$ signal and the backgrounds. Many variables were considered for the likelihood discriminant, including the lepton charge asymmetry, the $b$-tagging SV0 weight, as well as many kinematic and topological variables. The final set of variables was optimized to reduce the total error on the $t\bar{t}$ cross section measurement. Four variables were used to construct the final likelihood discriminant: $\ln(C)$, $\exp(-11\mathcal{A})$, $\eta_l$, and binary $\mathrm{SV0}_{max}$ (see Table 7.1 for definitions of these variables).

The number of $t\bar{t}$ events ($N_{t\bar{t}}$) in the selected sample was extracted via a binned maximum likelihood (ML) fit to the top likelihood distribution, and the $t\bar{t}$ cross section was derived using the fit results. The $t\bar{t}$ cross section was first measured separately in the $e + jets$ channel and the $\mu + jets$ channel. The measurements in the two channels were subsequently combined. The measured $t\bar{t}$ cross section is found to be:

$$e + jets \text{ channel: } \sigma_{t\bar{t}} = 164.4^{+16.2}_{-15.4}(\text{stat})^{+31.2}_{-36.2}(\text{syst})^{+5.8}_{-5.4}(\text{lumi})\ pb \quad (10.1)$$

$$\mu + jets \text{ channel: } \sigma_{t\bar{t}} = 167.8^{+13.9}_{-13.4}(\text{stat})^{+30.9}_{-34.8}(\text{syst})^{+5.9}_{-5.5}(\text{lumi})\ pb \quad (10.2)$$

$$e + jets \text{ and } \mu + jets \text{ combined: } \sigma_{t\bar{t}} = 166.4^{+10.5}_{-10.2}(\text{stat})^{+31.7}_{-33.6}(\text{syst})^{+5.9}_{-5.5}(\text{lumi})\ pb \quad (10.3)$$

assuming a top mass of 172.5 $GeV$. The results in the $e + jets$ and $\mu + jets$ channel agree very well with each other. The difference between the channels is much smaller than one standard deviation of the combined cross section, even if only the statistical error is considered. The dominant sources of the systematic error on the measurement are uncertainties in the Jet Energy Scale (JES), uncertainties in the modelling of the initial/final state radiation (ISR/FSR), uncertainties in the signal Monte Carlo (MC) generators, uncertainties in $b$-tagging calibration, and uncertainties in the $W + jets$ HF (heavy flavor) fractions. It is observed that the error on the cross section is dominated by the systematic error even with the small dataset.

The measured $t\bar{t}$ cross section can be compared to recent Standard Model calculations discussed in Section 2.2.4. Figure 10.1 shows the theoretical predictions along with the $t\bar{t}$ cross section measured with data. The cross section result from this measurement is consistent with the theoretical predictions. However, the large error on the measurement cannot rule out the existence of BSM models.

Figure 10.1 also shows the published $t\bar{t}$ cross sections from ATLAS and CMS using respectively 2.9 $pb^{-1}$ and 3.1 $pb^{-1}$ [161, 170]. Both the ATLAS and the CMS analyses were based on the cut-and-count method. ATLAS used a combination of measurements in the semileptonic channel and the dilepton channel, and CMS used only the dilepton channel. Our new result has improved the statistical and systematic errors compared to the earlier results with approximately 3 $pb^{-1}$.

Figure 10.2 shows a more detailed comparison of our result with the 2.9 $pb^{-1}$ measurement from ATLAS. The individual lepton plus jet channels are shown along with the combined measurement for each. One sees that the statistical error is reduced by a factor of $\sim 3$, because the integrated luminosity has been increased by a factor of $\sim 10$. There is also an improvement in the systematical error, which is attributed to the difference in the

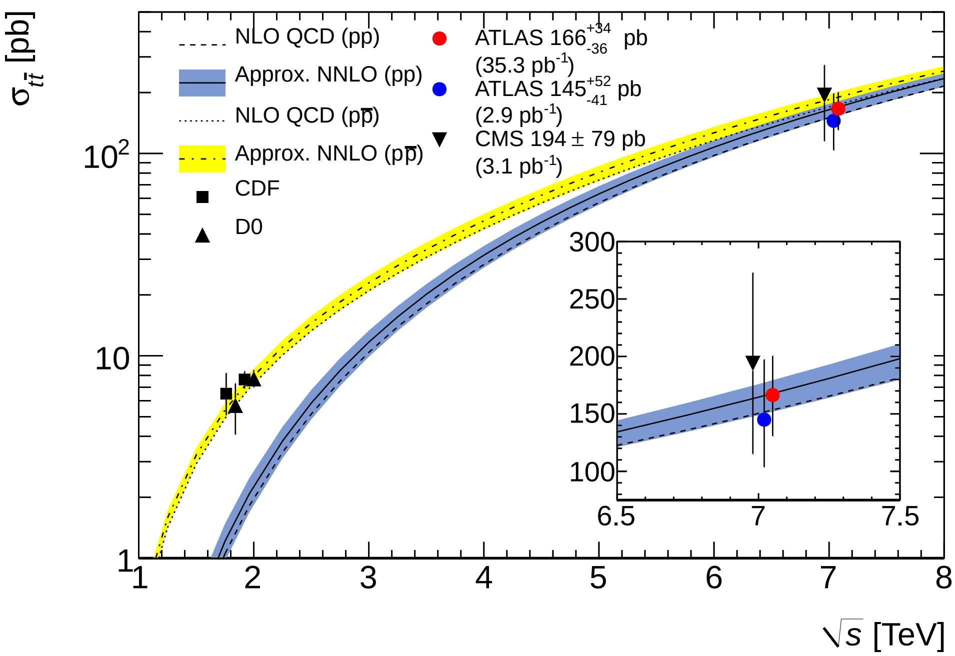


Figure 10.1: Comparison of the $t\bar{t}$ production cross section measured using data with the SM predictions. In addition to the combined result from this measurement, published $t\bar{t}$ cross sections from ATLAS and CMS using approximately 3 $pb^{-1}$ of data are also included [161, 170]. Both analyses were based on the cut-and-count method. The ATLAS result was from a combination of measurements using semileptonic and dilepton channels. The CMS result was from the dilepton channel.

analysis methods. The cut-and-count method used Monte Carlo predictions for the determination of most of its backgrounds and the theoretical uncertainty from the $W + jets$ background is large. While our measurement is subject to a large systematic error from $b$-tagging, it still has a improved systematic error compared to the cut-and-count method.

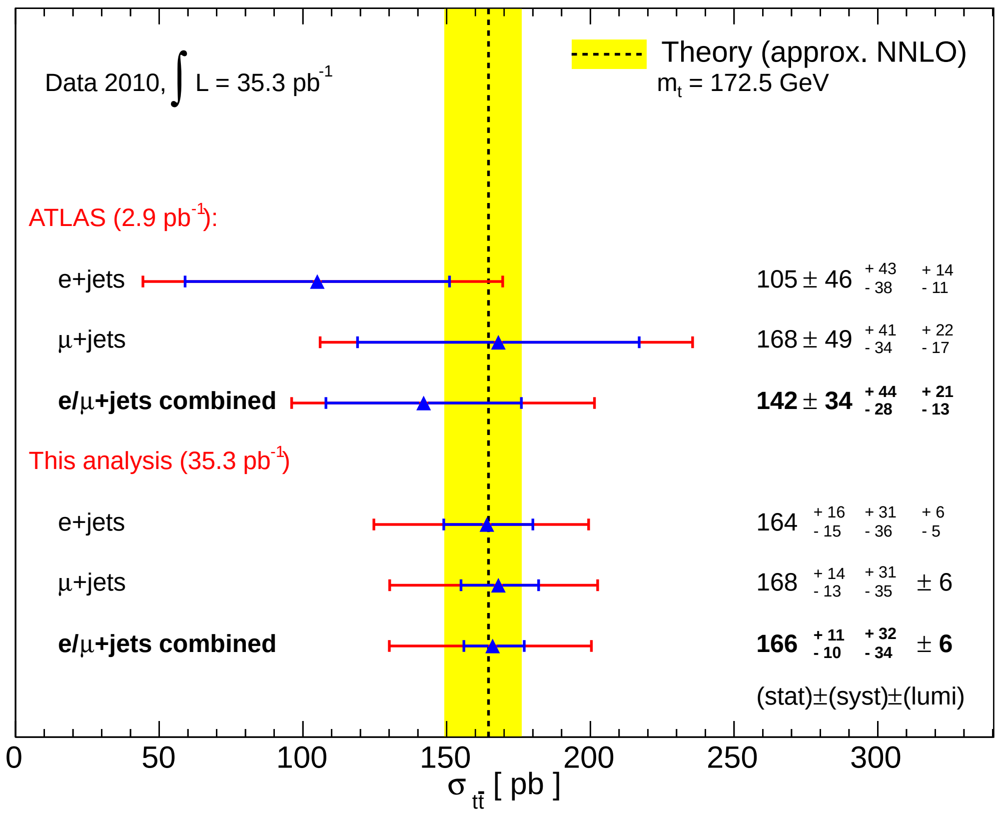


Figure 10.2: Comparison of this measurement with the previous ATLAS measurement in the semileptonic channel, using 2.9 $pb^{-1}$ of data based on the cut-and-count method

The analysis documented was one of the several analyses that sought to measure the $t\bar{t}$ cross section in the lepton plus jets channel using 2010 data. In particular, two other analyses also employed a multivariate approach to extract the $t\bar{t}$ cross section [171, 172]. At some level, a comparison of these three analyses, including ours, serves to cross check one another. One of the other two analyses also used $b$-tagging, as in our analysis. Here we refer to it as “Multivariate 1”. The second analysis did not use $b$-tagging. We refer to it as “Multivariate 2”. Both analyses employed slightly different variables and statistical techniques compared to this analysis. The results of these analyzes are shown in Figure 10.3, along with the results of our analysis.

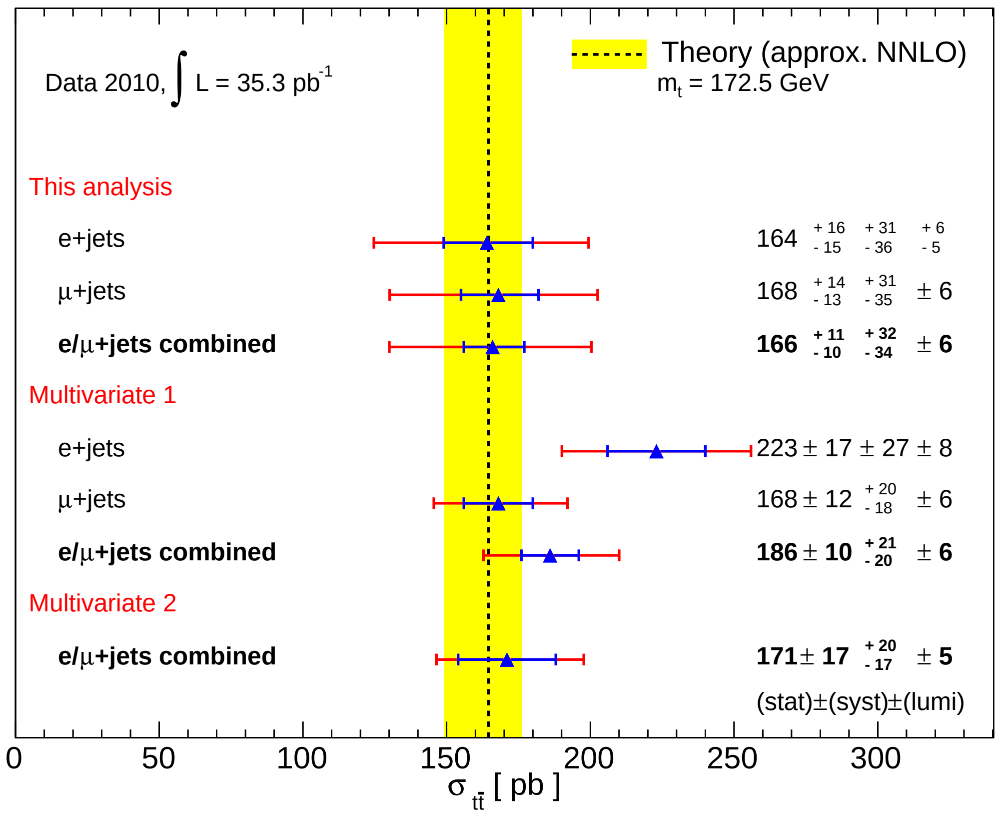


Figure 10.3: Comparison of the three multivariate analyses, including this analysis

The Multivariate 1 analysis used the following four variables: lepton $\eta$, $\exp(-8\mathcal{A})$, $H_T^{3\prime}$, and the average of $-log_{10}(w_{JetProb})$ of the two jets with the lowest JetProb weight, $w_{JetProb}$. The first two variables were also used in our analysis. The third variable, $H_T^{3\prime}$, is similar to the $H_T^{2\prime}$ variable that we considered (see Table 7.1). It is the scalar sum of the $p_T$ of jets, excluding the leading two jets, divided by the scalar sum of $p_z$ of jets, lepton and neutrino. The fourth variables is derived from the JetProb weight of the JetProb $b$-tagging algorithm (see Section 4.5).

The variables used by the Multivariate 1 analysis are very similar to those used in our analysis. However, there is one major difference. This analysis used a different tagger, the JetProb tagger, instead of the SV0 tagger used in this analysis. Further, it used a continuous distribution of the average of the two highest values of $-log_{10}(w_{JetProb})$. As mentioned in Section 4.5.2, the JetProb tagger was calibrated at two working points. In the Multivariate 1 analysis, the continuous distribution of the JetProb weights is calibrated using results at the two working points and extrapolating between them. The usage of the continuous variable instead of the binary variable is expected to improve the separation power of the likelihood discriminant. However, the correctness of extrapolation procedure for the calibration cannot be proved. If the distribution is not calibrated correctly, the difference between the data and MC distributions could bias the ML fit result. This may be a possible explanation as to why there is such a big difference between the $e + jets$ and $\mu + jets$ results of the Multivariate 1 analysis.

In addition to the difference in the variables used, Multivariate 1 also includes events in the 3-jet bin. This was not done in our measurement. In the Multivariate 1 analysis, likelihood discriminants are built separately in the 3-, 4- and $\geq$ 5 jet bins, and a comparison is made between the different jet multiplicity bins. Due to the limited statistics, the analysis did not extract the cross section in these bins separately. Instead, a combined ML fit was performed using the sum of the negative log-likelihood functions in 3-, 4- and $\geq$ 5 bins, separately for the $e + jets$ and $\mu + jets$ channel. The results were then combined to give the final result for the $l + jets$ channel. Inclusion of the 3-jet multiplicity bin improves the statistical error slightly, by about 10% compared to our analysis.

As seen in Figure 10.3, the Multivariate 1 analysis gives a smaller systematic error compared to our analysis. This is attributed to the different approaches taken by the analyses to estimate the systematic error. Our analysis, as well as the Multivariate 2 analysis, used the ensemble test procedure described in Section 8.3 to estimate the systematic error due to each individual source. The total systematic error is estimated by the quadratic sum of all the individual contributions. This method, by construction, gives the most conservative error.

In the Multivariate 1 analysis, a profile likelihood fit procedure was employed. The profile likelihood is obtained by adding nuisance parameters to the negative log-likelihood functions. One parameter is added for each source of systematic uncertainties. The nuisance parameter terms are added linearly in the profile likelihood. A fit to the discriminant distribution in data using the profile likelihood extracts the values of all the nuisance parameters as well as the number of signal and background events simultaneously. The systematic error can be obtained directly from the result of the fit. The profile fit procedure takes into account possible correlations between the individual sources of the systematic error. The individual contributions can in theory cancel one another. As such, this method yields a smaller error than our method. Also note that the profile likelihood fit by construction allows the systematic uncertainties to vary the central value of the measured cross section.

In addition to the different approaches taken to estimate the systematic error, there is also evidence that building separate profile likelihood in the different jet multiplicity bins and doing a combined fit with them reduces the systematic error. The systematic error could be different in different jet multiplicity bins and they could cancel one another during the fit.

The Multivariate 2 analysis used the following three variables: lepton charge, lepton $\eta$, and $\exp(-8\mathcal{A})$. This analysis did not use information from $b$-tagging. As a result, the separation power of its likelihood discriminant was much less significant than the Multivariate 1 analysis and our analysis. The worsened separation power leads to a larger statistical error compared to the other two analyses. On the other hand, this analysis is not affected by uncertainties associated with the $b$-tagging calibration and the $W + jets$ HF (heavy flavor) fractions. As a result, the systematic error on this measurement is smaller compared to the other two methods. The total error of this measurement is compatible with the other two analyses.

The low separation power of the likelihood discriminant also lowers the sensitivity of the ML fit to the signal contribution. This could result in a large shift of the central value of the measured cross section. Although this effect is not reflected in the number shown in Figure 10.3, when fitting to the likelihood in the individual channels, a large deviation compared to the result of the combined fit was observed [162].

The Multivariate 2 analysis also used events from the 3-jet bin, which should have reduced its statistical error. A combined fit using the sum of the negative log-likelihood functions in the 3-jet and $\geq -4$ bins for both the $e + jets$ and $\mu + jets$ channel is performed to extract the cross section number shown in Figure 10.3. Measurements in the individual channels were not performed in this analysis.

Besides the multivariate analyses, there were also analyses that fit to a single variable, such as the lepton $\eta$ distribution and the top mass distribution [162, 163]. These analyses are not as sensitive as the multivariate ones. However, they provide good cross checks to the multivariate analyses, because the single variables are sensitive to different systematic uncertainties.

All the analyses performed so far are statistically limited. The statistical error will be reduced by the larger amount of data that will be collected at ATLAS in 2011 and 2012. At 35.3 $pb^{-1}$, we have seen an improvement of a factor of $\sim$ 3 in the statistical error compared to the 2.9 $pb^{-1}$ analysis. It is expected that ATLAS will collect at least 1 $fb^{-1}$ of data in 2011. This translates to a factor of $\sim \sqrt{30} \sim 5$ improvement in the statistical error compared to the current analysis. This means the statistical error will be reduced to around 1-2% for our analysis.

Although the analyses are dominated by systematic uncertainties, most of these systematic uncertainties are also of a statistical nature. With more data, the uncertainties in various data/MC scale factors, including the $b$-tagging scale factors, will be largely reduced. The $W + jets$ HF fractions will also be more accurately measured. The Monte Carlo modelling of the signal and backgrounds can be better tuned using data. For example, the modelling of the ISR/FSR based on the AMBT1 UE (underlying event) tune used only about 6.8 $\mu b^{-1}$ of the 7 $TeV$ data [129, 173]. Larger datasets can be used to reduce this systematic.

Once the inclusive $t\bar{t}$ cross section can be accurately measured, further studies can be performed to study the differential cross section as a function of the $t\bar{t}$ kinematics. Even if the total $t\bar{t}$ cross section agrees with the Standard Model, the differential cross section could be different in a specific kinematic region. For example, the $t\bar{t}$ resonance can appear as an excess (bump) of events in the $t\bar{t}$ invariant mass spectrum. Since today's signal becomes tomorrow's background we can look forward to many searches for BSM physics using top quarks in the coming years.

# References

[1] J. R. Incandela, A. Quadt, W. Wagner, and D. Wicke, *Status and Prospects of Top-Quark Physics*, Prog.Part.Nucl.Phys. **63** (2009) 239–292, arXiv:0904.2499 [hep-ex].

[2] Particle Data Group, K. Nakamura et al., *Review of particle physics*, J.Phys.G **G37** (2010) 075021.

[3] D. Griffiths, *Introduction to elementary particles*. Wiley-VCH, Weinheim, Germany, 2008.

[4] C. Quigg, *Gauge theories of the strong, weak and electromagnetic interactions*, Front.Phys. **56** (1983) 1–334.

[5] R. Ellis, W. Stirling, and B. Webber, *QCD and collider physics*, Camb.Monogr.Part.Phys.Nucl.Phys.Cosmol. **8** (1996) 1–435.

[6] P. Nason, S. Dawson, and R. Ellis, *The Total Cross-Section for the Production of Heavy Quarks in Hadronic Collisions*, Nucl.Phys. **B303** (1988) 607.

[7] CTEQ Collaboration, R. Brock et al., *Handbook of perturbative QCD; Version 1.1: September 1994*, Rev. Mod. Phys. (1994) . Fermilab Library Only.

[8] N. Kidonakis and R. Vogt, *The theoretical top quark cross section at the Tevatron and the LHC*, Phys.Rev. **D78** (2008) 074005, arXiv:0805.3844 [hep-ph].

[9] S. Moch and P. Uwer, *Theoretical status and prospects for top-quark pair production at hadron colliders*, Phys.Rev. **D78** (2008) 034003, arXiv:0804.1476 [hep-ph].

[10] *The Coordinated Theoretical-Experimental Project on QCD*, http://www.phys.psu.edu/~cteq/.

[11] *MRS/MRST/MSTW PARTON DISTRIBUTIONS*, http://durpdg.dur.ac.uk/hepdata/mrs.html.

[12] *NNPDF Parton Distributions*, http://sophia.ecm.ub.es/nnpdf/nnpdf_pdfsets.htm.

[13] M. Botje, J. Butterworth, A. Cooper-Sarkar, A. de Roeck, J. Feltesse, et al., *The PDF4LHC Working Group Interim Recommendations*, arXiv:1101.0538 [hep-ph].

[14] U. Langenfeld, S. Moch, and P. Uwer, *New results for t anti-t production at hadron colliders*, `arXiv:0907.2527 [hep-ph]`.

[15] M. Aliev, H. Lacker, U. Langenfeld, S. Moch, P. Uwer, et al., *HATHOR: HAdronic Top and Heavy quarks crOss section calculatoR*, Comput.Phys.Commun. **182** (2011) 1034–1046, `arXiv:1007.1327 [hep-ph]`.

[16] S. Allwood-Spires, M. Barisonzi, H. Beauchemin, R. Bruneliere, J. Buchanan, N. F. Castro, E. Devetak, C. Feng, J. Ferrando, R. Hawkings, D. Hirschbuehl, U. Husemann, B. P. Kersevan, G. Khoriauli, T. Kuhl, T. Lenz, L. Mijovc, A. Papadelis, M. P. Sanders, L.-Y. Shan, P. Sturm, F. Veloso, W. Verkerke, N. Vlasov, and C. Wasicki, *Monte Carlo samples used for top physics: Top Working Group Note IX*, ATL-COM-PHYS-2010-836, CERN, Geneva, Oct, 2010. Supporting document for top paper.

[17] DØ Collaboration, V. Abazov et al., *$t\bar{t}$ production cross-section in $p\bar{p}$ collisions at $\sqrt{s}$ = 1.8-TeV*, Phys.Rev. **D67** (2003) 012004, `arXiv:hep-ex/0205019 [hep-ex]`.

[18] DØ Collaboration, *Measurement of the ttbar Cross Section in the lepton+jets Channel with 5.3 $fb^{-1}$*, DØ note 6037-CONF (2010) (Run II), 2010.

[19] CDF Collaboration, A. A. Affolder et al., *Measurement of the $t\bar{t}$ production cross section in $p\bar{p}$ collisions at* $\sqrt{s}$ = 1.8 *TeV*, Phys.Rev. **D64** (2001) 032002, `arXiv:hep-ex/0101036 [hep-ex]`.

[20] CDF Collaboration, *Measurement of the Top Cross Section in the Lepton + Jets Channel Using Simultaneous Kinematic Fits with 2.7 $fb^{-1}$ of CDF Data*, CDF public note 10137 (2010) (Run II), 2010.

[21] E. Bruning, Oliver S., E. Collier, P., E. Lebrun, P., E. Myers, S., E. Ostojic, R., et al., *LHC Design Report. 1. The LHC Main Ring*, 2004.

[22] E. Buning, O., E. Collier, P., E. Lebrun, P., E. Myers, S., E. Ostojic, R., et al., *LHC Design Report. 2. The LHC infrastructure and general services*, 2004.

[23] *LHC Images*, `http://lhc-machine-outreach.web.cern.ch/lhc%2Dmachine%2Doutreach/lhc_in_pictures.htm`.

[24] E. Benedikt, M., E. Collier, P., E. Mertens, V., E. Poole, J., and E. Schindl, K., *LHC Design Report. 3. The LHC injector chain*, 2004.

[25] *Summary of the analysis of the 19 September 2008 incident at the LHC. Rsum de l'analyse de l'incident survenu le 19 septembre 2008 au LHC*, , CERN, Geneva, Oct, 2008.

[26] M. Bajko, F. Bertinelli, N. Catalan-Lasheras, S. Claudet, P. Cruikshank, K. Dahlerup-Petersen, R. Denz, P. Fessia, C. Garion, J. Jimenez, G. Kirby, P. Lebrun, S. Le Naour, K.-H. Mess, M. Modena, V. Montabonnet, R. Nunes, V. Parma, A. Perin, G. de Rijk, A. Rijllart, L. Rossi, R. Schmidt, A. Siemko, P. Strubin, L. Tavian, H. Thiesen, J. Tock, E. Todesco, R. Veness, A. Verweij, L. Walckiers, R. Van Weelderen, R. Wolf, S. Fehr, R. Flora, M. Koratzinos, P. Limon, and J. Strait, *Report of the Task Force on the Incident of 19th September 2008 at the LHC. oai:cds.cern.ch:1168025*, LHC-PROJECT-Report-1168. CERN-LHC-PROJECT-Report-1168, CERN, Geneva, Mar, 2009.

[27] *Incident in LHC sector 3-4*, `http://press.web.cern.ch/press/PressReleases/Releases2008/PR09.08E.html`.

[28] *CERN releases analysis of LHC incident*, `http://press.web.cern.ch/press/PressReleases/Releases2008/PR14.08E.html`.

[29] ATLAS Collaboration, W. Armstrong et al., *ATLAS: Technical proposal for a general-purpose pp experiment at the Large Hadron Collider at CERN*, 1994.

[30] *ATLAS: Detector and physics performance technical design report. Volume 1*, 1999.

[31] *ATLAS: Detector and physics performance technical design report. Volume 2*, 1999.

[32] ATLAS Collaboration, G. Aad et al., *The ATLAS Experiment at the CERN Large Hadron Collider*, JINST **3** (2008) S08003.

[33] J. Pequenao, *Computer generated image of the whole ATLAS detector*, 2008.

[34] ATLAS Collaboration, *ATLAS inner detector: Technical design report. Vol. 1*, 1997.

[35] ATLAS Collaboration, *ATLAS inner detector: Technical design report. Vol. 2*, 1997.

[36] ATLAS Collaboration, M. Alam et al., *ATLAS pixel detector: Technical design report*, 1998.

[37] J. Pequenao, *Computer generated image of the ATLAS inner detector*, 2008.

[38] ATLAS Collaboration, *ATLAS liquid argon calorimeter: Technical design report*, 1996.

[39] ATLAS Collaboration, *ATLAS tile calorimeter: Technical design report*, 1996.

[40] J. Pequenao, *Computer Generated image of the ATLAS calorimeter*, 2008.

[41] ATLAS Collaboration, *ATLAS muon spectrometer: Technical design report*, 1997.

[42] ATLAS Muon Collaboration, E. Diehl, *ATLAS Muon Detector Commissioning*, `arXiv:0910.2767 [physics.ins-det]`.

[43] G. Mikenberg, *The ATLAS muon spectrometer*, Mod.Phys.Lett. **A25** (2010) 649–667.

[44] J. Wotschack, *MDT Parameter Book; draft 3*, , CERN, Geneva, 2007.

[45] D. Lellouch, L. Levinson, and K. Hasuko, *Naming and numbering scheme for the Endcap muon trigger system*, ATL-MUON-2001-002, CERN, Geneva, Jun, 2000.

[46] J. Pequenao, *Computer generated image of the ATLAS Muons subsystem*, 2008.

[47] M. M. Block, *Hadronic forward scattering: Predictions for the Large Hadron Collider and cosmic rays*, Phys.Rept. **436** (2006) 71–215, `arXiv:hep-ph/0606215 [hep-ph]`.

[48] M. M. Block and F. Halzen, *Forward hadronic scattering at 7 TeV: predictions for the LHC: an update*, `arXiv:1102.3163 [hep-ph]`.

[49] ATLAS Collaboration, E. Duckeck, G. et al., *ATLAS computing: Technical design report*, 2005.

[50] ATLAS Collaboration, *ATLAS level-1 trigger: Technical Design Report*, 1998.

[51] ATLAS Collaboration, *ATLAS DAQ, EF, LVL2 and DCS: Technical progress report*, 1998.

[52] ATLAS Collaboration, *ATLAS trigger performance: Status report*, 1998.

[53] *ATLAS High-Level Triggers, DAQ and DCS Technical Proposal*, 2000.

[54] ATLAS Collaboration, *ATLAS high-level trigger, data acquisition and controls: Technical design report*, 2003.

[55] ATLAS TDAQ Collaboration, A. dos Anjos, *The DAQ/HLT system of the ATLAS experiment*, PoS **ACAT08** (2008) 044.

[56] C. ATLAS, *Performance of the ATLAS Trigger in 2010 running at the LHC*, ATL-COM-DAQ-2011-009, CERN, Geneva, Jan, 2011.

[57] P. Calafiura, W. Lavrijsen, C. Leggett, M. Marino, and D. Quarrie, *The Athena control framework in production, new developments and lessons learned*, in *Computing In High-Energy Physics (CHEP '04) PROCEEDINGS*, pp. 456–458. 2005.

[58] *AthenaFramework*, `https://twiki.cern.ch/twiki/bin/view/Atlas/AthenaFramework`.

[59] F. Akesson and E. Moyse, *Event data model in ATLAS*, in *Computing In High-Energy Physics (CHEP '04) PROCEEDINGS*, pp. 255–258. 2005.

[60] ATLAS Collaboration, A. Farbin, *ATLAS analysis model*, J.Phys.Conf.Ser. **119** (2008) 042012.

[61] ATLAS Collaboration, *Expected performance of the ATLAS experiment: detector, trigger and physics*. CERN, Geneva, 2009.

[62] *ElectronReconstruction*, `https://twiki.cern.ch/twiki/bin/view/AtlasProtected/ElectronReconstruction`.

[63] *ElectronIdentification*, `https://twiki.cern.ch/twiki/bin/view/AtlasProtected/ElectronIdentification`.

[64] *MuonCombinedReconstruction*, `https://twiki.cern.ch/twiki/bin/view/AtlasProtected/MuonPerformance#MuonCombinedReconstruction`.

[65] *MuonRecoPedia*, `https://twiki.cern.ch/twiki/bin/view/AtlasProtected/MuonRecoPedia`.

[66] *JetAlgorithms*, `https://twiki.cern.ch/twiki/bin/view/AtlasProtected/JetAlgorithms`.

[67] *JetCalibration*, `https://twiki.cern.ch/twiki/bin/view/AtlasProtected/JetCalibration`.

[68] *ATLAS Flavour Tagging Working Group*, `https://twiki.cern.ch/twiki/bin/view/AtlasProtected/FlavourTagging`.

[69] *EtMiss*, `https://twiki.cern.ch/twiki/bin/view/AtlasProtected/EtMiss`.

[70] J. Cranshaw, A. Doyle, M. Kenyon, D. Malon, H. McGlone, et al., *Integration of the ATLAS tag database with data management and analysis components*, J.Phys.Conf.Ser. **119** (2008) 042008.

[71] *Tools for Making Derived Physics Datasets (DPD)*, `https://twiki.cern.ch/twiki/bin/view/AtlasProtected/DPDMakingTools`.

[72] *TopPhys Software Project*, https://twiki.cern.ch/twiki/bin/view/Atlas/TopPhys.

[73] *Known Issues with 16.0.3.3.3 TopPhys cache*, https://twiki.cern.ch/twiki/bin/view/AtlasProtected/TopRecoBugs#Known_Issues_with_16_0_3_3_3_Top.

[74] *ElectronsEnergyDirection*, https://twiki.cern.ch/twiki/bin/view/AtlasProtected/ElectronsEnergyDirection.

[75] M. Aharrouche, C. Anastopoulos, V. Dao, F. Derue, F. Dudziak, O. Fedin, D. Fournier, D. Froidevaux, J. Hartert, L. Iconomidou-Fayard, K. Kerschen, S. Koenig, T. Koffas, V. Maleev, E. Paganis, G. Psztor, J. Poveda, A. Robichaud-Vronneau, A. Schaffer, T. Sarangi, E. Sedykh, V. Solovyev, K. Tackmann, T. Theveneaux-Pelzer, P. Urquijo, M. Wielers, and S. L. Wu, *Expected electron performance in the ATLAS experiment*, ATL-PHYS-INT-2010-126, CERN, Geneva, Nov, 2010.

[76] *Definition of ElectronTight_withTrackMatch quality word*, https://svnweb.cern.ch/trac/atlasoff/browser/Reconstruction/egamma/egammaEvent/tags/egammaEvent-03-04-24-03/egammaEvent/egammaPIDdefs.h#L341.

[77] *Muon Types and Quality Levels*, https://twiki.cern.ch/twiki/bin/view/AtlasProtected/MCPAnalysisGuidelinesRel16#AnchorTypes.

[78] *QualityDefinitionMuid*, https://twiki.cern.ch/twiki/bin/view/AtlasProtected/QualityDefinitionMuid.

[79] *Muon Selection Guidelines*, https://twiki.cern.ch/twiki/bin/view/AtlasProtected/MCPAnalysisGuidelinesRel16#AnchorSelections.

[80] *Determination of the muon reconstruction efficiency in ATLAS at the Z resonance in proton-proton collisons at sqrt(s)=7 TeV*, ATLAS-CONF-2011-008, CERN, Geneva, Feb, 2011.

[81] L. Asquith, B. Brelier, J. M. Butterworth, M. Campanelli, T. Carli, G. Choudalakis, P. A. Delsart, S. De Cecco, P. O. Deviveiros, M. D'Onofrio, S. Eckweiler, E. Feng, P. Francavilla, S. Grinstein, I. La Plante, J. Huston, N. Ghodbane, D. Lopez Mateos, B. Martin, N. Makovec, S. Majewsky, M. Martinez, D. W. Miller, J. Monk, K. Perez, C. Roda, J. Robinson, A. Schwartzmann, F. Spano, K. Terashi, F. Vives, P. Weber, and S. Zenz, *Performance of Jet Algorithms in the ATLAS Detector*, ATL-COM-PHYS-2009-630, CERN, Geneva, Dec, 2009.

[82] B. Salvacha, S. Chekanov, and J. Proudfoot, *Comparison of MC based Jet Energy Scales applied after H1 calibration*, ATL-PHYS-INT-2009-050. ATL-COM-PHYS-2009-162, CERN, Geneva, Apr, 2009.

[83] D. Lopez Mateos, E. W. Hughes, and A. Schwartzman, *A Simple $p_T$- and $\eta$-Dependent Monte Carlo-Based Jet Calibration*, ATL-COM-PHYS-2009-076, CERN, Geneva, Feb, 2009.

[84] D. Lopez Mateos, E. W. Hughes, and A. Schwartzman, *Jet Energy Resolution Improvement After Calibration Using Longitudinal Calorimeter Segmentation in ATLAS*, ATL-PHYS-INT-2009-051. ATL-COM-PHYS-2009-163, CERN, Geneva, Apr, 2009.

[85] S. Cabrera Urban, M. J. Costa, N. Ghodbane, I. M. Nugent, S. Adomeit, J. F. Arguin, C. Bernius, D. Boumediene, J. Brau, D. Cinca, C. Doglioni, C. Escobar, K. Flavia Loureiro, D. Gillberg, J. Godfrey, Z. Greenwood, P. Haefner, D. Hellmich, J. Kroseberg, H. Liao, A. C. Martyniuk, D. Lopez Mateos, S. Marti i Garcia, R. Moles, M. Moren Llacer, A. Mc Carn, M. Neubauer, H. Okawa, D. ONeil, D. Pallin, T. Perez, M. A. Pleier, S. Protopopescu, R. Rajagopalan, J. Schovancova, A. Schwartzman, J. Searcy, A. Taffard, Y. Takahashi, M. Tomoto, M. F. Watson, and U. K. Yang, *Jets, Missing Transverse Energy and Taus for Top Physics Analyses in Release 16 with the 2010 Dataset*, ATL-COM-PHYS-2011-132, CERN, Geneva, Feb, 2011.

[86] S. Catani, Y. L. Dokshitzer, M. Olsson, G. Turnock, and B. Webber, *New clustering algorithm for multi - jet cross-sections in e+ e- annihilation*, Phys.Lett. **B269** (1991) 432–438.

[87] S. Catani, Y. L. Dokshitzer, M. Seymour, and B. Webber, *Longitudinally invariant $K_t$ clustering algorithms for hadron hadron collisions*, Nucl.Phys. **B406** (1993) 187–224.

[88] M. Cacciari and G. P. Salam, *Dispelling the $N^3$ myth for the $k_t$ jet-finder*, Phys.Lett. **B641** (2006) 57–61, `arXiv:hep-ph/0512210 [hep-ph]`.

[89] P. A. Delsart, *$k_T$ Algorithms in Athena: timing performances and new implementation*, ATL-COM-SOFT-2006-007, CERN, Geneva, Jun, 2006.

[90] Y. L. Dokshitzer, G. Leder, S. Moretti, and B. Webber, *Better jet clustering algorithms*, JHEP **9708** (1997) 001, `arXiv:hep-ph/9707323 [hep-ph]`.

[91] M. Cacciari, G. P. Salam, and G. Soyez, *The Anti-k(t) jet clustering algorithm*, JHEP **0804** (2008) 063, `arXiv:0802.1189 [hep-ph]`.

[92] *Jet energy scale and its systematic uncertainty in proton-proton collisions at sqrt(s)=7 TeV in ATLAS 2010 data*, ATLAS-CONF-2011-032, CERN, Geneva, Mar, 2011.

[93] *Properties of Jets and Inputs to Jet Reconstruction and Calibration with the ATLAS Detector Using Proton-Proton Collisions at* $\sqrt{s}$ = 7 *TeV*, ATLAS-CONF-2010-053, CERN, Geneva, Jul, 2010.

[94] *Determination of the ATLAS jet energy measurement uncertainty using photon-jet events in proton-proton collisions at sqrts = 7 TeV*, ATLAS-CONF-2011-031, CERN, Geneva, Mar, 2011.

[95] *Probing the jet energy measurement at the TeV-scale using the multi-jet balance technique in proton-proton collisions at sqrt(s) =7 TeV*, ATLAS-CONF-2011-029, CERN, Geneva, Mar, 2011.

[96] *ATLAS Calorimeter Response to Single Isolated Hadrons and Estimation of the Calorimeter Jet Scale Uncertainty*, ATLAS-CONF-2011-028, CERN, Geneva, Mar, 2011.

[97] K. Terashi, *Close-by Jet Effects on Jet Energy Scale Calibration in pp Collisions at sqrt(s)=7 TeV with the ATLAS Detector*, ATLAS-COM-CONF-2011-060, CERN, Geneva, Mar, 2011.

[98] *JetUncertainties*, `https://svnweb.cern.ch/cern/wsvn/atlasoff/Reconstruction/Jet/JetUncertainties/tags/JetUncertainties-00-03-01/`.

[99] *Jet energy resolution and selection efficiency relative to track jets from in-situ techniques with the ATLAS Detector Using Proton-Proton Collisions at a Center of Mass Energy sqrts = 7 TeV*, ATLAS-CONF-2010-054, CERN, Geneva, Jul, 2010.

[100] *JetResolutionPreliminaryResults*, `https://twiki.cern.ch/twiki/bin/view/AtlasPublic/JetResolutionPreliminaryResults`.

[101] *TopJetReconstructionEfficiency*, `https://twiki.cern.ch/twiki/bin/view/AtlasProtected/TopJetReconstructionEfficiency`.

[102] J. F. Arguin, D. Boumediene, M. Bondioli, G. Cortiana, M. Costa Mezquita, C. Cowden, P.-O. DeViveiros, C. Doglioni, J. Erdmann, J. Ferrando, A. Gaponenko, N. Ghodbane, C. Issever, H. Liao, P. Kovesarki, K. Kroeninger, B. Lemmer, J.-R. Lessard, M. Losada, S. Marti I Garcia, K. Loureiro Mattioli, M. Moreno Llacer, R. Nisius, H. Okawa, M. Petteni, R. Piegaia, S. Psoroulas, G. Romeo, F. Ruehr, F. Span, D. Urbaniec, D. Lopez Mateos, S. Adomeit,

O. Biebel, M.-A. Pleier, J. Kroseberg, D. Hellmich, U. Yang, A. Martyniuk, and D. Pallin, *Jet selection for top physics*, ATL-PHYS-INT-2010-134, CERN, Geneva, Dec, 2010.

[103] B. Alvarez, V. Boisvert, B. Clement, B. Cooper, T. Delemontex, J. Donini, L. Feligioni, A. Ferretto Parodi, F. Filthaut, F. Garberson, B. Guo, T. Golling, R. Goncalo, M. Hirose, F. Hirsch, L. Heinrich, J. Holzbauer, C. Jung, C. Kendziorra, A. Khanov, J. Kvita, C. Liu, A. Lucotte, M. zur Nedden, F. Parodi, A. Poll, F. Rizatdinova, M. Rose, L. Rossi, M. Saleem, R. Schwienhorst, P. Sinervo, C. Schiavi, K. Suruliz, M. Talby, N. Tannoury, B. Walsh, J. Wang, and C. Weydert, *b-jet Tagging for Top Physics: Perfomance studies, Calibrations and Heavy Flavor Fractions*, ATL-COM-PHYS-2011-124, CERN, Geneva, Feb, 2011.

[104] *Performance of Impact Parameter-Based b-tagging Algorithms with the ATLAS Detector using Proton-Proton Collisions at s = 7 TeV*, ATLAS-CONF-2010-091, CERN, Geneva, Oct, 2010.

[105] B. Heinemann, F. Hirsch, and S. Strandberg, *Performance of the ATLAS Secondary Vertex b-tagging Algorithm in 7 TeV Collision Data*, ATLAS-COM-CONF-2010-042, CERN, Geneva, May, 2010. (Was originally 'ATL-COM-PHYS-2010-274').

[106] *Calibrating the b-Tag and Mistag Efficiencies of the SV0 b-Tagging Algorithm in 3 $pb^{-1}$ of Data with the ATLAS Detector*, ATLAS-CONF-2010-099, CERN, Geneva, Dec, 2010.

[107] S. Aoun, J. Boudreau, J. Fleckner, F. Hirsch, C. Jung, J. Mueller, S. Strandberg, and M. Talby, *Calibration of b-Jet Tagging Efficiency using the $p_T^{rel}$ Method*, ATL-COM-PHYS-2011-043, CERN, Geneva, Jan, 2011. Preliminary version for Ed Board discussions.

[108] J. Boudreau, B. Clement, T. Delemontex, L. Feligioni, F. Filthaut, A. Lucotte, M. Muller, J. Mueller, K. Sapp, S. Strandberg, M. Talby, N. Tannoury, L. Vacavant, M. Verducci, G. Watts, and C. Weiser, *b-Jet Tagging Efficiency Calibration using the System8 Method*, ATL-COM-PHYS-2011-033, CERN, Geneva, Jan, 2011.

[109] F. Parodi, A. Ferretto, C. Schavi, A. Coccaro, and L. Rossi, *b-tagging calibration with $D^{star}$mu reconstructed in 7 TeV collisions with ATLAS*, ATL-COM-PHYS-2011-051, CERN, Geneva, Jan, 2011.

[110] T. Golling, B. Guo, C. Liu, T. Meguro, M. zur Nedden, J. Schwindling, P. Sinervo, K. Uchida, and J. Yu, *B-tagging calibration in ttbar final states and ttbar cross*

*section measurememts with ATLAS data at sqrts = 7 TeV*, ATL-COM-PHYS-2011-048, CERN, Geneva, Jan, 2011.

[111] F. Garberson and T. Golling, *Measurement of the mistag efficiency in Atlas data from ts to the SV0-mass of the tagged jets*, ATL-COM-PHYS-2011-029, CERN, Geneva, Jan, 2011.

[112] M. Saleem, A. Khanov, and F. Rizatdinova, *Measurement of the Mistag Rate in ATLAS Data*, ATL-COM-PHYS-2011-046, CERN, Geneva, Jan, 2011.

[113] *Release 16 Calibrations to be used for Winter 2010 conferences*, `https://twiki.cern.ch/twiki/bin/view/AtlasProtected/Analysis16`.

[114] *TriggerPhysicsMenu*, `https://twiki.cern.ch/twiki/bin/view/Atlas/TriggerPhysicsMenu`.

[115] *TopD2PD2010*, `https://twiki.cern.ch/twiki/bin/view/AtlasProtected/TopD2PD2010`.

[116] *TopPhysD2PDEventFilters2010*, `https://twiki.cern.ch/twiki/bin/view/AtlasProtected/TopPhysD2PDEventFilters2010`.

[117] *TopGRLs*, `https://twiki.cern.ch/twiki/bin/view/AtlasProtected/TopGRLs`.

[118] *Autumn 2010 Reprocessing Campaign*, `https://twiki.cern.ch/twiki/bin/viewauth/Atlas/DataPreparationReprocessing#Autumn_2010_Reprocessing_Campaig`.

[119] *DataPeriods*, `https://twiki.cern.ch/twiki/bin/view/AtlasProtected/DataPeriods`.

[120] *Updated Luminosity Determination in pp Collisions at root(s)=7 TeV using the ATLAS Detector*, ATLAS-CONF-2011-011, CERN, Geneva, Mar, 2011.

[121] *CoolLumiCalc*, `https://twiki.cern.ch/twiki/bin/view/Atlas/CoolLumiCalc`.

[122] ATLAS Collaboration, G. Aad et al., *Luminosity Determination in pp Collisions at sqrt(s)=7 TeV Using the ATLAS Detector at the LHC*, Eur.Phys.J. **C71** (2011) 1630, `arXiv:1101.2185 [hep-ex]`.

[123] M. Baak, C. Guyot, M. Hauschild, R. Hawkings, B. Heinemann, A. Hcker, M. Martnez-Prez, D. Malon, P. Onyisi, and E. Torrence, *Data Quality Status Flags and Good Run Lists for Physics Analysis in ATLAS*, ATL-COM-GEN-2009-015, CERN, Geneva, Mar, 2009.

[124] *ATLAS Good Run List Generator*, `https://atlasdqm.cern.ch/grl/`.

[125] M. Dobbs, S. Frixione, E. Laenen, K. Tollefson, H. Baer, et al., *Les Houches guidebook to Monte Carlo generators for hadron collider physics*, `arXiv:hep-ph/0403045 [hep-ph]`. Compiled by the Working Group on Quantum Chromodynamics and the Standard Model.

[126] ATLAS Collaboration, G. Aad et al., *The ATLAS Simulation Infrastructure*, Eur.Phys.J. **C70** (2010) 823–874, `arXiv:1005.4568 [physics.ins-det]`.

[127] *The Common Parameters used for ATLAS MC Production 2010*, `https://twiki.cern.ch/twiki/bin/view/AtlasProtected/McProductionCommonParameters`.

[128] A. G. Buckley and H. Schulz, *First tuning of HERWIG/JIMMY to ATLAS data*, ATL-COM-PHYS-2010-620, CERN, Geneva, Aug, 2010.

[129] *Charged particle multiplicities in p p interactions at $\sqrt{s}$ = 0.9 and 7 TeV in a diractive limited phase-space measured with the ATLAS detector at the LHC and new PYTHIA6 tune*, ATLAS-CONF-2010-031, CERN, Geneva, Jul, 2010.

[130] M. Mangano and T. Stelzer, *Tools for the simulation of hard hadronic collisions*, Ann.Rev.Nucl.Part.Sci. **55** (2005) 555–588.

[131] S. Frixione and B. R. Webber, *Matching NLO QCD computations and parton shower simulations*, JHEP **06** (2002) 029, `arXiv:hep-ph/0204244`.

[132] S. Frixione and B. R. Webber, *The MC@NLO 3.4 Event Generator*, arXiv:0812.0770. CAVENDISH-HEP-08-14, Dec, 2008. Comments: 30 pages.

[133] M. L. Mangano, M. Moretti, F. Piccinini, R. Pittau, and A. D. Polosa, *ALPGEN, a generator for hard multiparton processes in hadronic collisions*, JHEP **07** (2003) 001, `arXiv:hep-ph/0206293`.

[134] G. Corcella et al., *HERWIG 6.5: an event generator for Hadron Emission Reactions With Interfering Gluons (including supersymmetric processes)*, JHEP **01** (2001) 010, `arXiv:hep-ph/0011363`.

[135] G. Corcella et al., *HERWIG 6.5 release note*, `arXiv:hep-ph/0210213`.

[136] T. Sjostrand, S. Mrenna, and P. Z. Skands, *PYTHIA 6.4 Physics and Manual*, JHEP **05** (2006) 026, `arXiv:hep-ph/0603175`.

[137] S. Alioli, P. Nason, C. Oleari, and E. Re, *A general framework for implementing NLO calculations in shower Monte Carlo programs: the POWHEG BOX*, JHEP **1006** (2010) 043, `arXiv:1002.2581 [hep-ph]`.

[138] A. Shibata, M. Bosman, R. Hawkings, U. Husemann, S. Allwood-Spiers, L. Mijovic, B. Kersevan, G. Khoriauli, N. F. Castro, A. Lucotte, J. Donini, C. Feng, W. Verkerke, L. Fiorini, S. Grinstein, A. Gaponenko, D. Whiteson, B. Cooper, A. Messina, M. Gosselink, N. Vlasov, and M. Cristinziani, *Understanding Monte Carlo Generators for Top Physics*, ATL-COM-PHYS-2009-334, CERN, Geneva, Jun, 2009.

[139] M. Asai, *Geant4-a simulation toolkit*, Trans.Amer.Nucl.Soc. **95** (2006) 757.

[140] J. Allison, K. Amako, J. Apostolakis, H. Araujo, P. Dubois, et al., *Geant4 developments and applications*, IEEE Trans.Nucl.Sci. **53** (2006) 270.

[141] D. Cavalli, D. Costanzo, S. Dean, M. Dhrssen, S. Hassani, M. Heldmann, K. Jakobs, A. Nairz, A. Phillips, S. Resconi, E. Richter-Was, P. Sherwood, L. Vacavant, I. Vivarelli, J. B. De Vivie de Rgie, and I. Wingerter-Seez, *Performance of the ATLAS fast simulation ATLFAST*, ATL-PHYS-INT-2007-005. ATL-COM-PHYS-2007-012, CERN, Geneva, Jan, 2007.

[142] *TopMC2010*, https://twiki.cern.ch/twiki/bin/view/atlasprotected/TopMC2010.

[143] *Heavy Flavor Overlap Removal Tool*, https://twiki.cern.ch/twiki/bin/view/AtlasProtected/HforTool.

[144] *TopCommonObjects2010*, https://twiki.cern.ch/twiki/bin/view/AtlasProtected/TopCommonObjects2010.

[145] *L+jets MC Challenge: Moriond Rel.16*, https://espace.cern.ch/topxsec/Lists/Ljets%20MC%20Challenge%20Moriond%20Rel16/AllItems.aspx.

[146] N. Benekos, K. Benslama, S. Caughron, L. Cerrito, V. Dao, F. Derue, J. Erdmann, V. Ferrara, P. Ferrari, L. Fiorini, I. Fleck, S. Heim, A. Henrichs, S. Hasegawa, K. Ikematsu, H. Kandanyan, B. Kaplan, A. Krasznahorkay, J. R. Lessard, T. McLaughlan, Y. Ming, Y. Okumura, J. Palmer, A. J. Poll, O. Rosenthal, P. Ryan, A. Roe, G. Salamanna, R. Schwienhorst, T. Theveneaux-Pelzer, and H. Zhu, *Lepton trigger and identification for the Winter 2011 top quark analyses*, ATL-COM-PHYS-2011-123, CERN, Geneva, Feb, 2011. Supporting document for Winter 2011 top physics measurements.

[147] *PAUcaloIsolationTool*, https://twiki.cern.ch/twiki/bin/view/AtlasProtected/PAUcaloIsolationTool.

[148] *Electron/Gamma Object Quality Maps*, https://twiki.cern.ch/twiki/bin/view/AtlasProtected/ObjectQualityMaps.

[149] M. Agustoni, M. Aharrouche, A. Ahmad, N. Besson, M. Boonekamp, L. Carminati, J. de Vivie, H. De La Torre, J. Del Peso, J. Farley, V. Gallo, S. Glazov, C. Handel, S. Haug, M. Karnevskiy, I. Koletsou, N. Lorenzo Martinez, N. Makovec, L. Mandelli, Y. Nakahama, R. Turra, and G. Unal, *Electromagnetic energy scale in-situ calibration and performance: Supporting document for the egamma performance paper*, ATL-COM-PHYS-2011-263, CERN, Geneva, Mar, 2011.

[150] *Electron Energy Scale Offset and Resolution Smearing Results*, `https://svnweb.cern.ch/trac/atlasgrp/browser/CombPerf/EGamma/Calibrations/EnergyRescalerTool/tags/EnergyRescalerTool-00-00-06/EnergyRescaler.cxx`.

[151] *Muon Momentum Resolution in First Pass Reconstruction of pp Collision Data Recorded by ATLAS in 2010*, ATLAS-CONF-2011-046, CERN, Geneva, Mar, 2011.

[152] *Muon Momentum Scale and Resolution Updated in Release 16*, `https://svnweb.cern.ch/trac/atlasoff/browser/PhysicsAnalysis/MuonID/MuonIDAnalysis/MuonMomentumCorrections/tags/MuonMomentumCorrections-00-01-02/root/SmearingClass.h`.

[153] *JetEnergyResulutionProvider*, `https://twiki.cern.ch/twiki/bin/view/Main/JetEnergyResolutionProvider`.

[154] *HowToCleanJets*, `https://twiki.cern.ch/twiki/bin/view/AtlasProtected/HowToCleanJets#Bad_jets_rel16_data`.

[155] H. S. Bansil, E. F. Berglund, J. Bracinik, J. T. Childers, D. Damazio, V. Dao, O. Davignon, X. A. Del Popolo, M. Dieli, M. Goebel, A. Hamilton, D. Hayden, S. Heim, K. Heine, T. Kono, Z. Liang, F. Monticelli, P. R. Newman, A. Ruiz Martinez, G. Siragusa, R. Stamen, A. Tricoli, M. Wielers, and H. Zhang, *Performance of the Electron and Photon Trigger in p-p Collisions at sqrt(s) = 7 TeV*, ATL-COM-DAQ-2011-008, CERN, Geneva, Jan, 2011.

[156] *Electron/Gamma Efficiency Measurements*, `https://twiki.cern.ch/twiki/bin/view/AtlasProtected/EfficiencyMeasurements`.

[157] O. Arnaez and D. Froidevaux, *Electron efficiency measurements using ATLAS 2010 data at sqrt(s) = 7 TeV: Supporting note for the 2010 egamma paper*, ATL-COM-PHYS-2011-322, CERN, Geneva, Mar, 2011.

[158] B. Acharya, I. Besana, L. Bellagamba, G. Bruni, M. Cobal, M. Cristinziani, A. Favareto, T. Lari, A. Leyko, V. Lombardo, F. Meloni, M. Pinamonti, U. De Sanctis, J. Schwindling, K. Shaw, R. Di Sipio, R. Soualah, K. Suruliz,

C. Troncon, and J. Yu, *Cut-and-count measurement of the top quark pair production in the semileptonic decay channel at sqrt(s)=7 TeV with the ATLAS detector*, ATL-COM-PHYS-2011-122, CERN, Geneva, Feb, 2011.

[159] *TopSystematicUncertaities2010*, https://twiki.cern.ch/twiki/bin/view/AtlasProtected/TopSystematicUncertainties2010.

[160] M. Bosman, L. Fiorini, C. Helsens, A. Juste, L. Mir, J. Nadal, and V. Vorwerk, *Weighting method to propagate heavy-flavor tagging calibrations and related uncertainties*, ATL-COM-PHYS-2010-331, CERN, Geneva, Jun, 2010.

[161] ATLAS Collaboration, G. Aad et al., *Measurement of the top quark-pair production cross section with ATLAS in pp collisions at $\sqrt{s} = 7$ TeV*, Eur.Phys.J. **C71** (2010) 1577, arXiv:1012.1792 [hep-ex].

[162] B. Abi, M. Aletti, J.-F. Arguin, W. H. Bell, M. Bunse, R. Calkins, D. Chakraborty, V. Dao, T. Golling, B. Heinemann, F. Hirsch, D. Jana, K. Johns, V. Kaushik, A. Khanov, X. Lei, A. Lister, S. Nektarijevic, F. Rizatdinova, K. Rosbach, M. Saleem, P. Skubic, C. Suhr, and I. Watson, *Measurement of the Top Pair Production Cross Section in 7 TeV Proton-Proton Collisions using Pretag Kinematics*, ATL-COM-PHYS-2011-104, CERN, Geneva, Jan, 2011.

[163] M. Bosman, V. Ferrara, P. Ferrari, L. Fiorini, H. Garitaonandia, D. Geerts, C. Helsens, A. Henrichs, A. Juste, A. Keil, C. Lange, L. M. Mir, I. Mussche, O. Nackenhorst, J. Nadal, A. Quadt, A. Roe, E. Shabalina, G. Salamanna, D. Ta, M. Tsiakiris, W. Verkerke, V. Vorwerk, M. Vreeswijk, and H. Zhu, *Measurement of the top quark cross-section in the semileptonic channel at $sqrts = 7TeV$ with the ATLAS detector*, ATL-COM-PHYS-2011-111, CERN, Geneva, Feb, 2011.

[164] B. Abi, M. Bosman, V. Dao, L. Fiorini, K. Gellerstedt, C. Helsens, A. Henrichs, U. Husemann, J. Juste, C. Lange, A. Leyko, A. Lister, L. Mir, J. Nadal, M. Owen, M. Pinamonti, F. Rizatdinova, A. Roe, M. Saleem, E. Shabalina, J. Sjolin, and V. Vorwerk, *Mis-identified lepton backgrounds to top quark pair production for Moriond 2011 analysis*, ATL-COM-PHYS-2011-144, CERN, Geneva, Feb, 2011.

[165] *Jet Energy Scale Systematics for Multi-jet Analysis*, https://indico.cern.ch/getFile.py/access?contribId=3&resId=0&materialId=slides&confId=95052.

[166] *Multi-jet JES Uncertainty Provider*, https://indico.cern.ch/getFile.py/access?contribId=8&sessionId=1&resId=0&materialId=slides&confId=102861.

[167] *TopPdfUncertainty*, https://twiki.cern.ch/twiki/bin/view/AtlasProtected/TopPdfUncertainty.

[168] *Updated W+jets reweighting functions*, https://espace.cern.ch/topxsec/ljets/Lists/Posts/Post.aspx?List=d9d2475f%2D7439%2D4cf2%2Da834%2D59d6607cd956&ID=110.

[169] *TopFakes*, https://twiki.cern.ch/twiki/bin/view/AtlasProtected/TopFakes.

[170] CMS Collaboration, V. Khachatryan et al., *First Measurement of the Cross Section for Top-Quark Pair Production in Proton-Proton Collisions at sqrt(s)=7 TeV*, Phys.Lett. **B695** (2011) 424–443, arXiv:1010.5994 [hep-ex].

[171] B. Abi, M. Aletti, J. Arguin, W. Bell, M. Bunse, R. Calkins, D. Chakraborty, V. Dao, T. Golling, A. Henrichs, F. Hirsch, D. Jana, K. Johns, V. Kaushik, A. Khanov, X. Lei, A. Lister, S. Nektarijevic, F. Rizatdinova, K. Rosbach, M. Saleem, P. Skubic, C. Suhr, I. Watson, B. Acharya, M. Besana, L. Bellagamba, G. Bruni, M. Cobal, M. Cristinziani, A. Favareto, T. Lari, A. Leyko, V. Lombardo, F. Meloni, M. Pinamonti, U. d. Sanctis, J. Schwindling, K. Shaw, R. di Sipio, R. Soualah, K. Suruliz, C. Troncon, and J. Yu, *Top Quark Pair Production Cross-section Measurements in ATLAS in the Single Lepton+Jets Channel without b-tagging*, ATLAS-COM-CONF-2011-031, CERN, Geneva, Feb, 2011. CONF note number ATLAS-CONF-2011-023.

[172] The Top Quark Group, L. Bellagamba, M. I. Besana, M. Bosman, G. Bruni, M. Cobal, M. Cristinziani, A. Favareto, V. Ferrara, P. Ferrari, L. Fiorini, H. Garitaonandia, D. Geerts, C. Helsens, A. Henrichs, U. Husemann, A. Juste, M. Keil, C. Lange, T. Lari, A. Leyko, V. Lombardo, F. Meloni, L. M. Mir, I. Mussche, O. Nackenhorst, J. Nadal, M. Pinamonti, A. Quadt, A. Roe, G. Salamanna, U. Sanctis (de), J. Schwindling, E. Shabalina, K. Shaw, R. Sipio (di), R. Soualah, K. Suruliz, D. Ta, C. Troncon, M. Tsiakiris, L. Vacavant, W. Verkerke, V. Vorwerk, M. Vreeswijk, J. Yu, and H. Zhu, *Measurement of the top quark-pair cross-section with ATLAS in pp collisions at sqrt(s) = 7 TeV in the single-lepton channel using b-tagging*, ATLAS-COM-CONF-2011-028, CERN, Geneva, Feb, 2011.

[173] *Charged particle multiplicities in pp interactions at sqrt(s) = 7 TeV measured with the ATLAS detector at the LHC*, ATLAS-CONF-2010-024, CERN, Geneva, Jul, 2010.